Influence of sintering additives and substitution on magnetic and dielectric properties of Co_2Z hexaferrite

A
Thesis
Submitted for the award of degree of

Doctor of Philosophy

By

Anoop Pratap Singh

(Registration No. 901412008)

Under the supervisions of

Dr. Puneet Sharma

&

Dr. O. P. Pandey

THAPAR INSTITUTE
OF ENGINEERING & TECHNOLOGY
(Deemed to be University)

School of Physics & Materials Science

Thapar Institute of Engineering & Technology, Patiala (147004),
Punjab (India)

March 2022

Dedicated to my
Parents & God

Contents

CERTIFICATE

This is to certify that the thesis entitled “**Influence of sintering additives and substitution on magnetic and dielectric properties of Co_2Z hexaferrite**” which is being submitted by Anoop Pratap Singh for the award of the degree Doctor of Philosophy in School of Physics & Materials Science, Thapar Institute of Engineering & Technology (TIET), Patiala is an authentic record of candidate’s own work carried out by him under our supervision. The matter presented in this thesis has not been submitted in part or full for the award of any degree in any other University or Institute.

Date:

Place: Patiala

Dr. Puneet Sharma

(Professor)
School of Physics & Materials Science
Thapar Institute of Engineering &
Technology, Patiala (147004), Punjab.

Dr. O. P. Pandey

(Senior Professor)
School of Physics & Materials Science
Thapar Institute of Engineering &
Technology, Patiala (147004), Punjab.

Acknowledgement

First and foremost, I would like to express my sincere gratitude to my both advisors, **Dr. Puneet Sharma** (Professor) and **Dr. O. P. Pandey** (Senior Professor), School of Physics and Materials Science (SPMS), Thapar Institute of Engineering and Technology (TIET) Patiala, Punjab, for their unconditional support, patience, motivation, during my stay at TIET. Their advice was invaluable throughout my thesis research and writing. This thesis would not have been possible without their encouragement and support. I will be eternally grateful to them for their continuous support.

I offer my special thanks to **Dr. Kulvir Singh** (Professor), Head, School of Physics & Materials Science, Thapar Institute of Engineering & Technology (TIET), Patiala, for providing all the necessary facilities in the department. I extend my gratitude to my doctoral committee members **Dr. S. D. Tiwari**, **Dr. D. P. Singh**, and **Dr. Rajesh Khanna** and all faculty members of the SPMS who supported and encouraged me especially, **Dr. B. N. Chudasama** and **Dr. Jayant Kolte**.

I am thankful to my seniors **Dr. Samiksha Verma**, **Dr. Shivani Malhotra**, and fellow labmates **Dr. Chhavi Pahwa**, **Dr. Santhoshkumar Mahadevan**, **Dr. Shivani Jindal**, **Mr. Parminder Singh**, **Ms. Sonal Singh**, **Ms. Anupriya Choudhary**, and **Ms. Hemanita Sharma**.

I would like to thank SAI Lab, Thapar Institute of Engineering & Technology for XRD and SEM facility.

I am grateful to all non-teaching staff of School of Physics and Materials Science who never turn me down whenever I approached for any help.

I gratefully acknowledge the **Visvesvaraya Ph.D. Scheme (DoRSP/Deity/1637), Ministry of Electronics and Information Technology (MeitY), Government of India, New Delhi-110003 (India)**, for the financial support in the form of Junior Research Fellow and Senior Research Fellow.

I gratefully acknowledge DST-FIST for providing magnetic measurement facility.

I would like to convey my sincere gratitude to my friends **Dr. Satwinder Singh**, **Dr. Prabal Pratap Singh**, **Dr. Ayush Gupta**, **Dr. Gaurav Singla**, **Dr. Paramjot Jha**, and **Dr. Rohit Gupta** for creating cheerful atmosphere during my stay.

I am highly thankful to my parents **Shri Suresh Singh**, and **Smt. Rajkumari Singh** for their love, encouragement, and moral support during my study. I like to mention my special thanks to my wife **Mrs. Aparna Singh Bais** for her close companionship, sacrifices, constant inspiration, and encouragement.

Above all, I pay my profound gratitude to The Almighty God for giving me strength, love and blessings.

Anoop Pratap Singh

List of publications

1. **Anoop Pratap Singh**, O.P. Pandey and Puneet Sharma, Impedance spectroscopy and magnetic studies on Co_2Z ferrite sintered with SiO_2 and Bi_2O_3 additives, Mater. Chem. Phys. **277**, 125574 (2022).
2. **Anoop Pratap Singh**, O.P. Pandey and Puneet Sharma, Impedance spectroscopy and magneto-dielectric analysis of La^{3+} substituted Co_2Z hexaferrite, Ceram. Int. **47**, 22550-22557 (2021).
3. **Anoop Pratap Singh**, O.P. Pandey and Puneet Sharma, Effect of Sintering Additives on Structural, Magnetic and Dielectric Properties of $Ba_3Co_2Fe_{24}O_{41}$ Ferrite, J. Supercond. Nov. Magn. **33**, 519-526 (2020).

Other publications

1. Samiksha Verma, Santhoshkumar Mahadevan, Chhavi Pahwa, **Anoop Pratap Singh**, Sukhleen Bindra, Neha Aggrawal and Puneet Sharma, Improved Magnetic and Microwave Properties of La-Substituted Barium Hexaferrite Screen-Printed Thick Films, J. Supercond. Nov. Magn. **33**, 2507-2512 (2020).

List of Conferences (National/International)

1. Webinar **invited talk** on "Magnetic and Dielectric properties of La^{3+} substituted Co_2Z hexaferrite for anti-electromagnetic shielding, anti-radar interference and electronic digital data storage devices" in Word Congress on Advanced Nano Science Nanotechnology at **Belgium** on 20-21 July 2021.
2. **Oral presentation** on "Impedance spectroscopy and Magneto-capacitance analysis of Ca^{2+} substituted Co_2Z Hexaferrite" in National Conference on Nanomaterials for Energy and Advanced Technologies (NEAT-2021) at DIT University, Dehradun on 25- 26 March 2020.
3. **Oral presentation** on "Structural, magnetic and dielectric properties of La^{3+} substituted Co_2Z hexaferrites for tele-communicational antennas and EMI shielding applications" in International Conference on Materials Science and Engineering at Kyoto Research Park, **Kyoto**, **Japan** on 26-28 December 2019.
4. **Oral presentation** on "Effect of various additives on microstructure and magnetic properties of Z-type hexaferrite" in National conference on Physics and Chemistry of Materials at Maharaja Agrasen Institute of Technology (MAIT) on 22-23 April 2019.

5. Attend national symposium on materials for advanced technology (MAT-2017), DIT University, Dehradun on 20-21 February, 2017 (**Best Poster Award**).
6. Attended International Conference on Magnetic Materials and Applications (ICMAGMA2017), at Defense Metallurgical Research Laboratory (DMRL), Hyderabad and Magnetics Society of India on 1-3 February, 2017 (Poster Presentation).
7. Attended Summer School on Magnetism (SSM-2016), at Thapar University, Patiala (Punjab) on 11-15 July 2016.
8. **Oral presentation** on "Effect of two step preparation on structural and magnetic properties of Z-type hexaferrite in a National Conference on "Advanced Material Processing & Characterization", under the American Chemical Society (ACS), Chandigarh University, Chandigarh on 27 May 2016.

Workshops

1. Attend four days webinar workshop on Modern Approach on Magnetism and Material Science in Engineering organized by Department of Physics, Maharaja Institute of Technology Mysore and IEEE on 15-18 September 2020.
2. Attended webinar five days on Recent Trends in Advanced Materials and Devices organized by Department of Physics and Department of Electronics & Communication Engineering, Dr. B. R. Ambedkar National Institute of Technology Jalandhar on 21-25 September 2020.
3. Attend one day webinar workshop on Innovation in Antenna Design and Analysis organized by IEEE, RFID, Amity and Altair India on 9 July 2020.
4. Attend two days webinar workshop on MIMO Antennas for 5G Communications using CST studio suite organized by Department of Electronics Science, University of Delhi, South Campus, New Delhi and Jyoti Electronics, Ahmedabad on 5-6 June 2020.
5. Attend workshop of Visvesvaraya Ph.D. Scheme for Electronics & IT/ITES second workshop for presentation of research work at Indian Institute of Science, Bengaluru on 20-21 February, 2017.
6. Attend National Workshop on Advanced Techniques for Surface Characterization, Thapar University, Patiala (Punjab) on 28-30 October 2015.
7. Attend workshop on Nano Science & Technology at Beant College of Engineering & Technology, Gurdaspur, (Punjab) on 13-17 April 2015 **(Best Poster Award).**

List of Figures

List of Tables

List of Symbols

M_s	Saturation magnetization
H_c	Coercivity
M_r	Remanent magnetization
T_c	Curie Temperature
D	Crystallite size
ε'	Real permittivity
ε''	Imaginary permittivity
Z'	Real impedance
Z''	Imaginary impedance
Z''/Z''_{max}	Scaling of Imaginary impedance
ω/ω_{max}	Scaling of angular frequency
M'	Real electric modulus
M''	Imaginary electric modulus
μ	Permeability
Ω	Angular frequency
T	Tesla
Oe	Oerested
χ^2	Chi square
R_p	Profile residue factor
R_{wp}	Weighted profile
R_{exp}	Expected profile
σ	Conductivity
α_E	Magneto-dielectric coefficient
H_a	Magnetic anisotropy
μ_B	Bohr magneton

f_m	Peak frequency of loss spectra
E_g	Activation energy
C_g	Grain capacitance
C_{gb}	Grain boundary capacitance
R_g	Grain resistance
R_{gb}	Grain boundary resistance
CPE	Constant phase element
n	Exponent factor for conductivity
R_0	Pre-exponent of resistance
τ	Relaxation time
τ_0	Pre-exponent of relaxation time
$tan\delta_\varepsilon/\varepsilon'$	Form of dielectric loss
$tan\delta_\mu/\mu'$	Form of magnetic loss
P	Electric polarization
B	Magnetic field
E	Electric field
Q	Quality factor
λ	Wavelength
μ_i	Initial permeability
RL	Reflection loss
BW	Band width
η_0	Impedance of free space
f_r	Cut-off frequency
$n = \sqrt{\mu\varepsilon}$	Miniaturization factor
ρ	resistivity
A	Cross sectional area of pellet
t	Thickness of pellet

$\hbar$	Dirac constant
V	Applied *ac* voltage
I	Applied *ac* current
Ψ	Phase difference between V & I
k	Boltzmann Constant

Abbreviations used

Co_2Z	Z-type ($Ba_3Co_2ZFe_{24}O_{41}$)
M-type	$BaFe_{12}O_{19}$
Y-type	$Ba_2Co_2Fe_{12}O_{22}$
W-type	$BaCo_2Fe_{16}O_{27}$
M-H	Magnetic hysteresis loop
RT	Room temperature
XRD	X-ray diffraction
SEM	Scanning Electron Microscopy
VSM	Vibrating Sample Magnetometer
FTIR	Fourier transform infrared radiation
nm	Nanometre
μm	Micrometre
Hz	Hertz
kHz	Kilohertz
MHz	Megahertz
GHz	Gigahertz
MR	Magneto-electric resistance
FWHM	Full width at half maxima
MCA	Magneto-crystalline anisotropy
ME	Magneto-electric
MD	Magneto-dielectric
FMR	Ferromagnetic resonance frequency

Preface

Co_2Z ferrite ($Ba_3Co_2Fe_{24}O_{41}$) has gained considerable attention in high-frequency microwave devices. The ferromagnetic resonance of 1.3 GHz and low losses at microwave frequencies makes it a suitable material for miniaturized mobile and wireless LAN communication. Co_2Z ferrite also exhibits magneto-electric (*ME*) coupling for application in nonvolatile memories, spintronics, and microwave devices. The magnetic and dielectric properties of Z-type ferrites were studied with different cations substitutions for Ba^{2+}, $Co^{2+,}$ and Fe^{3+}. The dielectric loss of the material is associated with the microstructural characteristics namely grain size, shape, and the concentration of the porosity. The higher temperature sintering improves the dielectric losses due to the grain growth and the reduction of the Fe^{3+} into Fe^{2+}. The magnetic and dielectric losses can be minimized with the varying sintering process conditions, time, and temperature. Some sintering additives are also used to modify the magnetic, dielectric, and microstructural features. Additives facilitate to form liquid phase along the grain boundary and lead to refining the grains. The small grain size significantly decreases the dielectric losses. Recently the dielectric properties and impedance spectroscopy of Z-type hexaferrite have been investigated in GHz. At higher frequencies, the contribution of grain boundary is very difficult to achieve. Generally, the electrical response of the grain and grain boundaries are obtained in the frequency range of 10 kHz to 1 MHz.

In this dissertation, Z-type hexaferrite ($Ba_3Co_2Fe_{24}O_{41}$) is synthesized and the effect of the various sintering additives (SiO_2, MgO, Al_2O_3 & Bi_2O_3) and cation substitutions (La^{3+}, Ca^{2+} for Ba^{2+} and Al^{3+} for Fe^{3+}) on structural, magnetic and dielectric properties were investigated.

Chapter 1 (Introduction)

In this chapter, a brief introduction and classification of the hexaferrites are given. The magneto-crystalline anisotropy properties and the crystal structure of Co_2Z hexaferrite are discussed in brief. Various applications of Z-type ferrites are mentioned. In the last, the motivation and objectives of the research work are given.

Chapter 2 (Literature review)

In this chapter, the important work carried out during the last few years has been reviewed and it presented in four sections. In the first section, the effect of different processing methods adopted for the preparation of pure Z-type ferrite is summarized. In the second section, the influence of different sintering additives including SiO_2, and Bi_2O_3 etc. are discussed. In the last sections, the effect of various substitutions for Ba and Fe ions in Co_2Z hexaferrites are reviewed. The emphasis is laid on the structural, magnetic, and dielectric properties of Z-type ferrites. In the last, the motivation and objectives of the dissertation are given.

Chapter 3 (Experimental & characterization techniques)

In this chapter, the synthesis methodology adopted for Co_2Z hexaferrite ($Ba_3Co_2Fe_{24}O_{41}$) is given. Different characterization techniques namely X-ray diffraction (XRD), Vibrating Sample Magnetometer (VSM), Scanning Electron Microscope (SEM), and Impedance Analyzer (LCR Meter), and their measurement conditions are described.

Chapter 4 (Results and discussions (Co_2Z ferrite))

In this chapter, the structural, magnetic, and dielectric properties of pure Z-type hexaferrite has been discussed. The effect of processing parameters (calcination and sintering temperature) is also investigated. The impedance data simulated with the proposed an equivalent electrical circuit for grain and grain boundaries, suggests that the conduction mechanism within the grain and along grain boundaries is governed by the two types of electric charge carriers. The imaginary modulus and complex electric modulus have shown different contributions which are present in the material.

Chapter 5 (Results and discussions (Substituted))

In this chapter, the influence of cation substitution is carried out on the structural, magnetic, and dielectric properties of Co_2Z ferrite. La^{3+} & Ca^{2+} ions substituted for Ba^{2+} ion Al^{3+} ion for Fe^{3+} ion. The imaginary permittivity spectra (ε'' *vs* frequency) of the Ca^{2+} substituted sample is shown abnormal dispersion behaviour. The relaxation process of carriers depends on the substitution of the cation. The electric barrier potential between grain and grain boundaries has significantly changed with the substitution. The complex electric modulus demonstrates the contribution of grain and grain boundaries.

Chapter 6 (Results and discussions (Sintering additives))

In this chapter, the influence of different sintering additives (SiO_2, MgO, Al_2O_3 & Bi_2O_3) has been studied. The charge transfer mechanism is discussed with the help of impedance and modulus studies. The effective resistance of additives is evaluated by the impedance data simulation. It is evidence that the sintering additives segregate along the grain boundary that adds additional electric resistance (barrier potential) along the path.

Chapter 7 (Conclusions)

In this chapter, the results obtained from various substitutions (La^{3+}, Ca^{2+} & Al^{3+}) and sintering additives (SiO_2, MgO, Al_2O_3 & Bi_2O_3) in $Ba_3Co_2Fe_{24}O_{41}$ are summarized. The important parameters and the obtained magnetic and dielectric properties are also compared with other results. The future scope of the research work is also given at the end of the chapter.

Chapter 1

Introduction

Overview

In this chapter, a brief introduction and classification of the hexaferrites are given. The magneto-crystalline anisotropy properties and its refined crystal structure of Co_2Z hexaferrite are discussed in brief. Various applications of Z-type ferrites are mentioned. In the last, the motivation and objectives of the research work are given.

1.1. Introduction

Ferrites are insulating magnetic oxides with promising electromagnetic properties, which make them suitable for high-frequency device applications. Structurally, ferrites are categorized as cubic ferrites (spinels and garnets) and hexagonal ferrites. On the basis of magnetic properties, these ferrites are subdivided into soft and hard ferrites. Soft ferrites are easy to magnetize and demagnetize and possess low coercivity (H_c) and high magnetization (M), whereas hard ferrites have high remanent magnetization (M_r), and high H_c, which are hard to magnetize and demagnetize. Their high permeability (μ), permittivity (ε), and low losses at *dc* to millimeter wave frequencies make them useful for high-frequency applications [1,2].

The cubic ferrites have low magneto-crystalline anisotropy (*MCA*) and low ferromagnetic resonance (*FMR*) which restricts their operating frequency below 3 GHz [2,3]. On the contrary, the ferrites with hexagonal crystal symmetry have high anisotropy energies (H_a) leading to their high operable frequencies above 100 GHz [1]. This difference in the properties is suitably exploited for a wide variety of applications from microwave absorbers to non-reciprocal devices and magneto-dielectric substrate material for antenna miniaturization [4].

Depending upon the molecular formula, these hexaferrites are characterized as M, Y, W, U, X, and Z-type hexaferrite [5]. Their structures can be described by the stacking sequence of the basic building blocks; Spinel (S) and Hexagonal (R and T) blocks. Further, on the basis of *MCA*, hexaferrites can be divided into two main groups (a) uniaxial ferrites – which have magnetization along *c*-axis (b) ferroxplana ferrites – having magnetization along the basal plane (*c*-plane). The important classes of hexaferrites along with their magnetic characteristics are depicted in Table 1.1 [1]. The ternary composition diagram of various hexaferrites are shown in Fig 1.1 [6].

Table 1.1. Classification and magnetic properties of hexaferrites.

Type	**Example**	**Stacking Sequences**	***Ms* (G)**	***Hc* (Oe)**	***Ha* (Oe)**	***FMR* (GHz)**
M	$BaFe_{12}O_{19}$	RSR*S*	4000	3187	17460	Upto 36
Y	$Ba_2Co_2Fe_{12}O_{22}$	$(TS)_3$	2300	60	28000	Upto 14
Z	$Ba_3Co_2Fe_{24}O_{41}$	RSTSR*S*T*S*	3390	23	12000	1.3
W	$BaCo_2Fe_{16}O_{27}$	$RS_2R^*S_2^*$	4800	80	21000	3
U	$Ba_4Zn_2Fe_{36}O_{60}$	RSR*S*TS*	4200	2600	10000	30
X	$Ba_2Co_2Fe_{28}O_{46}$	$(RSR^*S_2^*)_3$	3400	50	9500	3

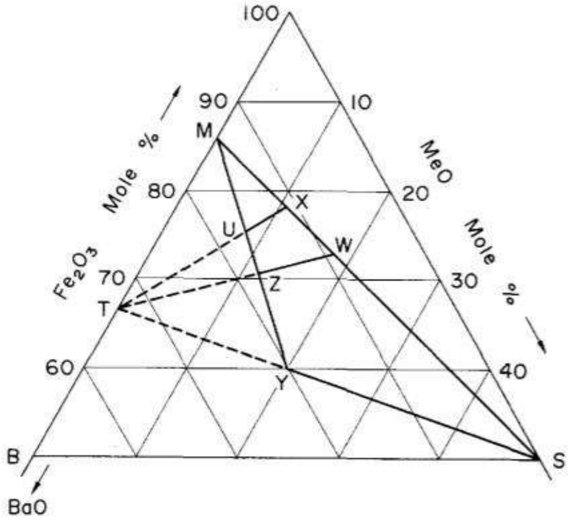

Fig. 1.1 Ternary composition diagram of hexagonal ferrites.

Among the various hexaferrite, Z-type hexaferrite possesses soft magnetic nature with excellent electromagnetic properties and are suitable for various microwave application from antenna miniaturization to microwave shielding. The important characteristic features of Z-type ferrite are explained below.

1.2. Crystal structure of Z-type hexaferrite

The origin of magnetic properties of Z-type hexaferrite lies in its crystal structure which is a superposition of M-type ($BaFe_{12}O_{19}$) and Y-type ($Ba_2Co_2Fe_{12}O_{22}$) hexaferrites. The unit cell of Z-type ferrite is associated with 22 close-packed oxygen layers, stacked in four S-blocks, two R, and two T-blocks, respectively. This arrangement can be depicted as RSTSR*S*T*S*, where (*) indicates that the corresponding blocks are rotated by 180° along the *c*-axis [7]. The unit formula of the S block is $Me_2Fe_4O_8$ (where Me = a divalent metal ion) which consists of two layers of four oxygen atoms with three metal atoms between each layer. The R block (AFe_6O_{11}, where A: Pb, Ba, Sr or rare-earth ions) consists of three hexagonally packed layers of four oxygen atoms each, where one of the oxygen atoms in the middle layer is replaced with similar size Ba^{2+} metal ion. There is a five-coordinate trigonal bipyramidal site in which the cation is surrounded by five oxygen anions, i.e., a unique position only found in the R block. The T block is made of four oxygen layers, with a barium atom replacing an oxygen atom in the middle two layers, to give the unit formula $Ba_2Fe_8O_{14}$.

S-Block = 4 (spin up) octahedral + 2 (spin down) tetrahedral

R-Block = 3 (spin up) and 2 (spin down) octahedral + 1 (spin up) trigonal bipyramidal

T-Block = 4 (spin up) and 2 (spin down) octahedral + 2 (spin down) tetrahedral

There are ten different interstitial sub-lattices in the unit cell of Z-type hexaferrite which comprises of six-octahedral sites ($12k_{VI}$, $4f_{VI}$, $4e_{VI}$, $4f_{VI^*}$, $12k_{VI^*}$, and $2a_{VI}$), three-tetrahedral sites ($4e_{IV}$, $4f_{IV}$, and $4f_{IV^*}$), and one five-fold trigonal bipyramidal site ($2d_V$) [8]. Fe^{3+} ions distributed in various crystallographic sites (octahedral, tetrahedral, and trigonal bipyramidal) give rise to a magnetic moment of 60 Bohr magneton (μ_B) per unit cell.

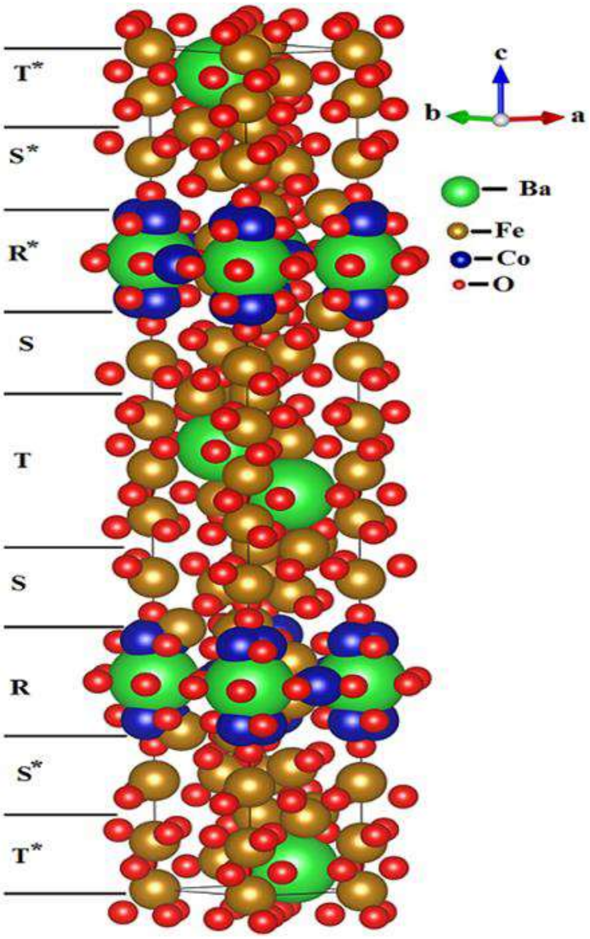

Fig. 1.2 Crystal structure of Z-type hexaferrites.

1.3. Magneto-crystalline anisotropy of Z-type hexaferrites

As mentioned, the magnetic vector has different preferences of alignment in different hexaferrite. The M-type ferrites have high uniaxial *MCA*, and suitable for permanent magnets, magnetic recording media, magnetic strip cards, and non-reciprocal devices [9-11]. Whereas, Y-type ferrites show planar anisotropy where the magnetization vector is aligned in the basal plane, however, it changes its direction and makes an angle with *c*-axis at a temperature below 215 K [12]. The Y-type hexaferrite provides a wide range of applications such as high-frequency noise absorbers, transformer cores, and in high-quality filters because of their relatively high μ, inexpensive fabrication, and stability [13]. Contrary to M and Y-type, Z-type hexaferrites are the remarkable case of possessing three types of anisotropy; below 220 K, the magnetization vector is aligned with an angle to the *c*-axis. At room temperature (*RT*) the magnetization direction is along the basal plane, above 480 K, *c*-axis is in the preferred orientation. The in-plane rotation of magnetization around *c*-axis is easy at *RT* which makes its magnetic moment to follow an alternating field giving them μ higher than Y-type hexaferrites [14].

1.4. Dielectric properties of the material

The dielectric substance is electrically insulating and becomes polarized when an electric field is applied across the surface of the material. Dielectric properties of the materials are referred as a function of charge storage and dissipation properties of electric and magnetic energy. The crystalline solids have a unique arrangement of ions, atoms, or molecules in all three directions. Microscopically, the dielectric properties of the materials depend upon the intrinsic constituents of atoms. Dielectric polarization is a fundamental phenomenon of charge carriers in which the electrical charge shifts and creates electrical dipoles. The positive charges are displaced toward the direction of the applied field and the negative charge shift in the opposite direction of the field. It builds up the internal electric field in the opposite direction of the applied field. The dielectric polarization depends upon the frequency and the temperature which can be understood by studying the following dielectric properties which reflect the charge storage and conduction within the material.

1.4.1. Complex permittivity and loss tangent

When a dielectric material is situated in the presence of an *ac* field, the response of the dipoles is measured in terms of complex dielectric permittivity and mathematically denoted by $\varepsilon^* (\omega) = \varepsilon'(\omega) + j\varepsilon''(\omega)$, where ε' interprets the efficiency of the dielectric material stored in the form of electrical energy and ε'' assigns the loss of electric energy which appears in the part of heat. Physically ε' measures how much alignment of the dipoles (degree of the polarization) in the action of field and ε'' evaluates ionic conduction (loss factor) in the dielectric [15]. ε' & ε'' depends on the frequency, temperature, and the magnitude of the field. As frequency increases, the magnitude of ε' decreases due to the polarization of charge carriers. Beyond the sufficient frequency, charges cannot follow the rapidly switching field, and ε' decreases. The ratio of the imaginary and real part of the complex permittivity is called the loss tangent or dissipation factor [16]. Mathematically tangent loss is given by $\tan\delta_\varepsilon = \varepsilon''/\varepsilon'$.

1.4.2. Complex electric impedance

The concept of electrical impedance was first proposed by ***O. Heaviside*** in the 1880s [17]. The vector diagrams and complex numbers were demonstrated by ***A.E. Kennelly*** [18] and ***C.P. Steinmetz*** [19]. The impedance represents the resistive or capacitive part of the material, and the phase difference between the input voltage and output current plays a significant role in deciding its complex behavior. The real part of the electric impedance (Z') measures the ability of the material to resist the electric current within the material. But the imaginary impedance (Z'') represents how much is the electric charge storage. Impedance interprets the complex resistance which encounters in the gradient flow of charges. The dielectric permittivity is correlated to impedance as [20]

$$\varepsilon^{*} = (1/j\omega C_0 Z^{*})$$

Where ω is the angular frequency, and C_0 is the capacitance of free space.

$$C_0 = (t/A\omega\varepsilon_0)$$

Where t is the thickness, and A is the surface area of the pellet.

$$\varepsilon' = (t/A\omega\varepsilon_0)\ [Z''/(Z'^2 + Z''^2)]$$

1.4.3. Complex electric modulus

The complex electric modulus is the reciprocal of complex permittivity.

$$M^{*} = M' + jM'' = 1/\varepsilon^{*} = j\omega C_0 Z^{*}$$

The real and imaginary parts of electric modulus are expressed as:

$$M' = \varepsilon'/(\varepsilon'^2 + \varepsilon''^2)$$

$$M'' = \varepsilon''/(\varepsilon'^2 + \varepsilon''^2)$$

The electric modulus spectra measure the distribution of charge carrier energies or configuration of the structure, electrical relaxation, and suppressed polarization effect at the interface between the electrode and dielectric material.

1.4.4. *AC* conductivity

Electric conductivity is the thermally activated phenomenon in which weak bonds break under the action of the applied electric field. Conductivity is the dynamic response of holes/electrons and ions depending on the temperature and frequency. Fig. 1.3 shows the frequency-dependent *ac* conductivity in three different regions, (1) low-frequency region, (2) middle-frequency region, and (3) conductivity dispersion at high frequency [21-23]. The low-frequency region represents the polarization contribution of electrode-dielectric material interfaces. The large charge accumulates at low frequency, dealing with the conductivity which gradually increases. In the middle region, the conductivity pattern is independent of the frequency, called the *dc* conductivity. In higher frequency, the trend of conductivity increase with frequency. This frequency-dependent conductivity is evaluated by Jonscher power law which states:

$$\sigma(\omega) = \sigma_0 + A\omega^{n}$$

where $\sigma(\omega)$ is the total conductivity, σ_0 is the *dc* conductivity, $A\omega^n$ represents the dispersion component of *ac* conductivity in power form of angular frequency ω, exponent n $(0 \leq n \leq 1)$ interprets the degree of interaction between mobile ions and lattice and A is evaluated strength of polarization [24, 25].

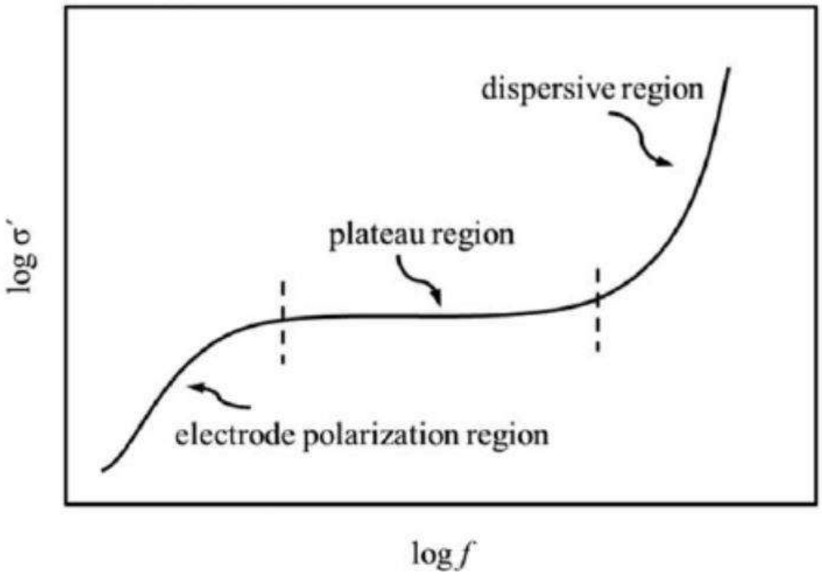

Fig. 1.3 Systematic diagram of *ac* conductivity as a function of frequency temperature.

1.5. Various models of dielectric behaviors

The charge transportation mechanism in the dielectric materials was explained by various models, the few important are explained below:

1.5.1. Maxwell-Wagner model

In this model two layers were considered, one layer is of insulating material having lower conductivity and the other layer consists of ferrite or semiconducting material with relatively higher conductivity. The degree of polarization of the ferrite increased with the applied field. Microscopically the insulating layers are separated into the conductive layer. Therefore, the charge carriers are restrained at the boundary layer. This polarization is also observed in the electrode polarization where dielectric material is situated in the two metallic electrodes. The separation of the charge originated with additional polarization at the internal phase boundaries. This mechanism appears in inhomogeneous materials (semi-crystalline).

1.5.2. Brick layer model

Dijk & Burggraaf (1981) and ***Verkerk et al.*** (1982) presented the brick layer model to study the grain boundaries, structure, and conductivity of the solid solution [26, 27]. This model assumed that the microstructure is an array of cubic grains separated by flat grain boundaries. The dimensions of the grain is larger than the thickness of the grain boundaries. The flow of the current is unidirectional and the curvature of the current path at the vicinity of the grain is negligible. The probability of the current flow is through grain and across grain boundaries or along grain boundaries. When current flow through the grain boundary, the brick layer model suggests an equivalent parallel electric circuit. This model also considers the conductive grains blocked by grain boundaries or lower conductive grains separated by the higher conductive grain boundaries [28].

1.5.3. Overall polaron tunneling model (OLPT)

Long proposed a polaron tunneling mechanism [29]. In the frequency-dependent loss, the electron is settled in energy levels that are closely related to the Fermi energy level. During the relaxation process, the electron reaches the lattice sites where the energy level is reduced. The activation energy of the electron is given by the formulae $W_H \approx W_P/2$, where W_P is the energy of the polaron. The small polaron is formed by the local bond deformation (broken). In this process, the energy levels are not overlapped and the energy of the electron transfer is independent of the separation of the sites. If ω is the characteristic vibrational frequency for lattice distortion, the transition occurs between high to low-temperature regions at $\hbar\omega/4$. At the deformed lattice (ionic conduction), the polarization changes under the long-range coulomb interaction. This is related to the *ac* loss where the energy levels are overlapped. The activation energy is decreased during the electron transfer [29].

1.5.4. Correlated barrier hopping model (CBH)

Pike introduced the correlated barrier hopping model (CBH) to explain *ac* loss in scandium oxide films [30]. ***Elliott*** assumed that charge carriers can jump from the electric barrier potential [31]. These barriers are separated by the different energy levels. The potential barrier will be reduced when an electron jumps to the positive defects centers in accordance with the coulomb interaction. The simplest single CBH model was used to understand the electron pair hopping in chalcogenide glasses. Glass defects structure shows the negative energy under the interaction of the electron lattice. The order of the defects centers from another center is a few interatomic distances. These defected centers are an analogy to the trapping charge centers that plays an important role in dielectric materials [32].

1.6. Applications of Z-type hexaferrites

1.6.1. Mobile antennas

The mobile antenna is used to receive or transit electromagnetic signals. The antenna is fabricated on the ferrite substrates to reduce the dimension of the antenna. The low magnetic and dielectric loss, higher μ & ε material are preferred for antenna preparation. The higher ε

absorbs the incident signal and the impedance matching between the ground plane of the antenna and free space is increased. This problem can be resolved by choosing equal μ & ε. In GHz range, Z-type hexaferrite fulfills the required condition. Recently Z-type ferrite-based antennas are designed by selecting μ' & ε' around 8 to 10 in the frequency range of 10 MHz – 1 GHz. As the frequency is increased up to 3 GHz, μ' & ε' decreased by 1.5 & 7.36, respectively [33, 14].

1.6.2. Multilayer chip inductors

Multilayer chip inductors (MLCs) is circuitry elements used in a notebook computer, transistor, and LC filters. The higher μ, resonance frequency, ρ, and low $tan\delta_\varepsilon$ are required to fabricate the MLCs. Co_2Z hexaferrite has higher μ and resonance frequency up to 3 GHz compared to spinel ferrites [34]. Recently, the Z-type based MLCs are used in the frequency range of 300 MHz- 800 MHz [34, 35] and the required parameters as μ_i from 2 to 15, f_r from 600 MHz to 1.2 GHz, Q = 20 to 30, ε = 23 to 35, ρ in the order of 10^7-10^9 Ω-cm, $tan\delta_\varepsilon$ = 0.003, $tan\delta_\mu$ = 0.039 at 200 MHz [36-49].

1.6.3. Microwave absorbers or EMI shielding

Microwave absorber or Electromagnetic interference (EMI) shielding material is used to reduce electromagnetic radiation or interference in military vehicles, airplanes, tanks, and stealth technology. The higher μ'' & ε'' material is preferred for absorbance. The higher resonance frequency and f_r also play an important role in EMI shielding. Co_2Z ferrite has higher μ, resonance frequency, and cutoff frequency (f_r) up to 3 GHz [43, 50-57]. Recently used Z-type material for absorber has shown required μ' = 1-3.36 at 8 -100 GHz, resonance frequency = 3.16 -14.5 GHz, RL = -30 dB to -48.5 dB at 9.7 GHz - 17.6 GHz. The thickness of the sample should be between 2.9 mm to 5 mm [58-67].

1.7. Motivation

Considering its multi domain applications, the research has been focused toward the Z-type hexaferrites. However, processing of Z-type hexaferrite is always challenging due to associated narrow composition range and phase formation temperature. By adopting the suitable processing condition, single phase Z-type can be formed. Also, the magnetic and dielectric losses can be minimized with the varying sintering condition *viz.* time and temperature. Further, it is always beneficial to add some sintering additive which not only lower down the sintering temperature but also refines the microstructure. The dielectric loss of the material is associated with the microstructural characteristics namely grain size, shape, and the concentration of the porosity. The other alternative to modify the magnetic and dielectric is cationic substitutions for Ba^{2+}, $Co^{2+,}$ and Fe^{3+} ions, which also affect its properties.

Largely, dielectric properties of Z-type ferrite have been investigated in the GHz range with and without substitution. At higher frequencies, the contribution of grain boundaries is very difficult to understand, generally, the electrical response of the grain and grain boundaries is observable in the frequency range of 10 kHz to 1 MHz. Only a few dielectric studies on pure Z-type hexaferrite are carried out in this frequency range, however, the Z-type hexaferrite prepared with the sintering additives and substitution is still lagging. Therefore, the main focus of this work is to prepare single-phase Z-type hexaferrite and investigate the effect of sintering additives and substitution on structural, magnetic, and dielectric properties.

1.8. Objectives

1. To study the effect of various processing parameters on the properties of Z-type hexaferrite.

Rationale: The single-phase formation of Z-type ferrites depends upon the calcination temperature and holding time, whereas the microstructural characteristic (grain size and shape) and sintered density are governed by sintering conditions. Therefore, the studies pertaining to processing conditions are crucial to obtain single-phase ferrite along with high sintered density and good microstructural features.

2. To investigate the effect of various ions substitution (La^{3+}, Ca^{2+} & Al^{3+}) on the structural, magnetic and dielectric properties of Z-type hexaferrites.

Rationale: The dielectric and magnetic properties of Z-type ferrite strongly depends upon the various cationic substitution. The three different kinds of substitution were chosen, a trivalent cation i.e. La^{3+} for Ba^{2+}; divalent Ca^{2+} for Ba^{2+}; and a nonmagnetic trivalent Al^{3+} ion for Fe^{3+} ions. The substitution of La^{3+} ion may affect the properties in two ways, firstly by reducing the unit cell size due to its smaller ionic radii, which enhances the super-exchange interactions among the Fe site; secondly by reducing Fe^{3+} ion to Fe^{2+} to maintain charge neutrality. Further, Ca^{2+} substitution will help to separate out the Fe^{3+} reduction effect caused by La^{3+} substitution due to its similar valence state. Last but not the least, nonmagnetic Al^{3+} substitution may substitute antiparallel Fe^{3+} site, which enhances its magnetic properties such as saturation magnetization. In summary, we expect large intrinsic variation and so on the properties of synthesized materials.

3. To investigate the effect of sintering additives (SiO_2, MgO, Al_2O_3 & Bi_2O_3) on structural, magnetic, and dielectric properties of Z-type hexaferrite.

Rationale: Different sintering additives (SiO_2, MgO, Al_2O_3 & Bi_2O_3) are used to lower the sintering temperature. The four different kinds of additives with different melting points were chosen. A low melting point additive will melt at sintering temperature and percolate the grain, whereas a high melting points additive may remain along grain boundaries in particulate form. The presence of additive along grain boundaries may hinder the motion of the charge carriers differently and modifies its dielectric properties. On the other hand segregation of additives along grain boundaries hinders the reversal of magnetic moment and may enhance the coercively. The aim of the sintering additives is to introduce the resistive layer along the grain boundaries to reduce the dielectric losses. Additives also refine the grain size.

In summary, processing conditions, substitutions and additives play different roles in modifying the dielectric and magnetic properties. For instance, a high sintering temperature is required to attain the high sintered density, however, it has an adverse effect on the phase purity and microstructure. Similarly, Magnetic properties can be enhanced by La^{3+} substitution, but the reduction of Fe^{2+} may deteriorate the dielectric properties. Lastly, the role of different additives on sintering temperature and microstructure is well investigated and showed the diverse effect of magnetic and dielectric properties. Therefore to obtain, a single-phase Z-type ferrite, a compromise has to be made among the phase, microstructural, electric, and magnetic properties. As mentioned earlier, the aim of this study is to thoroughly investigate the effect of processing conditions, cationic substitution, and additives on the dielectric and magnetic properties of Z-type hexaferrite, which may be useful for device-based applications.

Chapter 2

Literature review

Overview

In this chapter, the important work carried out during last few years has been reviewed and presented in four sections. In the first, effect of different processing methods adopted for the preparation of pure Z-type ferrite are summarized. In the second, the influence of the different sintering additives including SiO_2, MgO, Al_2O_3 and Bi_2O_3 are discussed. In the last section, the effect of various substitutions for Ba and Fe ions in Co_2Z are reviewed. The emphasis given on the structural, magnetic, and dielectric properties of Z-type ferrites.

2.1. Preparation of Co_2Z type hexaferrite

The various researchers adopted different methods to prepare single phase Z-type ferrite. They used several chemical and ceramic methods with different processing conditions. The effect of processing condition on structural, electrical and magnetic properties investigated over the years are summarized below:

Zhang et al. in 2000 [68] synthesized hexagonal ferrite, by gel self-propagating method. The frequency-dependent spectra showed higher value of μ_i, f_r, and quality factor (Q) for the sintered ferrites. The densification and microstructure were found to affect the magnetic properties. The frequency-dependent ρ, ε, and their mechanism were discussed. ***Pullar & Bhattacharya*** in 2001 [69] developed Z-type ferrite $Sr_3Co_2Fe_{24}O_{41}$ by using inorganic sol-gel precursor and their magnetic properties upto a maximum field of 5 T were studied. The H_c and magnetization was found 5.6 kAm^{-1}& 48.5 emu/g, respectively. ***Zhang et al.*** in 2001 [55] prepared Co_2Z by gel self-propagation method and optimized the temperature conditions to obtain pure Z-type phase and found different intermediate phase along with major Z-type phase. ***Temuujin et al.*** in 2005 [70] investigated the benefits of wet and dry ball milling to prepare Z-type and showed that wet milling increases the crystallization rate due to reduced particle size. The pure Z-type phase was formed by the reaction between intermediate M-type & Y-type phases. On the other hand, in dry milling intermediate phases undergo various surfae amorphization which provided heterogeneous crystallization. **Bae *et al*.** in 2009 [71] prepared Z-type hexaferrite by one step mixing calcination ceramic processes (MCP) and compared their magnetic results with sol-gel (SGP) and conventional ceramic process (CCP). $tan\delta$ of MCP Co_2Z reduced from 0.17 at 50 MHz to 0.068 at 300 MHz whereas $tan\delta$ of 0.12 & 0.09 were found for SGP and CCP process, respectively. ***Kikuchi et al*.** in 2011 [72] prepared Sr_3Co_2Z by polymerizable complex method. The *M-H* loops showed M_s & H_c were 50.5 emu/g and 0.014 T, respectively at *RT*. ***Qin & Verweij*** in 2012 [73] fabricated Z-type by modified Pechini method and showed higher μ and low losses above 1 GHz.

Daigle et al. in 2012 [74] proposed a modified co-precipitation method to synthesize high-quality Co_2Z hexaferrite particles. The complex μ and ε of oriented compact were measured at different applied field and processing conditions. The μ greater than 5 were observed in L-band. ***Tainaka et al.*** in 2013 [75] synthesized $Sr_3Zn_2Fe_{24}O_{41}$ Z-type ferrite by heating at 1463 K for 5 hours in the air environment. The magnetic properties of Z-type were measured by VSM. The M_s of $Sr_3Zn_2Fe_{24}O_{41}$ (23.5 μ_B/formula unit) was found to be higher than $Sr_3Co_2Fe_{24}O_{41}$ (22.7 μ_B/formula unit). ***Solanki et al.*** in 2014 [76] synthesized Z-type hexaferrite from the sol-gel auto combustion method. The combusted powder was sintered at 500 °C and 950 °C for 5 hours in a muffle furnace. The influence of different sintering temperatures on crystal structure, crystallite size, microstructure, and dielectric properties was studied. XRD analysis identified that heat treatment significantly affected the formation of the hexaferrite phase. The *ac* conductivity increased with increased frequency which justified the Maxwell-Wagner two-layer model.

Jia et al. in 2015 [77] prepared $Sr_3Co_2Fe_{24}O_{41}$ by hydrothermal method and showed the influence of the atomic ratio (Sr/Fe), on the composition and magnetic properties of Z-type ferrite. The H_c was found to decrease with increased temperature indicated that pure Z-type phase is increasing. ***Zhang et al.*** in 2015 [78] synthesized Co_2Z in different gaseous atmosphere (Air, O_2 & N_2) and reported the magnetic and electric properties of Z-type ferrite. The presence of O_2 showed low magnetic and dielectric losses with reducing the Fe^{2+} ions. The sintered sample at 1300 °C showed the magnetic and dielectric losses lesser than 0.05 & 0.005, respectively in the frequency range 30 MHz – 300 MHz. ***Rhee et al.*** in 2015 [79] synthesized the Z-type ferrite with equimolar ratio of Ba and Sr ($Ba_{1.5}Sr_{1.5}Co_2Fe_{24}O_{41}$) by solid-state reaction method. $Ba_{1.5}Sr_{1.5}Co_2Fe_{24}O_{41}$ was synthesized through different calcination steps (SC12) and demonstrated the increased μ and $tan\delta_\mu$ compared to Z-type, which was prepared by a different method of calcination. Co_2Z (SC12 method) sintered at 1125 °C with slow cooling rate showed $tan\delta_\mu$ below 0.1 at 750 MHz. The μ', ε' and $tan\delta_\varepsilon$ were obtained 7.9, 10.9 and 0.01, respectively at 750 MHz. ***Tang et al.*** in 2015 [80] evaluated the chemical ionic states of $Sr_3Co_2Fe_{24}O_{41}$ annealed in the air by using X-ray photoelectron spectroscopy. The results exhibited the presence of both Fe^{3+} & Fe^{2+} in the sample with Fe^{2+} (36.3 %). The binding energy of Fe^{3+} & Fe^{2+} is closely related to Fe_3O_4 & $CoFe_2O_4$ while Co^{2+} & Co^{3+} matched with $CoFe_2O_4$ & $NiCo_2O_4$.

Lee et al. in 2016 [81] prepared Co_2Z hexaferrite by solid state method and eliminated secondary Y-phase by acid etching. The calcined and acid etched samples showed $tan\delta$ of 0.012 & 0.037 at 1 & 2 GHz, respectively. ***Alhwaitat et al.*** in 2019 [82] prepared Zn_2Z ($Ba_3Zn_2Fe_{24}O_{41}$) via two different methods; ball milling and sol-gel method and showed variation in M_s with sintering temperatures. ***Guo et al.*** in 2018 [83] synthesized Z-type by citric acid sol-gel method and showed the variation in M_s and H_c after first and second calcination process.

Salazar et al. in 2019 [84] synthesized $Sr_3Co_2Fe_{24}O_{41}$ with the help of citrate and Pechini methods and measured the magnetic properties of the prepared samples. ***Salazar et al.*** in 2020 [85] studied the magnetic domain structure of Sr_3Co_2Z hexaferrite with the help of Lorentz microscopy and electron holography. In the recently reported study, ***Lather et al.*** in 2022 [86] studied the effect of particle size in sol-gel prepared powders on the magnetic properties of $Sr_3Co_2Fe_{24}O_{41}$ & $Ba_3Co_2Fe_{24}O_{41}$. The *M-H* loop at *RT* confirmed that the H_c increased significantly with reduction of particle size.

Several researchers have also studied the magneto-dielectric and magneto-electric effect in such pure Z-type ferrite. ***Zhang et al.*** in 2012 [87] demonstrated the magneto-dielectric (*MD*) effect of $Sr_3Co_2Fe_{24}O_{41}$ at different temperatures and frequencies. The high negative *MD* effect was seen near room temperature which showed maximum value at low-frequency regions. *MD* effect results indicated a quadratic relationship with magnetization and induced magnetic field which changed the transverse conical spin structure and spin-phonon coupling. ***Wu et al.*** in 2012 [88] prepared pure phase ($Sr_3Co_2Fe_{24}O_{41}$) possessing ferroelectricity, ferromagnetism, and magneto-electric coupling at room temperature. They prepared four-state memory prototype, in which the information was written by electric and magnetic field while read with the help of magneto-dielectric coefficient (α_E) in the presence of a small bias magnetic field. ***Ebnabbasi et al.*** in 2012 [89] measured the magneto-electric effect of $Sr_3Fe_{24}Co_2O_{41}$ at room temperature. The M_r measured with applying *dc* voltage or electric field on the hexaferrite slab. The M_r variation was up to 18.0 % under influence of 10000 V/cm electric fields. A similar change was observed in microwave μ < 3 GHz. The ε changed ~ 16.0 % at 1 GHz in 320 Oe magnetic field.

Okumura et al. in 2013 [90] investigated the magneto-electric effect (direct and converse) in which electric polarization (*P*) originated by magnetic field (*B*) and magnetization (*M*) induced due to the electric field (*E*), respectively were major features. Linear *B* profile of *ME* coefficient calculated by converse effect was matched with the pattern obtained by the direct effect. *M-H* plots showed that *M* changed in opposite direction in the presence of *E* field. ***Wang et al.*** in 2014 [91] studied the magneto-resistance (*MR*) and magneto-electric (*ME*) effect of on $Sr_3Co_2Fe_{24}O_{41}$. *ME* current induced *MR* was around 32.2 % at *RT* in ~ 125 Oe magnetic field strength.

Xiang et al. in 2011 [92] interpreted the magnetic and dielectric properties for miniaturization antenna. The μ of 7.28 at 1 GHz and loss $tan\delta_\mu = 0.07$ were reported. The miniaturization factor *n* approached 10 at 2 GHz. ***Sharma et al.*** in 2013 [93] investigated and compared the magnetic and dielectric properties Co_2Z with NZFO ferrite for antenna applications in 1.5 GHz to 3.5 GHz frequencies range. The magnetic and dielectric losses were 0.006 & 0.002 for Co_2Z and 0.004 & 0.0018 for NZFO at 3.5 GHz. ***Tang et al.*** in 2015 [94] investigated the impedance and electric modulus of $Sr_3Co_2Fe_{24}O_{41}$ at different frequency and temperatures. The imaginary impedance (Z'') and modulus (M'') indicated that the charge carriers are associated with thermodynamic condition showed a distributed relaxation time. The scaling behavior of both Z'' & M'' showed that this distribution is temperature independent. The Cole-Cole plots of impedance data confirmed two types electrical response related to grain and grain boundaries having the activation energies 0.66 eV & 0.67 eV, respectively. ***Li et al.*** in 2017 [95] prepared polycrystalline $Sr_3Co_2Fe_{24}O_{41}$ & $Ba_3Co_2Fe_{24}O_{41}$ by sol-gel method and their temperature-dependent relaxation was analyzed by the dielectric and impedance spectroscopy. The dielectric ε was observed at low frequency due to the higher concentration of Fe^{2+}, and dielectric relaxation observed at high temperature attributed to thermally activated charge carriers. This dielectric relaxation is originated from the carriers hopping between Fe^{2+} & Fe^{3+}. Relaxation is low at higher temperatures due to low conduction.

Li et al. in 2018 [96] prepared $Ba_{1.5}Sr_{1.5}Co_2Fe_{24}O_{41}$ by sol-gel method and investigated their impedance behavior. The complex impedance data simulated with an appropriate electrical circuit suggested that electric response is obtained by both grain and grain boundary having activation energy 0.62 eV & 0.67 eV, respectively.

The above discussion suggests that the pure Z-type phase is formed by the intermediate phases (M & Y-type). The processing parameters (time and temperature) influence the densification, magnetic and dielectric properties of the material. The H_c depends on the grain size and reduces with large grains. The ball milling increases the crystallization process in the prepared sample. The demerit of the chemical method is to form Fe^{2+} ions which increase the magnetic and dielectric losses. The benefit of ball milling is that it only reduces the size of the particles by a mechanical process. However, at higher sintering temperatures Fe^{2+} and oxygen vacancy are originated leading to increase in losses. Therefore, it is necessary to optimize the processing parameters for synthesizing Z-type hexaferrite with minimized magnetic and dielectric losses. The cation substitution and sintering additives are also used to reduce the concentration of Fe^{2+} and porosity. Table 2.1 summarizes the results of above mentioned studies.

The literature review related to additives and substitution is given in Section 2.2 & 2.3, respectively.

Table 2.1 Summarized pure Co_2Z ferrite preparation and their effect on structural, magnetic and dielectric properties.

S. No.	Calcination/ sintering condition	Structural properties	Magnetic Properties	Dielectric properties
Compared study of sol-gel & solid state				
1	Pure Z-type obtained in sol-gel at 1210 °C for 4 hours while in solid state at 1290 °C/ 4 hours	Sintered at lower temperature, Sol-gel grain size (5 μm) < solid state (10-15 μm)	Higher μ_i	ρ (sol-gel) = 2.1×10^7 Ω-cm < ρ (solid) = 2.7×10^7 Ω-cm, ε & $Fe^{3+} \rightarrow Fe^{2+}$ transition reduced in sol-gel [68].
2	Conventional ceramic (CC) power calcined at 1300 °C for 4 hours and sol-gel (SG) powder pre-calcined at 1000 °C & post calcined at 1300 °C/ 4 hours	Z-phase controlled by phase purity of M & Y-type	M_s = 51.47 emu/g & H_c = 22.17 Oe for CC & M_s = 51.06 emu/g & H_c = 18.52 Oe, $tan\delta_\mu$ = 0.09 for CC & $tan\delta_\mu$ = 0.12 for SG at 300 MHz	[71]
3	Ball milled powder preheated at 900 °C for 2 hours and sintered at 900 °C, 1250 °C, 1300 °C for 2 hours. Sol-gel power preheated at 655 °C for 5 hours & sintered at 900 °C, 1100 °C, 1250 °C for 2 hours	900 °C sintered sample shown α-Fe_2O_3, $BaFe_2O_4$, $ZnFe_2O_4$ while 1250 °C & 1300 °C shown major Z-type phase. At higher sintering temperatures crystallization of platelet increased	Ball milled sample shown M_s increased & H_c decreased with increased temperature while for sol-gel sample M_s increased & H_c first decreased further increased	[82]
Sol-gel method				
4	Precalcined at 600 °C & post calcination at 1200 °C	Precalcined phases α-Fe_2O_3, BaM, & $CoFe_2O_4$ finally converted into Z-phase	M_s = 48.5 emu/g & H_c = 5.6 kA/m	[69]
5	Sintered at 1200 °C/ for 4 hours	Z-phase is stable in 1000 °C, 1100 °C & 1200 °C/4 hours, grain size increased	μ_i and Q increased	ρ = 2.89×10^7 Ω-cm [55]
6	Single Sr_3Co_2Z formed at 1200 °C		M_s = 50.5 emu/g & H_c = 0.014 T	[72]
7	Sintering range of 1100 °C - 1300 °C. Z-phase obtained at 1250 °C (ambient oxygen).	μ' = 6.8	$tan\delta_\mu$ = 0.01 – 0.1	ε_r = 15 & $tan\delta_\varepsilon$ = 0.01 [74]
8	Sintered at 1190 °C - 1210 °C for 5 hours	W-type coexisted above 1200 °C and	M_s = 23.5 μ_B/ formula unit & H_c	[75]

		at 1195 °C less secondary phase, platelet like random grains	= 1.4×10^3 μ_B/ formula unit	
9	Presintered at 500 °C and post sintering at 950 °C	At 500 °C $CoFe_2O_4$, α-Fe_2O_3, $Ba_3Fe_2O_6$ & at 950 °C $Ba_3Co_2Fe_{24}O_{41}$, $Ba_2Co_2Fe_{12}O_{22}$ phases obtained	Post calcined powder shows lower specific magnetization than preheated	Grain boundaries activated at low frequency while grain activated at higher frequency [76].
10	Sintered at 1100 °C, 1150 °C, 1185 °C & 1200 °C	Sr/Fe = x/8, at x = 1.25, α-Fe_2O_3, $Sr_3Fe_2(OH)_{12}$ phases appeared.	H_c decreased with increased temperature	[77]
11	Precalcined at 400 °C & post calcined at 1200 °C, 1250 °C, 1300 °C, 1315 °C & 1350 °C for 5 hours	At 1350 °C W-phase existed while < 1300 °C Z-phase obtained. Hexagonal morphology increased with increased temperature.	Maximum M_s = 41.7 emu/g & H_c = 19.8 Oe sample. μ' = 3.36 at 100 MHZ for 1300 °C.	[83]
12	Preheated at 400 °C for 1 hour & final heated at 1000 °C and 1200 °C for 5 & 10 hours		Lorentz microscopy indicated magnetic domain wall present. In plane orientation revealed strong magnetic field	[85]
13	Precalcined at 1000 °C for 4 hours & 1200 °C for 12 hours		M_s = 51.9 emu/g & H_c = 50 Oe	[88]
14	Calcined 1200 °C for 5 hours	Grain size in the range of 15- 50 nm	M_s increased with decreased temperature. $tan\delta_\mu$ = 0.006 at 3.5 GHz	$tan\delta_\varepsilon$ = 0.002 at 3.5 GHz [93].
15	Presintered 550 °C for 5 hours & post sintering 1200 °C for 12 hours	More dense grain is formed in $Sr_3Co_2Fe_{24}O_{41}$ compared to $Ba_3Co_2Fe_{24}O_{41}$. Fe^{2+} is formed during higher sintering		Two type of relaxation is observed. The charge carriers hopping of Fe^{2+}-Fe^{3+} associated to relaxation [95].
16	Presintered 550 °C for 5 hours & post sintering 1200 °C for 12 hours	U & W-phase coexisted with Z-phase		Electric response is obtained from grain & grain boundary having activation energies 0.62 eV & 0.67 eV, respectively [96].

Solid state method				
17	Wet milled powder precalcined at 1080 °C and post calcined at 1230 °C	Intermediate M & Y-type phases obtained by wet milling and dry milling provided heterogeneous crystalline states, dry milled grain is smaller than wet milled		[70]
18	Precalcined at 1250 °C for 4 hours & postsintered at 1150 °C - 1350 °C in different atmosphere (air, O_2 & N_2)	Inhibits the formation of Fe^{2+}	M_s of air and O_2 medium sample ~ $50\ Am^2Kg^{-1}$. H_c of N_2 medium < O_2 & air medium. $tan\delta_\mu < 0.05$ in frequency of 30 MHz – 300 MHz. $\mu'_{O2} = 12$	$tan\delta_\varepsilon < 0.005$ in frequency range of 30 MHz – 300 MHz. Cole-Cole plots shows non-Debye type relaxation [78].
19	Single calcined at 1200 °C for 3 hours (C12), First calcination at 1000 °C & 1200 °C for 3 hours (C10C12), SC12 first calcined at 1000 °C & post calcined at 1200 °C.	C12 & C10C12 have M & Y-type phase. SC12 has Z-type.	$M_s = 55.5$ emu/g & $H_c = 24.4$ Oe (SC12). $tan\delta_\mu < 0.1$ at 750 MHz, $\mu' = 7.9$	$\varepsilon' = 10.9$, $tan\delta_\varepsilon = 0.01$, Impedance factor = 321 Ω [79].
20	Annealed at 1200 °C for 16 hours & further annealed 600 °C for 6 hours	Binding energies of Fe^{3+} (710.9 eV) & Fe^{2+} (709.2 eV) closed to Fe_3O_4 & $CoFe_2O_4$. Binding energies of Co^{2+} (780.2 eV) & Co^{3+} (782.5 eV closed to $CoFe_2O_4$ & $NiCo_2O_4$		[80]
21	Precalcined at 1080 °C & recalcined at 1300 °C for 6 hours	Precalcined sample has M & Y-phase. Acid etching sample shown hexagonal pores (Y-phase remove).	M_s of acid etching sample (= 55 emu/g) > M_s (= 51 emu/g) of recalcined sample. $tan\delta_\mu = 0.037$ & $\mu' = 1.8$ at 2 GHz	[81]
22	Precalcined at 1000 °C for 16 hours & finally sintered at 1200 °C for 16 hours	*MD* effect shown quadratic relationship with magnetization explained by transverse conical structure and spin-photon coupling	Magnetization increased in two steps up to saturation. Negative *MD* effect observed at room temperature.	[87]

23	1210 °C for 16 hours		18.0 % change in remanence observed with electric field 10000 V/cm	16.0 %, ε changed with magnetic field 320 Oe. $\rho = 4.28 \times 10^8$ Ω-cm [89].
24	Preheated 1000 °C for 16 hours & post heated 1160 °C - 1200 °C for 16 hours	Magnetic field (*B*) induced electric polarization and electric field (*E*) induced magnetization (*M*)	Linear *ME* coefficient obtained from converse effect. Reversal and multilevel switching of *M* by applying electric field	[90]
25	Calcined at 1100 °C for 16 hours & sintered at 1200 °C for 16 hours	*ME* current originated from magnetic spin configuration strongly on magnetic field and temperature controlled by sweep rate of magnetic field.	M_s = 53.6 emu/g & H_c = 17.2 Oe	*ME* current formed giant magneto-resistance (32.2 %) at 125 Oe [91].
26	Precalcined 1240 °C - 1300 °C for 2 hour and sintered at 950 °C - 1100 °C for 3 hours	As Fe_2O_3 content decreased Y-phase convert into Z-phase. With 10 Fe_2O_3, W-phase appeared due to Z-phase decomposition. Grain increased from 3 μm to 7 μm as sintering temperature increased	μ' increased with decreasing 11.2 to 10.4 of Fe_2O_3. Sample sintered at 1050 °C shown $tan\delta_\mu$= 0.07 & μ = 7.28 at 1 GHz	[92]
27	Powder calcined at 1000 °C for 16 hours and annealed in air at 1200 °C for 16 hours	U & W-phase coexisted with Z-phase		Z'' & M'' spectra implied distribution of relaxation time is temperature independent. Cole-Cole plots shown grain and grain boundaries contribution having activation energies 0.66 eV & 0.67 eV, respectively [94].
28	Precalcined at 600 °C for 3 hours and post calcined at 1300 °C – 1350 °C for 2-3 hours. Samples sintered at 1250 °C, 1310 °C & 1330 °C for 4 hours	Z-type phase present from 600 °C. W-type obtained at higher temperature sintering while <	μ_i = 11.9 at < 500 MHz	[73]

		1300 °C, Y-type phase present.		
29	Preheated at 400 °C for 1 hour & post heated at 1000 °C, 1200 °C for 5 & 10 hours	U-type phase co-existed with Z-phase. Hexagonal morphology does not obtain.	M_s = 50.1 ± 0.1 emu/g, H_c = 20 ± 1 Oe	[84]

2.2. Effect of additives

The magnetic and dielectric properties are associated to the microstructural constituents (grain and grain boundaries). The small grain size exhibits lower magnetic and dielectric losses. The heterogeneous dielectric structure of the material is already discussed in Section 2.1, formed due to the presence of dislocation, void, defect, oxygen vacancy, Fe^{2+} ions and grain boundary. The uncontrolled conduction of the charge carriers in grain compared to the alignment of charge along the grain boundary or resonance frequency of charge lags behind the frequency of the applied field introduced dielectric loss. This loss is originated due to the heterogeneous structure. Some metal oxides are used as an additive for better sintering characteristic and densification [97]. These oxides reportedly not only refine grains, lower down sintering temperature, reduces defects but also improves the magnetic and dielectric properties of the material. The following section review the work carried out based on various sintering additives.

Zhang et al. in 2001 [98] investigated the effect of Bi_2O_3 additive and showed better densification at low sintering temperatures. Bi_2O_3 is found to segregate along the grain boundary and showed improved Q and f_r. ***Zhang et al.*** in 2002 [99], observed similar effect with Bi_2O_3 investigated in $Ba_3Co_{2(1-x-y)}Zn_{2x}Cu_{2y}Fe_{23.5}O_{41}$ synthesized from dry gel self-propagation method. The magnetic properties were found to be unaffected by small amount of Bi_2O_3. The variation of μ_i (~ 4) was attributed to the dense microstructure having small grain size, while Q of 50 and f_r > 1 GHz were obtained. Higher resistivity of 3.3×10^7 Ω-cm with Bi_2O_3 were obtained compared to 2.7×10^7 Ω-cm for pure sample. ***Wang et al.*** in 2002 [100] investigated the effect of B_2O_3, LiF, and CaF_2 additives in $Ba_3Co_{2-x}Cu_xFe_{24}O_{41}$, x = 0.0 to 0.8 synthesized by citrate precursor method. Single Z-type phase was obtained below 900 °C with 2.0 wt. % of additive mixture. The sintered sample showed uniform microstructure with average grain size less than 2 µm. The μ_i ~ 7, f_r above 1.2 GHz, and *dc* resistivity > 10^8 Ω-cm were obtained.

Umemoto et al. in 2003 [101] produced $(Sr_xBa_{1-x})_3Me_2Fe_{24}O_{41}$ ($0 \leq x \leq 1$), with different amounts of additives B_2O_3, CuO, and Bi_2O_3 and showed that the sintering characteristics depends upon the relative Sr fraction and additives. ***Endo et al.*** in 2004 [102] selected borosilicate glass, zinc borosilicate glass, Bi_2O_3 based glass, CuO, and Bi_2O_3 as additives in M-type, Y-type and Z-type hexaferrite in weight percent of 0.5 to 20. It is found that CuO exists in grain, whereas Bi_2O_3 segregated along the grain boundary and significantly reduces the sintering temperature below 960 °C. ***Wang et al.*** in 2004 [103] improved the electromagnetic properties of Co_2Z ferrite in higher frequency domain with different weight percent of SiO_2 additive. The grain growth was suppressed with SiO_2 addition and showed decreased μ_i & ε. The ferromagnetic resonance shifted to higher frequency bands $\geq$ 2 GHz. The maximum Q was obtained higher than 25 at 1 GHz with used 8.0 wt. % of SiO_2. ***Huang et al.*** in 2004 [104] prepared $Ba_3(Co_{0.4}Zn_{0.6})_2Fe_{23.4}O_{41}$ with $Ba_{0.5}Sr_{0.5}TiO_3$ (BST) additive by solid-state method. Increasing BST content, Z-phase coexisted with M and perovskite phase which resulted an increase in grain growth with increases complex permeability and permittivity.

Jia et al. in 2007 [105] investigated the existence of M, and small niobate phase with Z-type due to Nb_2O_5 additive. The secondary phase was responsible for reducing magneto-crystalline anisotropy of the system. This additive has increased the grain growth with corresponding increase in μ_i. At high sintering temperature of 1260 °C, a secondary niobate phase-separated out which impeded the abnormal grain growth. The μ_i of 32-33, coercive force 454-455 A/m, and resonance frequency of 300 MHz were achieved by using 0.8 wt. % Nb_2O_5. ***Kracunovska et al.*** 2008 [106] showed that addition of 3.0 wt. % Bi_2O_3 as sintering agent reduces sintering temperature to 950 °C at the cost of μ which was reduced to 3 from 20 at 10 MHz.

Jia et al. in 2009 [107] introduced Y_2O_3 in Z-type hexaferrite to achieve high f_r and low ε. With increasing Y_2O_3 content Z-type phase coexisted with a small garnet. The resonance frequency increased with a reduction in ε. ***Jia et al.*** in 2010 [108] have introduced SiO_2 into $(Co_{0.4}Zn_{0.6})_2Z$ ferrite and found Z-type ferrite coexisted with a minor silicate phase that suppress the grain growth. This additive is segregated along the grain boundary as an inactive layer which was found to provide resist charge conduction. With increasing SiO_2 dopant, the static μ and ε significantly decreased. The SiO_2-doped sample showed lower magnetic tangent loss compared to pure Z-type ferrite. All samples with SiO_2 showed a lower value of dielectric loss in the frequency range of 400 MHz - 1 GHz. ***Jia et al.*** in 2010 [109] introduced MgO as a low-temperature sintering agent in Z-type ferrite. The doped sample had a major Z-phase with a minor W-phase. MgO decreased the ε and improved the dielectric loss tangent by reducing the electronic transition between Fe^{2+} and Fe^{3+}.

Jia et al. in 2010 [110] studied the influence of $Ba_{0.5}Sr_{0.5}TiO_3$ (BST) additive in Z-type ferrite on densification, microstructure, and electromagnetic properties. BST was found to promote grain growth and increases sintering density. The static μ increased with decreasing magneto-crystalline anisotropy and increasing grain size and bulk density. The increase in ε was due to change in the valence state of Fe ions and polarization of the perovskite phase. ***Mu et al***. in 2010 [111] doped $MgTiO_3$ into Co_2Z hexaferrite synthesized by solid-state reaction method and investigated their magnetic and dielectric properties. With increasing $MgTiO_3$ dopant (0.0 – 5.0 wt. %), the cutoff frequency increased significantly from 0.33 to 1.8 GHz. The minimum magnetic and dielectric losses were obtained with 8.0 wt. % of $MgTiO_3$ below 1.8 GHz. ***Zhang et al***. in 2011 [112] used Z-type hexaferrite in the frequency band of 10 MHz to 1 GHz to overcome Snoek's limit. The microstructural inhomogeneity and material processing parameters enhanced $tan\delta_\mu$. The effect of processing parameters on magnetic properties was demonstrated in this paper. The variation of μ and loss increased with different processing parameters and microstructural inhomogeneities. ***Ryou et al.*** in 2012 [113] showed that the Al_2O_3 additive greatly reduced the μ and ε in the extended frequency range.

Cao et al. in 2014 [114] synthesized Z-type hexaferrite composed of Bi_2O_3 by solid-state reaction method. The results showed lower sintering temperature, improved densification, and homogeneous microstructure than pure sample sintered at the higher temperature. The proper content of the additive showed a high Q-factor in the higher frequency. ***Gan et al.*** in 2014 [115] introduced SiO_2 into $Ba_{1.5}Sr1_{.5}Co_2Fe_{24}O_{41}$ to enhance the high-frequency magnetic properties. The addition of SiO_2 decreased the average grain size, and improved the magnetic properties. The μ_i reduced from 5.2 to 2.6, and the f_r enhanced corresponding to SiO_2 content. The maximum Q was obtained with 4.0 wt. % of SiO_2. ***Su et al.*** in 2014 [116] synthesized $Ba_3Co_{2+x}Ir_xFe_{24-2x}O_{41}$ with Bi_2O_3 additive which balanced the μ and ε.

Zhang et al. in 2015 [117] produced magneto-dielectric material by adding different amounts of SnO_2 in $(Ba_{0.5}Sr_{0.5})_3Co_2Fe_{24}O_{41}$. The moderate SnO_2 enhanced the densification of the ferrite to achieve lower magnetic and dielectric losses. The higher content of SnO_2 is responsible for secondary W-type phase and reduces sintering density. The specific amount 0.1 & 0.2 wt. % of SnO_2 showed the matching value of μ and ε around 15. ***Chang et al.*** in 2015 [118] used $BaCu(B_2O_5)$ (BCB) to lower the sintering temperature of $Ba_3(Co_{0.4}Zn_{0.6})_2Fe_{24}O_{41}$ [$(Co_{0.4}Zn_{0.6})_2Z$]. 5.0 wt. % BCB enhanced density about 95.0 % of theoretical density and showed uniform of microstructure with few pores. The variation of μ and ε was not observed from 10 MHz to 800 MHz. The magnetic and dielectric loss was reduced within a wide frequency range. However, $tan\delta_\varepsilon$ & $tan\delta_\mu$ were 0.003 and 0.039, respectively at 200 MHz by using 5.0 wt. % BCB.

Guo et al. in 2016 [119] prepared $Ba_{1.5}Sr_{1.5}Co_2Fe_{24}O_{41}$ ferrite with Bi_2O_3-B_2O_3-SiO_2-CuO (BBSC) glass using the traditional solid-state method. BBSC promoted the single-phase formation of Z-type and increased densification. With increased BBSC glass from 1.0 to 4.0 wt. %, M_s successively increased from 36.5 to 50.3 emu/g while initially H_c and μ' increased first and then decreased.

Rane et al. in 2017 [120] investigated low-temperature cofired ceramic LTCC substrate material $Ba_3Co_xZn_{2-x}Fe_{24}O_{41}$. The synthesized hexaferrite sintered at 900 ℃ with 2.0 wt. % of Bi_2O_3 showed a sintered density of 95.0 % and bulk resistivity of more than 10^9 Ω-cm. The optimum M_s = 47–52 emu/g and H_c = 10–20 Oe was obtained for $Ba_3Co_{0.8}Zn_{1.2}Fe_{24}O_{41}$ and $Ba_3Co_{1.6}Zn_{0.4}Fe_{24}O_{41}$, respectively. The resonance frequency above 1 GHz and μ of 6–7 was obtained. ***Chen et al.*** in 2017 [121], sintered two hexaferrites named $3Ba_{0.7}Sr_{0.3}O.2CoO.10.8Fe_2O_3$ (Z-type) and $Ba_2Co_2Fe_{12}O_{22}$ (Y-type) at 1000 ℃ with Bi_2O_3 additive and used them as magnetic substrates to fabricate miniaturized antennas.

Zheng et al. in 2018 [122] have introduced nano-crystalline $ZnAl_2O_4$ (ZA) into Z-type and investigated the influence of ZA on their microstructure, μ and ε as well as loss in the frequency range, 10 MHz to 1 GHz. With employing ZA amount from 0.0 to 15.0 wt. %, μ' and ε was found to decrease at low frequencies. However, the losses were minimized, and the stability of μ and ε with frequency was enhanced.

The additives are segregated along the grain boundaries by adding their additional resistance. This resistance electronically introduces an electrical resistance for the charge. In the presence of additives, the migration of charge from one grain to another is a hindrance that leads to lower the dielectric losses. The tendency of additives is generally to refine the microstructure with a small grain size. The fraction of the grain boundary increases which also reduces the motion of the carriers. Additives restrict the formation of Fe^{2+} and super-exchange between Fe^{3+} & Fe^{2+} ions, resulting in the low dielectric loss. These grain boundaries enhance the pinning centers and show lower coercivity. The non-magnetic insulating layer of additives reduces the connection between the magnetic ions (Fe^{3+} & Co^{2+}). The applied external magnetic field cannot easily penetrate the insulating layer and thus leading to reduce the $tan\delta_\mu$. Therefore, additives not only reduce the size of the grain but also decrease the magnetic and dielectric losses.

In summary, the effect of additives affects the microstructural features either by lowering the sintering temperature, by impeding the grain growth, or by enhancing sintering density. Table 2.2 summarizes the important results of the above mentioned studies.

Table 2.2 Summarized effect of additives on macrostructure, magnetic and dielectric properties.

S. No.	**Additives**	**Calcination / sintering condition**	**Structural properties**	**Magnetic properties**	**Dielectric properties**
Solid state method					
1	Bi_2O_3	Precalcined at 1280 °C for 4 hours & sintered at 900 °C - 980 °C	Lower sintering temperature, densification & platelet morphology of grains. Bi_2O_3 segregated along the grain boundary	μ_i (~ 2) decreased due to Fe^{2+} formation	Q and f_r increased [98]
2		Sintered at 860 °C - 900 °C	Y-phase traced with Z-phase. Grain size (= 2 μm) are small & homogeneous.	Small amount of Bi_2O_3 is not able to change M_s, H_c & M_r. $\mu_i = 4$	$\rho = 3.30 \times 10^7$ Ω-cm of Bi_2O_3 sample $> \rho = 2.70 \times 10^7$ Ω-cm of pure Z-type, $Q = 50$ & $f_r >$ 1 GHz [99]
3	Bi_2O_3, V_2O_5, B_2O_3 & CuO	Heated temperature 1300 °C reduced to 900 °C with additives		$tan\delta_\mu$ decreased, magnetic properties better for 1300 °C than 900 °C	σ is higher for low sintered at < 900 °C [101]
4	Borosilicate glass, zinc borosilicate glass, Bi_2O_3, CuO	Calcined at 1200 °C and sintered at 960 °C	Bi_2O_3 existed within grain boundaries. grain size lies in the range of 0.1 μm to 3 μm	μ' increased & μ'' decreased	ε increased [102]
5	$Ba_{0.5}Sr_{0.5}TiO_3$ (BST)	Calcined at 1130 °C for 2 hours & sintered at 1240 °C, 1275 °C, & 1290 °C for 2 hours	As BST increased Z-phase existed with M-type and perovskite and grain size increased.	H_c decreased with increased BST. μ increased. Complex permeability increased with BST (0.0 to 1.5 %)	ε increased. Complex ε increased with BST (0 to 1.5 %) [104]

6	Nb_2O_5	Calcined at 1280 °C for 6 hours & sintered at 1220 °C - 1280 °C for 6 hours	Excess amount of Nb_2O_5, M-type & niobate phase increased restrict abnormal grain growth., maximum μ_i = 32-33 & resonance frequency > 400 MHz	Maximum H_c obtained 454-455 A/m with 0.80 wt. % sintered at 1260 °C for 6 hours	[105]
7	Y_2O_3	Calcined 1200 °C for 6 hours & sintered 1200 °C - 1300 °C for 3 hours	As Y_2O_3 increased major Z-phase & small garnet phase appeared	μ_i increased first and then decreased with increased Y_2O_3	When Y_2O_3 varied from 0 to 1, ε decreased & ferro-electric resonance peak shifted towards higher frequency [107]
8	SiO_2	Calcined at 1270 °C for 2 hours & sintered at 900 °C for 3 hours	Homogeneous hexagonal plate structure, average grain size decreased with 0.50 wt. % SiO_2	μ_i and $tan\delta_\mu$ decreased	$\rho > 10^8$ Ω-cm, ε decreased, $tan\delta_\varepsilon$ lower between 400 MHz- 1 GHz [108]
9	MgO	1270 °C for 2 hours & sintered 900 °C for 3 hours	Average grain size decreased with increased MgO. Sintered density lies in the range of 5.26 - 5.29 g/cm^3	M_s & H_c increased with increased MgO	Higher ρ & Q, for excess MgO decreased ε & $tan\delta_\varepsilon$ increased by reducing electronic transition between Fe^{2+} & Fe^{3+} [109]
10	$Ba_{0.5}Sr_{0.5}TiO_3$ (BST) / $Pb_{0.95}Sr_{0.5}(Zr_{0.52}Ti_{0.48})O_3$ (PZT)	Calcined at 1270 °C for 2 hours & 1250 °C for 3 hours	Average grain size & density increased with increased BST. Over 1.50 wt. % some hole appeared in grain.	Decreased magneto-crystalline anisotropy	ε increased with doping [110]

11	$MgTiO_3$	Calcined 1250 °C for 4 hours & 1270 °C for 2 hours	Grain size lies 5-15 µm	μ increased with increased $MgTiO_3$. μ'' decreased at > 300 MHz	f_r from 0.33 GHz to 1.8 GHz [111]
12	Bi_2O_3	1168 °C for 2 hours & 1000 °C or 1270 °C for 2 hours	W-phase appeared & grain size < 3 µm with 3.0 wt. % of Bi_2O_3.	μ_i sintered at 1268 °C > sintered at 1000 °C	Q is higher [114]
13	SiO_2	Calcined at 1250 °C for 2 hours & sintered at 1200 °C - 1250 °C for 3 hours	Well defined hexagonal Z-phase ≤ 4.0 wt. % & > 6.0 wt. %, SiO_2 phase existed along the grain boundaries. Average grain size decreased with increased SiO_2	μ_i decreased from 5.8 to 2.6 with increased SiO_2 may be due to reduce grain size	f_r increased. maximum Q = 14 with 4.0 wt. % SiO_2 [115]
14	Bi_2O_3	Calcined at 1000 °C for 6 hours & sintered at 1250 °C - 1280 °C for 4 hours	In range of 1200 °C -1300 °C, Y-phase appeared while at > 1300 °C, W-phase existed	$tan\delta_\mu/\mu'$ lowered for random oriented poly-crystalline ferrite. μ & ε is similar in the range of 0.3 GHz to 1 GHz	$tan\delta_\varepsilon/\varepsilon'$ is also lowered like $tan\delta_\mu/\mu'$ [116]
15	SnO_2	Calcined at 1250 °C for 3 hours & sintered at 1170 °C for 3 hours	At ≤ 0.20 wt. % of SnO_2 uniform microstructure while with increased SnO_2 content abnormal grain growth observed.	Low $tan\delta_\mu$. μ & ε matched	Low $tan\delta_\varepsilon$ & refractive index (n) = 15 [117]
16	$BaCu(B_2O_5)$ (BCB)	Calcined at 1250 °C for 4 hours & sintered at 925 °C for 2 hours	5.0 wt. % BCB provided 95.0 % density and homogeneous microstructure	With 5.0 wt. % BCB $tan\delta_\mu$ = 0.039 at 200 MHz. M_s reduced from 57.42 to 56.10 emu/g with increased 1 to 5.0 wt. %	$tan\delta_\varepsilon$ = 0.003 at 200 MHz [118]

17	Bi_2O_3, B_2O_3, SiO_2 & CuO (BBSC)	Presintered at 1100 °C for 4 hours & dried 1100 °C for 1 hours	With increased BBSC glass, particles irregularly growth. With 2.0 wt. % provided grain size of 3-5 μm	With 3.0 wt. % glass, M_s = 49.6 emu/g, H_c = 164 Oe & $tan\delta_\mu$ = 0.03 at frequency of 10-600 MHz	[119]
18	Bi_2O_3	Calcined at 1240 °C & sintered at 1000 °C, 1100 °C, 1200 °C	Y-phase appeared with decreased temperature from 1200 °C to 1000 °C. Z-phase obtained at 1000 °C with 3.0 wt. % Bi_2O_3	μ' & μ'' increased at 1 GHz	ε' increased from 1000 °C & becomes almost equal for 1100 °C & 1200 °C. ε'' increased in range of 2-4 GHz [121]
19	$ZnAl_2O_4$ (ZA)	Presintered 1200 °C for 2 hours & 1200 °C for 3 hours		μ' decreased from 12.0 to 4.3 at low frequency for ZA (0.0 to 15.0 wt. %). At 5.0-10.0 wt. % of ZA, $tan\delta_\mu$ of order 10^{-2} at 300 MHz	ε' decreased from 27.4 to 10.7 at low frequency for ZA (0 to 15 wt. %). At 5-10.0 wt. % of ZA, $tan\delta_\varepsilon$ of order 10^{-3} at 300 MHz [122]
Sol-gel method					
20	B_2O_3, LiF & CaF_2	Calcined at 1100 °C - 1150 °C & sintered at 870 °C, 890 °C & 920 °C	Density increased with Cu content, additives reduced sintering temperature, grain size < 2 μm	μ_i increased from 4.2 to 7 with Cu	$\rho > 10^8$ Ω-cm, f_r > 1.2 GHz [100]
21	SiO_2	Heated at 1150 °C-1200 °C & fired at 900 °C for 6 hours	Homogeneous hexagonal platelet grains with high density. Average grain size (2.2 μm) of SiO_2 < pure Z-type (0.5 μm)	μ_i decreased, ferromagnetic resonance frequency shifted towards higher frequency	ρ increased with SiO_2, $tan\delta_\varepsilon$ decreased, Q > 25 at 1 GHz [103]
22	Bi_2O_3	Calcined 900 °C - 1350 °C for	Between 1000 °C & 1100 °C majored M-	μ = 20 stable upto 100 MHz, μ'' is maximum	[106]

		4 hours & 1330 °C for 4 hours	phase, at 1230 °C Y-phase	at 700 MHz. μ = 3 with 3.0 wt. % of Bi_2O_3	
23	Bi_2O_3	Calcined at 1200 °C for 12 hours & sintered at 900 °C for 2 hours	M_s = 47-52 emu/g, H_c = 10-20 Oe	μ = 6-7	$\rho > 10^9$ Ω-cm, f_r = 1 GHz [120]
24	Al_2O_3	Heated at 900 °C & 1100 °C and further heated 1250 °C & 1350 °C		μ & $tan\delta_\mu$ reduced	ε & $tan\delta_\varepsilon$ reduced [113]

2.3. Effect of substitution

The crystal structure and blocks of Z-type hexaferrite can be modified by partially/fully substituted alkali and alkaline earth metals. Various affords have been made to enhance the magnetic and dielectric properties of hexaferrites by substituting within the complex structure for Ba or Sr. Among the various substitution for Ba ion, the rare earth La^{3+} ion is the most investigated one followed by Ca^{2+} ion and Mg^{2+} ions. Below some important work carried out for Ba substitution are discussed.

Xu et al. in 2009 [60] prepared La-substituted Z-type ferrites, $Ba_{3-x}La_xCo_2Fe_{24}O_{41}$ (x = 0.00 – 0.30) by sol-gel method and investigated the effect of La^{3+} ions on microstructure, complex μ, ε and microwave absorption. With the increase of La contents from x = 0.0 – 0.3, the unit cell parameters gradually increases and the abnormality of grain growth reduces as compared to pure Z-type. La^{3+} substitution increased M_s and reduced H_c. The complex μ, ε, and microwave absorbance of the material increased by La substitution in the frequency range of 0.5 GHz - 15 GHz. ***Rashad et al.*** in 2013 [123] doped La^{3+} ions ($Ba_{3-x}La_xCo_2Fe_{24}O_{41}$, x = 0.0, 0.05, 0.10 and 0.15) in Co_2Z-type hexagonal ferrite via co-precipitation method. The crystallite size increased with La content, and microstructure appeared as hexagonal platelet. The M_s = 53.7 – 55.5 emu/g increased while M_r and H_c decreased with increasing La^{3+}content. The *dc* resistivity decreased with increasing La^{3+} substitution. The imaginary complex permeability showed two characteristic resonance peaks, while the real part of the complex permeability demonstrated decreasing trend in X-band frequencies. ***Rashad et al.*** in 2013 [124] synthesized La-substituted Z-type hexaferrite ($Ba_{3-x}La_xCo_2Fe_{24}O_{41}$) powders (x = 0.0, 0.05, 0.10 and 0.15) by combusted sol-gel method and their magnetic and dielectric behavior in 2018 GHz range were investigated. The atoms are preferentially oriented via basal plane with La^{3+} ion doping and the microstructure of prepared powders showed a hexagonal platelet-like structure. The value of M_s, M_r & H_c obtained were 48.68 emu/g, 2.86 emu/g and 41.05 Oe, respectively in substituted powders. The degree of the electron hopping between Fe^{3+} to Fe^{2+} increased with increased La^{3+} ratio. ε'& ε'' increased while μ' decreased and μ'' increased. La-substituted Z-type showed high electric and magnetic dispersion 2-18 GHz.

Xu et al. in 2011 [125] prepared Sm-substituted $Ba_{3-x}Sm_xCo_2Fe_{24}O_{41}$ (x = 0.0 – 0.25) by conventional ceramic method. The ε' & ε'' was enhanced with Sm concentration and further decreased at x > 0.10. The grain growth rate was decreased with increased Sm. The *M-H* curves indicated that M_s, H_c & M_r is increased with the Sm contents. ***Kumar & Gaur*** in 2018 [126] synthesized rare earth (RE = La, Pr & Sm) substituted $Sr_{2.9}RE_{0.1}Co_2Fe_{24}O_{41}$ via sol-gel auto-combustion method. They determined the effect of rare earth elements on structural, ferroelectric, magnetic, and electrical properties. FTIR showed the bond stretching of the synthesized samples. The maximum saturation polarization for Pr doped samples was 0.019, 0.042, and 0.061 μC/cm^2 at 10, 20, and 30 kV/cm applied field. *M-H* curves showed the maximum H_c of 128 Oe for the La, while maximum M_s of 67 emu/g was observed for Sm doped sample. Complex impedance spectra manifested that the large impedance is observed for La-doped samples. The obtained bulk resistances was 1.77, 2.59, 1.75, and 1.96 MΩ for pure, La, Pr, and Sm doped samples, respectively. ***Tran et al.*** in 2019 [127] prepared $Ba_{3-x}La_xCo_2Fe_{24}O_{41}$ (x = 0.0 – 0.5) via solid-state reactions. The electronic structure analysis showed oxidation states of Fe and Co in Z-type ferrites are 3^+ & 2^+, respectively. The exchange interactions between magnetic moments of Fe ions increased due to La substitution, and resulting M_s increased without changing the soft magnetic behavior (H_c = 2.2 – 3.6 kA/m).

Aoyama et al. in 2006 [128] prepared $Ba_{(1-x)}Sr_{3x}Co_2Fe_{24}O_{41}$ (x = 0 - 0.5) by wet milling and two step calcination. Z-type phase remains unchanged with excessive amount of Sr. ***Lim et al.*** in 2015 [129] prepared $Ba_{3-x}Sr_xCo_2Fe_{24}O_{41}$ (x = 0.0, 0.5, 1.0 & 1.5) by solid state reaction method. The lattice constants decrease with increased Sr concentration. The values of M_s decreased while H_c increased with the Sr substitution. ***Manhas et al.*** in 2018 [130] synthesized $Ba_{3-x}Sr_xCo_2Fe_{24}O_{41}$ (x = 0.0, 0.5, 1.0, 1.5 & 2.0) and investigated the influence of Sr^{2+} ions on their structural and magnetic properties. The M_s increased up to x = 1.0 and with further increasing Sr contents M_s decreased for x = 1.5 and enhanced for x = 2.0 H_c & M_r showed decreasing trend for all Sr contents.

Xu *et al.* in 2011 [131] $Ba_{3-x}Nd_xCo_2Fe_{24}O_{41}$ (x = 0.00, 0.05, 0.10, 0.15 & 0.25) synthesized by solid state reaction and investigated the influence of substitution on their microstructure and electromagnetic properties. The μ & ε is evaluated in the frequency (0 GHz - 18 GHz). ε' & ε'' increased with lower value of Nd and decreased for its high content. In lower frequency region, μ'' decreased for Nd substitution and increased above 7 GHz. M_s & H_c of $Ba_{2.75}Nd_{0.25}Co_2Fe_{24}O_{41}$ was 79.38 emu/g & 36.94 Oe, respectively.

The effect of Ca^{2+} substitution for Ba or Sr ions specially in M-type and W-type hexaferrites [132, 133] were largely carried out. The Ca, Sr, and Ba lie in the same column of periodic table and has the same electronic configuration in the outermost shell. The ionic radii of Ca (0.99 Å) is lower than the radius of Ba (1.35 Å) and Sr (1.13 Å). So far only one work on Ca substituted Z-type hexaferrite is reported by ***Zheng et al.*** in 2018 [134]. They prepared $Ba_{3-x}Ca_xCo_2Fe_{24}O_{41}$ (x = 0.0 – 1.5) by solid state method and investigated its magnetic properties, permeability spectra, and $tan\delta_\mu$ in the frequency range of 0.1 GHz - 10 GHz. The crystal composition and microstructure analysis showed that the Z-type phase coexisted with W-type as Ca content increased. The μ' linearly decreased from 8 to 4.1 GHz with varying Ca concentrations from 0.0 to 1.5. A specific ratio of Ca^{2+} substitution (x = 0.2) showed minimum $tan\delta_\mu$ through the frequency and x ≥1 possessed low $tan\delta_\mu$ at high frequency ranges. The combined phase of Co_2Z & Co_2W provided the homogeneous microstructure to decrease the $tan\delta_\mu$ over high-frequency ranges.

From the above review work it can be concluded that substitution for barium significantly affects the magnetic and dielectric properties.

Apart from, substitution for Ba^{2+} ions, many investigations also have been carried out for Co^{2+} and Fe^{3+} substitutions on hexaferrites [135-147]. A few important works for Fe^{3+} substitution is reviewed below.

Bao et al. in 2002 [148] prepared a series of $Ba_3Co_2Fe_{23-12x}Mn_{12x}O_{41}$ for multilayer chip inductor to measure the ε and loss tangent depending on frequency, temperature, and composition. The results confirmed that dielectric increases with increased temperature because the number of electric charge carriers and their drift mobility increased due to the thermal treatment. Although, the ε and $tan\delta_\varepsilon$ reduced with increased frequency and decreased temperature, attributing to the Maxwell-Wagner effect. With increased Mn content, the relaxation peaks shifted towards higher frequency regions. The substitution of Mn reduced the Fe^{2+} ions on B-sites implied that the loss tangent was reduced. ***Bao et al.*** in 2002 [149] investigated the electric and dielectric properties of $Ba_3Co_2Fe_{23-12x}Mn_{12x}O_{41}$ hexaferrites, $0 \leq x < 0.1$. The *dc* resistivity and required activation energy for conduction enhanced as Mn content increased. The μ_i is effectively controlled by substituting Mn.

Singha et al. in 2019 [150] synthesized Co_2Z type hexaferrites ($Ba_{1.5}Sr_{1.5}Co_{2-z}Ho_zMn_xNi_yFe_{24-x-y}O_{41}$) with Ho-substituted for Co and co-substituted Mn, Ni for Fe via the sol-gel auto-combustion method. The microstructural analysis confirmed the hexagonal structure with a single-phase crystal structure. The crystallite size increased with increased X-ray density while the porosity decreased for various dopants. The magnetic measurements showed maximum M_s = 44.04 emu/g and H_c = 2240 Oe for x = y = z = 0 and x = y = 1 & z = 0.20, respectively.

Several research works have been accomplished to achieve better magnetic and dielectric properties by doping trivalent Al ion [141, 142, 151-153]. ***Wu et al.*** in 2013 [154] prepared $(Ba_{0.5}Sr_{0.5})_3Co_2Fe_{22-x}Al_xO_{38}$ (x = 0.0, 0.4, 0.8, 1.2, 1.6, 2.0 & 2.4) compound having 1.0 wt. % of boric acid with the help of conventional ceramic technique. Al substitution not only significantly increases the sintering density and *dc* resistivity but also decreases magneto-dielectric loss. H_3BO_3 additive reduced the sintering parameter and influenced some of the magnetic properties (μ & resonance frequency). The higher sintered density led to enhancement of ε' from 10.2 to 11.3. ***Tiwari & Vitta*** in 2016 [155] studied the magnetic and dielectric properties of $Sr_3Co_2Fe_{24-x}Al_xO_{41}$ (x = 0 & 0.45). The hysteresis at room temperature for x = 0 showed ferromagnetic behavior while the substituted compound represented the discontinuous step, indicating the successive evolution of magnetic structure at different fields. In both samples, the ε and ρ decreased with increased frequency. The resistivity of the pure sample reduced from 10^6 Ω-cm to 6×10^4 Ω-cm while for x = 0.45 decreased from 10^7 Ω-cm to 6×10^4 Ω-cm. ***Asl et al.*** in 2016 [156] prepared Al & Cr co-substituted Z-type hexaferrites by co-precipitation assisted solid-state synthesis method. XRD patterns showed that the major Co_2Z phase coexists with M & Co_2Y types. The lattice parameters increased with increased Al & Cr substitution, and SEM micrographs confirmed variation in the size of particle in the range of 50 nm-300 nm. The magnetic measurements showed that the M_s and H_c both increased with dopant. The highest reflection loss of substituted Z-type is -37 dB at frequency 9.9 GHz which is greater than -20 dB. These results demonstrated that Al-Cr substituted Z-type is suitable in microwave absorber technology in the frequency range 8 – 12 GHz.

Lim & Kim in 2017 [157] synthesized $Ba_{1.5}Sr_{1.5}Co_2(Fe_{1-x}Al_x)_{24}O_{41}$ (x = 0.00, 0.01, 0.03 and 0.05) via polymerizable complex method. Hysteresis curves were not saturated with Al content because the magnetic anisotropy was reduced. Al ions occupied preferential spin-up sites and modified spin structure, but H_c increased. Mössbauer spectra suggested that Al ions occupied tetrahedral sublattice. ***Basandrai et al.*** in 2018 [65] prepared nanoparticles of Z-type hexaferrites $Ba_3Cu_2Al_{x/2}Cr_{x/2}Fe_{24-x}O_{41}$, where x varies from 0 to 1.0 by sol-gel auto combustion method. FTIR analysis showed bands 415-480 cm$^{-1,}$ and 550-590 cm^{-1} which represented the variation in bond length for Fe-O at octahedral and tetrahedral positions. The hysteresis curves demonstrated M_s of 17.5 emu/g, H_c of 911.11 Oe and M_r of 41.5 emu/g for x = 1. Radiation absorbance showed the maximum radiation loss -31.10 dB for x = 0.5 at 11.14 GHz frequency.

Wu et al. in 2020 [158] investigated the influence of aluminum doping on magneto-electric properties, Sr_3Co_2 $(Fe_{1-x}Al_x)_{24}O_{41}$, from x = 0.00 to 0.08. It was found that spin structure (conical) got stabilized with aluminum doping and increased its magnetic properties where for $x \leq 0.04$ ferroelectric phase was obtained. ***Wu et al.*** in 2021 [159] sintered Al-doped polycrystalline hexaferrites $Sr_3Co_2(Fe_{1-x}Al_x)_{24}O_{41}$, x = 0.00, 0.02 & 0.04, under high oxygen atmospheric pressure and investigated magneto-electric effect at room temperature. The transverse conical spin structures were found to show magneto-electric effect at higher field more than 1 T.

Mu et al. in 2011 [160] prepared $Ba_3Co_2Dy_xFe_{24-x}Ti_xO_{41}$, where x varies from 0.0 to 1.0 by conventional sintering method. The M_s decreased while H_c increased with the Dy concentration. The μ_i was found to be maximum at 300 MHz for x = 0.5. ***Rasly & Rashad*** in 2013 [161] prepared $Ba_3Co_2Sn_xZn_xFe_{24-2x}O_{41}$ ($0 \leq x \leq 0.1$) using citrate precursor process to study their magnetic properties. The co-substitution Sn-Zn showed maximum M_s for x = 0.1. M_r & H_c to increase with Sn-Zn. **Li *et al.*** in 2013 [162] synthesized $Ba_3Co_2Fe_{24-x}Ti_xO_{41}$(x = 0.0 – 0.6) by conventional sintering method to study the magnetic properties. M_s & H_c increased to maximum and then decreased with Ti concentration. ***Magham et al.*** in 2017 [63] prepared $Ba_3Co_2Cr_{2x}Fe_{24-2x}O_{41}$ (x = 0, 0.3, 0.6 & 0.9) and evaluated magnetic properties. The *M-H* loops showed M_s decreased with increased Cr whilst M_r & H_c increased. **Kulik *et al.*** in 2020 [163] prepared $Ba_3Co_{2+x}Fe_{24-2x}M_xO_{41}$ (M = Ir, Hf & Mo for x = 0 & 0.05) showed the lower $tan\delta_\mu$ and $tan\delta_\varepsilon$ with similar ε and μ over VHF – UHF band. The μ increased linearly with the ionic radii of the dopants. The magnetic ($tan\delta_\mu/\mu'$) and dielectric ($tan\delta_\varepsilon/\varepsilon'$) form factors were 0.038 and 0.0006 at 650 MHz.

The above discussion suggests that the cation substitution not only influences sintering temperature and microstructure but also affects the magnetic and dielectric properties of the material. The conduction mechanism of the electric charge is changed with changing internal electric barrier potential (resistance). The super-exchange interaction between Fe^{3+} & Fe^{2+} depends on cation selection. Table 2.3 summarizes the important results obtained from the above mentioned studies.

Table 2.3 Summarized effect of substitution on microstructure, magnetic and dielectric properties.

S. No.	**Cation**	**Calcination /sintering condition**	**Structural properties**	**Magnetic properties**	**Dielectric properties**
		Sol-Gel Method			
1	La^{3+}	Prefired at 400 °C & sintered at 1000 °C, 1100 °C, 1200 °C, 1250 °C and 1300 °C for 5 hours	Z-phase obtained at 1250 °C & 1300 °C. La^{3+} suppressed abnormal grain growth. La doped grain size (0.5-1.0 µm) < pure Z-type (2-3 µm)	M_s increased & H_c decreased. Maximum $tan\delta_\mu = 0.71$. μ' reduced & μ'' increased	Maximum $tan\delta_\varepsilon = 0.29$. ε' & ε'' increased with Fe^{2+} formation [60]
2		Preheated at 600 °C for 4 hours & post annealed at 1300 °C for 6 hours	With La^{3+} substituted < 0 & > 0.15 shown symmetrical hexagonal plate shape	Higher M_s due to W-phase & lower H_c, M_r implied pure Z-phase existed. μ' reduced & μ'' increased	ρ decreased with increased La^{3+} contents [123]
3		600 °C for 4 hours & 1250 °C for 5 hours	Crystallite size increased with La^{3+} substituted. Hexagonal platelet structure. Average grain size of modified Co_2Z (0.5-2 µm) < pure Z-type (1-3 µm)	Low H_c due to Z-type & M_s increased with La^{3+} because exchange interaction increased in Fe^{3+}-O-Fe^{2+} at 12k & 2b sites	ε' decreased & ε'' increased. ρ decreased with La^{3+} [124]
4	La, Pr & Sm	Presintered at 1270 °C for 4 hours & sintered at 1000 °C for 2 hours	Platelet like grain structure. Average grain size of pure, La, Pr & Sm samples are 1.8, 3.0, 2.5 & 2.0 µm	H_c =128, 48, 80 Oe & M_s = 63, 57, 67 emu/g for La, Pr & Sm, respectively	Maximum saturation polarization are 0.019, 0.042 & 0.061 µC/cm^2 for Pr at, 10, 20 & 30 kV/cm [126]
5	Sr	Calcined at 1200 °C for 5 hours	Nanosize hexagonal grain	M_s increased & H_c decreased with Sr substitution. M_s increased by bonding decreased in Fe^{3+}-O^{2-}-Fe^{2+}	[130]
6	Nd	Calcined at 1250 °C for 5 hours	Small, perfect and homogeneous grain. Average grain size of pure (15 µm) > Nd doped (5-10 µm)	μ'' decreased with Nd & above 7 GHz	ε' & ε'' increased first and then decreased with increased Nd [131]

7	Ho, Ni, Mn	Heated at 1150 °C for 4 hours & sintered at 1200 °C	Crystallite size = 43-60 nm, porosity decreased, regular hexagonal shape in the range = 1-10 µm, density increased with substitution	M_s decreased while H_c increased. Maximum M_s = 44.04 emu/g & H_c = 224 Oe .	[150]
8	Al, Cr	Dried at 100 °C & calcined at 1000 °C for 3 hours	Small M & Y-phase traced. Particles are irregular, platelet and spherical. Average particles size decreased with increased Al & Cr	Substitution from 0 to 0.4, M_s = 60-73 emu/g & H_c = 1306- 1850 Oe. Super-exchange increased between magnetic ions at different sublattices	[156]
9	Al	Heated at 300 °C for 3 hours & sintered at 1190 °C, 1210 °C & 1230 °C for 10 hours related Al contents are 0, (0.01 & 0.03) & 0.05, respectively	Spin structure is modified by lower magnetic anisotropy	M_s decreased by preferential occupation of Al ions in spin up sites. H_c increased because H_a decreased	[157]
10	Al, Cr	Heated at 280 °C - 300 °C for 3 hours & sintered at 1200 °C for 5 hours	Grain size decreased with increased substation	H_c increased from 477.77 to 911.11 Oe with substituted limit (0.5 to 1.0). M_s is also increased similar to H_c	ε first increased and then decreased [65]
11	Sn, Zn	600 °C for 4 hours & annealed at 1200 °C to 1300 °C for different times	For 1200 °C, Y, W & Z-phases coexted while at 1300 °C, major Z-phase with minor W-phase. density decreased with increased substitution	M_s decreased while H_c increased	[161]
Solid State method					
12	Sm	Calcined at 1250 °C for 5 hours	Sm^{3+} suppressed grain growth & decreased grain size	M_s, M_r & H_c increased. μ' non changeable & μ'' decreased with increased Sm^{3+} content	ε' initial increased for x = 0 & decreased for x > 0.10 [125]
13	La	1000 °C for 12 hours & annealed at 1260 °C for 24 hours	Oxidation state of Co is stable while Fe is changed & densities changed with La content	M_s increased with La substitution & H_c = 2.2-3.6 kA/m	[127]
14	Sr	Precalcined 1080 °C for 2 hours & post calcined at 1230 °C for 2 hours	Platelet grain size = 20 µm. Mechanical process reduces particle size and diffusion path increased	Anisotropy crystalline decreased with Sr	[128]

15		Calcined at 1000 °C & sintered at 1200 °C	Single Z-type phase	M_s increased while H_c decreased. Planar anisotropy reduced with different ionic radii of Ba^{2+} & Sr^{2+}	[129]
16	Ca	Calcined at 1100 °C for 10 hours & sintered at 1200 °C for 16 hours	With Ca substitution, average grain size decreased microstructure becomes homogeneous. W-phase increased with Ca content	μ'' & $tan\delta_\mu$ reduced at higher frequencies	[134]
17	Mn	Calcined at 1270 °C for 6 hours & sintered between 1100 °C & 1260 °C	Density almost constant. Relaxation peak shifted towards higher frequency domain with Mn content		ε increased with increased sintered temperature. ε & $tan\delta_\varepsilon$ decreased with increased frequency & decreased with temperature [148]
18		Calcined at 1270 °C for 6 hours	Density reached 93.5 % for 900 °C while 94 % for 1140 °C	μ_i first increased with Mn content, reached maximum at x = 0.02 and decreased further substitution	f_r reduced to lower frequency [149]
19	Al	Calcined at 1250 °C for 2 hours & sintered at 980 °C for 3 hours	Average grain size decreased with increased Al substitution. Bulk density increased with Al_2O_3 from x = 0.0 to 1.2 and maximum at x = 1.6.	μ' decreased with increased Al_2O_3 due to low M_s & small grain size. μ'' is lower in 10 MHz - 1 GHz	ε' increased from 10.2 to 11.3 with increased Al_2O_3 & decreased with increased excess Al_2O_3 [154]
20		Calcined at 1200 °C for 12 hours & sintered at 1200 °C for 12 hours	Platelet like grains	M_s decreased from 31 μ_B/formula unit to 22 μ_B/formula unit for pure Co_2Z. For x = 0.45, M_s decreased from 28 μ_B/formula unit to 20 μ_B/formula unit with increased temperature 200 K to 400 K	ε & ρ decreased with Al substitution. Al substitution reduced exchange between Fe^{3+} & Fe^{2+} [155]
21		Calcined at 1000 °C for 10 hours & sintered at 1250 °C for 10 hours	Al doping stabilized transverse conical spin structure	Low H_c. At x = 0.08, switched magnetic field leads to switching ferroelectric polarization.	[158]

22		Calcined 1000 °C for 10 hours in box type furnace. Sintered at 1250 °C in tube furnace for 10 hours & in box furnace at 1250 °C for 10 hours	Knee feature indicated transverse structure at *RT* associated to the magneto-electric effect	For both box & tube furnace, M_s decreased & H_c increased	[159]
23	Dy	Presintered at 1200 °C for 2 hours & sintered at 1250 °C for 3 hours	With higher value of Dy $Dy_3Fe_5O_{12}$ phase obtained along grain boundaries and grain size decreased	M_s decreased & H_c increased with increased Al contents. Maximum $\mu' = 17$ at 300 MHz (for x = 0.5)	Lower f_r around 800 MHz (for x = 0.5) [160]
24	Ti	Calcined at 1080 °C for 4 hours & 1300 °C for 4 hours	Anisotropy field H_θ increased. μ'' showed two absorption line with different frequencies, one related to	μ' first increased to maximum (18) at x = 0.3-0.45 & decreased to 16. μ'' also increased to 9.8 at x = 0.3 - 0.45 & decreased to 8 at x = 0.6	[162]
25	Cr	Sintered at 1300 °C for 10 hours & sintered at > 1250 °C	Average grain size around 100 nm. Density is almost constant.	M_s decreased with increased Cr content while H_c & M_r increased	Microwave absorption 98.8 % at 5.34 GHz [63]
26	Ir, Hf & Mo	Calcined at 1000 °C for 6 hours & sintered at 1250 °C for 4 hours	W or Y-phase existed with Z-phase	$tan\delta_\mu/\mu' = 0.038$ at 650 GHz. Lower $\mu' \sim 6$ at 1.25 GHz & maximum $\mu' \sim 10$ at 0.7 GHz	$tan\delta_\varepsilon/\varepsilon' = 0.0006$ at 650 GHz. $\varepsilon' \sim 12$ for Hf doped sample $< \varepsilon' \sim 9$ for Mo & Ir samples [163]

Chapter 3

Experimental & characterization techniques

Overview

In this chapter, the synthesis methodology of Co_2Z hexaferrite ($Ba_3Co_2Fe_{24}O_{41}$) is given. Different characterization techniques namely; X-ray diffraction (XRD), Vibrating Sample Magnetometer (VSM), Scanning Electron Microscope (SEM) and Impedance Analyzer (LCR Meter) and their measurement conditions are briefed.

Many techniques have been introduced to prepare hexaferrites using different methods (hydrothermal [164], co-precipitation [165], micro emulsion [166], sol-gel [167] and self-propagation [71]. In this work, Z-type $Ba_3Co_2Fe_{24}O_{41}$ (Co_2Z) ferrite powders were prepared by solid state method [168]. The preparation method are described below:

3.1. Synthesis of Co_2Z hexaferrite

To prepare $Ba_3Co_2Fe_{24}O_{41}$, analytical grade high purity (Sigma Aldrich 99.99 %) $BaCO_3$ (197.34 g/mol), Fe_2O_3 (159.69 g/mol) and Co_3O_4 (240.80 g/mol) were used. The chemical reaction is given below:

$$9\,BaCO_3 + 2\,Co_3O_4 + 36\,Fe_2O_3 = 3\,Ba_3Co_2Fe_{24}O_{41} + O_2\,(\uparrow) + 9\,CO_2\,(\uparrow)$$

The raw materials were weighted in stoichiometric proportion and ground for 30 minutes using mortar pestle. Further, it was wet-mixed for 6 hours in a planetary ball mill using acetone media. Ball to charge ratio and rotation per minute (rpm) was kept constant at 3:1 at 300 rpm, respectively. After drying the as-mixed powder was calcined at 1150 ℃ for 6 hours in a resistance furnace followed by re-calcination at different temperatures (1150 ℃ - 1300 ℃). The heating and cooling were kept at 5 °C/minute. To obtain the fine powder, the calcined powders were ball milled for 4 hours in tungsten jar. The rpm and ball-to-charge ratio were 300 and 1:10, respectively. After milling the powder was dried and mixed with 10.0 % polyvinyl alcohol (PVA) binder and compressed into cylindrical pellets of 10 mm diameter at 125 MPa using uniaxial hydraulic press. Finally, the obtained pellets were sintered at different temperatures (1150 ℃ - 1250 ℃) for 1 hour in a resistance furnace. The schematic of the preparation method is shown in Fig. 3.1.

After obtaining the adequate processing conditions following series for Ba^{2+} and Fe^{3+} substitution were prepared:

1. $Ba_{3-x}La_xCo_2Fe_{24}O_{41}$, ($x = 0.0, 0.1, 0.2, 0.4, 0.6$).

2. $Ba_{3-x}Ca_xCo_2Fe_{24}O_{41}$ ($x = 0.0, 0.1, 0.2, 0.4, 0.6$).

3. $Ba_3Co_2Fe_{24-x}Al_xO_{41}$ ($x = 0.0, 0.4, 0.6, 0.8, 1.0$ & 1.8).

In another series, $Ba_3Co_2Fe_{24}O_{41}$ were prepared with SiO_2, MgO, Al_2O_3 & Bi_2O_3 and additives as per equation-

$(1-x)\,Ba_3Co_2Fe_{24}O_{41} + x$ (Additives); ($x = 0.0, 1.0, 2.0, 3.0$) wt. %.

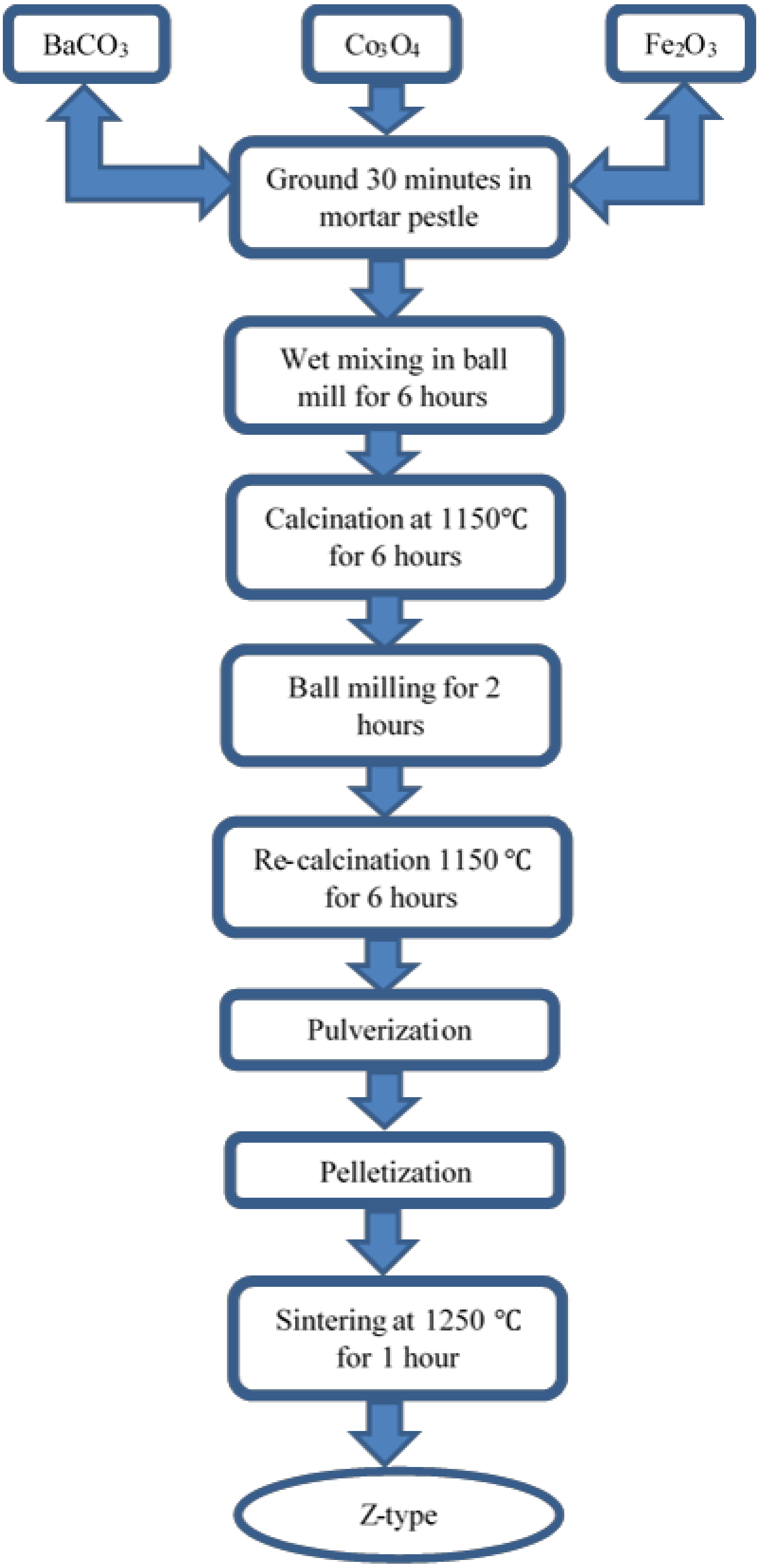

Fig. 3.1 Flow chart of Co_2Z hexaferrite synthesis by solid state method.

3.2. Characterization techniques

Different characterization and analytical tools named as X-Ray Diffraction (XRD), Energy Dispersive X-ray Spectroscopy (EDX), Scanning Electron Microscopy (SEM), Vibrating Sample Magnetometer (VSM) and Impedance Analyzer (LCR meter) were employed.

3.2.1. X-ray diffraction (XRD)

XRD is a powder diffraction technique to identify phases of a crystalline material. In this technique, a beam of monochromatic X-rays are made incident on the sample and the beam diffracted from the different planes of periodically arranged lattice is analyzed. The diffraction condition depends on the atomic configuration of the crystal lattice and its periodicity. Depending upon the path difference between the diffracted beam constructive or destructive interference occurs. Bragg's law states the constructive interference, $2d_{hkl}\ sin\theta = n\lambda$, where λ is X-ray wavelength and d_{hkl} is the inter-planar spacing between planes characterized by Miller indices (*hkl*). Fig. 3.2 shows the schematic diagram of the diffraction of X-rays by a periodically arranged atoms inside a crystalline solid [169].

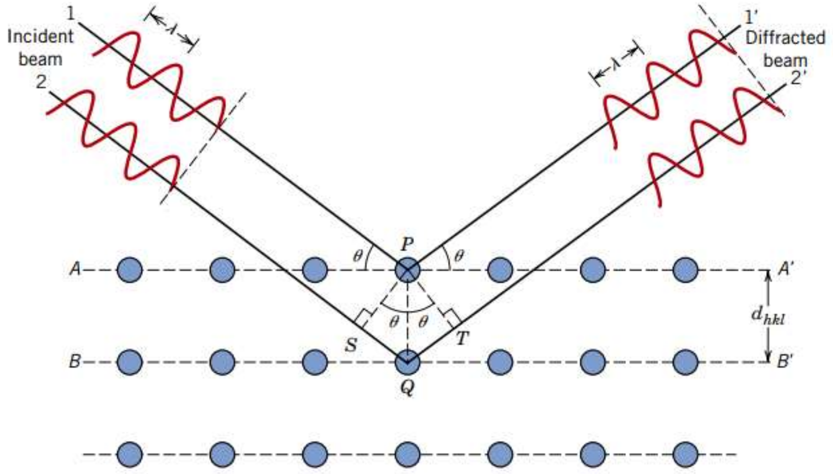

Fig. 3.2 Bragg's diffraction at different atomic planes.

In the present case, XRD measurements were carried out on powder samples in the Bragg-Brentano geometry. A sample holder having a groove of size 10 mm × 10 mm × 0.5 mm was used. This groove was filled with the powder sample and presented properly. It was assumed that powder exactly filled the groove. A PANalytical X'pert pro diffractometer was used in this work shown in Fig.3.3. For all samples, slit width on the incident side was kept 5 mm. Cu-k_α radiation (λ = 1.54005 Å) was used. The data was acquired with a step size of 0.0131° and a scanning rate of 2°/min. Rietveld refinement of the XRD patterns was carried out by FullProf Suite software. The Rietveld refinement performed the least square refinements until the best fitting condition was achieved between the observed diffraction pattern and the entire calculated pattern for the crystal structure. Before the refinement, background noise was reduced from the diffraction pattern. The peak shape of the patterns is considered as Pseudo-Voigt. The refinement parameters are profile residual factor (R_p), weighted profile residual (R_{wp}), expected profile residual (R_{exp}) and χ^2 measures the goodness of fit quality factor which should be ~ 1. Three-dimensional crystal structures were obtained by VESTA software.

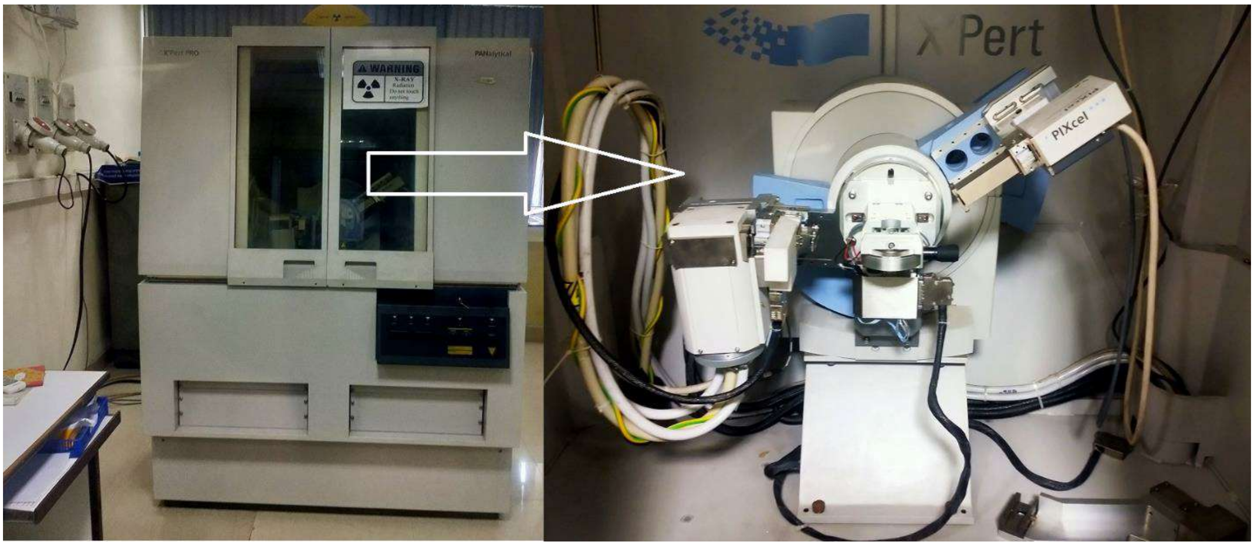

Fig. 3.3 PANalytical X'pert Pro instrument.

3.2.2. Scanning Electron Microscope (SEM)

Scanning electron microscope is used to analyze the microstructural features of the samples. For it, a focused electron beam is allowed to fall on the sample as shown in Fig. 3.4 (a). When an electron beam falls on the surface of the sample, it interacts with certain volume of the sample which depends on the operating voltage of SEM as shown in Fig. 3.4 (b).

During the interaction of the primary beam of the electron with the sample, many other signals are generated. These are secondary electrons, backscattered electrons and other radiations. When the primary beam impacts on the sample, loosely bound electrons having energy in the range of 3 eV – 5 eV, called secondary electrons are emitted. These electrons provide the topographic information of the sample surface. A fraction of the electron beam is reflected by the electromagnetic field of the nucleus and escapes from the surface with a greater scattered angle of 180°, defined as backscattered electrons. The electrons existing in the different shells of the sample when knocks out by primary electron, their position is filled by the other outer shell electrons existing in upper shells, by releasing an X-ray photon. These photons represent the characteristic feature of the elements, also called characteristic X-rays. The characteristic X-rays are utilized for determination the chemical composition of the sample. When an electron beam sticks to the surface, an electron-hole is formed inside the inner shell, and the hole is filled by the outer shell electron. During this process, excessive energy is transferred to the different electron which is emitted out in the form of Auger electrons. As electrons recombine to the hole vacancy, some amount of the energy is emitted in the form of X-ray, called cathode luminescence.

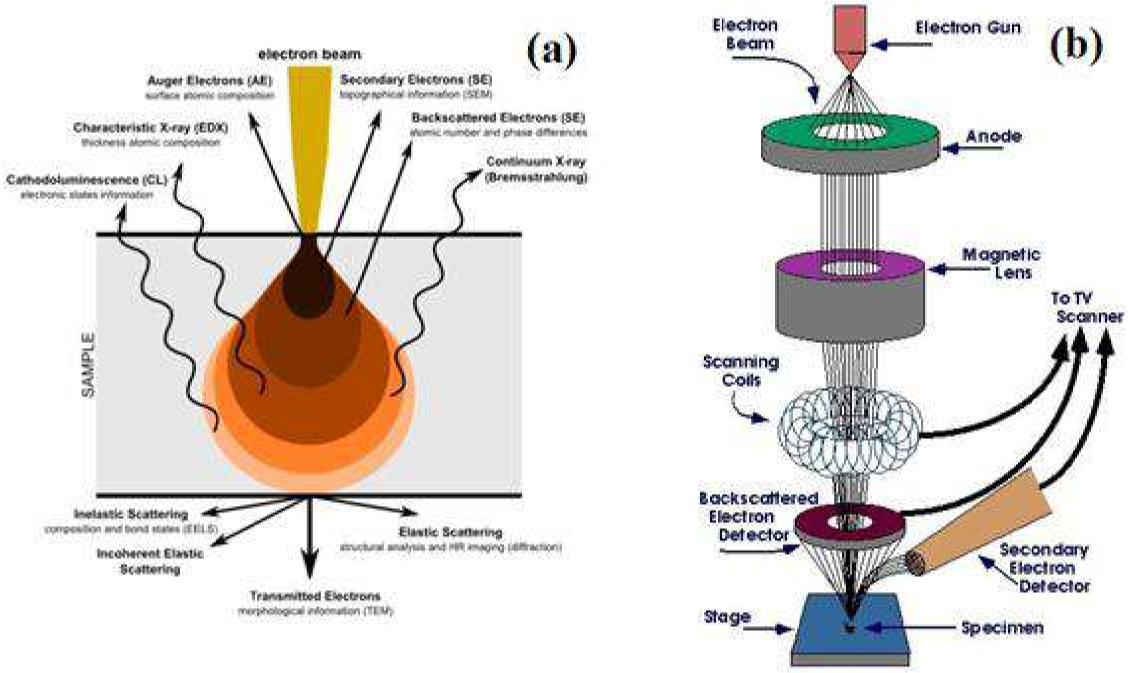

Fig. 3.4 (a) Electron-sample interaction volume originates various signals and (b) A schematic geometry of SEM.

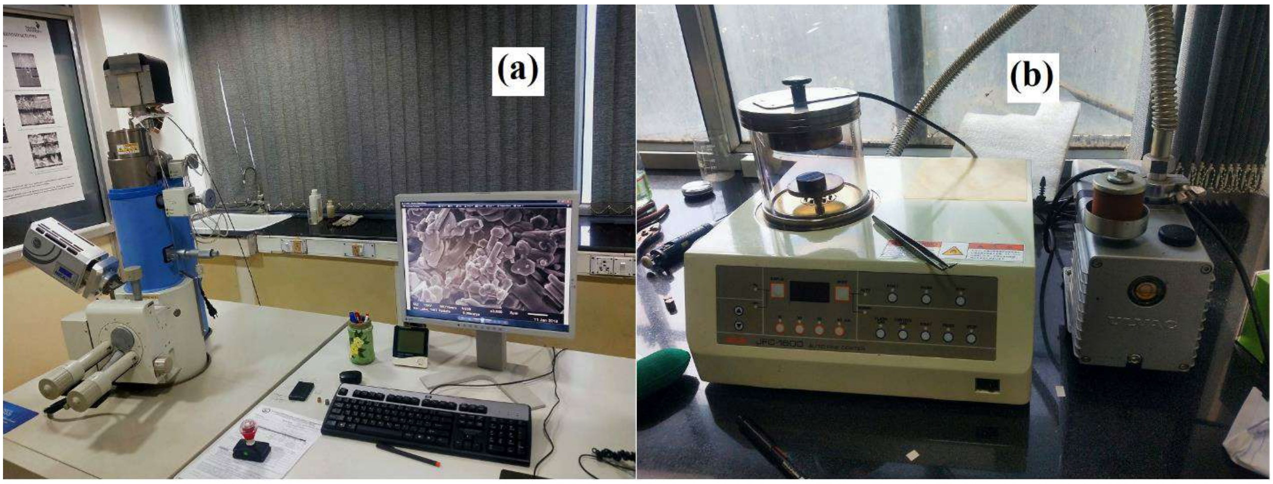

Fig. 3.5 (a) SEM instrument and (b) sputter coater.

The photographs of the SEM instrument is shown in Fig. 3.5 (a). For microstructural analysis, a pellet (diameter of 10 mm & thickness of 1.25 mm) was fractured. This fractured surface was gold coated using a sputter coater was shown in Fig 3.5 (b). JEOL-JSMIT100 SEM machine was used for microstructural analysis of the samples in this thesis. This machine is equipped with an Oxford EDS detector (INCA x-act). The grain size was calculated by ImageJ software.

3.2.3. Vibrating Sample Magnetometer (VSM)

Vibrating sample magnetometer (VSM) works on Faraday law. Fig. 3.6 shows the photograph of the VSM instrument. VSM measures magnetization of the material as a function of applied magnetic field. The saturation magnetization (M_s), coercivity (H_c) & remanent magnetization (M_r) are marked in Fig. 3.7, defined as Hysteresis loop. The magnetization of the sample is measured by vibrating sample in an external field. This causes a variation in magnetic flux and originates a voltage in the sensing coil which is proportional to the magnetization of the sample. Thus by measuring the induced voltage in sensing coils, magnetization of the sample can be measured.

For VSM measurement, powder sample was densely packed in a cylindrical vial of 5 mm length. The *M-H* loops of the Co_2Z hexaferrite were measured in the maximum field range of ± 10 kOe at room temperature. The step size was 200 Oe and the magnetic field was swifted at a ramp rate of 39.4 Oe/sec. The standard Ni-sample was used to calibrate the magnetometer. No other secondary treatment was done during the measuring of the data.

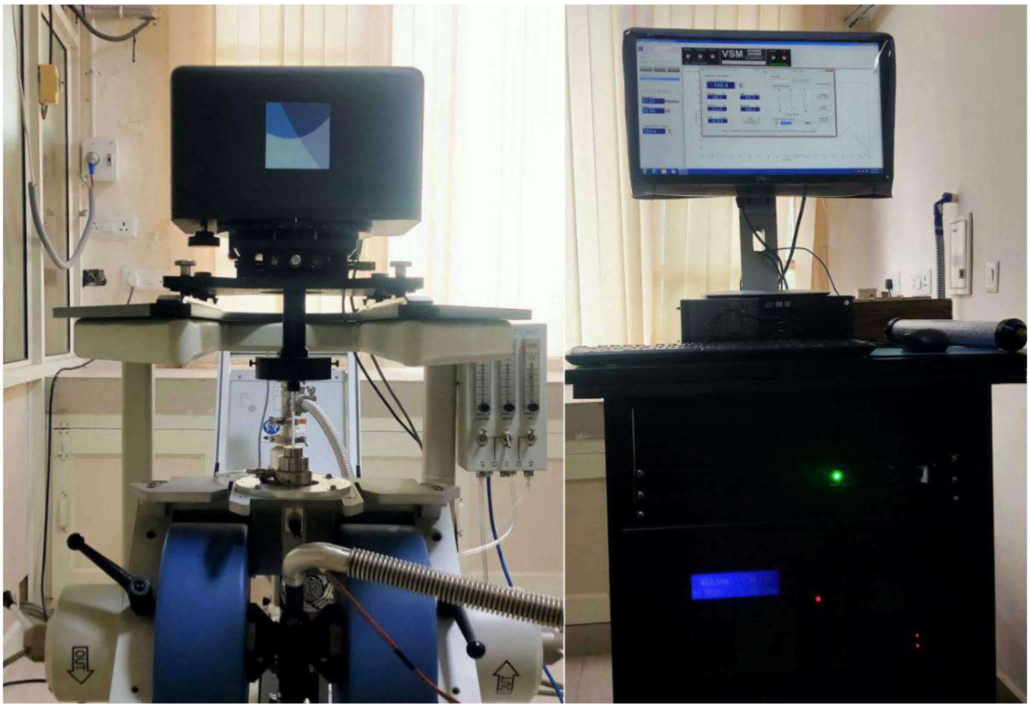

Fig. 3.6 VSM instrument.

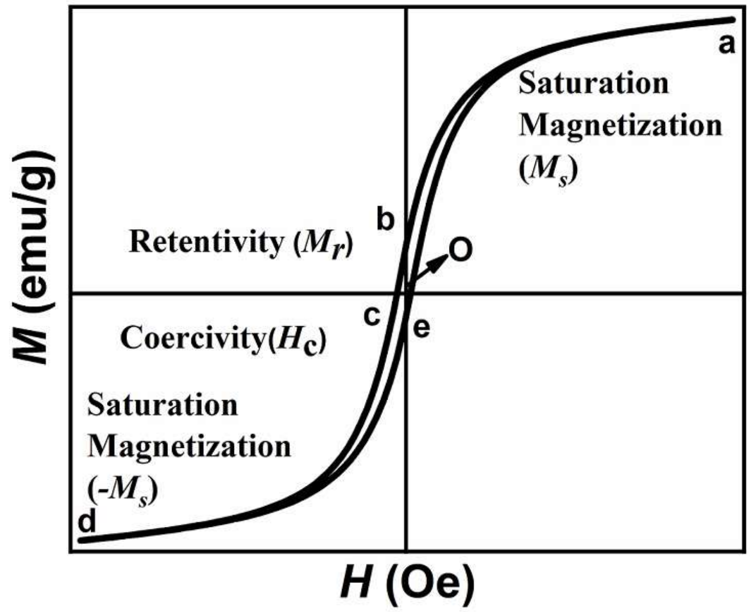

Fig. 3.7 Hysteresis loop of the magnetic material.

3.2.4. Impedance Analyzer (LCR Meter)

Impedance analyzer characterizes the electrical properties of the material and material-electrode interface. It can distinguish the dynamics of the mobile or bound charge carriers in the bulk or interface of the semiconductor or ferrite. In the present work a gold coated pellet (diameter = 10 mm & thickness < 2 mm) is placed between two metallic electrodes. Solatron is used for frequency generator. Fig. 3.8 (a) shows Solarton impedance analyzer. This assembly is connected to SMaRT software which is programmed and calibrated before using. The heating rate was kept at 5°/min for temperature dependent stability around ± 1 ℃ (Fig. 3.8 (b)). A voltage is applied across the surface of the sample with varying frequency and temperature, and the dielectric response of the carriers within the material is collected, called impedance data. This data is obtained in terms of real and imaginary impedance & permittivity. The frequency dependent impedance studies were carried out in the frequency range of 10 Hz – 1 MHz.

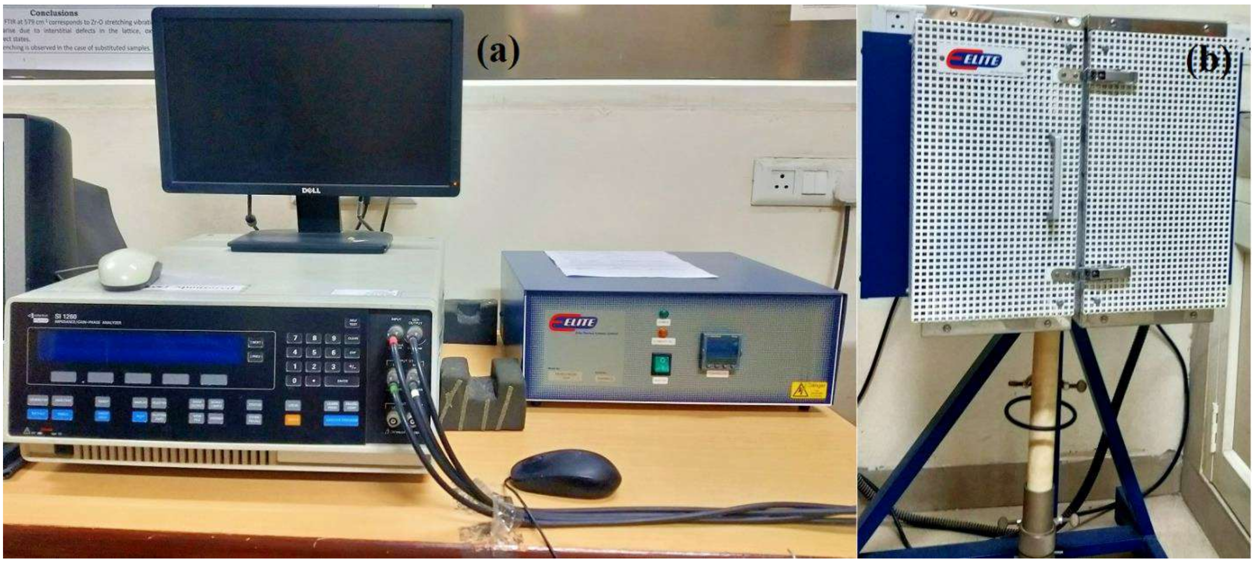

Fig. 3.8 (a) Solarton impedance analyzer and (b) furnace.

The complex impedance plots (Z'' *vs* Z') known as Cole-Cole or Nyquist plot (Fig. 3.9 (a) & (b)) demonstrates insight the conduction mechanism of the material and the interface between material-electrode [178]. This conduction mechanism is associated to grain and grain boundaries. The perfect or depressed semicircle shape gives information about how many types relaxation and conduction are present in the material. The diameter of the semicircular arc represents the electrical resistance (*R*) which is experienced by the carriers. Physically this resistance denotes the electric barrier potential of the material. The curvature of the arc depicts the capacitive power (*C*) of the material. The frequency is increased from right to left in Cole-Cole plot. Generally, the contribution of the grain is obtained at higher frequency while the contribution of the grain boundary and electrode effect is associated to the lower frequency domain. Fig. 3.9 (b) shows response different types of co0tributions [170].

The impedance data is analyzed with the appropriate electrical circuit. This impedance data is simulated by EIS Spectrum Analyser 1.0 software. The best fit experimental data provides all information related to the conduction mechanism. The selection of the electric circuit depends on the microstructural constituents; grain and grain boundary, porosity, defects and secondary phase. The dielectric response is the microscopic phenomenon in which electric charges are released from the stored energy. This response is the time scale related to the orientation of the dipoles.

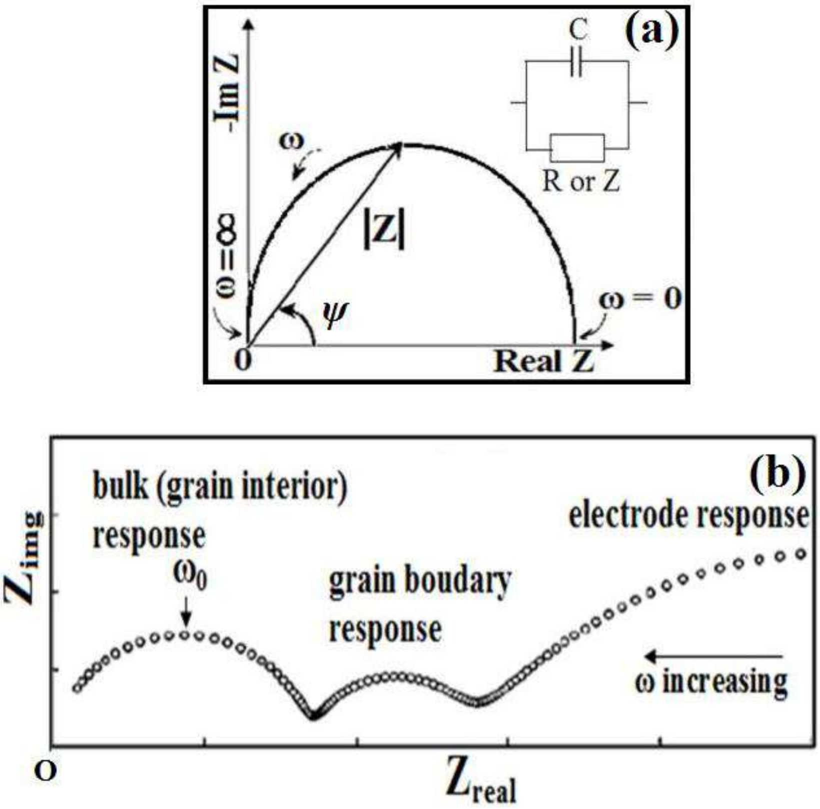

Fig. 3.9 (a) Cole-Cole demonstrates impedance magnitude |Z| makes an angle of ψ and (b) the contribution of grain, grain boundary and electrode effect.

In a definite time, the dipolar molecules revert their orientation in the direction of the field, which is defined as relaxation time, $\tau = 1/2\pi f$, f is the characteristic frequency. With removing the applied field, dipoles return to their equilibrium position (lower energy states). τ is evaluated by the frequency-dependent behavior of Z'' (Z'' *vs* f) and characteristic frequency is associated with the loss peak of Z''. As the field is applied, the dielectric behavior of the sample is decreased because all polarized molecules are aligned in the direction of the field.

Therefore, a straight line pattern parallel to the frequency axis is obtained. Physically these molecules show relaxation in a non-alignment direction and the energy storage is not possible. The small and big polar ions obtain their relaxation in the frequency range of kHz- MHz. The order of τ is millisecond to the microsecond. In the low-frequency domain, ε is higher because all types of molecules are aligned, showing maximum energy stored. While at higher frequencies, very small dipoles are aligned and exhibit lower energy storage (low capacitance). The ε of the sample is also related to the interfacial polarization. The interfacial polarization occurs at the boundary of two different phases or at contact points of the sample and the electrode. In dielectric material, many charge carriers are activated. The time of activation and characteristic frequency of different charges are different. This means that charges show a distribution of the relaxation about the mean position of the periodic time. It is very difficult to distinguish which relaxation starts first and what is the relaxation frequency. The period of relaxation is different for different charges. The amplitude of the peak represents the relaxation position. This peak becomes small or large depending on the relaxation frequency. In normalization of Z'' (Z''/Z''_{max} *vs logf*), all distributions achieve the unique amplitude ~ 1 while the corresponding frequency is different. The unique relaxation frequency is not possible for all charge carriers because the frequency is the characteristic feature at which charges are activated. Therefore, the normalized behavior of Z'' is identified as different relaxation on their relative frequencies. The scaling behavior of Z'' (Z''/ Z''_{max} *vs log* (ω/ω_{max}) is used to verify these relaxations that are thermally activated, which means relaxations which are temperature dependents or independent. In this process, the axis of scaling (Y-axis) has unit amplitude while the frequency axis (X-axis) represents relaxation around the origin. The unit amplitude is associated with the grain conduction while side branches of all curves are related to the contribution of the grain boundaries. Generally, the scaling factor shows the symmetric behavior around the frequency axis, suggesting that the relaxation occurs in a system where grain is covered by the grain boundary. Therefore, relaxation is also affected by the grain boundary. If symmetry is broken, it indicates that the contribution of one side grain boundary is absent. The overlapping of all curves into a master curve, suggests that the distribution of the relaxation time is temperature-independent [171, 172]. Physically localized conduction is governed by parental charge carriers. New born charges are not available for dielectric relaxation.

In 1986, ***Svante Arrhenius*** first studied the collision problem of particles and discovered a statistical formula, called the Arrhenius law. This formula gives an idea of how much energy is sufficient for collision (reaction). The relaxation time in terms of activation energy can be expressed as $\tau = \tau_0 \, exp \, (E_g/kT),$ where τ_0 is the pre-exponential factor, E_g is the activation energy, k is the Boltzmann constant and T is the absolute temperature. Comparing the logarithmic form of $ln\tau = ln\tau_0 + E_g/kT$ and standard straight line equation $y = mx + c$, where $m = E_g/k$. The activation energy is calculated by plotting $ln\tau$ *vs* $1/T$ and $E_g = mk = slope*k$, the activation energy represents the amount of energy spent to break internal atomic bonds. These bonds originate newly electron-hole pairs to govern electric conduction. Sometimes two E_g are observed in the Arrhenius plot. At low temperatures, E_g is associated with oxygen vacancy, originating at higher sintering temperatures while at higher temperatures E_g is related to the newly born electron-hole pair. The value of E_g for oxygen is lower compared to the electron-hole formation. A higher activation energy is required to remove a charge from the higher electric barrier potential.

Chapter 4

Results and Discussion (Co_2Z ferrite)

Overview

In this chapter, the results of synthesized Co_2Z hexaferrite powder at different processing conditions is given. The effect of the different calcination and sintering temperatures on structural, magnetic, and dielectric properties of Z-type ferrite is discussed.

4.1. Pure Z-type hexaferrite

In this section, the results pertaining to pure Z-type phase is presented. The samples were prepared using solid state method. The influence of processing parameters (calcination and sintering temperature) on structural, magnetic and dielectric properties have been studied.

4.1.1. Phase identification

To synthesize single phase $Ba_3Co_2Fe_{24}O_{41}$ (Co_2Z) hexaferrite, the as-mixed powders were calcined in two different steps. In the first step, powder was calcined at 1150 ˚C for 6 hours. The XRD analysis confirmed the coexistence of both M and Y-type phases as shown in Fig. 4.1 (a). Their relative intensity peaks are matched with the hexagonal space group $P6_3/mmc$ for M-type (JCPDS: 00-007-0276) and Y-type (JCPDS: 00-019-0100) hexaferrites. The powder obtained after first step of calcination is recalcined in the temperatures range of 1150 ˚C – 1300 ˚C for 6 hours. The XRD pattern of the recalcined powders are given in Fig. 4.1 (b). The single phase Co_2Z was obtained upto 1250 ˚C. Their peak positions are matched with the hexagonal space groups of Z-type (JCPDS: 00-019-0097). At 1300 ˚C, the peaks of W-type (JCPDS: 00-019-0098) phase has also been observed along with Co_2Z ferrite. As it is clear from the XRD patterns that powders recalcined at 1150 ˚C show pure Co_2Z phase, therefore two step calcination temperature 1150 ˚C is selected for further processing.

To obtain the optimal sintering temperature, the calcined powder are sintered in the form of cylindrical pellets at different temperatures varying from 1175 ˚C – 1300 ˚C and their sintered density were calculated. These sintered pellets were further crushed to powder for their XRD analysis to reconfirm the phase stability. Fig. 4.1 (c) illustrates the XRD profile of sintered samples at various temperatures. The XRD clearly shows that Co_2Z phase is stable at 1250 ˚C sintering temperature. However, above 1250 ˚C, formation of W-type phase is observed. The sintered density of the pellets were calculated and found maximum (4.9 g/cm^3) at 1250 ˚C, which is 91.0 % of theoretical density (5.3 g/cm^3). Further XRD pattern of 1250 ˚C sintered samples were refined by Fullprof method and shown in Fig. 4.2. The R_p, R_{wp}, and R_{exp} values were below 10 with χ^2 value nearly 3, which confirm the goodness of refinement. The refinement confirms the single Z-type phase without any secondary phase. The refined parameters (*a* & *c*) were 5.88 Å and 52.29 Å, respectively. The calculated crystallite size was 44 nm and nearly constant for each sintered specimen.

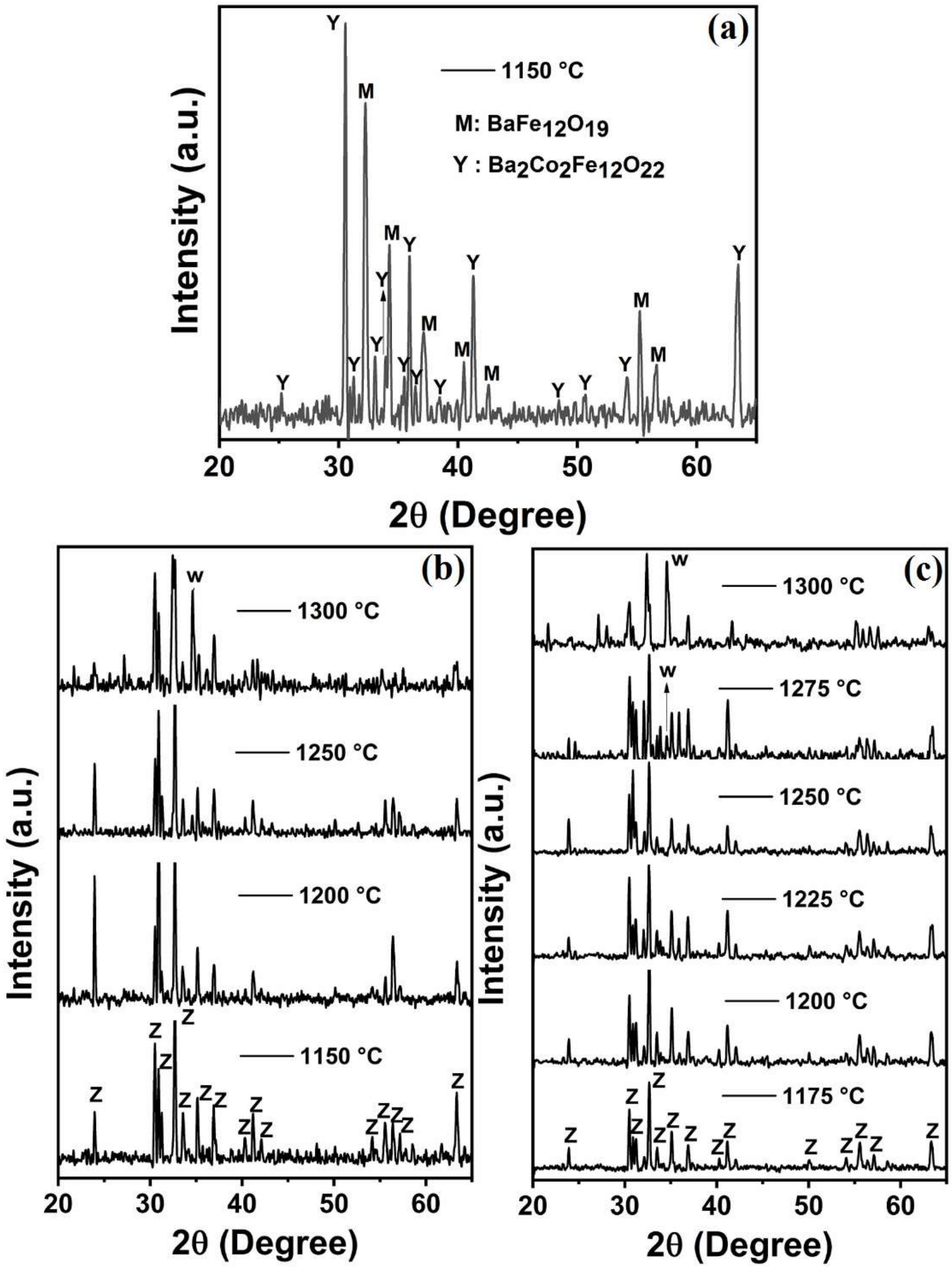

Fig. 4.1 X-ray diffraction pattern (a) calcined powder at 1150 ˚C (b) re-calcined powder at different temperatures (c) re-calcined at 1150 ˚C and sintered at different temperatures.

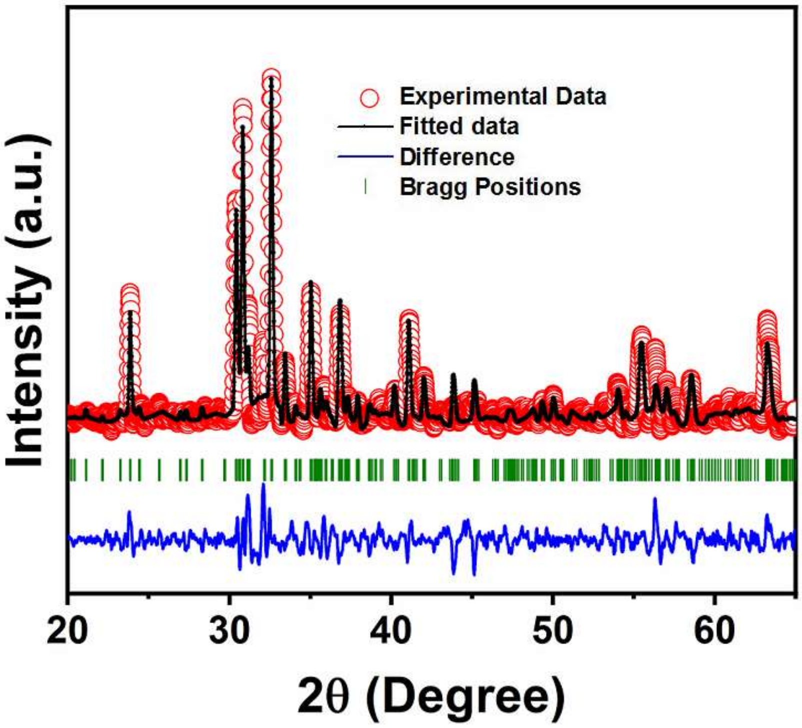

Fig. 4.2 Refined XRD pattern of Co_2Z ferrite sintered at 1250 ˚C for 1 hour.

4.1.2. Magnetic properties

Fig. 4.3 represents *RT* hysteresis loops of re-calcined samples at different temperatures. The M_s is constant up to 1250 ˚C and found higher for 1300 ˚C due to formation of W-type phase. Fig. 4.4 represents *RT* hysteresis loops of samples sintered at different temperatures. The hysteresis loop shows the soft magnetic behavior of the samples. The measured H_c, M_s and M_r are given in Table 4.1. No change in the magnetic properties were observed up to 1250 ˚C irrespective of sintering temperatures. However, similar to the calcined sample, an abrupt increase in M_s is also observed for sample sintered at 1300 ˚C due to W-type phase. The value of H_c increased at 1300 ˚C which may be due to the contribution of W-type & Z-type phases. H_c depends on the grain morphology and decreased with increased grain size.

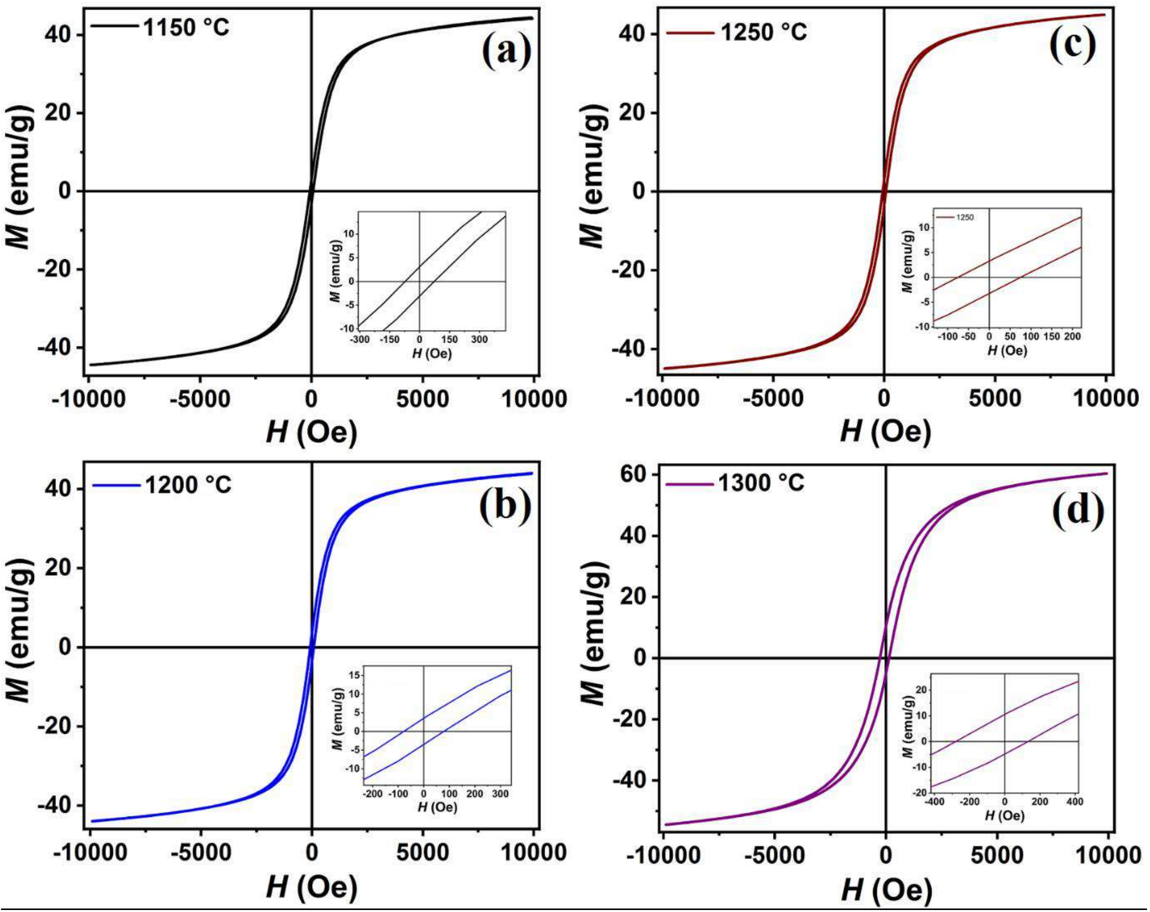

Fig. 4.3 Magnetic hysteresis loops of re-calcined Co_2Z ferrites at different temperatures (a) 1150 ℃, (b) 1200 ℃, (c) 1250 ℃ & (d) 1300 ℃. Inset shows enlarged view of H_c & M_r.

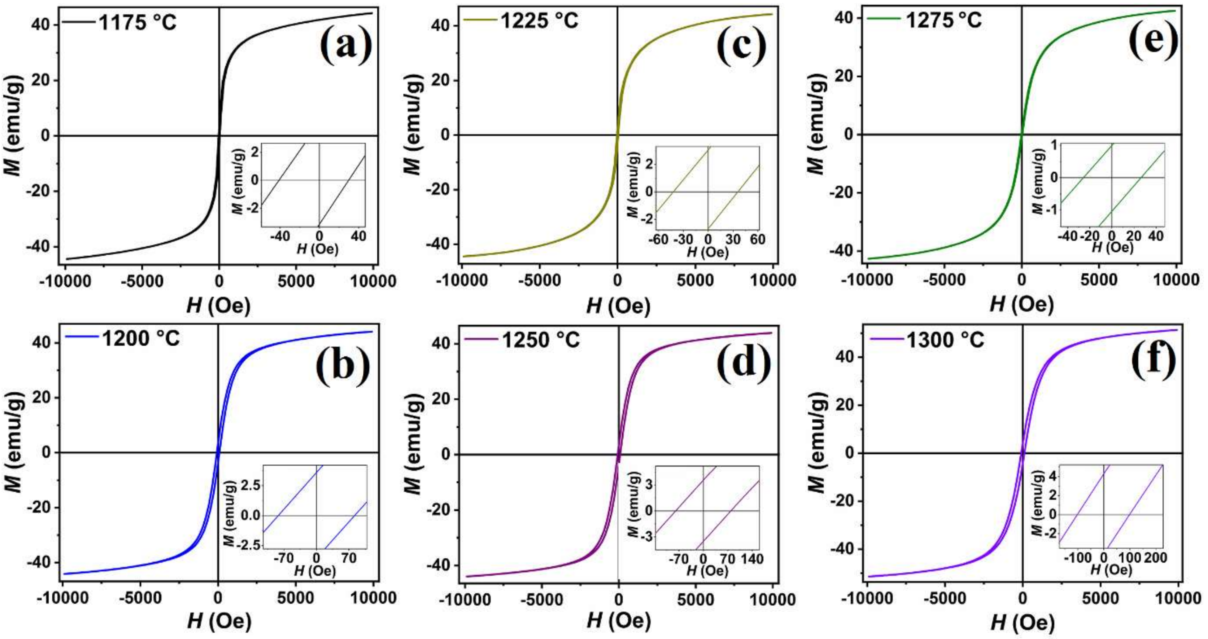

Fig. 4.4 Magnetic hysteresis loops of sintered Co_2Z ferrites at different temperatures (a) 1175 ℃, (b) 1200 ℃, (c) 1225 ℃, (d) 1250 ℃, (e) 1275 ℃ & (f) 1300 ℃. Inset shows enlarged view of H_c & M_r.

Table 4.1 Magnetic properties of samples calcined and sintered at different temperature.

Sample	**Temperature (°C)**	***M_s* (emu/g)**	***H_c* (Oe)**	***M_r* (emu/g)**
Calcined powder	1150	44.2	72.7	3.1
	1200	44.0	78.2	3.5
	1250	44.9	75.3	3.2
	1300	60.4	280.7	10.5
Sintered pellets	1175	44.3	41.3	4.2
	1200	44.0	81.9	3.6
	1225	44.3	42.2	3.0
	1250	45.3	79.2	0.9
	1275	43.6	25.9	1.0
	1300	51.3	102	4.2

4.1.3. Microstructural analysis

Fig. 4.5 shows the SEM micrograph of fractured surface of Co_2Z sample sintered at 1250 ˚C. A well compact hexagonal platelets with an average grain size of 2.45 µm were observed. The sintered density of sample is 4.9 g/cm^3 (~ 91.0 % of theoretical density). The orientation of the grains is related to the magneto-crystalline anisotropy.

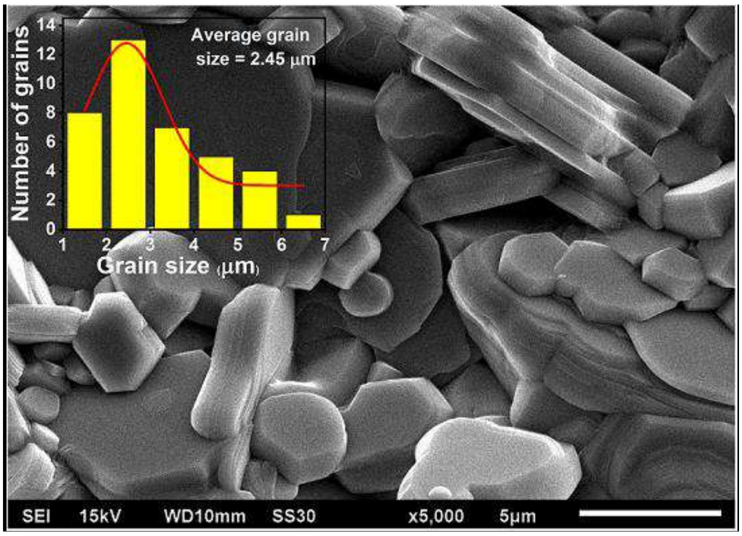

Fig. 4.5 SEM micrograph of fractured Co_2Z ferrite sintered at 1250 ˚C.

4.1.4. Complex permittivity analysis

The ε of the material is the ability to store the electrical energy at molecular levels. In the presence of applied electric field, the permittivity phenomena become complex in nature and mathematically represented by the formula $\varepsilon = \varepsilon' + j\varepsilon''$, where ε' & ε'' interprets the real and imaginary part of the permittivity, respectively. Physically ε' represents the degree of dipole alignment while ε'' denotes the strength of the ionic conduction. Fig. 4.6 (a & b) demonstrates the variation of ε' & ε'' with frequency and temperature. The magnitude of ε' is high at low frequency and increases with an increase in temperature which suggests that polarization increases from the grain boundary.

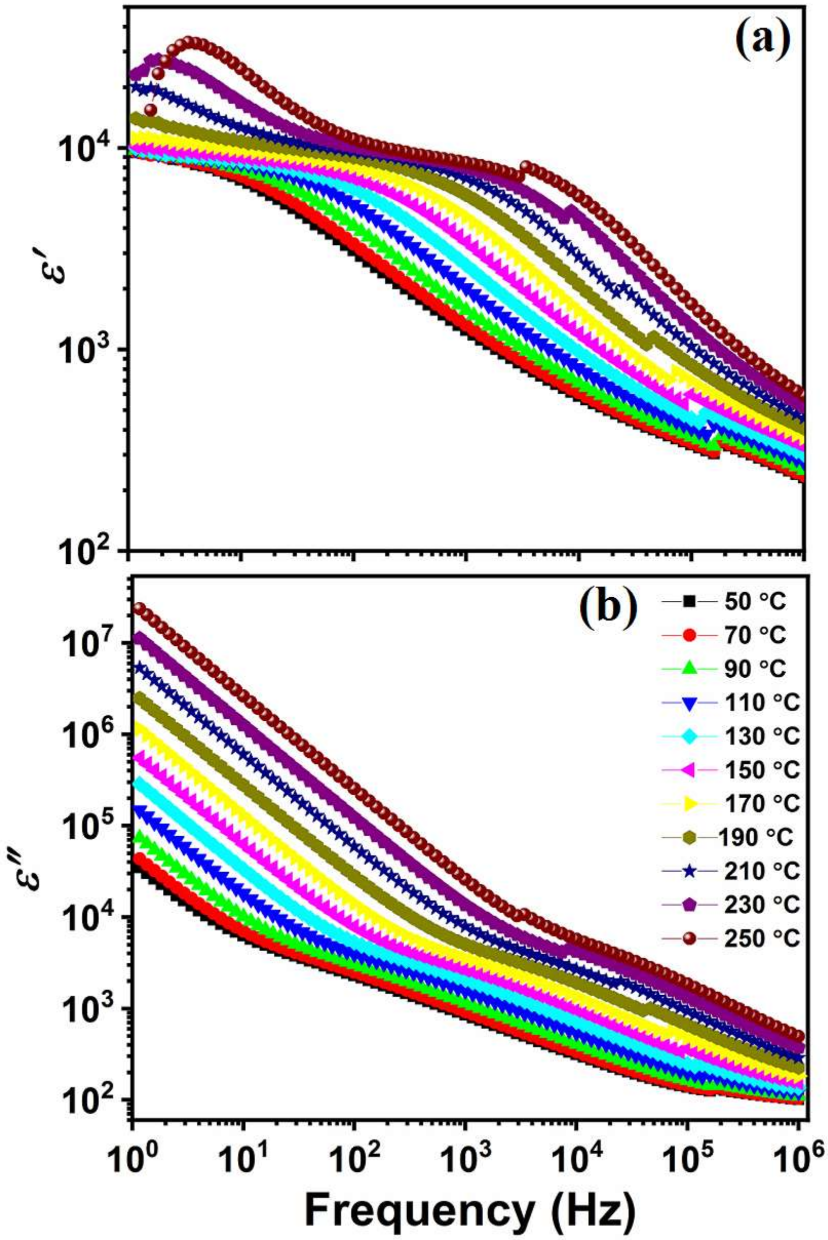

Fig. 4.6 Variation of (a) ε' and (b) ε'' of sintered Co_2Z ferrite as a function of frequency at different temperatures.

This polarization is associated to the localized displacement of the hopping electrons of Fe^{3+} - Fe^{2+} in the direction of the applied field. ε'' is found to increase with temperature which suggests that ionic conduction is increasing. At a sufficiently higher frequency, the orientation of the dipoles is not able to follow the frequency, and the mobility of the charge carriers decreases. Therefore, ε' & ε'' decreases with increased frequency and temperature. At low frequencies, a strong interaction is available between the dipoles and becomes weak at higher frequencies leading to lower ε. In the low-frequency domain, the polarization arises due to the interfaces (boundaries) while at higher frequency regimes, the polarization governs by the ionic and electronic contribution. The interfacial polarization is associated with grain boundaries. These boundaries introduced a resistive path for the charge carriers and the mobility of the carriers is decreased, resulting in the decrease in ε. The dielectric properties of the materials are also dependent on the grain size. As the grain size is decreased the fraction length of the grain boundary increased which affects the motion of the charge.

In Co_2Z ferrites two types of charge carriers (N-type (electron) and P-type (hole)) are available. As the frequency is increased the electrons are aligned in the opposite direction of the field while holes are oriented in the field direction. The electrons are originated from Fe^{3+} & Fe^{2+} hopping while holes are obtained by Co^{3+} & Co^{2+} hopping. The mobility of both carriers are different. Due to this reason, two patterns are observed in Fig. 4.6 (a & b).

4.1.5. Complex impedance analysis

Impedance spectroscopy investigates the electrical response of the grain and grain boundaries. In general, real impedance (Z') measures the resistive strength of the material. The amplitude of Z' decreases with frequency as well with temperature as shown in Fig. 4.7 (a). This indicates negative temperature coefficient of semiconductor, i.e., conductivity increases due to the contribution of thermally activated ions with temperature. The constant value of Z' till certain limit of frequency determines the frequency-independent behavior of charge carriers that measures the *dc* conduction of material. The region of stable frequency dispersion increases with the rise in temperature due to increased concentration of thermally activated ions. Furthermore, the curves are merged at higher frequency (~ 10^5 Hz) irrespective of varying temperature, which indicate the reduction of space charges contribution at high frequency.

Fig. 4.7 (b) demonstrates the variation of the imaginary impedance (Z'') as a function of frequency at different temperatures. The value of Z'' increases with frequency till it attains its maximum value due to relaxation mechanism and then decreases afterwards. The relaxation frequency (f_m) and peak broadening corresponds to maximum value of Z'' that increases with temperature which determines the thermal relaxation behavior of charge carriers. The magnitude of Z'' decreases with temperature that indicates conduction of charge carriers. At lower temperature, immobile charges are activated, whereas at higher temperatures, defects are triggered [173, 174].

Fig. 4.7 (c) depicts the normalized spectra of the Z'' with frequency at different temperatures. The relaxation frequency (f_m) of Z'' shifts towards higher frequency with temperature, which suggests relaxation is temperature dependent. This is due to the reduction of electron hopping, charge density and the mobility of the carriers with temperature [175].

Fig. 4.7 (d) represents the relaxation time (τ) of grain boundary as a function of $1/T$ evaluated by using formula, $\tau = 1/2\pi f_m$. The relaxation time (τ) decreases with temperature, which is related to the dissipated thermal energy of induced dipoles which follows the *ac* electric field [176]. The activation energy (E_g) is calculated by the fitting Arrhenius relation $\tau = \tau_0 \exp(E_g/kT)$, where τ_0 is pre-exponential factor, k is Boltzmann constant, and T is absolute temperature. The Arrhenius plot has two distinct slopes in the different temperature regimes named E_1 (high temperature) and E_2 (low temperature). Two different E_g suggests that the dielectric relaxation is governed by different type of conduction mechanisms. This conduction is caused by space charges due to oxygen vacancies, and the electron/hole hopping between Fe^{2+} to Fe^{3+} and Co^{3+} to Co^{2+} ions [177-179]. The full width at half maxima (*FWHM*) of normalized curve of impedance spectra is more than 1.144 decades that infers a deviation from ideal Debye type relaxation. This deviation is caused by charge carrier diffusion, and non-uniformity of the microstructure that leads to spatial dispersion of conductivities and electrical response time [180-182]. The activation energy is higher at high temperature because oxygen vacancy experiences a low potential barrier for electric conduction. This higher activation energy provides information to generate electron/hole charge carriers for conduction. The scaling behavior (Z''/Z''_{max}) *vs log* (ω/ω_{max}) is plotted and shown in inset of Fig. 4.7 (d). If all curves overlap into a single master curve, the distribution of relaxation is temperature-independent. The scaling behavior shows that all other peaks do not overlap with the master curve, which indicates a temperature-dependent relaxation process [183]. The poly-dispersive behavior of the relaxation curve identifies the dynamic process of charge carriers activated at different time scales that suggest more than one activation energy is available in the material. The results support the explanation of activation energy which is shown in Fig. 4.7 (d). This different type of relaxation arises due to the different interactions of the dipoles.

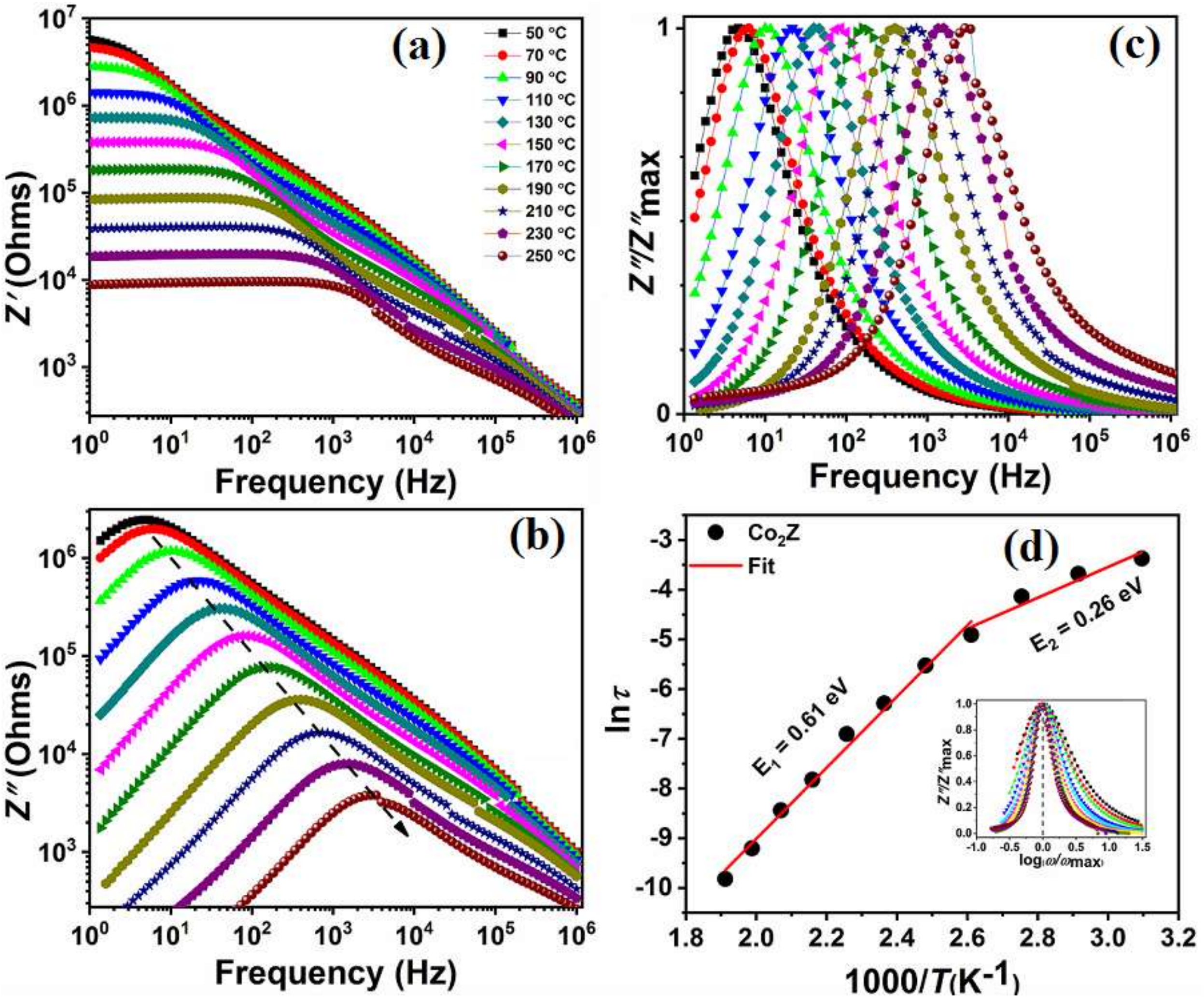

Fig. 4.7 (a & b) Variation of (a) Z' and (b) Z'' as function frequency at different temperatures, (c) normalized imaginary impedance spectra (Z''/Z''_{max} *vs.* frequency) and (d) temperature dependent relaxation time (τ). Inset shows scaling behavior of impedance spectra.

To study the effect of microstructure on electric properties, Cole-Cole (Nyquist) plots of complex impedance (Z'' *vs* Z') is fitted with the suitable equivalent electric circuit based on a brick layer model [184-187] as shown in Fig. 4.8 (a). The equivalent circuit consists of resistance (R) and capacitance (C) for grain, and grain boundaries are represented by (R_g, C_g) and (R_{gb}, C_{gb}), respectively. The subscript '*g*' stands for grain and '*gb*' for grain boundaries. *CPE* demonstrates constant phase elements that denote the deviation from an ideal Debye type relaxation. The presence of a single semi-circle suggests that grain boundary contribution dominates the conduction process [188-190]. With increased temperature, the diameter of the semi-circle reduces which suggests a decrease in resistance of grain and grain boundaries [191]. Fig. 4.8 (b) illustrates the fitted electrical resistance of grain and grain boundaries obtained by

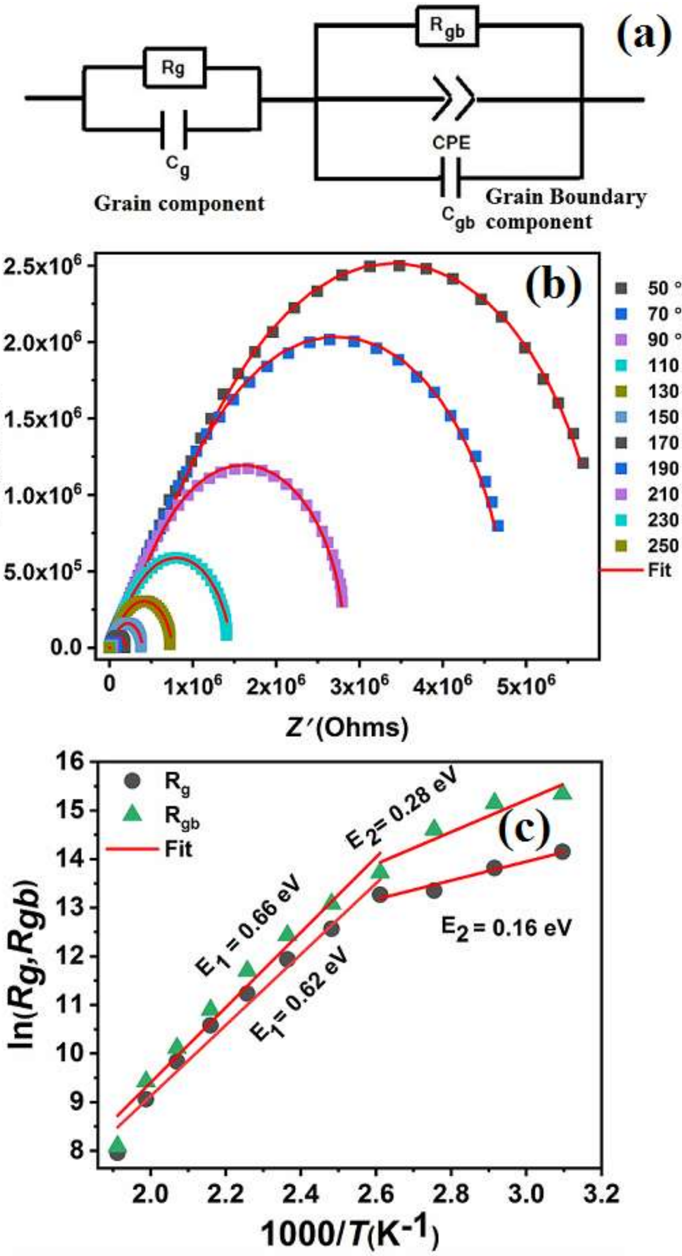

Fig. 4.8 (a) Equivalent electric circuit based on brick layer model (b) Cole-Cole plots of electric impedance spectra (Z'' *vs* Z') and (c) Arrhenius plots of grain and grain boundaries resistances (R_g & R_{gb}) obtained from impedance data simulation.

the equivalent circuit (see Fig. 4.8 (a)) at different temperatures. The resistances follow the Arrhenius formula, $R = R_0 \exp(E_g/kT)$, where R_0 is pre-exponential resistance. The value of R_g & R_{gb} decreases with temperature that suggest the resistive nature of grain and grain boundaries decreases which is discussed in Fig. 4.8 (b). The activation energy of grain and grain boundary above 100 ˚C confirms that the potential barrier difference between them reduces which is already reported [192]. The similar value of activation energies for R_g & R_{gb} indicates that the charge carriers perform localized electric conduction between grain and grain boundaries.

4.1.6. Complex electric modulus analysis

The electric modulus spectroscopy is used to understand the effect of grains distribution and hopping mechanism of charge carriers. Fig. 4.9 (a & b) depicts the real (M') and imaginary part of electric modulus (M'') over wide frequency range at different temperatures. The value of M' and M'' is low at low frequency, which increases with frequency. The low value of relaxation frequency indicates the short-range conduction of space charge carriers. The relaxation peak switches along higher frequency side with increased temperature which suggest that relaxation of the electric charge carriers are influenced by the thermal conditions (temperature) and provides thermally activated ions for long range conduction [193].

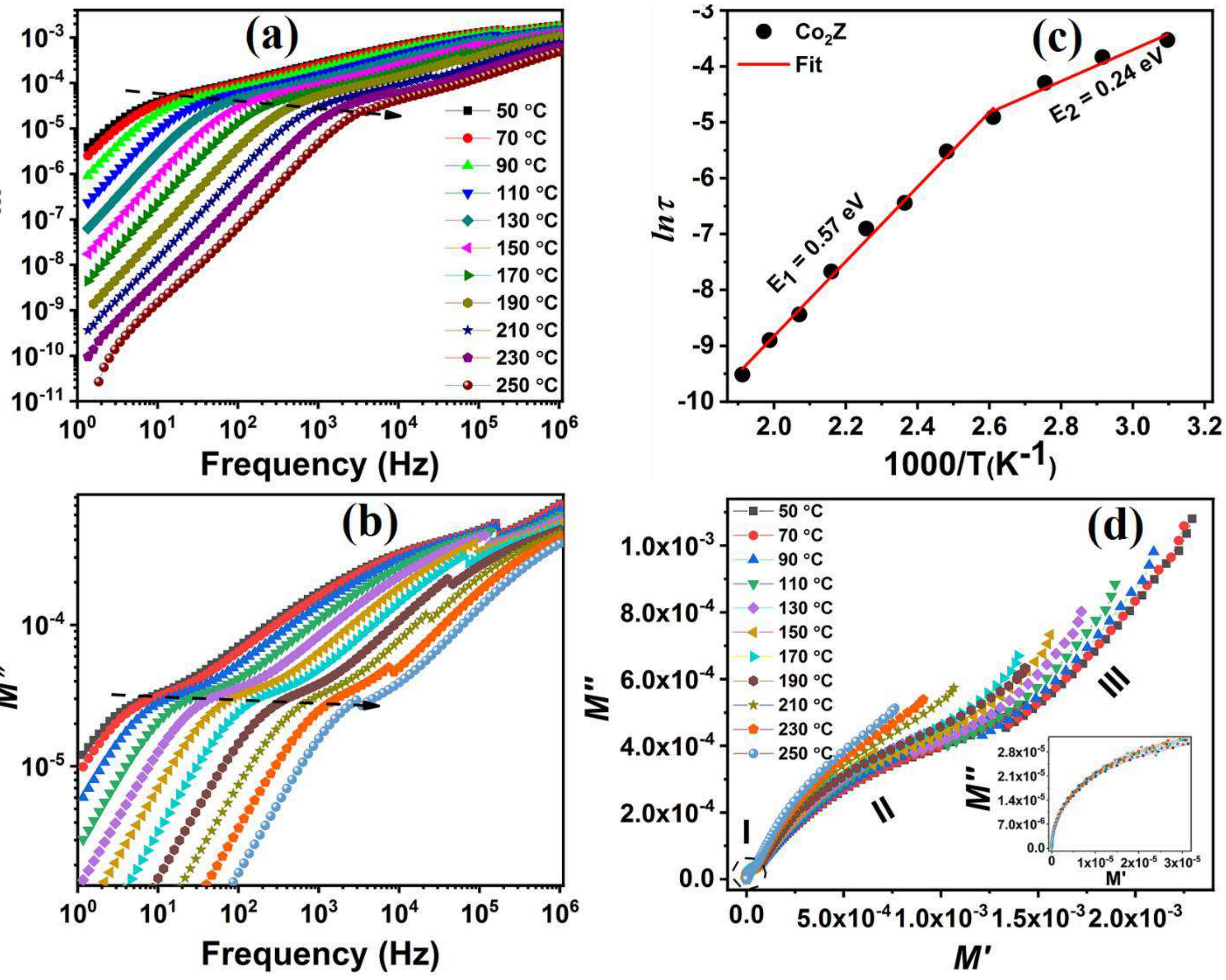

Fig. 4.9 Variation of (a) M' and (b) M'', (c) temperature dependent τ and (d) Cole-Cole plots of electrical modulus spectra (M'' vs M').

To investigate the relaxation mechanism of charge carriers, relaxation time (τ) is obtained from M'' *vs f* plot at difference temperatures. Fig. 4.9 (c) shows the temperature dependent τ behavior. The decrease of τ with temperature indicates that the negative temperature coefficient of sample. The maximum value of τ (τ_{max}) represent that the charge carriers are mobile over the short-distances, whereas minimum τ (τ_{min}) signify long-range conduction. The obtained activation energies are 0.24 eV & 0.57 eV for lower and upper temperature range, respectively. The comparable value of activation energy of impedance (Z'') and modulus (M'') spectra implies that the relaxation and conduction mechanism may be due to the similar kind of the charge carriers.

To analyze the contribution of microstructure and electrode in individual relaxation process, Cole-Cole plot of electric modulus spectrum (M'' *vs* M') has been plotted as shown in Fig. 4.9 (d). Double semicircular arcs are coupled to constant straight-line pattern, which determines capacitive contribution of grain, grain boundary and interfacial polarization [194, 195]. Small and large arcs is associated to the different mobility of the charge carriers in the electric conductions. It implies that the contribution of grain is more significant only at high frequency region whereas impact of grain boundary is also considered in low-frequency region. The center of the semi-circular arc lies below M'-axis, indicates a non-Debye type relaxation process [196]. The diameter of the semi-circular arc shift towards higher value of M' with temperature that suggest an increase in capacitance. This behavior is opposite to impedance spectra as shown in Fig. 4.8 (b) [197]. Further analysis shows that at low-frequency region, the small semi-circular arc separates from the origin implying that dielectric relaxation process or electrode polarization is present [198].

It can be seen that process parameters pays an important role in the formation of pure phase and sintering characteristics as well.

Sub-conclusion

Pure Co_2Z hexaferrite was synthesized by the solid-state method at different temperatures. The XRD analysis confirmed that after the first calcination (1150 °C) mixed phases of M & Y-type hexaferrite were formed. Further, the single-phase Co_2Z was found to be stable between 1150 °C – 1250 °C temperatures after the second calcination. The highest sintering density (4.9 g/cm^3) with well-defined hexagonal grains was obtained at 1250 °C. The dielectric, impedance and electric modulus studies showed that conduction and relaxation processes were temperature dependent. Complex electric modulus distinguished the capacitive contribution of the grain and grain boundary which were not observed in Complex electric impedance spectra. A comparative study of samples calcined at 1150 °C and sintered at various temperatures is given in Table 4.2.

Table 4.2 Magnetic properties of pure Co_2Z ferrite.

Samples	**Temperature (°C)**	**sintering density (g/cm^3)**	M_s **(emu/g)**	H_c **(Oe)**
Sintered pellets	1175	4.6	44.3	41.3
	1200	4.8	44.0	81.9
	1225	4.8	44.3	42.2
	1250	4.9	45.3	79.2
	1275	4.7	43.6	25.9
	1300	4.6	51.3	102

From the above comparative study, Co_2Z hexaferrite with maximum M_s and high sintering density was obtained at 1250 °C sintering temperature. Therefore, for substitution and additive studies, the sintering temperature of 1250 °C is chosen.

Chapter 5

Results and Discussion (Substituted)

Overview

In this chapter, the experimental results of synthesized Co_2Z hexaferrite with substitution for Ba^{2+} by La^{3+} & Ca^{2+} and Fe^{3+} by Al^{3+} are investigated. The effect of substitution on structural, magnetic, and dielectric properties of Z-type ferrite is discussed in detail.

5.1. Effect of La^{3+} and Ca^{2+} substitution

5.1.1. Phase identification

Fig. 5.1 (a & b) shows the representative XRD patterns of sintered $Ba_{3-x}La_xCo_2Fe_{24}O_{41}$ (La-Z) and $Ba_{3-x}Ca_xCo_2Fe_{24}O_{41}$ (Ca-Z) samples. A single Z-type phase is obtained up to x = 0.2 for La^{3+} substitution, above this W-type phase (JCPDS: 00-019-0098) emerges out. While in Ca-Z, W-type phase is present for all compositions. The lattice parameter '*c*' of La-Z slightly increases from 52.01 Å to 52.20 Å upto x = 0.20 with the substitution despite its smaller ionic radii La^{3+} (1.17 Å) compared to Ba^{2+} (1.49 Å). This is associated with the reduction of Fe^{3+} (0.64 Å) to Fe^{2+} (0.76 Å) [123, 199, 200]. Wheras, for Ca-Z, the decrease in lattice parametes is related to the substitution of smaller Ca^{2+} ion without Fe^{3+} reduction as Ca and Ba ions posses same valency. These results are in agreement with the reported values [123, 125, 126, 200-202].

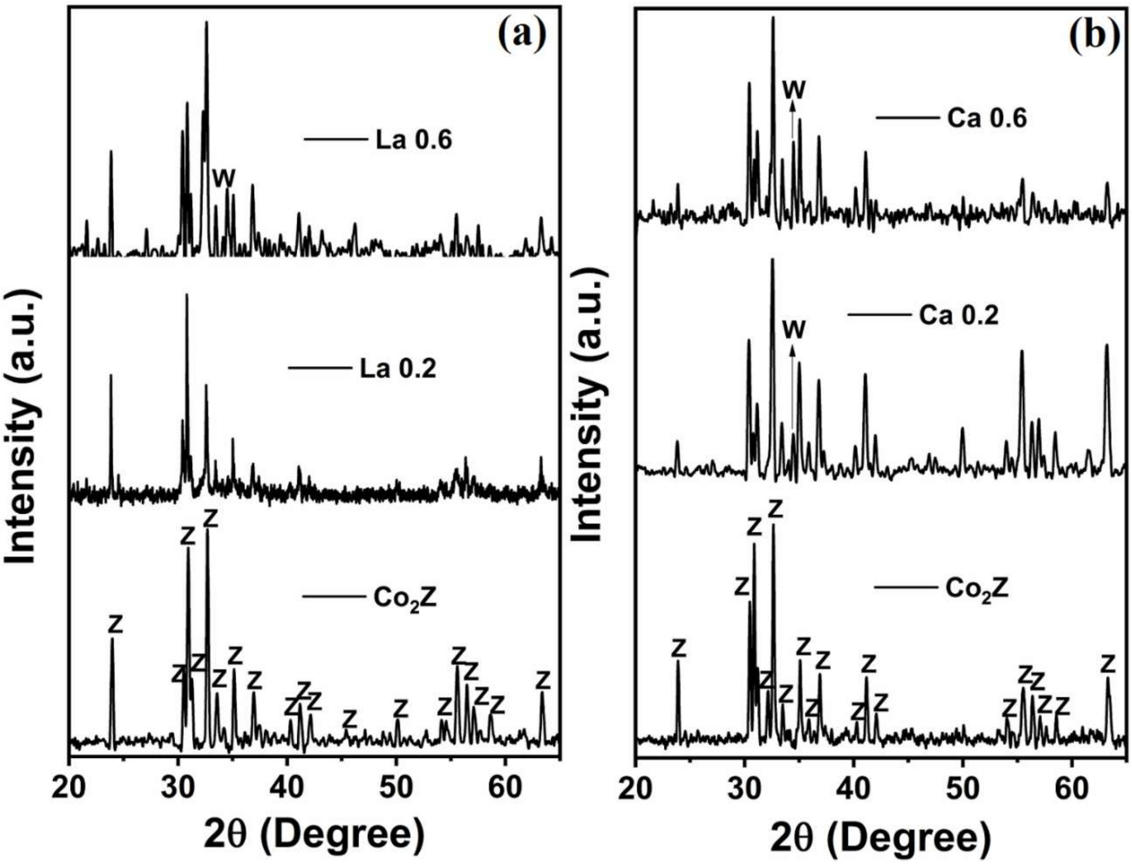

Fig. 5.1 X-ray diffraction patterns of sintered (a) La-Z & (b) Ca-Z.

5.1.2. Microstructural analysis

Fig. 5.2 (a-d) & Fig. 5.3 (a-d) shows the fractured surface SEM micrographs of La & Ca-substituted Co_2Z ferrites. The strutural features exhibits well sintered homogeneous hexagonal platelet structure. The size of Ca-substituted grains are larger than La-substituted. Amoung La-

Z samples x = 0.2 composition showed the larger grain size. Further increasing the La content platelet size decreases. The smaller platelete may be due to the presence of secondary W-type phase, which provide a pinning effect to the grain [201]. For Ca-substituted, it showed exagerrated grain growth desipte the presence of W-type phase. The sintered density of all samples is approximately 4.9 g/cm^3.

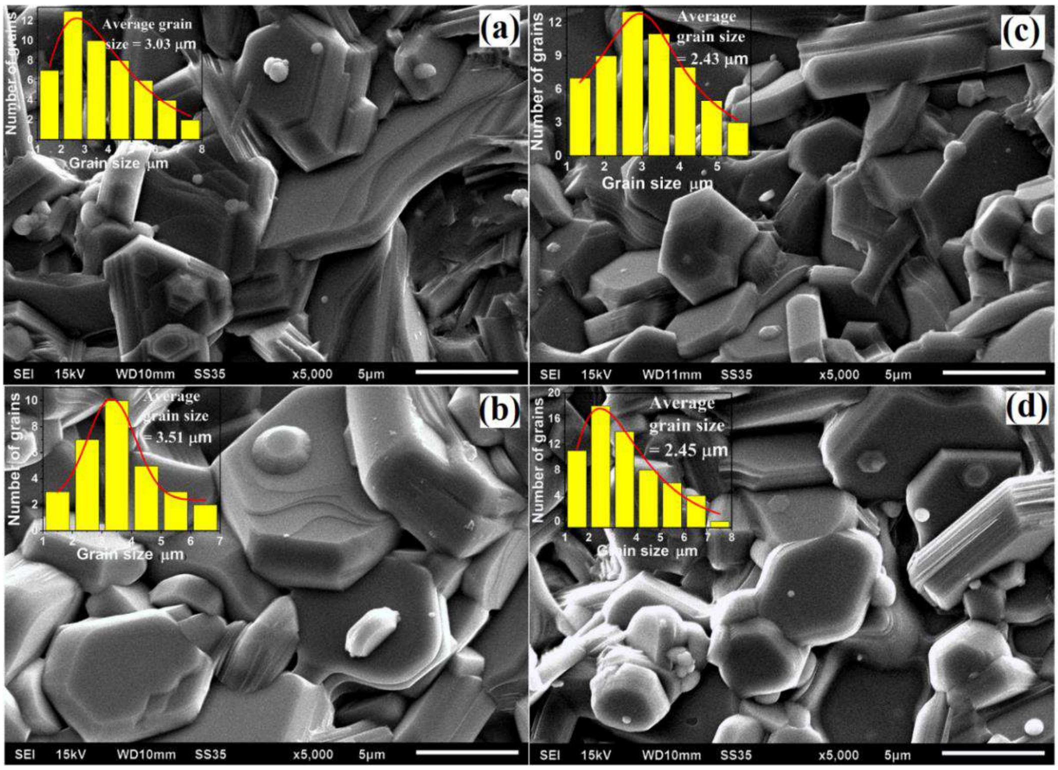

Fig. 5.2 SEM micrographs of fractured surface of La-substituted Co_2Z (a) x = 0.1, (b) x = 0.2, (c) x = 0.4 & (d) x = 0.6.

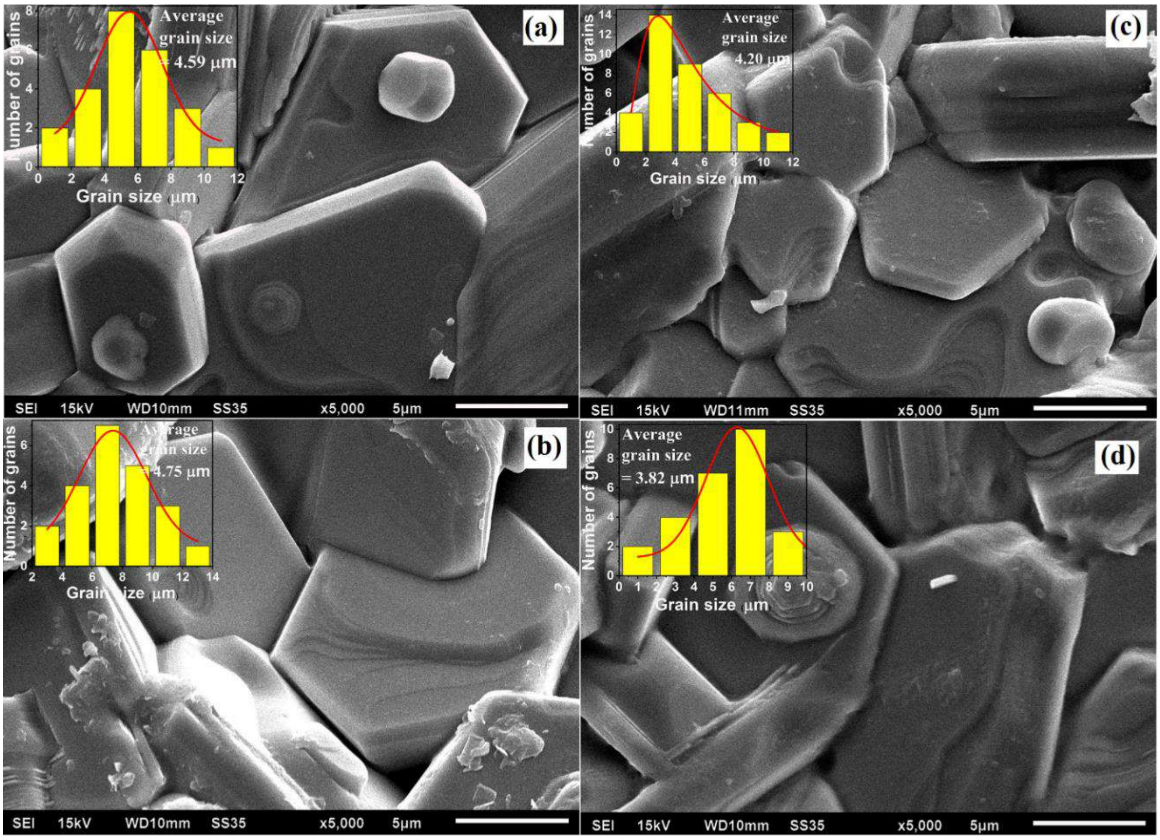

Fig. 5.3 SEM micrographs of fractured surface of Ca-substituted Co_2Z (a) x = 0.1, (b) x = 0.2, (c) x = 0.4 & (d) x = 0.6.

5.1.3. Magnetic properties

Fig. 5.4 (a & b) demonstrates the *M-H* loop for La & Ca-substituted Co_2Z hexaferrites. The M_s, H_c, and M_r are given in Table 5.1. The value of M_s increased for both La & Ca-substituted compared to pure Co_2Z sample. M_s mainly depends on the phase present [203, 204]. La^{3+} & Ca^{2+} substitution causes formation of W-type phase, which increases the M_s. Similar results were also reported in La & Ca-substituted Z-type ferrites [202, 203]. The value of H_c lies between 31.3 Oe – 78.0 Oe for La-substituted samples, while Ca-substituted samples shows similar value. The slight variation in H_c may be related to changes in grain size and morphology as is evident from the microstructures.

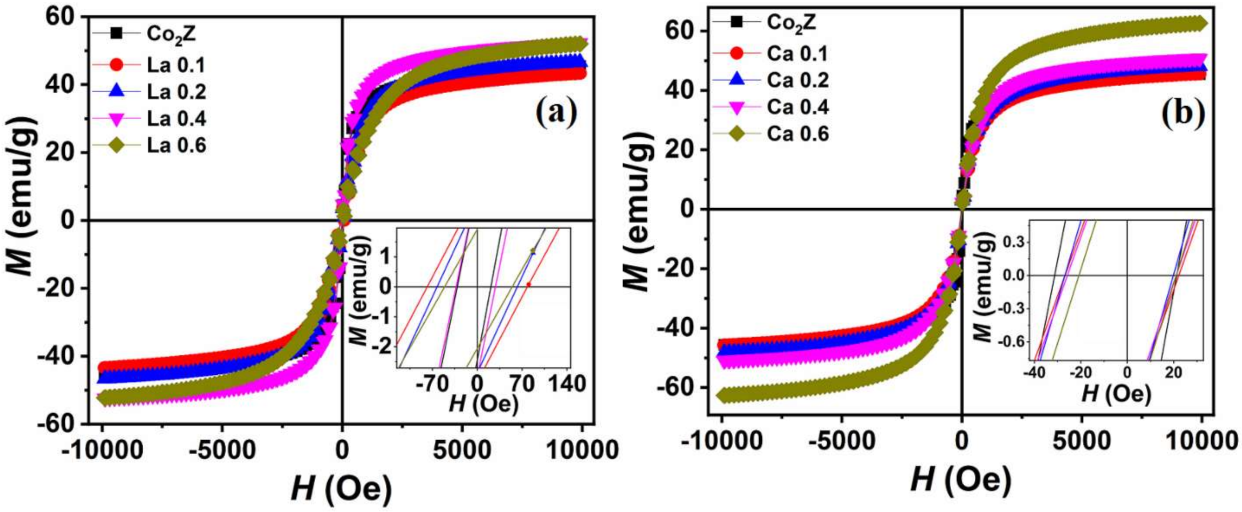

Fig. 5.4 Magnetic hyteresis loop of Co_2Z ferrite (a) La-Z and (b) Ca-Z. Inset shows the enlarged view of H_c.

Table 5.1 Magnetic properties of La & Ca-substituted Co_2Z ferrites.

Contents	**La substituted**				**Ca substituted**	
	M_s (emu/g)	H_c (Oe)	M_r (emu/g)	M_s (emu/g)	H_c (Oe)	M_r (emu/g)
0.0	45.3	79.2	0.9			
0.1	43.3	78.0	3.1	45.5	27.1	1.5
0.2	46.6	62.8	2.8	48.2	26.9	1.9
0.4	52.3	32.8	3.3	50.7	25.7	1.5
0.6	52.0	50.9	1.9	62.6	20.7	1.3

5.1.4. Complex permittivity analysis

Fig. 5.5 (a & b) shows dielectric loss spectra (ε'') for La-Z and Ca-Z as function of frequency at various temperatures. It is seen that ε'' rapidly decreases with frequency and increases with temperature. This behavior can be explained by the classical theory of the dipoles interaction [205]. At low frequencies, higher mobility of electrons ensures higher relaxation which approaches to lower value with increase in frequency [205].

Further it is reported that, interfacial polarization is dominated at low frequency while the electronic and ionic polarization are dominated at higher frequencies [206]. The magnitude of ε'' for La-Z was found higher compared to Ca-Z due to multiple relaxation possible with La^{3+} substitution due to the presence of Fe^{2+} and Fe^{3+} ions. The rise in ε'' with temperature confirms the semiconductor like behavior of the sample. In Ca-Z sample, above 10^3 Hz, a hump is observed in the curves for all temperatures which suggests the dispersion behavior of ε''. This attribute suggests that the space charge carriers increases at grain boundaries and also at the interface of Z-type and W-type phases irrespective to higher frequency of the applied field.

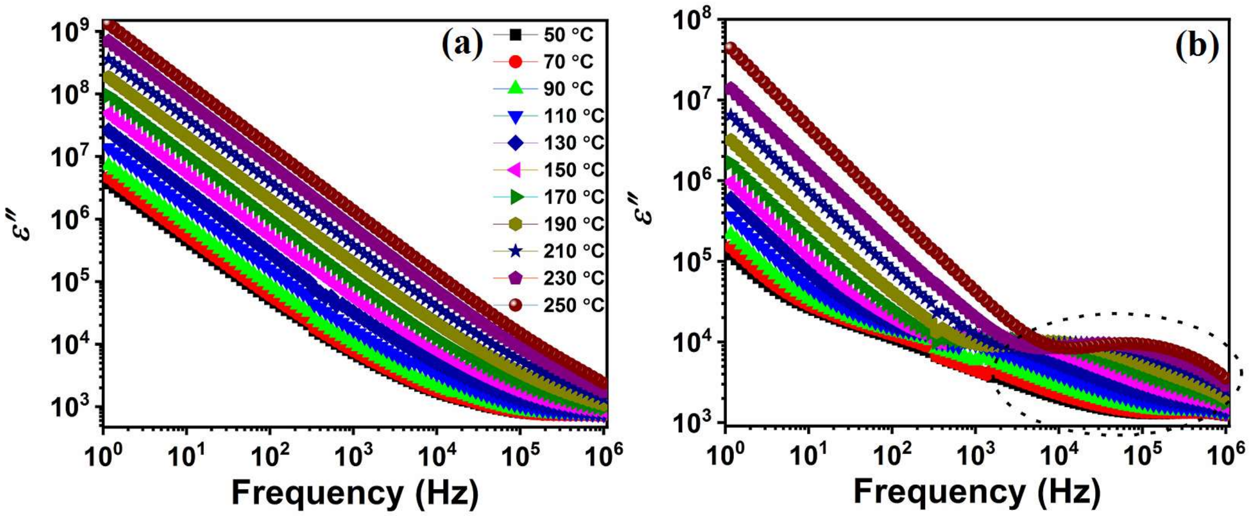

Fig. 5.5 Variation of ε'' (a) La-Z & (b) Ca-Z as function of frequency at different temperatures.

Physically dispersion behavior mainly originates due to additional capacitance introduced by grain boundaries and interphase boundaries of the different phases [207]. This dispersion tendency is rarely observed in dielectric material, defined as abnormal dispersion phenomena [208]. To understand the complex charge transfer between microscopic elements, impedance studies were carried out and presented in the following section.

5.1.5. Complex Impedance analysis

Electrical responses of grain and grain boundaries are investigated by impedance spectroscopy. Fig. 5.6 (a & b) shows the imaginary part of impedance (Z'') as a function of frequency for La-Z and Ca-Z at different temperatures. The plots show an increase in Z'' with frequency which reaches to maximum and then decreases. The maximum values of Z'' is comparable with La, Sm, and Pr doped Co_2Z [200]. The broad peak in all samples is due to charge relaxation, which switches towards higher frequency with increased temperature. It indicates that the charge relaxations are thermally activated [125]. The decreased magnitude of Z'' with increase in temperature suggest that losses are decreasing in the resistive part of the sample. In La-Z, the relaxation peaks are occurring at higher frequency compared to that of Ca-Z, implies that migration of the charge carriers is reduced and strongly depends on the type of the cation substitution. The ionic state of a system gives a decisive performance in impedance behavior. The variation in the ionic state improves conduction process by enhancing the hopping mechanism through electron exchange between Fe^{3+} and Fe^{2+} which enhances the conductivity of La-Z [109, 210, 211]. Also, the impedance loss is more in Ca-Z due to slight improvement in grain size with Ca^{2+} substitution. This is in direct relation with lowering grain boundary contribution in Ca-Z system which increase the *ac* conduction. The lower height of Z'' for La-Z suggests the conduction is more as compared to Ca-Z.

The higher Fe^{2+} ions due to La^{3+} substitution conjugate a greater number of Fe^{+3}-Fe^{2+} dipoles and causes relaxation at higher frequencies. The variation of τ with temperature (Fig. 5.6 (c)) shows two slopes in the plot, suggesting parallel charge conduction mechanism in the system. Two activation energies are associated where one is related to oxygen vacancies and second one is assigned for hole/electron. The oxygen vacancies are originated at higher sintering process which provided the conduction electrons. The value of first ionization activation energy for oxygen vacancies are 0.23 eV in La-Z and 0.24 eV in Ca-Z. The activation energies determined by the slope of curves were found to be (0.59 eV & 0.23 eV) for La-Z and (0.64 eV, 0.24 eV) for Ca-Z. Very lower difference is observed between the activation energies of La-Z &8 Ca-Z compared to pure Co_2Z ferrite (Fig. 5.6 (c)), implies that similar type of the charge carriers is responsible for the electric conduction along the grain boundaries.

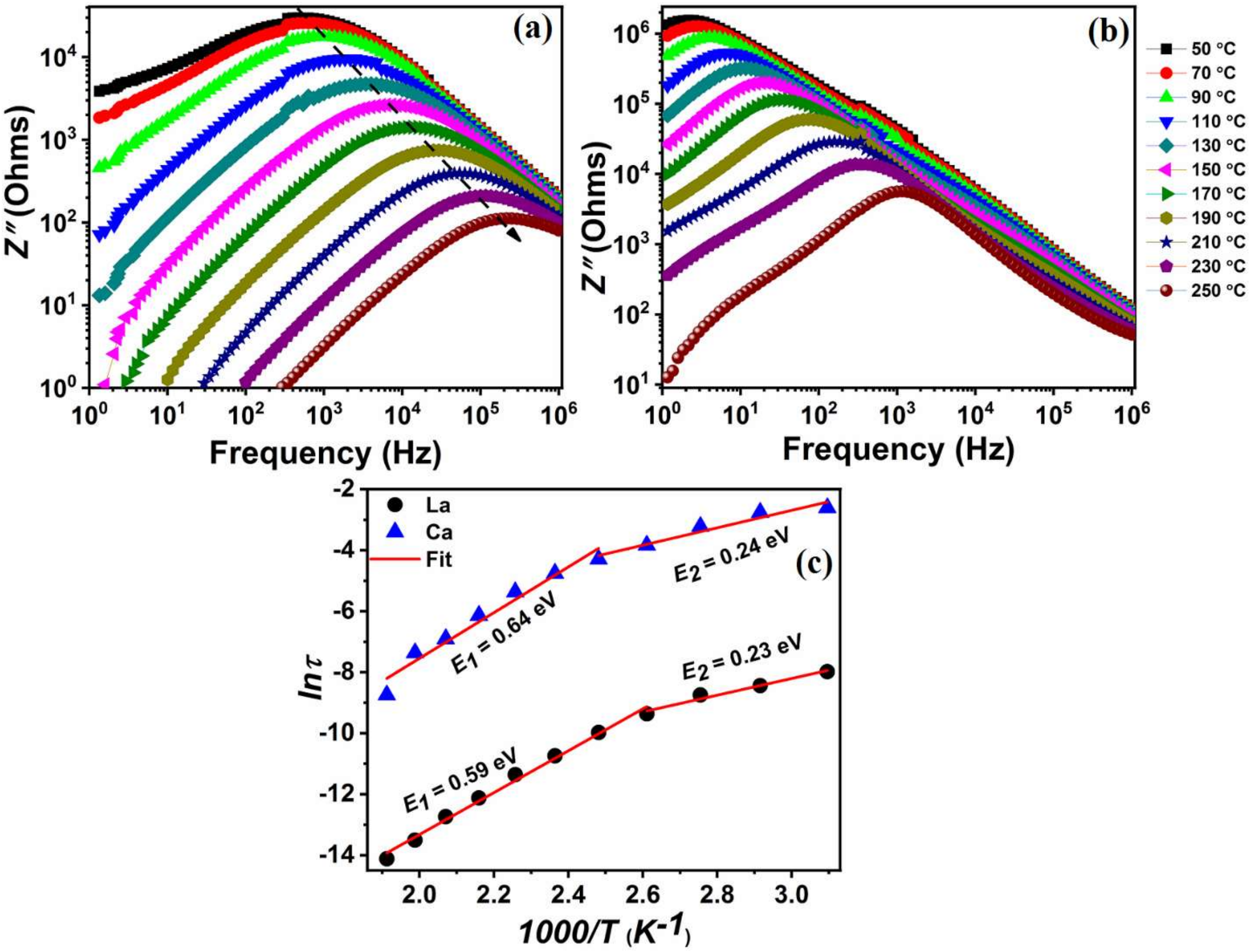

Fig. 5.6 Variation of Z'' with frequency at different temperatures (a) La-Z, (b) Ca-Z and (c) temperature dependent τ.

To identify the contribution of grain and grain boundaries to charge conduction, the Cole-Cole plots (Z'' *vs* Z') were fitted with an appropriate equivalent electric circuit and shown in Fig. 5.7 (a-d). The appearance of single semicircle suggests that grain and grain boundaries contributions are not resolved [207, 212]. The resistance (R) and capacitance (C) for grain (g) and grain boundaries (gb) are denoted by (R_g, C_g) and (R_{gb}, C_{gb}), respectively. *CPE* interprets a constant phase element which denotes the deviation from an ideal Debye type relaxation. With increasing temperature; the diameter of the semicircle decreases, which shows that the grain and grain boundaries resistance are decreased [190]. The circumference of semicircular arc for La-Z is small compared to Ca-Z, indicates the impedance of La-Z is higher.

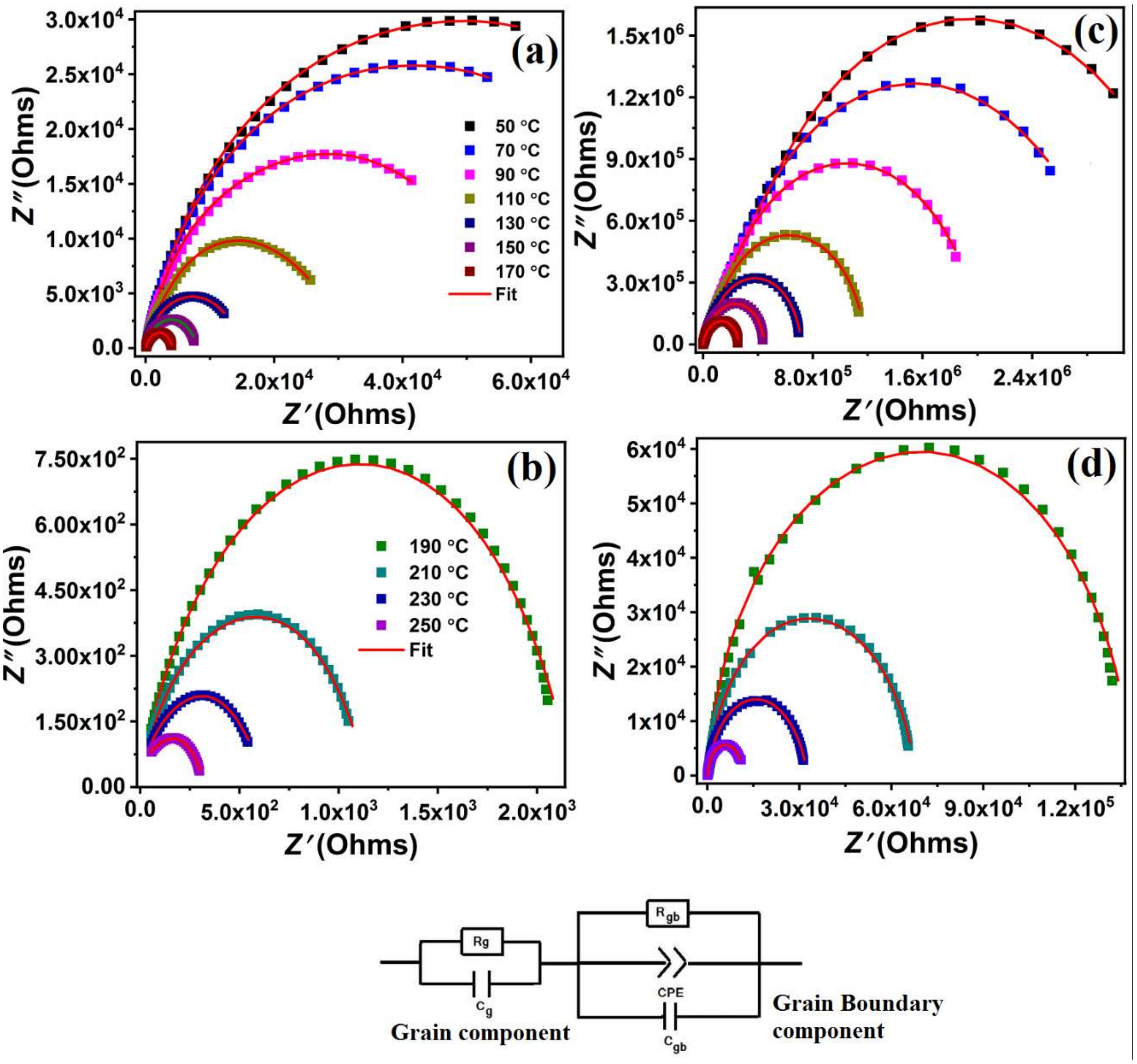

Fig. 5.7 Fitted Cole-Cole plots of impedance spectra (Z'' *vs* Z'), (a & b) La-Z and (c & d) Ca-Z at different temperatures with their equivalent electrical circuit.

Fig. 5.8 (a & b) shows the fitted electrical resistances of grain and grain boundaries, obtained by using the equivalent circuit at difference temperatures. The values of R_g and R_{gb} decreases with increase in temperature. The higher R_g and R_{gb} of Ca-Z than La-Z is due to large grain boundary fraction as a consequence of smaller grains which provides more hindrance to charge motion. For Ca-Z, the similar activation energies of grain and grain boundary above 100 °C suggests potential barrier height difference between them is very low [191]. The large difference in the activation energies of grain and grain boundaries for La-Z suggests that conduction is governed by the multiple charge carriers. Further, $R_{gb} > R_g$ may be due to space charge polarization as described in Maxwell–Wagner model [192]. It has been already discussed related to La-Z that the grain boundaries reduced with increase the size of grain. With reducing the grain boundary barriers, the lower activation energy is required compared to Ca-Z.

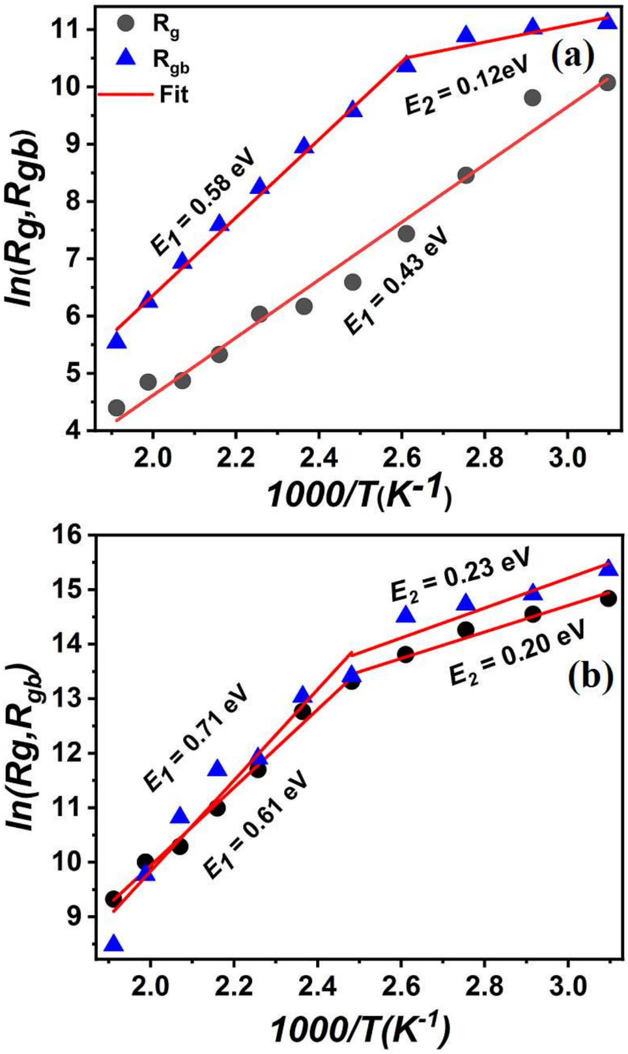

Fig. 5.8 Arrhenius plots of grain and grain boundaries resistances (R_g & R_{gb}) obtained from equivalent circuits of (a) La-Z and (b) Ca-Z.

5.1.6. Complex electric modulus analysis

Fig. 5.9 (a & b) shows the frequency dependence curves of M'' at various temperatures. A single relaxation peak is observed in La-Z while double relaxation appeared in Ca-Z (given by dotted circles Fig. 5.9 (a & b). It is notable that peak shift towards higher frequency with temperature confirmed that charge relaxation is thermally activated. The relaxation peak also gives the information about the hopping mechanism of charge carriers [213]. The magnitude of the relaxation peak is higher for La-Z compared to Ca-Z, implies that the capacitance of La-Z is more compared to Ca-Z. Peak height is also dependent on the grain size and hopping of the electrons [214]. The appearance of two relaxation peaks in Ca-Z, suggests that two type of electric charge carriers are thermally activated.

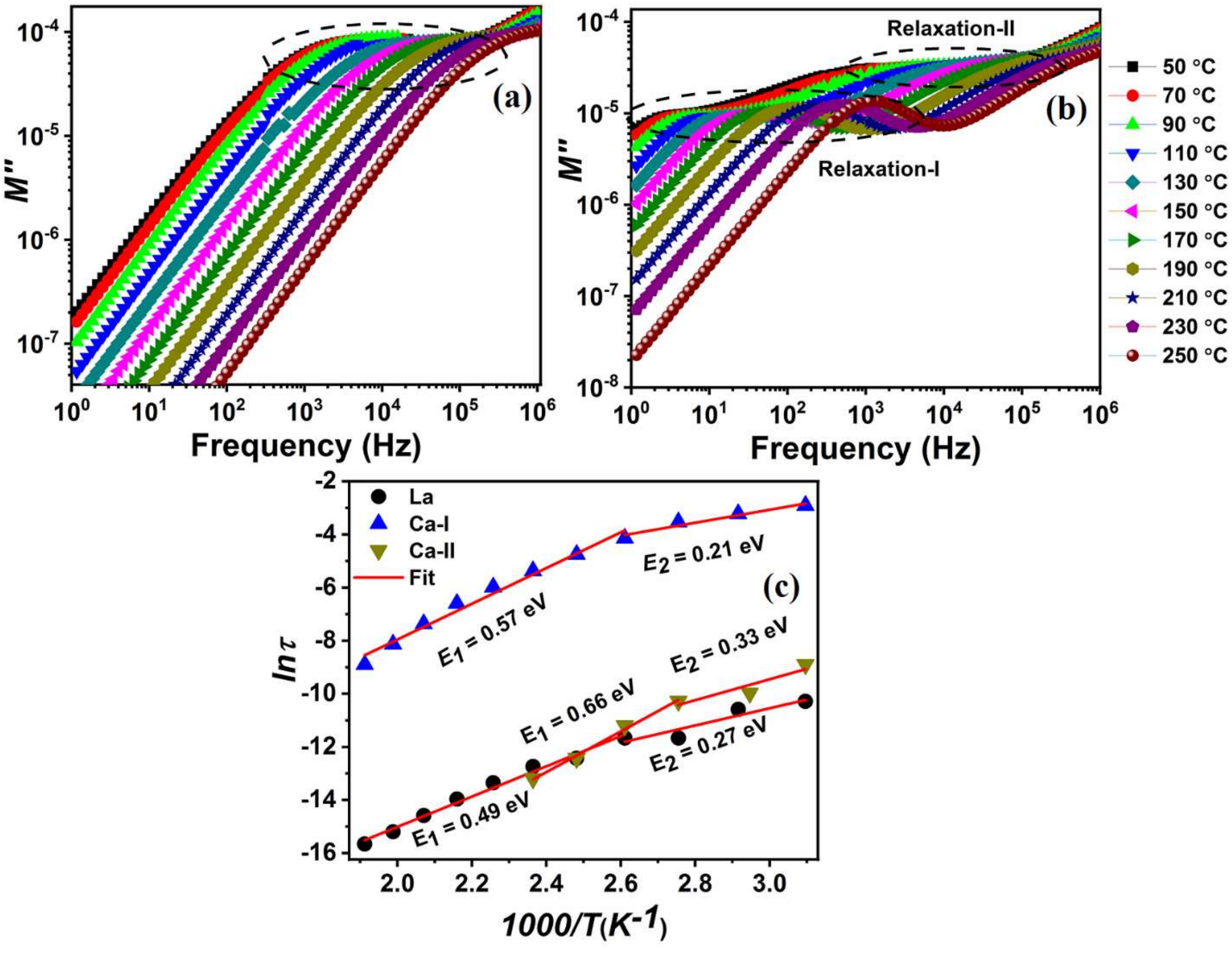

Fig. 5.9 Variation of M'' (a) Co_2Z, (b) La-Z and (c) temperature dependent τ.

τ is estimated from M'' *vs* f plot at different temperatures. Fig. 5.9 (c) shows the decreasing tendency of τ with temperature implies negative temperature coefficient of the material. The maximum value of τ ($\tau_{\max}$) represent that charge carriers are mobile over the long distances. For the minimum value of τ (τ_{min}) implies that charge carriers behave like a confined particle in the potential well and migrate over the short distances. The obtained activation energies (E_1 & E_2) correspond to first relaxation (0.57 eV, 0.21 eV) & second relaxation (0.66 eV, 0.33 eV) for Ca-Z and only single relaxation (0.49 eV & 0.27 eV) for La-Z. A single activation energy is obtained for grain in La-Z, impels that a unique charge carrier is activated within the grain while in Ca-Z two types charge are associated with grain and grain boundaries. The activation energy from Z'' and M'' represent dielectric relaxation and long rang conduction, respectively [208]. The comparable activation energies of Ca-Z and La-Z, suggest that the relaxation and conduction may correspond to the same type of charge carriers. However, a slight reduction in activation energy of La-Z in M'' compare to Z" implies that charge carriers require low energy for conduction. The charge carriers experienced weak strength of electric field when it moved far from the ionic position of lattice site. Therefore, the lower activation energy is sufficient to break the electrical barrier potential in long conduction.

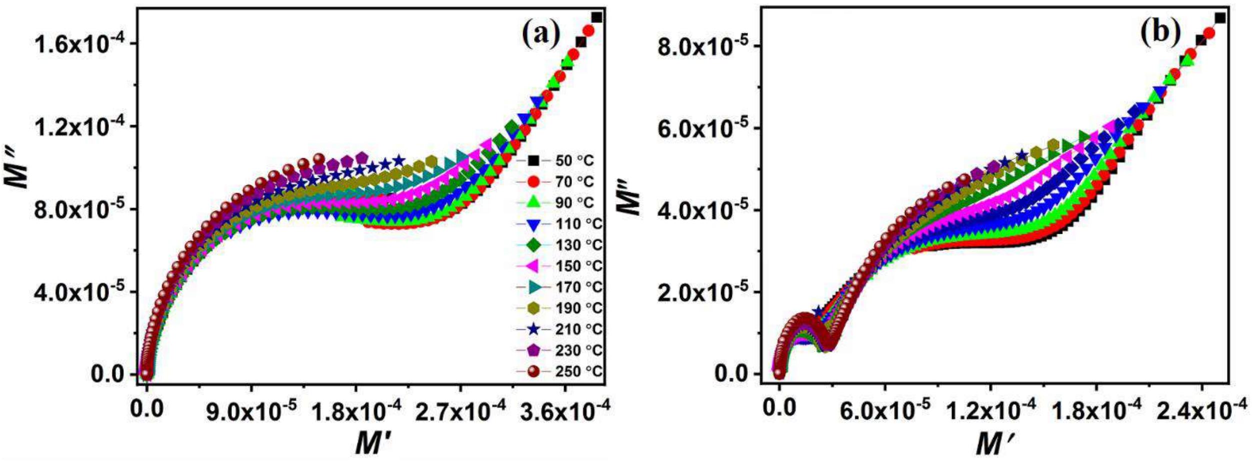

Fig. 5.10 Cole-Cole plots of complex electrical modulus spectra (*M″ vs M′*) of (a) La-Z and (b) Ca-Z at different temperatures.

To differentiate individual relaxation process similar to Cole-Cole plot of complex impedance; the complex electric modulus spectrum (*M′ vs M″*) for La-Z & Ca-Z at various temperatures were plotted and shown in Fig. 5.10 (a & b). Double semicircular arcs connected to the constant straight-line pattern in Ca-Z are characterized to the capacitive contribution of grain, grain boundary and interfacial polarization effect [215]. However, La-Z shows only one semicircle corresponding to grain boundary contribution where, the contribution of grain seems to be suppressed due to high mobility of charge carrier within the grains. It is reported that the center of the semicircle arc lies below the real axis, confirms a non-Debye type relaxation [194]. The diameter of semicircular arc shifted towards large value of M' with increasing temperature, implies that capacitance increases. This phenomenon is just opposite to resistance behavior of the Z-type, shown in Fig. 5.7 (a-d) [196].

5.2. Effect of Al^{3+} substitution for Fe^{3+}

In this section, series of $Ba_3Co_2Fe_{24-x}Al_xFe_{41}$ (x = 0.0, 0.4, 0.6, 0.8, 1.0 & 1.8) were synthesized. A comparative study of dielectric, impedance and electric modulus for x = 0.4 & 1.8 is presented here.

5.2.1. Phase identification

Fig. 5.11 shows the XRD patterns of Al^{3+} substitution for Fe^{3+} sintered powders of Co_2Z ferrites. The Al^{3+} substitution for x = 0.4, 0.6, 0.8, 1.0 & 1.8 are denoted by Al 0.4, Al 0.6, and so on, respectively. The calculated lattice parameters (*a* & *c*) and crystallite size (*D*) are shown in Table 5.2. The reduction of *a* & *c* is associated with the small ionic radii of Al^{3+} (0.535 Å) compared to Fe^{3+} (0.645 Å) [157]. The *D* increases with increased Al^{3+} substitution, suggests that Al^{3+} substitution promotes grain growth.

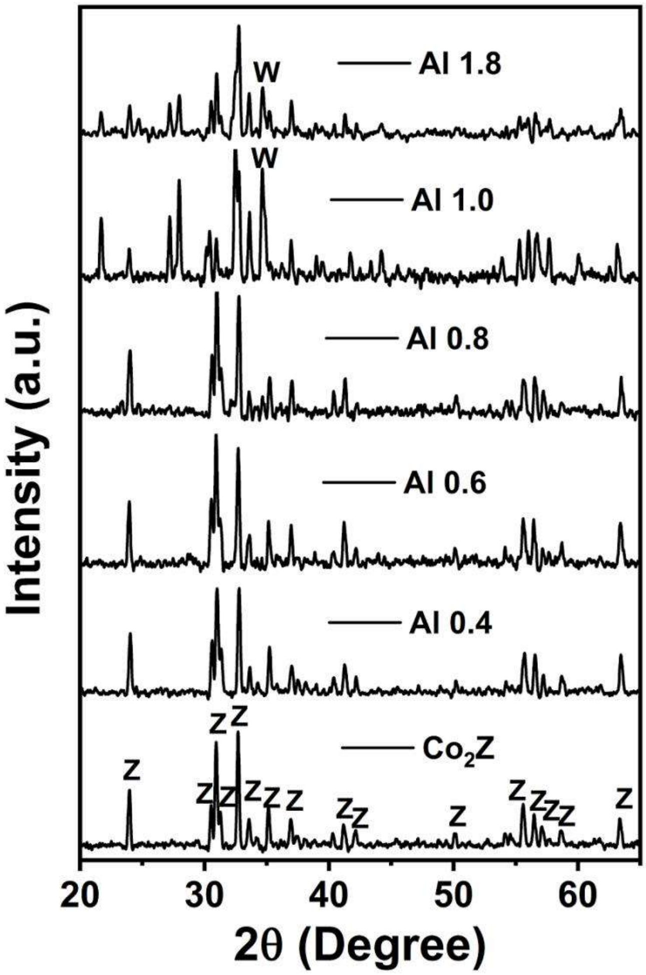

Fig. 5.11 X-ray diffraction patterns of Al-substituted Co_2Z ferrite.

Table 5.2 Lattice parameters and crystallite size of Al-substituted Co_2Z ferrites.

Contents	**Phases**	**Al substituted Co_2Z**		
		a (Å)	*c* (Å)	*D* (nm)
0.0	Z-type	5.87	52.15	37.9
0.4	Z-type	5.88	51.89	72.9
0.6	Z-type	5.85	52.00	76.3
0.8	Z-type	5.85	51.89	84.9
1.0	Z-type	5.85	52.24	127
	W-type	5.89	32.89	
1.8	Z-type	5.86	52.18	146
	W-type	5.90	32.92	

5.2.2. Microstructural analysis

Fig. 5.12 (a-e) shows the SEM micrographs of fractured surface of Al-substituted Co_2Z ferrites. Well sintered hexagonal platelet were observed for all compositions. It is observed that with increasing Al^{3+} substitution grain size increases which in accordance with XRD data. With further substitution from x = 1.0 to 1.8, the hexagonal platelets are found to be vertically aligned. The measured sintered density was greater than 4.7 g/cm^3.

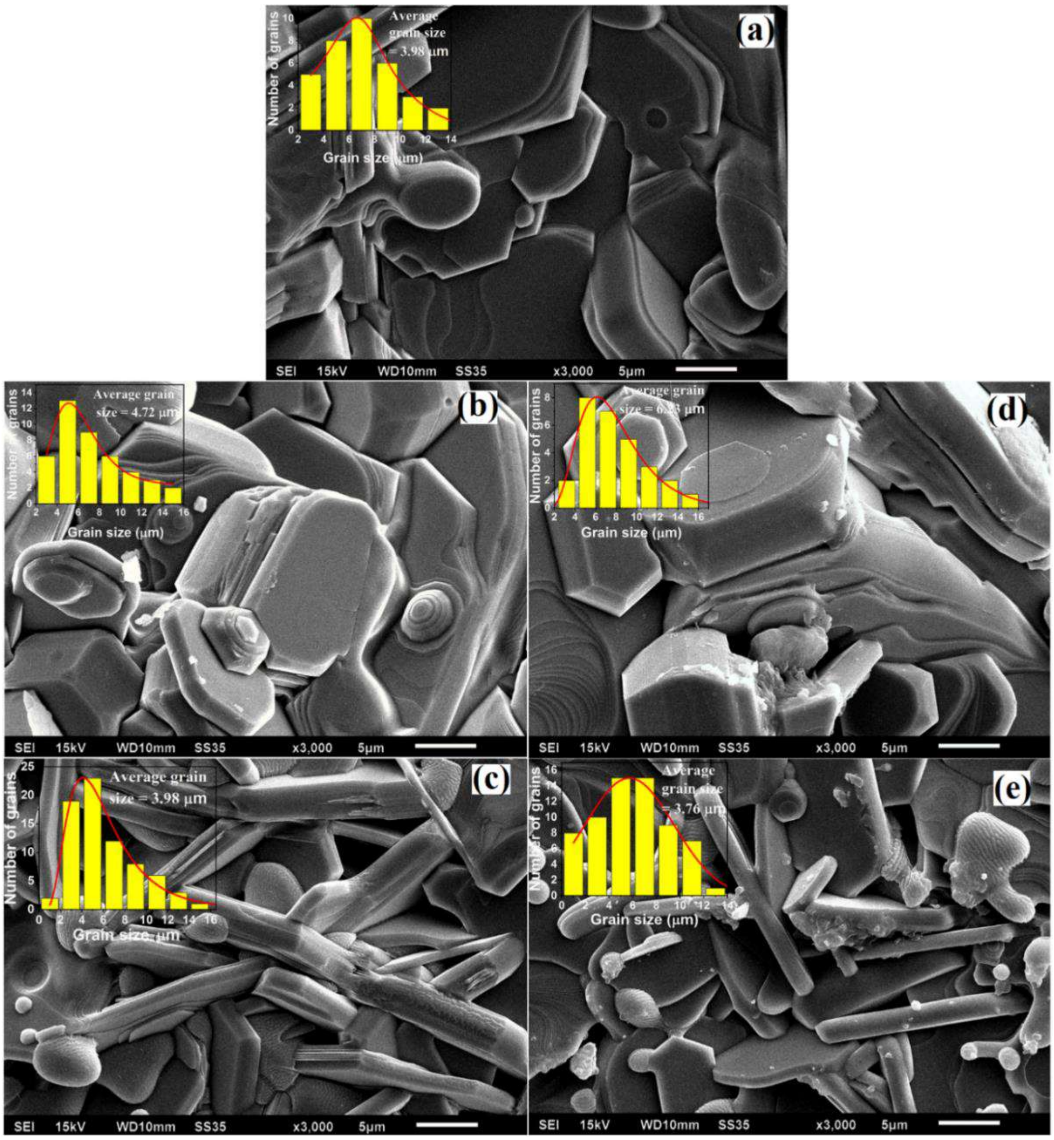

Fig. 5.12 SEM micrographs of fractured surface of Al substituted Co_2Z ferrites, (a) Al 0.4, (b) Al 0.6, (c) Al 0.8, (d) Al 1.0 & (e) Al 1.8.

5.2.3. Magnetic properties

Fig. 5.13 illustrates *RT* hysteresis loop of Al-substituted Co_2Z ferrites. The measured values of M_s, H_c and M_r are given in Table 5.3. It is observed that M_s is reduced up to x = 0.8 compared to non-substituted Co_2Z ferrite. The partial substitution for Fe^{3+} ions by nonmagnetic Al^{3+} affects the magnetic moments in spin-up positions located at sublattice sites [157]. With increasing Al^{3+} content above x = 0.8, the increase in M_s is due to the secondary W-type phase formation. For x = 1.8, M_s further decreases, implies that the magnetic moment of both phases Z-type & W-type is reduced. H_c is found to decrease with the substitution due to increase in grain size, the higer value for x = 1.0 is an implication of W-type phase formation. At x = 1.8, the decreases in H_c may be associated with dilution of magnetic anisotropy at higer content. M_r is higher for substituted Co_2Z, suggest higher field is required for demagnetization.

Table 5.3 Magnetic properties of Al-substituted Co_2Z ferrites.

Contents	Al substituted		
	M_s (emu/g)	H_c (Oe)	M_r (emu/g)
0.0	45.3	31.3	0.9
0.4	42.0	23.9	20.6
0.6	43.4	20.8	23.4
0.8	38.6	20.2	23.9
1.0	43.6	45.9	20.6
1.8	38.0	32.3	20.8

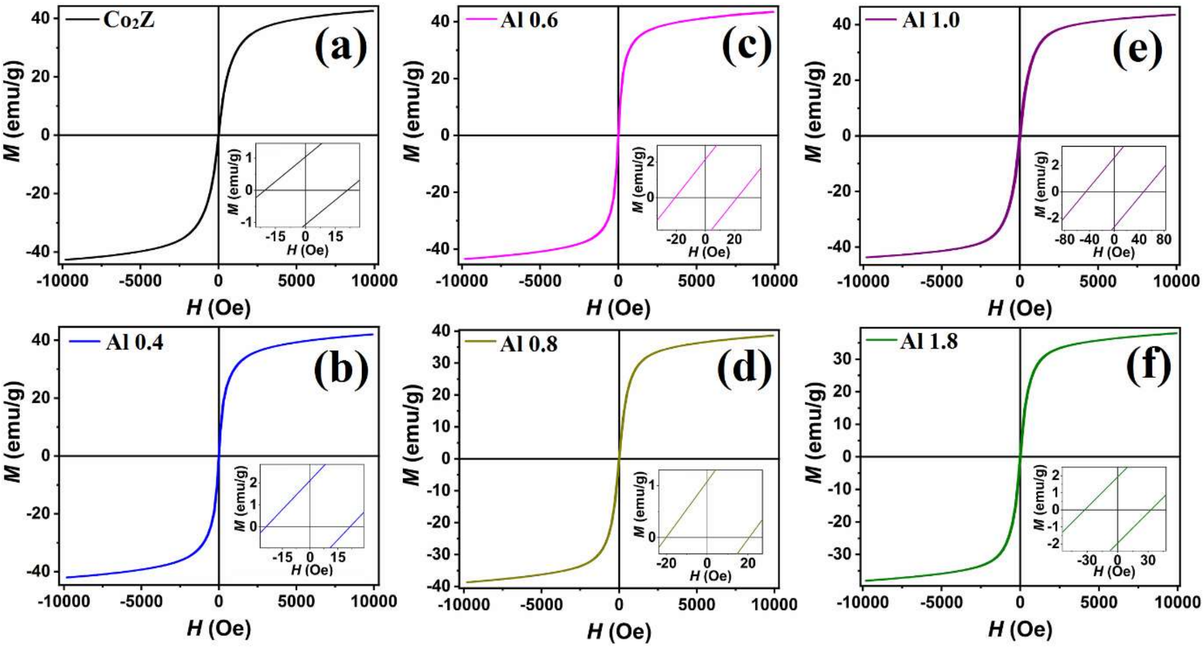

Fig. 5.13 Magnetic hysteresis loop of Al-substituted Co_2Z ferrites. (a) Co_2Z, (b) Al 0.4, (c) Al 0.6, (d) Al 0.8, (e) Al 1.0 & (f) Al 1.8. The inset enlarges views of H_c.

5.2.4. Complex permittivity analysis

Fig. 5.14 (a & b) and Fig. 5.14 (c & d) shows frequecy dependent behavior of ε' & ε'' for Al 0.4 & Al 1.8 at different temperatures. Both shows similar trend with frequency as discussed in previous sections. The sample with higher Al^{3+} substitution (x = 1.8) shows relatively higer ε', which may be due to presence of W-type phase and interphase boundary with Z-type phase. Further in low frequency region, ε' curves are well separted for higher temperature iimplies the strong relaxation. At low temperatures, the decreases in separation may be due to the weak relaxation in low frequency [174]. A step-like relaxation between 10^3 Hz – 10^5 Hz is present, which is more dominant for x = 1.8 and in agreement with non-Debye type relaxation [216]. Two negative gradients named slope 1 & slope 2 shift towards higher frequency regime with temperature suggests the frequency-independent electric conduction of the charge carriers [217].

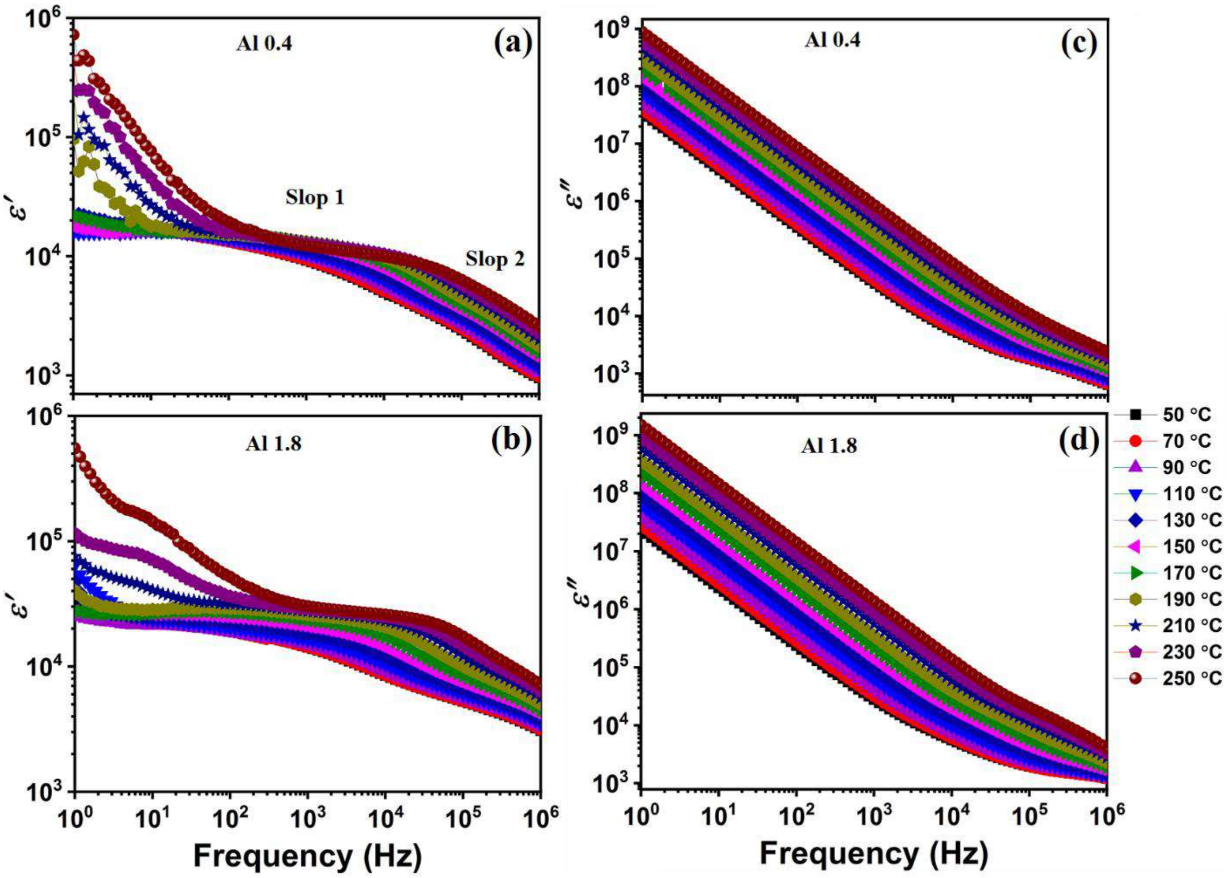

Fig. 5.14 Variation of (a & b) ε' and (c & d) ε'' for Al 0.4 & Al 1.8 as function of frequency at different temperatures.

5.2.5. Complex impedance analysis

Fig. 5.15 (a & b) shows the variation of Z' with frequency at various temperatures. At lower frequency and temperature, Z' is higher and decreases with increasing temperature, which implies that the conduction mechanism increases. At all temperatures first Z' remains constant and then decreases above a certain frequency, which varies with temperature. This is due to conduction of charge carriers which requires different thermal energy to overcome the potential barrier [218]. At lower frequency, magnitude of Z' for Al 1.8 is higher than Al 0.4 suggesting that the mobility of the charge carrier is low at higher Al content. At higher frequency, all Z' curves appears to merge out due to the presence of space charge polarization along grain boundaries [219, 220]. The merging of the curves for Al 1.8 is stronger compared to Al 0.4, which implies that higher space charge density exists along the boundaries. The length of the Z' parallel to the frequency axis is slightly larger for Al 0.4 than Al 1.8, which confirms that conduction is taking place at lower frequency**.**

Fig. 5.15 (c & d) demonstrates that the magnitude of Z''_{max} is higher for Al 1.8 than Al 0.4, which implies that the electrical conduction mechanism increases with increasing Al^{3+} substitution. The relaxation peak shifts towards higher frequency side with increased temperature, implies that the charge carriers are thermally activated. The peak maxima of Z'' appears at very low frequency for Al 1.8 compared to Al 0.4 suggests that relaxation changes occurs with excessive Al^{3+} substitution.

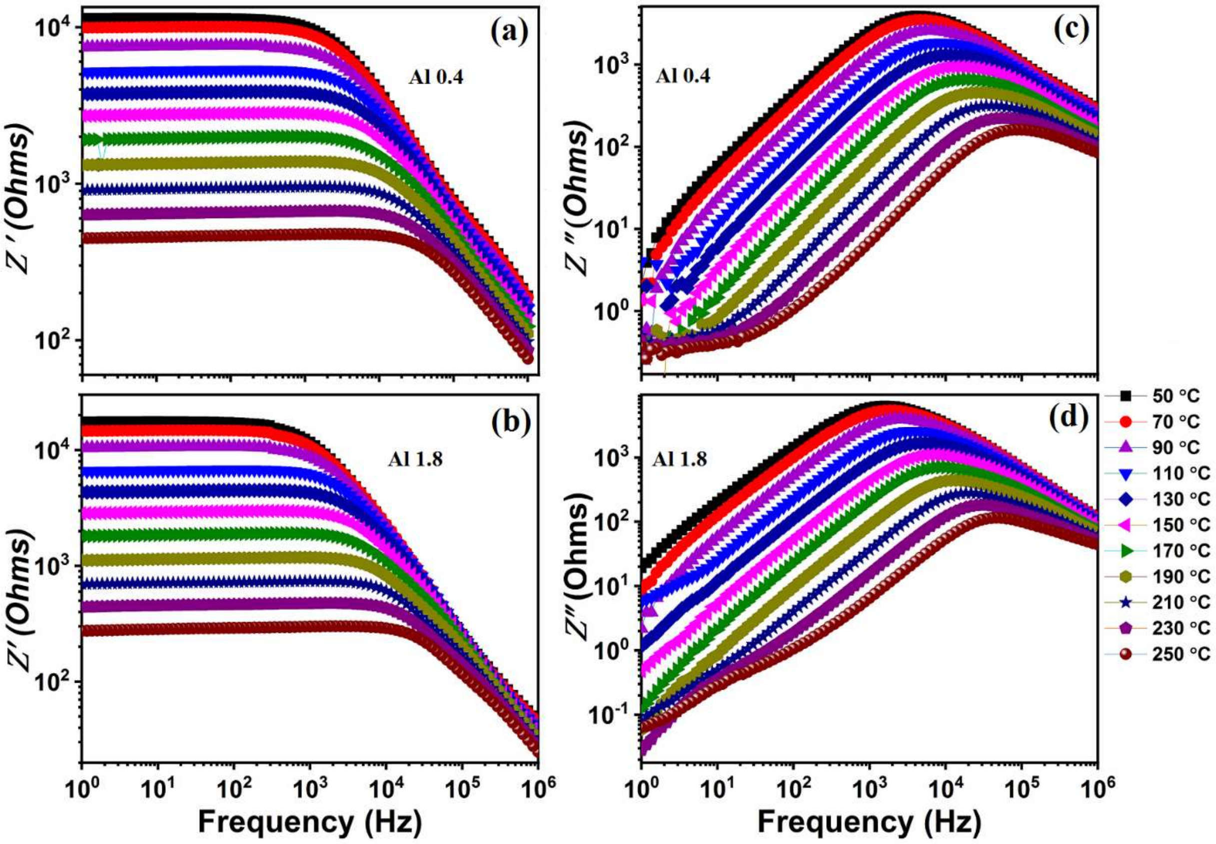

Fig. 5.15 Variation of (a & b) Z' and (c & d) Z'' with frequency at different temperatures for Al 0.4 & Al 1.8, respectively.

Fig. 5.16 (a & b) shows the normalized pattern of the impedance with frequency at different temperatures. The relaxation peaks switches towards higher frequency side with increasing temperature, implying that the relaxation is temperature-dependent. The relaxation peak for Al 1.8 appears at a lower frequency compared to Al 0.4, which suggests that the Al^{3+} substitution decreases the relaxation peak frequency.

The scaling behavior of Al-substituted Co_2Z ferrites are given in Fig. 5.16 (c & d). Since all impedance loss profiles are overlapped, it suggests that the distribution of τ is temperature independent. The *FWHM* is higher than 1.144 decades, suggesting that the dynamic process of the dielectric response is non-Debye type relaxation [221, 222].

Fig. 5.16 (e) demonstrates the *τ vs. 1/T* for Al substituted Co_2Z ferrites. The Arrhenius plots have two gradients (slopes), E_1 (higher temperature) & E_2 (lower temperature), which implies that charge carriers are activated in different temperature ranges. The calculated activation energies are (0.31 eV, 0.13 eV) for Al 0.4 while (0.41 eV, 0.18 eV) corresponds to Al 1.8. The different activation energies implies that dielectric relaxation is associated with various charge carriers. The activation energies (0.61 eV, 0.26 eV) of pure Co_2Z ferrites have already been discussed in Fig. 4.8 (d), and is much higher compared to Al-substituted samples. Therefore, electric charge conduction is taking place at lower energies in Al-substituted samples.

Physically Al^{3+} ion substitution reduces the strength of the intrinsic potential barrier. The higher activation energy of Al 1.8 compared to Al 0.4 contradicts the low barrier. This ambiguity is explained by the SEM image analysis (Fig. 5.12 (a & e)). The microstructure shows that Al 1.8 sample has larger fraction of grain boundaries than Al 0.4 which provide hindrance to conduction. The Cole-Cole plots of Al 0.4 and Al 1.8 is depicted in the Fig. 5.17 (a-d).

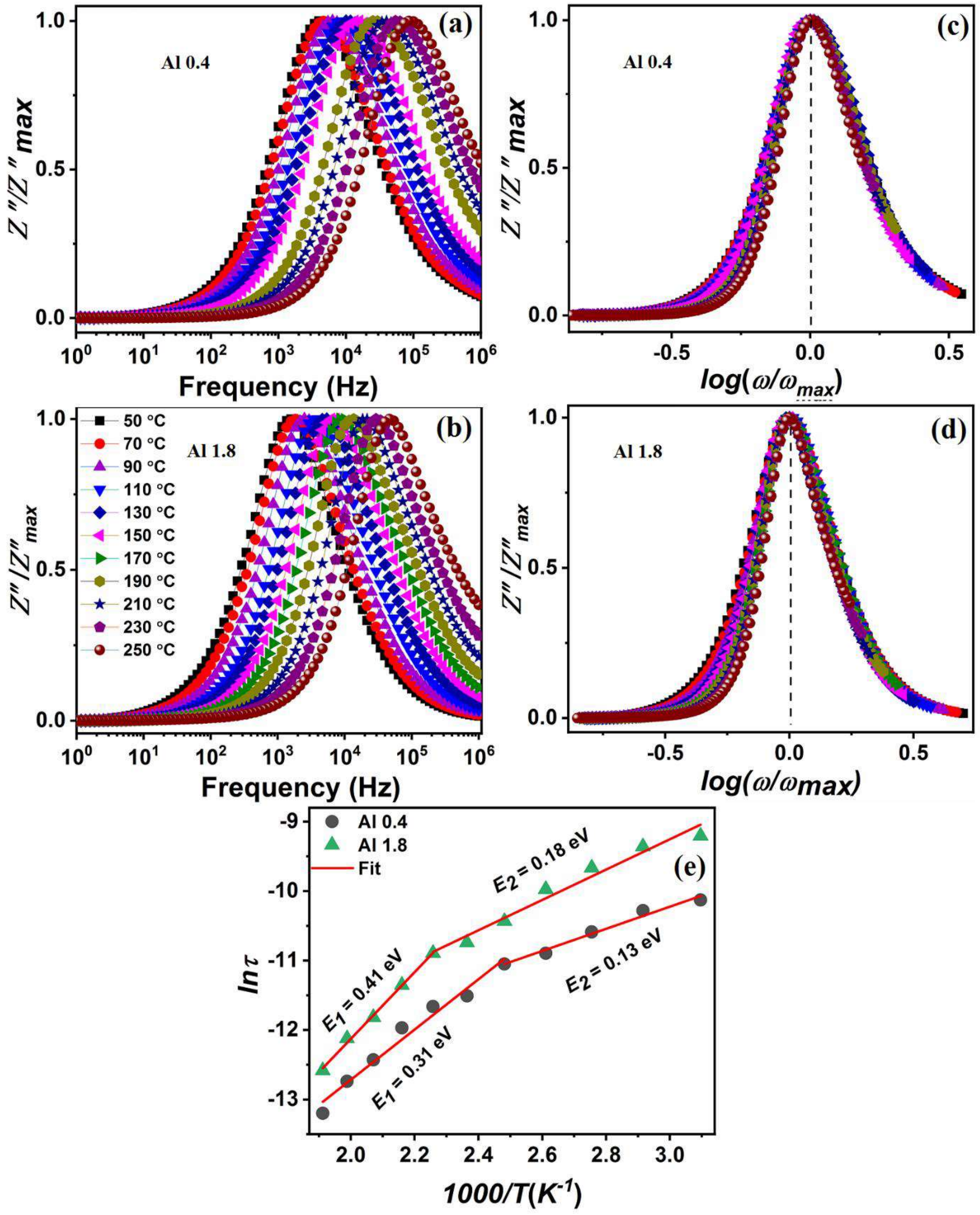

Fig. 5.16 (a & b) Normalized impedance (Z''/Z''_{max}) spectra as a function of frequency, (c & d) scaling behavior spectra (Z''/Z''_{max} *vs* $log(\omega/\omega_{max})$) for Al 0.4 & Al 1.8 and (e) temperature dependent τ.

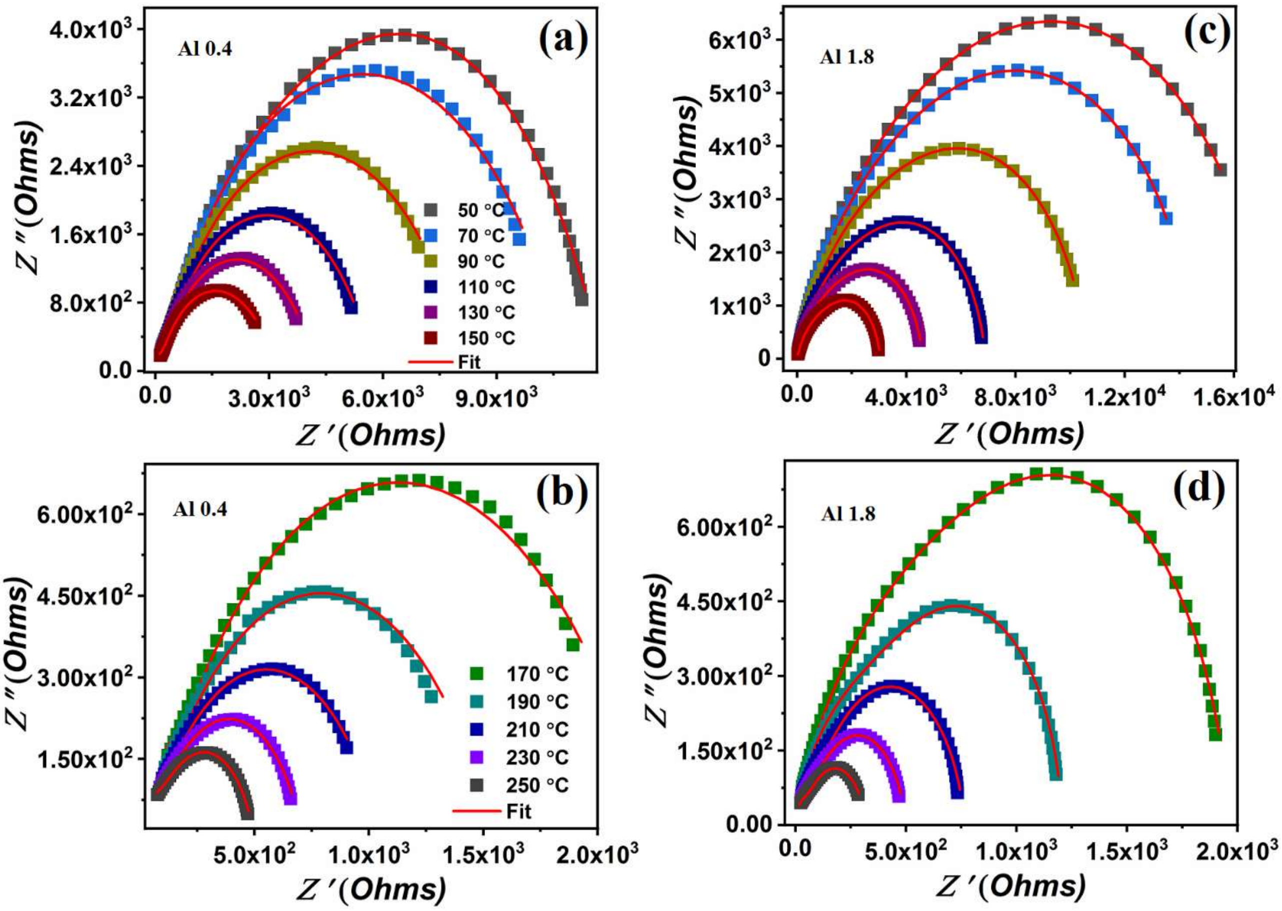

Fig. 5.17 Fitted Cole-Cole plots of complex impedance (*Z″ vs. Z′*) (a & b) Al 0.4 and (c & d) Al 01.8.

The used equivalent circuit for Al-substituted is similar to the pure Co_2Z ferrite (Fig. 4.8 (a)). The diameter of the arcs decreases with increasing temperature. It confirms that the potential barrier decreases, which counters the charge carriers during the conduction [223]. The diameter of Al 1.8 is higher compared to Al 0.4, which implies that the intrinsic strength of the potential barrier is highly attributed to the excessive Al^{3+} ion substitution and poly dispersive in nature. [174, 224].

Fig. 5.18 (a & b) represents the Arrhenius fitted electrical resistances of grain and grain boundaries obtained from the fitting complex impedance data. It is to be noted that the R_g & R_{gb} decreases with increasing temperature, indicating the typical semiconducting nature of the Al-substituted Co_2Z ferrites. The higher resistance of the grain boundary compared to grain resistance suggests that space charge polarization and oxygen vacancies are present along the grain boundary.

The separation of the resistances is more for Al 0.4 compared to Al 1.8, which informs that higher space charge polarization accumulates along the grain boundary in Al 0.4. According to the principle of electrodynamics, the electrical charge is distributed along the outer surface of the spherical conductor. Koop's theory assumes that grains are highly conductive, which is justified by the Maxwell-Wagner law. This grain is analogous to the spherical conductor; therefore, all electronic charge (space charge) covers the grain boundary region associated with the conductive grains. The linear fitted resistances provide the activation energy of the grain and grain boundary. The value of the activation energies of R_{gb} for both Al 0.4 & Al 1.8 is comparable to the activation energy calculated from the relaxation plots of Z''. The lower value of E is observed for grains (Al 0.4) compared to Al 1.8. This implies that higher Al content impedes the charge motion in grains. Initially charge originated from oxygen vacancies, requires low activation energy, whereas electron/hole movement requires high activation energy. The value of energies for Rg & Rgb is very close to each other in Al 1.8, indicating the same type of charge carriers are activated along the grain boundary and inside the grain. The order of the energy for grain in Al 0.4 is also almost similar (0.12 eV ~ 0.16 eV) suggesting that the same types of charges are activated.

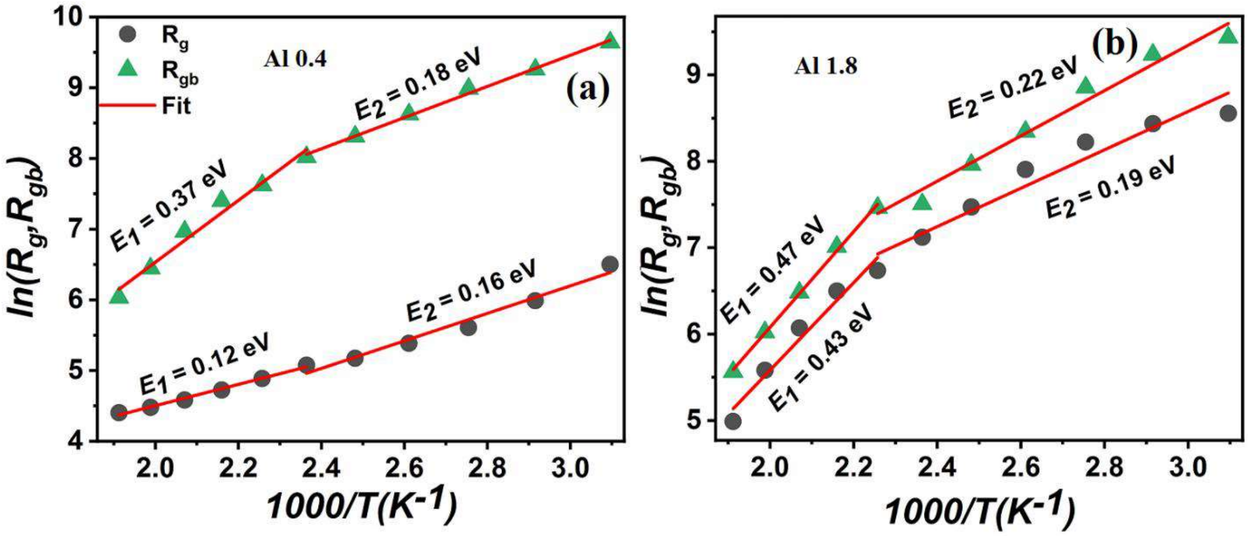

Fig. 5.18 Arrhenius plots of grain and grain boundary resistance evaluated from the impedance data simulation of an equivalent circuit (a) Al 0.4 & (b) Al 1.8.

5.2.6. Complex electric modulus analysis

Fig. 5.19 (a & b) shows the variation of M' with frequency at different temperatures. At low frequency, M' is very low, confirming the capacitive contribution of the electronic polarization which is weak [225]. With increased frequency, M' increases and approaches to a maximum saturate value, called M'_{max}. The magnitude of the M' is lower for Al 1.8 compared to Al 0.4, which implies that the saturation point is obtained at low frequency. The reduction of peak frequency may be related to the secondary W-type phase.

Fig. 5.19 (c & d) shows the variation of M'' with frequency at different temperatures. A single relaxation peak appears, which shifts towards higher frequency, implying that the relaxation process of the charge carriers is thermally activated. At low frequency, the charge carriers can migrate for long-range distances. Apart from the peak frequency, the charge is confined in the potential well and can move under short-range forces [226]. Under the peak frequency, the charge diffuses from long-range to short-range distances.

The relaxation time (τ) for M'' is shown in Fig. 5.19 (e). τ decreases with increasing temperature, implies that the negative temperature coefficient of the Al substituted Co_2Z ferrite. The minimum value of τ corresponds to those charge carriers which are confined in the potential well. The maximum τ is related to the long-range forces, while the intermediate τ signifies the long-range to short-range conduction. The comparable activation energies of Z'' and M'' suggest that low temperature relaxation and higher temperature conduction mechanism possesses the same type of the charge carriers. The lower value of energies (0.08 eV for Al 0.4 & 0.06 for Al 1.8 eV) is associated with the non-localized motion of the carriers.

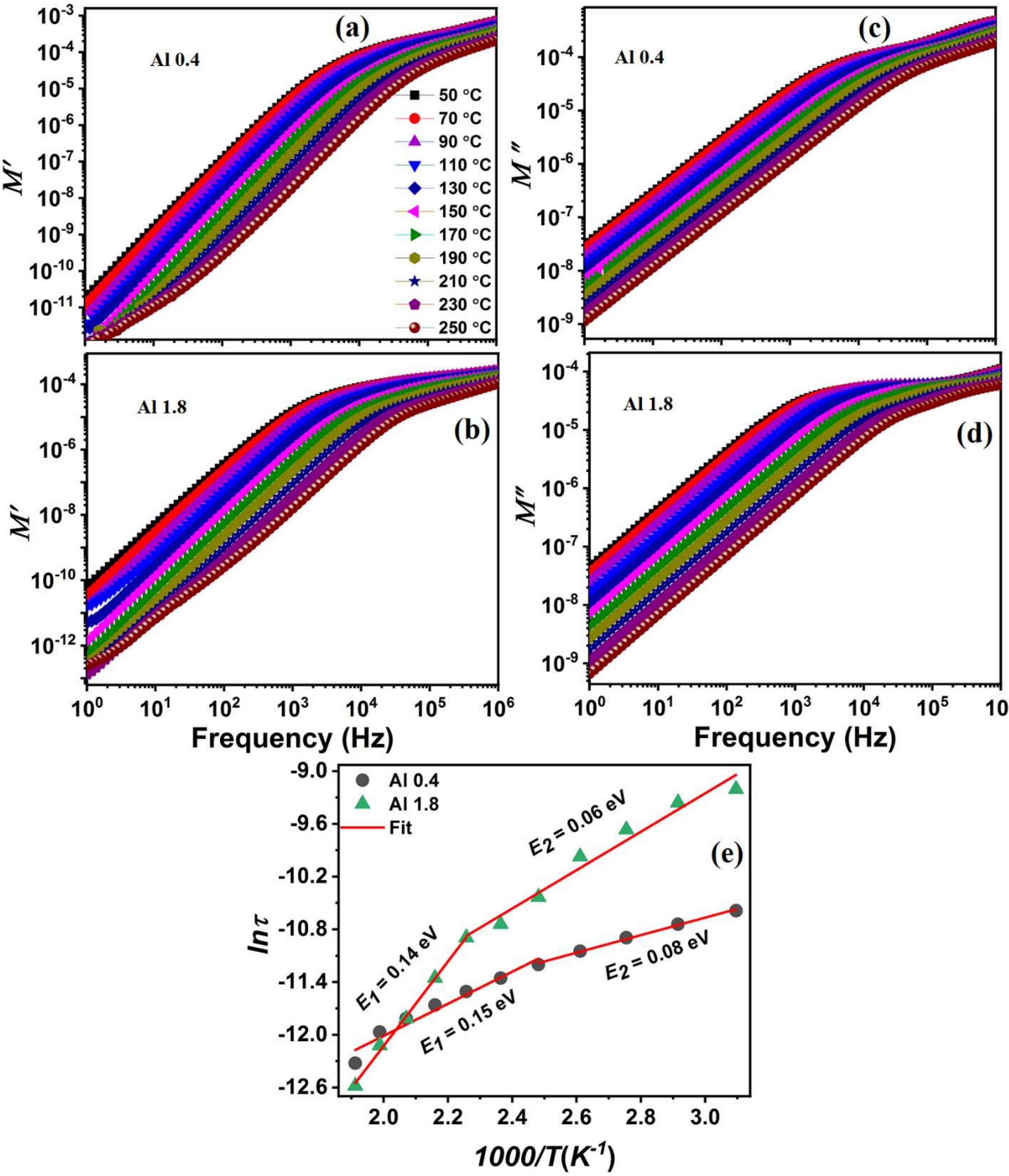

Fig. 5.19 Variation of (a & b) M' and (c & d) M'' spectra with frequency at different temperatures for Al 0.4 & Al 1.8 and (e) temperature dependent τ.

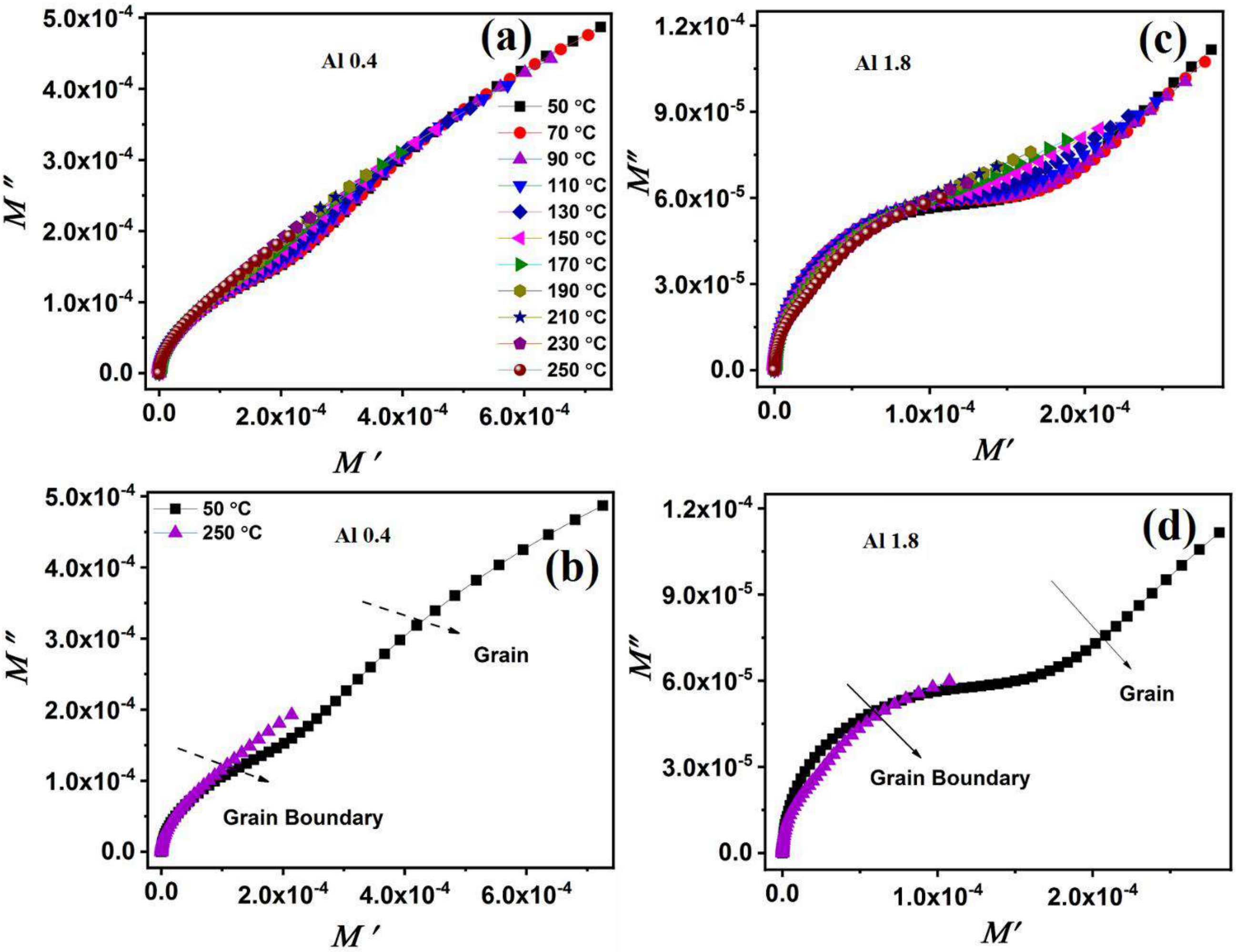

Fig. 5.20 Cole-Cole plots of complex electric modulus (*M″ vs M′*) spectra (a & b) Al 0.4 and (c & d) Al 1.8.

To distinguish the different relaxation of the material exerting external effects, complex electric modulus (*M″ vs. M′*) is employed and given in Fig. 5.20 (a-d). Plots show two patterns; first patterns along the lower frequency region represent the capacitive contribution of the grain boundary, while the second line pattern demonstrates the contribution of the grain. Fig. 5.20 (a & b) shows that the contribution of the grain is higher compared to the grain boundary. The contribution of the grain decreases with increasing temperature. The comparison of Fig. 5.20 (b & d) illustrates that the contribution of the grain boundaries is much higher than the grains. The diameter of the arcs reduces towards a higher value of *M′*, which implies that the capacitance increases with temperature. This property is just opposite to the resistive nature demonstrated by impedance Cole-Cole plots (Fig. 5.17 (a-d)).

Sub-conclusion

Series of $Ba_{3-x}La_xCo_2Fe_{24}O_{41}$, ($x = 0, 0.2, 0.4, 0.6$) powder were prepared by solid state method. XRD study showed that pure Z-type phase existed up to $x \leq 0.2$, and then secondary W-type phase were also found. Hysteresis loop analysis showed that M_s was increased with La^{3+} substitution. The analysis of electric impedance and electric modulus indicated the hopping and relaxation mechanism of the electric charge carriers which significantly increased with the increase in La concentration compared to pure Z-type hexaferrite. The diameter of the fitted Cole-Cole plots of complex impedance spectra suggested that the impedance of the La-substituted sample was less compared to pure Co_2Z ferrite.

$Ba_{3-x}Ca_xCo_2Fe_{24}O_{41}$ (x = 0.0, 0.1, 0.2, 0.4, 0.6) were synthesized by the solid-state reaction method. XRD profile showed that the Z-type phase coexist with W-type phase for all compositions. Hysteresis loops suggested that M_s increases due to the presence of W-type phase. The value of H_c decreased due to grain growth. The ε'' spectra showed abnormal behavior above 10^3 Hz frequency. The relaxation process of the electric charge carriers appeared to start at lower frequency. The intermediate potential barrier of the material was increased with Ca^{2+} substitution. The modulus spectra showed two relaxation peaks (in low & high frequency domain) implied that two types of charge carriers are present. Additionally complex electric modulus spectra distinguished the capacitive contribution of grain and grain boundary, which indicated that the moment of the charge carriers was reduced within the grain while along the grain boundary, it remained conserved.

$Ba_3Co_2Fe_{24-x}Al_xO_{41}$ (x = 0.0, 0.4, 0.6, 0.8, 1.0 & 1.8) were prepared by the solid-state method and effect of substitution was carried out on the magnetic and dielectric properties. XRD pattern showed single phase below x = 1.0. Hysteresis loops showed that the magnetization was reduced with Al substitution. The normalized behavior of impedance showed the relaxation frequency of the charge was slightly changed. The same activation energies of fitted relaxation time corresponding to imaginary impedance implied that the potential barrier along the grain boundary was unaffected by Al substitution. The fitted Arrhenius spectra of grain and grain boundary resistance implied that the Al substitution controls the migration of the charge carriers. The important values of all substituted samples are given in Table 5.4.

Table 5.4. The values of M_s, H_c, ε', ε'' & $\tan\delta_\varepsilon$.

Samples	**Content (x)**	**M_s (emu/g)**	**H_c (Oe)**	**At 1 MHz**		
				ε'	**ε''**	**$\tan\delta_\varepsilon$**
Co_2Z	0.0	45.3	31.3	231.4	101.73	0.0076
La-Z	0.2	46.6	62.8	1616.8	721.5	0.0077
Ca-Z		48.2	26.9	3554.6	1233.8	0.0060
Al	0.4	42.0	23.9	949.9	638.0	0.0117
	1.8	38.0	32.3	3069.5	1217.0	0.0069

Table 5.4 shows the magnetic and dielectric properties of cation-substituted Co_2Z ferrite. Substituted samples show a high dielectric constant without any observable change in the losses at 1 MHz frequency. It may be expected that substituted samples show better dielectric properties for antenna and multilayer chip inductors, operable above 1 GHz frequency.

Chapter 6

Results and Discussion (Sintering additives)

Overview

In this chapter, the results of synthesized Co_2Z hexaferrite with different sintering additives (SiO_2, MgO, Al_2O_3 & Bi_2O_3) are presented. The effect of sintering additives on structural, magnetic, and dielectric properties of Z-type ferrite is also discussed.

6.1. Effect of sintering additives

After the successful preparation of single phase Co_2Z powder, it was mixed with different sintering additives, which help to improve the sintering characteristics. The main purpose of the study is to investigate the effect of these additives on structural, dielectric and magnetic properties rather than sintering behavior. Four different additives, i.e. SiO_2, MgO, Al_2O_3 and Bi_2O_3 were chosen considering their different melting points. The weight percent for all additive were fixed to 1.0 wt. %, 2.0 wt. % and 3.0 wt. %; named SiO_2 (1.0 wt. %, 2.0 wt. % & 3.0 wt. %) as Si-1, Si-2 and Si-3. Similar convention was adopted for other additives. All the samples with additives were sintered at 1250 ℃. In the following section, the effect of sintering additives on structural, magnetic and dielectric properties of sintered Z-type ferrites are discussed.

6.1.1. Phase identification

Fig. 6.1 (a & b) shows the representative X-ray diffraction pattern of Co_2Z ferrite with various sintering additive for 1 and 3 weight percent, respectively. All diffraction peaks correspond to single phase Z-type ferrite. However, a small trace of M-type phase was present with SiO_2 additive at an angle 32.11°. No peak shift were observed with the additives. The lattice parameters (*a* & *c*) for all the samples were calculated by equation $\frac{1}{d^2} = \frac{4}{3}(\frac{h^2+hk+k^2}{a^2}) + \frac{l^2}{c^2}$, where, *d* is inter-planar spacing, and *h, k* and *l* are the miller indices of planes [227]. The calculated lattice parameters were constant for all additives which suggest that additive ions do not substitute at lattice site. The crystallite size of pulverized powders were calculated by the Debye–Scherrer equation [228] and found to be higher with the sintering additives. Table 6.1 shows the lattice parameters, crystallite size and sintered density of 3.0 wt. % additives.

Table 6.1 Lattice parameters, sintered density and crystallite size of Co_2Z ferrites.

Sample	*a* (Å)	*c* (Å)	Sintered density (g/cm^3)	Crystallite size (nm)
Co_2Z	5.86	52.13	4.7	57.9
SiO_2	5.87	52.12	4.8	91.4
MgO	5.87	52.13	4.8	106.5
Al_2O_3	5.87	52.15	4.8	81.0
Bi_2O_3	5.87	52.14	4.7	96.2

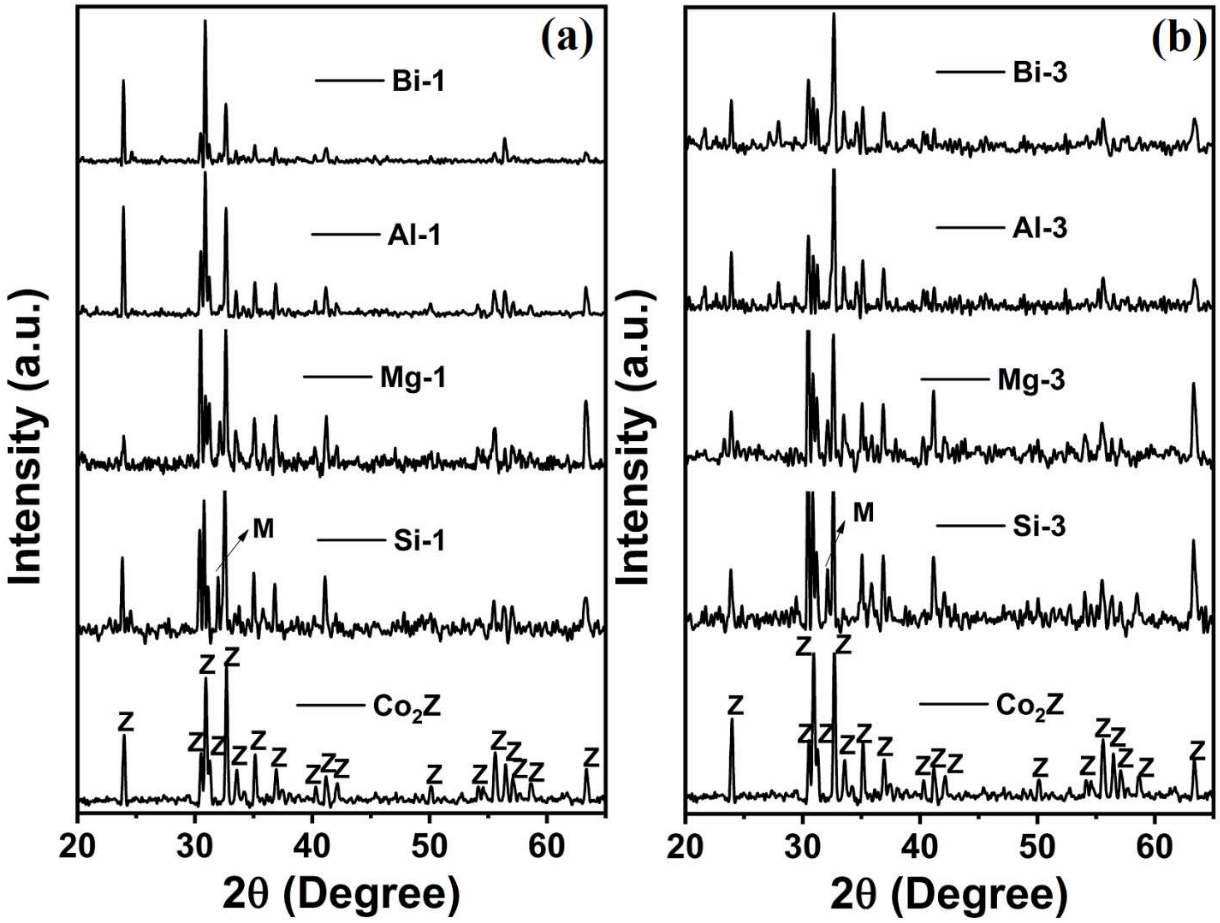

Fig. 6.1 X-ray diffraction pattern of Co_2Z ferrite with different SiO_2, MgO, Al_2O_3 & Bi_2O_3 additives (a) 1.0 wt. % & (b) 3.0 wt. %.

6.1.2. Microstructural studies

Fig. 6.2 (a-e) and Fig. 6.3 (a-d) shows the SEM micrographs of sintered samples with different additives (1.0 & 3.0 wt. %). The sintered density of ~ 4.8 g/cm^3, i.e., > 90.0 % of the theoretical density (5.35 g/cm^3), suggest that all samples were well sintered. No variation in sintered density with different additives indicates that the densification was primarily dominated by high sintering temperature. However, for low temperature sintering these additives play a significant role in densification as reported elsewhere [98]. The notable changes in micrographs showed the dominant role of additives in microstructural control. The randomly oriented platelets with limited porosity were observed for all the samples. Co_2Z ferrite sintered without additives shows small size elongated and hexagonal platelets. Whereas, SiO_2, Al_2O_3 and Bi_2O_3 promotes hexagonal platelet shaped structure of different size. The distinct microstructural features with MgO may ascribe to different kinetics of additive during sintering. It is quite possible that additives may diffuse inside the grain from grains boundaries or remains at boundaries during sintering. The largest hexagonal platelets were observed with Bi_2O_3 additive due to low melting point of Bi_2O_3 (817 °C). The liquid phase formation along grain boundaries promotes grain growth during sintering; contrary to the pinning action by high melting point additives.

The EDS spectrum of Co_2Z ferrites sintered with different additives are shown in Fig. 6.4 (a-e). The presence of Ba, Fe, Co and O in all Co_2Z ferrite along with peaks of Si, Mg, Al and Bi confirms the presence of respective additives.

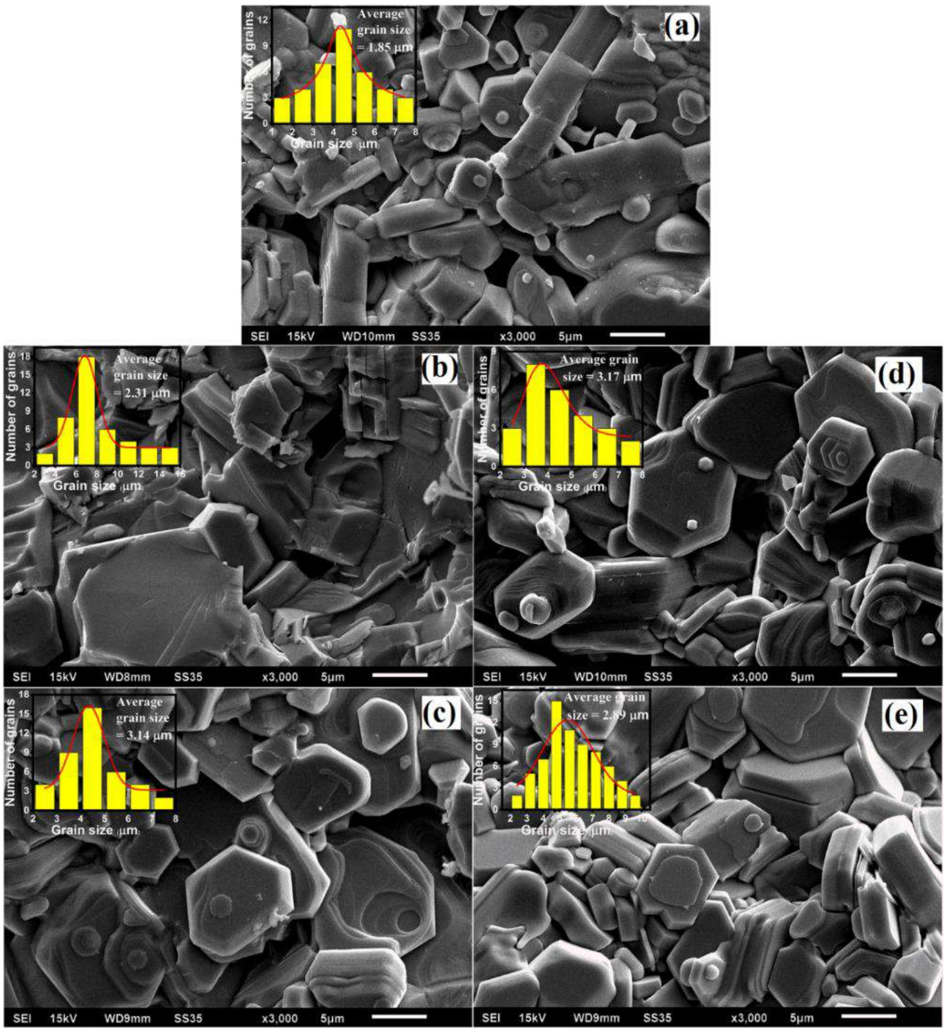

Fig. 6.2 SEM micrographs of fractured surface for sintered Co_2Z (a) pure, (b) SiO_2, (c) MgO, (d) Al_2O_3 & (e) Bi_2O_3 at 1.0 wt. % additives.

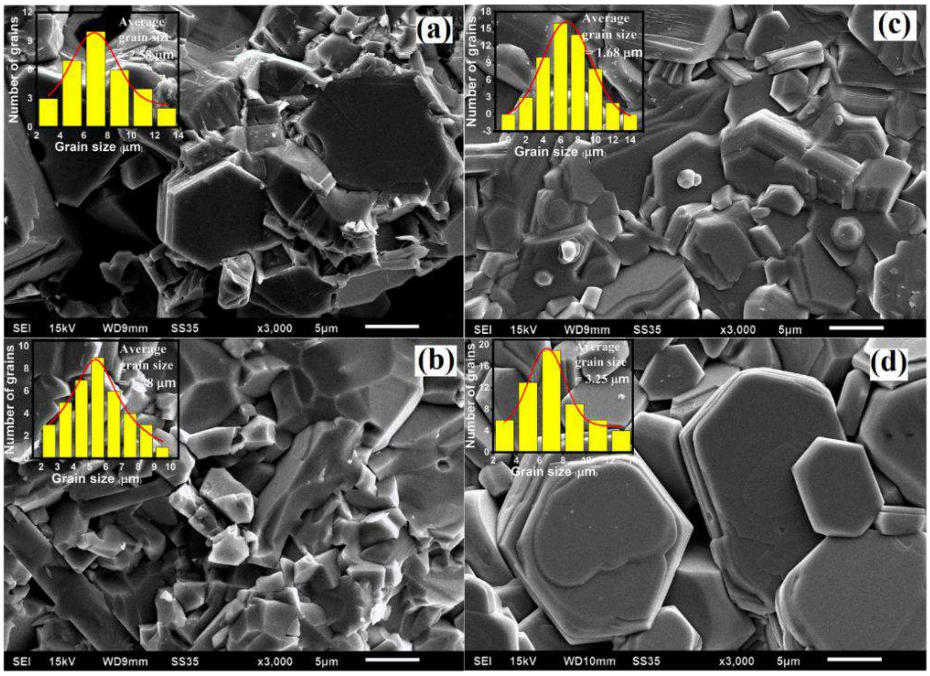

Fig. 6.3 SEM micrographs of fractured surface of Co_2Z (a) SiO_2, (b) MgO, (c) Al_2O_3 & (d) Bi_2O_3 at 3.0 wt. % additives.

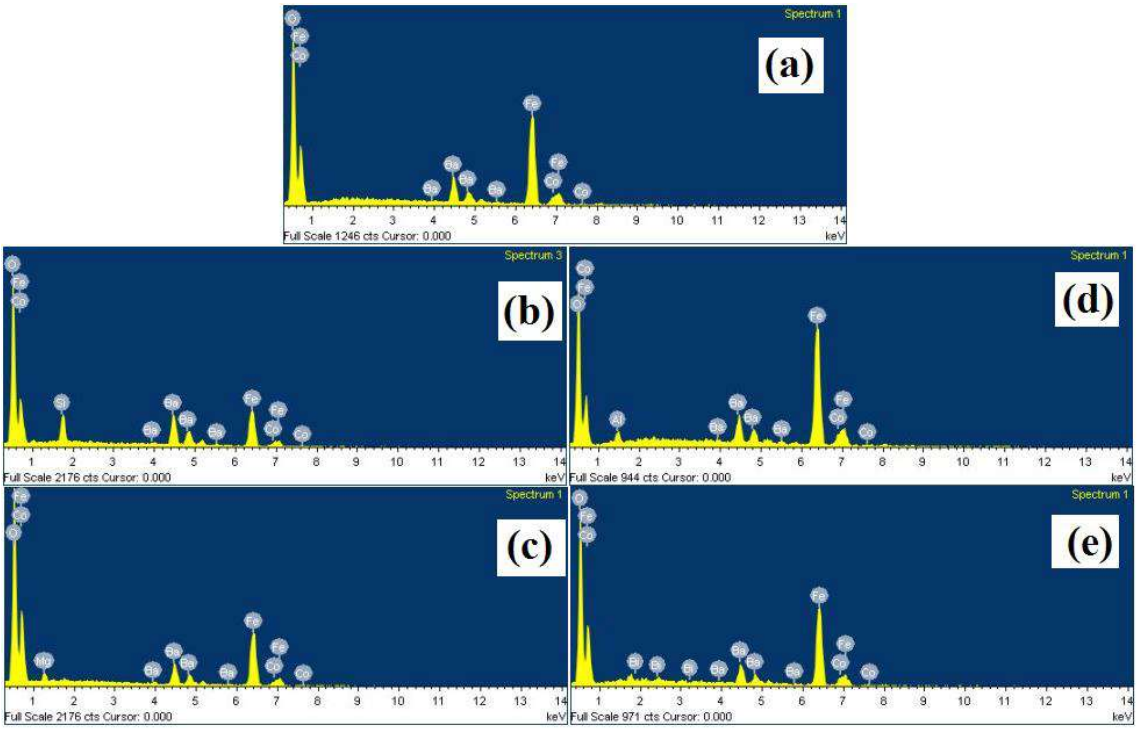

Fig. 6.4 EDS spectra of Co_2Z ferrite (a) pure, (b) SiO_2, (c) MgO, (d) Al_2O_3 & (e) Bi_2O_3 for 3.0 wt. % additives.

6.1.3. Magnetic properties

Fig. 6.5 (a & b) shows the representative *M-H* behaviour of Co_2Z samples with 1.0 wt. % and 3.0 wt. % additives. The variation in M_s and H_c is shown in Table 6.2. The M_s value lies between 36 - 56 emu/g. The M_s found to decrease for MgO, Al_2O_3 and Bi_2O_3 additives is due to their non-magnetic nature. The observed marginal difference in M_s with Al_2O_3 and Bi_2O_3 may be ascribed to better crystallinity in the ceramics as is evident from micrographs with large hexagonal platelets (Fig. 6.3 (c & d)). The M_s is decreased from 45.3 emu/g to 36.1 emu/g with MgO additive. The decrease in M_s may be a consequence of MgO diffusion within the grains during sintering and reduction in crystallinity. The formation of minor M-type phase in Co_2Z with SiO_2 additives leads to an enhancement in M_s (55.6 emu/g). The H_c is found to increase with all additives due to the pinning effect. The H_c depends on grain size, defect, porosity and grain morphology. The presence of minor hard magnetic M-type phase Co_2Z ferrite with SiO_2 leads to high H_c as compared to other additives. The relatively low H_c with Bi_2O_3 is attributed to exaggerated grain growth during sintering.

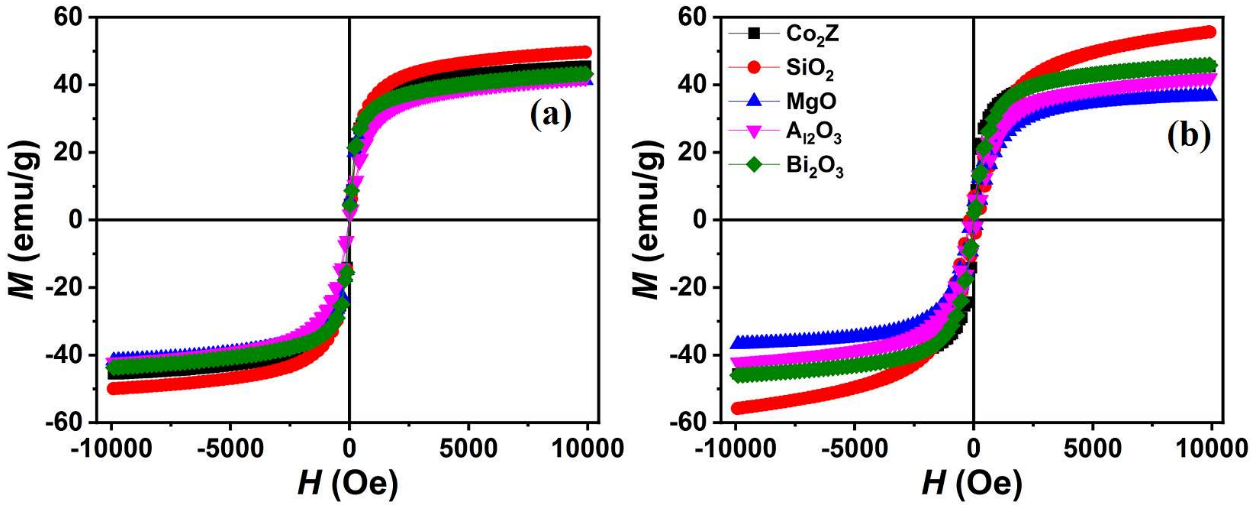

Fig. 6.5 (a & b) Magnetic hysteresis loops of Co_2Z ferrite with different sintering additives.

Table 6.2 Magnetic properties of Co_2Z ferrite with different addtives.

Wt. %	**M_s (emu/g)**				**H_c (Oe)**			
	SiO_2	MgO	Al_2O_3	Bi_2O_3	SiO_2	MgO	Al_2O_3	Bi_2O_3
0	45.3				79.2			
1	49.6	41.4	42.1	43.3	32.1	39.3	25.6	27.6
2	49.5	38.7	43.4	43.2	53.0	50.1	29.4	22.7
3	55.6	36.1	41.9	44.5	185.7	124.2	23.8	26.6

6.1.4. Relative permittivity measurements

Fig. 6.6 (a–d) shows *RT* frequency dependent ε', ε'' and respective tangential losses ($tan\delta_\varepsilon$) of Co_2Z ferrites with different additives. Both ε' & ε'' decreases with increasing frequency and becomes nearly constant for all samples. The higher value of ε' and ε'' at low frequency can be explained by Koop's model in which dielectric structure is consisted of conducting grains separated by resistive grain boundaries [229]. The surface charge polarization at the interface of grain and grain boundary is responsible for their high values. At high frequencies, surface charge polarization diminished, where only electronic and ionic polarization dominates. The decrease in ε' and ε'' at higher frequencies were ascribed to suppression of surface polarization [229]. It is well observed that Co_2Z with additives possess lower ε' and ε'' values in the measured frequency range. The variation can be explained on the basis of their platelet size and hindrance to charge motion by additives. A small platelet structure has higher surface area fraction, which give rise to surface polarization. It can be seen that large platelet of Co_2Z with Bi_2O_3 additive possess minimum ε' throughout the frequency range. All additives are primarily insulating in nature and remains at grain boundary, which makes them more resistive and decreases the conduction loss.

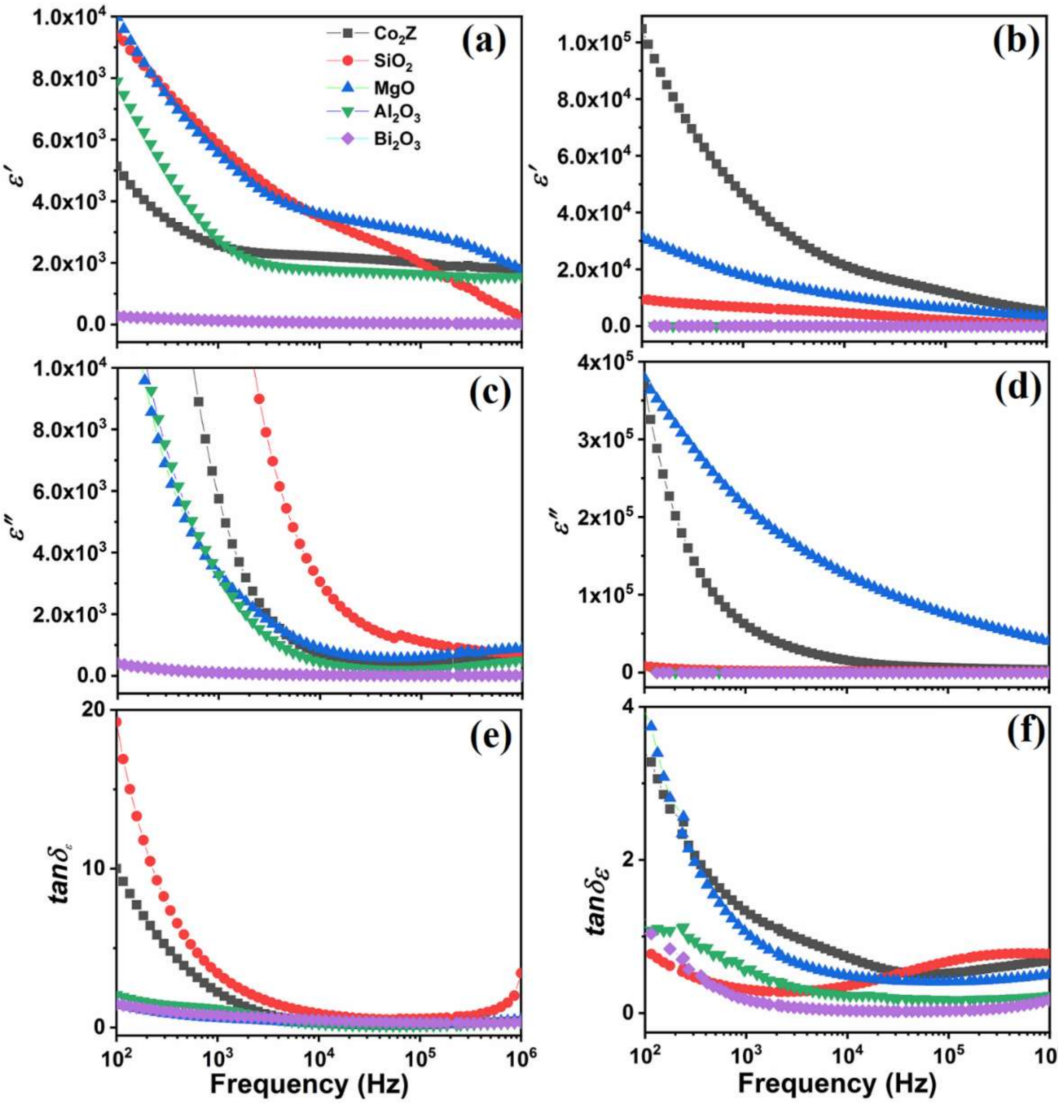

Fig. 6.6 Variation of (a & b) ε', (c & d) ε'' and (e & f) tangent loss ($tan\delta_\varepsilon$) for 1.0 wt. % and 3.0 wt. % additives.

Fig. 6.6 (b) shows ε'' have lower values with 3.0 wt. % of additives compared to the 1.0 wt. % [230]. The magnitude of ε'' is increased in MgO sample because Mg^{2+} can diffuse in the grain and originated Fe^{2+} ions. The Co_2Z with Bi_2O_3 have minimum losses (Fig. 6.6 (c)) attributed to liquid phase sintering where of liquid phase of Bi_2O_3 encapsulates around Co_2Z grains and provide more hindrance for grain to grain conduction.

From the above studies for all additives, it has been observed that SiO_2 and Bi_2O_3 have more pronounced effect and shows smaller grain size. Moreover, these additives are supposed to present along grain boundaries, therefore to understand the contribution of additives and grain boundaries for charge conduction, the temperature dependent impedance studies are carried out for these two additives at 1 weight percent. Pure, SiO_2 & Bi_2O_3 samples are denoted by Co_2Z-P, Co_2Z-Si and Co_2Z-Bi, respectively.

6.1.5. Complex impedance analysis

The complex electric impedance is given by formula $Z^* = Z' + j\,Z'' = -j\omega C_0\varepsilon^*$, where ω (= $2\pi f$) is the angular frequency, C_0 is the capacitance of vacuum. The real and imaginary part of impedance can be represented in the terms of ε' and ε'' as $Z' = \frac{1}{2\pi f C_0}\left[\frac{\varepsilon''}{\varepsilon'^2+\varepsilon''^2}\right]$ & $Z'' = \frac{1}{2\pi f C_0}\left[\frac{\varepsilon'}{\varepsilon'^2+\varepsilon''^2}\right]$. Fig. 6.7 (a-c) shows the variation of Z' as a function of frequency at different temperatures for Co_2Z-P, Co_2Z-Si and Co_2Z-Bi, respectively. Generally, Z' represents the resistive strength of the material. The amplitude of Z' decreases with increasing frequency and temperature, which denotes the negative temperature coefficient of semiconductor, the conductivity increases with increasing temperature. At low frequency range, dielectric behavior dominates due to activation of various polarization mechanism (space charge, orientational, ionic and electronic polarization), whereas at higher frequency inactive ions and dipolar polarizability accelerate the *ac* conduction [231]. With increase in temperature Z' decreases as thermally activated ions contribute to conduction mechanism. The constant Z' (parallel to frequency axis) represents that charge carriers are frequency independent and defined as *dc* conduction of the material. All samples show low frequency dispersion at room temperature, however, with increase in temperature steady plateau region increases. Finally, the merging of the curves occurs at frequency ~ 10^5 Hz irrespective of temperature, which suggests the release of space charge through grain boundaries [231-234]. The effect of Bi_2O_3 on Z' is more pronounced compared to SiO_2 additive. Bi_2O_3 form liquid phase at relatively lower temperature which encapsulates the larger surface areas of grains and provides additional resistance to charge motion.

Fig. 6.7 (d-f) shows Z'' plot with applied frequency at different temperatures for Co_2Z-P, Co_2Z-Si and Co_2Z-Bi, respectively. It is to be noted that Z'' increases with frequency and attain its maximum (Z''_{max}) due to relaxation mechanism and then decreases gradually for all samples. Higher broadening in Co_2Z-Bi suggests that charge relaxations are taking place over wider frequency range compared to Co_2Z-P and Co_2Z-Si. Therefore, frequency and temperature dependent loss profile (Z'') strongly depends upon type of sintering additive.

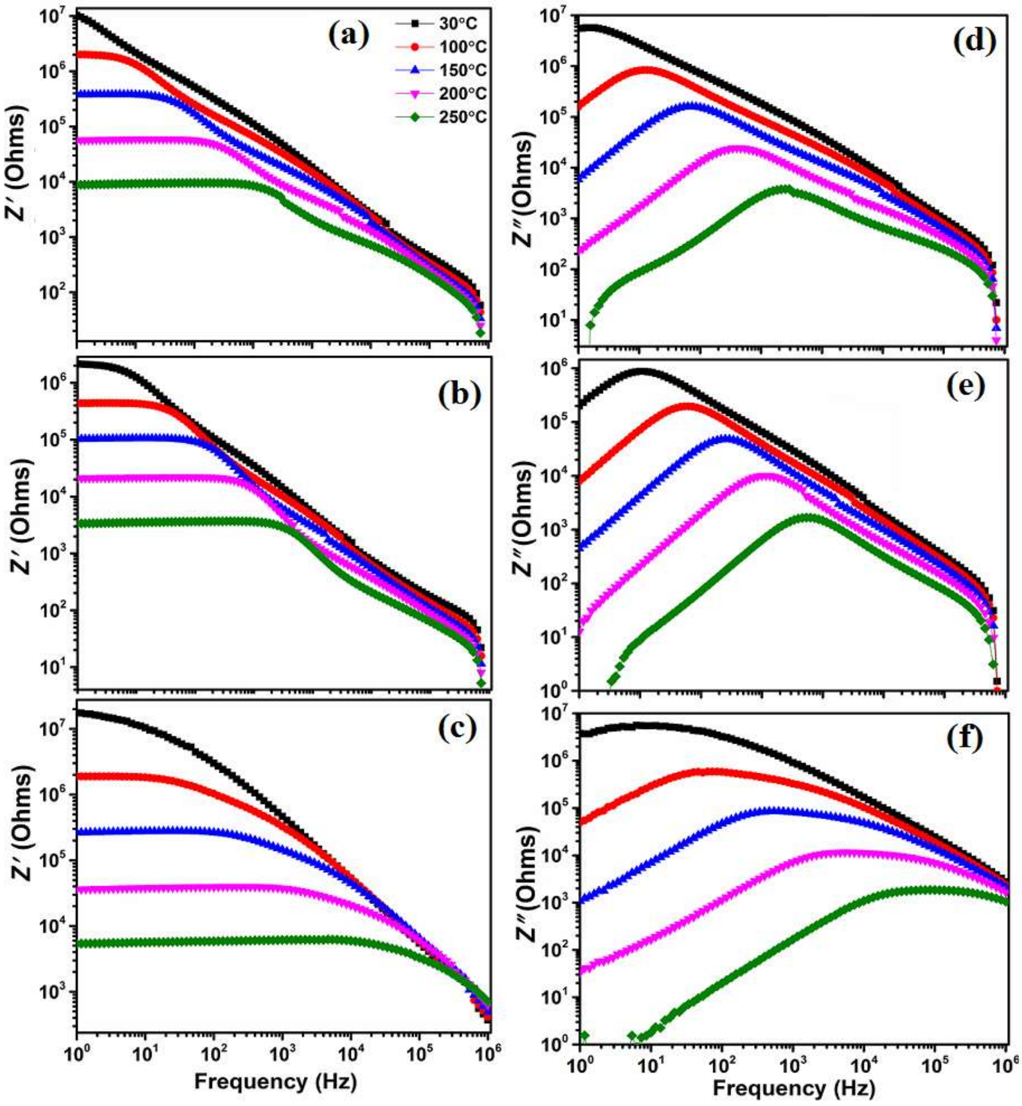

Fig. 6.7 (a-c) Variation of Z' and (d-f) Z'' as function of frequency at different temperatures for Co_2Z-P, Co_2Z-Si, and Co_2Z-Bi, respectively.

Fig. 6.8 (a-c) shows the normalized plots of Z'' with increasing frequency at different temperatures. A systematic peak (relaxation frequency) shift towards higher frequency with temperature indicates that relaxations are temperature dependent. Observation of relaxation at higher frequency for Co_2Z-Si and Co_2Z-Bi compared to Co_2Z-P confirms the presence of additive at grain boundaries. Fig. 6.8 (d) shows τ of grain boundary as a function of $1/T$, evaluated using formula, $\tau = 1/(2\pi f_{max})$, where f_{max} represents the peak frequency. τ decreases with increasing temperature, where the dissipated thermal energy helps to form dipoles which follow the *ac* field [176]. It can be seen that Arrhenius plot has two slopes in different temperature regime, named as E_{g1} (high temperature) and E_{g2} (low temperature). Two different E_g suggests that charge transport is taking place by different conduction mechanisms. The conduction is taking place by two type of charge carrier, first the space charge due to oxygen vacancies and second is electron/hole hopping between Fe^{2+}- Fe^{3+} & Co^{3+}- Co^{2+} ions [177-179].

The full width at half maxima of impedance loss spectra greater than 1.144 decades implies the deviation from ideal Debye type relaxation. This deviation is originated from the diffusion of charge carriers and non-uniformity of the microstructure which leads to spatial distribution of conductivities and electrical response time [180-182]. In low temperature regime, E_{g2} is comparable for all samples, however, E_{g1} values are different and maximum value is found for Co_2Z-Bi sample. At low temperature, the oxygen vacancies are responsible for conduction. Since all samples sintered at high temperature contains oxygen vacancies, therefore the activation energies are comparable. The higher value of activation energy for Co_2Z-Bi sample is due to low melting point of Bi_2O_3. During sintering, Bi_2O_3 liquidify and percolates the larger area of ferrite grain which provide a higher potential barrier for conduction by electron/hole hopping.

To understand physical nature of dielectric relaxation and the conduction mechanism of the thermally induced dipoles, scaling behavior i.e. (Z''/Z''_{max}) *vs.* $\log(\omega/\omega_{max})$ were plotted and shown in Fig. 6.9 (a-c). If all curves overlap into a single master curve, the distribution of relaxation is temperature independent. However, in the present study loops obtained at 30 °C and 100 °C were mismatched irrespective of additives whereas, loop obtained above 100 °C were seen nearly overlapped. The poly-dispersive nature of the relaxation curve justifies that the dynamic process of charge carriers are activated at different time scales and confirm the possibility of more than one activation energies as is evident from Fig. 6.8 (d). Hence, distribution of relaxation time is temperature dependent [235]. Further, deduced *FWHM* for all peaks are more than 1.144 decades, which illustrates deviated Debye type relaxation due to microscopic inhomogeneities due to additive.

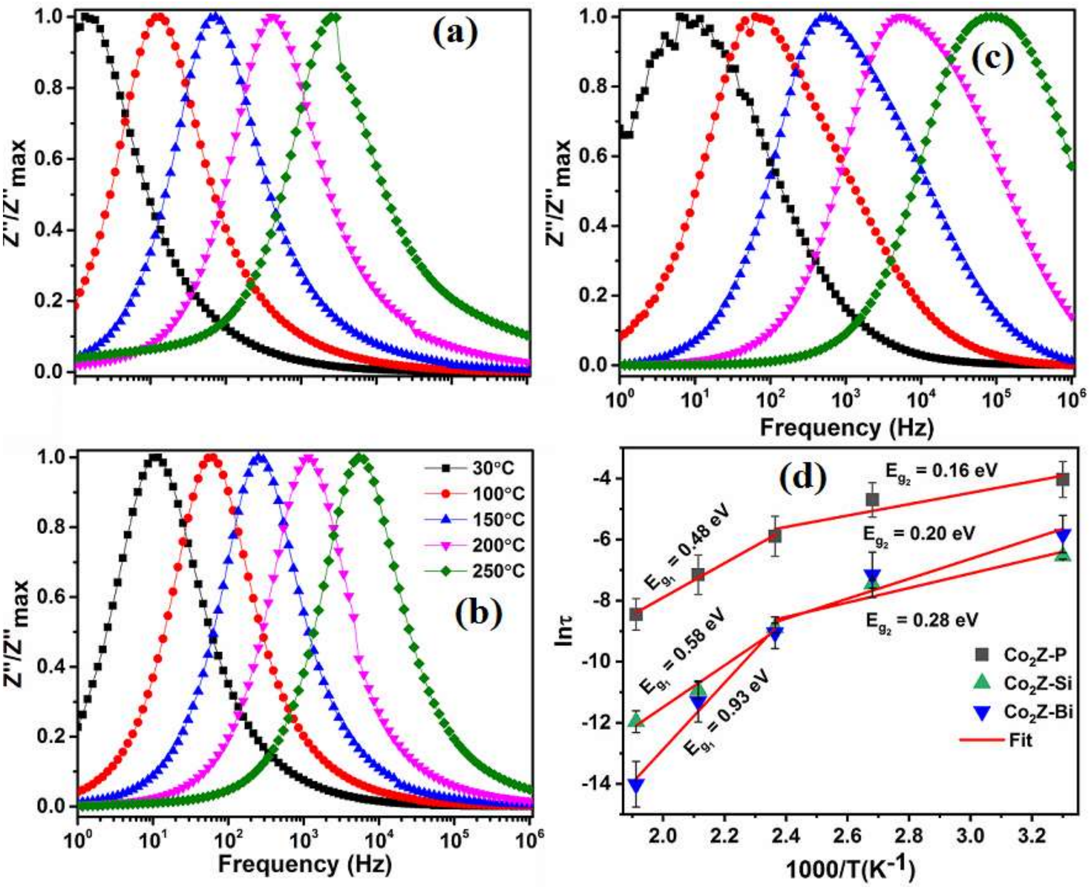

Fig. 6.8 Normalized imaginary impedance spectra (a) Co_2Z-P, (b) Co_2Z-Si, (c) Co_2Z-Bi and (d) variation of relaxation time with error bar as function of *1000/T* (K^{-1}).

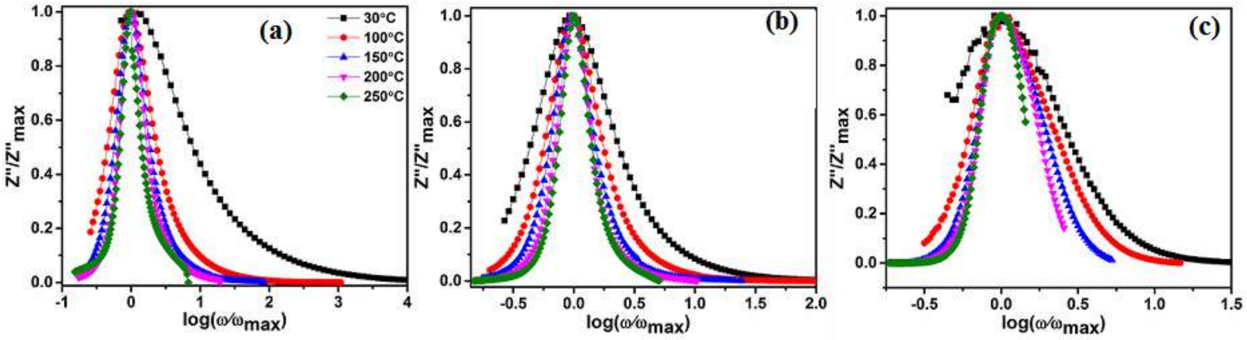

Fig. 6.9 Scaling behavior of imaginary impedance spectra (a) Co_2Z-P (b) Co_2Z-Si and (c) Co_2Z- Bi.

Table 6.3 Fitted EIS spectra parameters C_g, C_{gb}, $(CPE)_{gb}$ for Co_2Z-P, Co_2Z-Si & Co_2Z-Bi.

Temperature	**Co_2Z-P**			**Co_2Z-Si**			**Co_2Z-Bi**		
(°C)	C_g (nF)	C_{gb} (nF)	$(CPE)_{gb}$ ($\times 10^{-8}$)	C_g (nF)	C_{gb} (nF)	$(CPE)_{gb}$ ($\times 10^{-9}$)	C_g (nF)	C_{gb} (nF)	$(CPE)_{gb}$ ($\times 10^{-9}$)
30	1.99	6.02	9.60	9.76	2.41	9.51	0.32	0.14	0.15
100	1.94	6.14	0.23	24.84	1.96	8.13	0.73	0.12	5.52
150	9.21	8.94	0.12	14.46	1.59	6.18	0.44	6.08	0.40
200	8.07	0.91	0.29	1.31	3.34	5.63	11.83	0.73	9.21
250	8.88	0.37	4.08	1.81	5.44	4.48	83.69	0.07	0.63

To understand the correlation between microstructure and electric properties, Cole-Cole plots of complex impedance (Z'' *vs* Z') at different temperatures are given in Fig. 6.10 (a-c). Basically log-log scale of complex impedance is used to justify the several types of diffusion and conduction characteristics including ionic conduction (obtained in linear-linear scale) of the specimen [236]. All plots were fitted by (Electrochemical Impedance Spectroscopy) EIS spectrum analyzer software with error less than 5.0 %. The arcs appear from right to left having different diameters indicates the multiple relaxation processes occurring in this material. Fig. 6.10 (d) shows electrical equivalent circuit consisted of resistances (R_g, R_{gb}) and capacitances (C_g, C_{gb}) of grain and grain boundaries. The fitted parameters of EIS spectra such as C_g, C_{gb} and *CPE* (pre-exponential factor) are mentioned in Table 6.3 for Co_2Z-P, Co_2Z-Si and Co_2Z-Bi, respectively.

The microstructure predominantly consisted of grain and grain boundaries, and can be well observed by complex impedance plane plots (Z'' *vs* Z') which consisted of two semi circles (not shown) [237]. The first represented grain pattern and second one is due to the grain boundary [237]. Generally, the semicircular arc pattern is given by the parallel *RC* electric circuit for both patterns. The *CPE* is connected with *RC* circuit to define the inhomogeneity of the microstructure (grain boundary). Logically two *RC* circuits for grain and grain boundary are connected in series similar to microstructure where grain and grain boundary are naturally connected in series. This is a standard circuit as described in Maxwell-Wagner model. The complex impedance of specimen [187] can be described in the function of R_g, R_{gb} and C_g & C_{gb} as:

$$Z' = \frac{R_g}{1+(\omega R_g C_g)^2} + \frac{R_{gb}}{1+(\omega R_{gb} C_{gb})^2} \; \& \; Z'' = R_g\left[\frac{\omega R_g C_g}{1+(\omega R_g C_g)^2}\right] + R_{gb}\left[\frac{\omega R_{gb} C_{gb}}{1+(\omega R_{gb} C_{gb})^2}\right]$$

The *CPE* (constant phase element) indicates a departure from ideal Debye relaxation [238]. Mathematically, *CPE* is described as $Y = 1/Z = \beta(j\omega)^{\alpha}$, where β is the proportionality constant of admittance $|Z|^{-1}$ and α denotes phase shift, ($\alpha = 0$ for ideal resistor, and $\alpha = 1$ for ideal capacitor) [177]. For samples containing additive, the equivalent circuit is fitted with an additional resistance (R_{ext}) in series to *CPE* due to presence of additives along grain boundaries (Fig. 6.10 (e)). All Nyquist plots were fitted with equivalent circuits, the representative fit is also shown in Fig. 6.10 (f) along with chi square value. The *CPE* is mainly used in electric circuit due to the inhomogeneous dielectric structure of the ferrite. Additives are insulating in nature and showed highest resistance for charge conduction. Therefore, the presence of additive along the grain boundary provided more resistive path. The irregularity of the grain boundary is denoted by *CPE* directly associated with the additive layer (equivalent R_{ext} -*CPE* circuit). This assumption and the fitting suggested the additive resistance is in series with *CPE* element. The normal impedance of *CPE* is given as $Z_{CPE}(\omega) = \frac{1}{\beta(j\omega)^{\alpha}}$ which characterized the phase shift. By applying Euler equation $(e^{j\theta} = \cos\theta + j\sin\theta)$, total impedance of *CPE* including additive along the grain boundaries is described by the formula: $Z(\omega) = R_{ext} + \beta^{-1}(j\omega)^{-\alpha} = R_{ext} + \beta^{-1}\omega^{-\alpha}\left[\cos(-\frac{\pi}{2}\alpha) + j\sin(-\frac{\pi}{2}\alpha)\right]$ [239, 240].

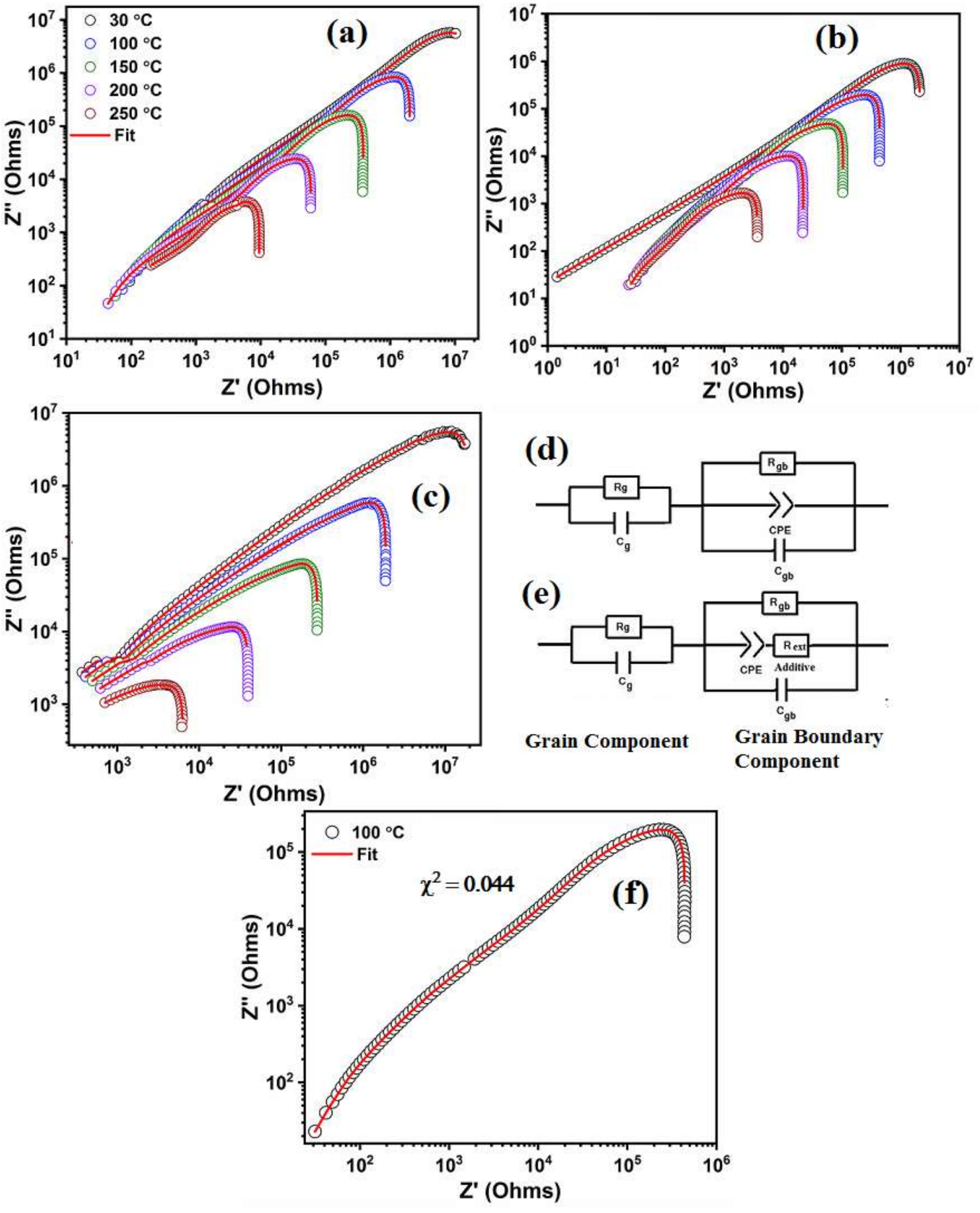

Fig. 6.10 Cole-Cole of complex impedance spectra (a) Co_2Z-P, (b) Co_2Z-Si, (c) Co_2Z-Bi, (d-e) corresponding equivalent circuit and (f) in large view of fitted Cole-Cole plot for Co_2Z-Si marked with χ^2 value at 100 ℃ .

With additives, Maxwell-Wagner inhomogeneous dielectric structure i.e. grain (conductive), grain boundary (insulating) can be modified with an additional additive at boundaries. Fig. 6.11 (a-c) shows variation of R_g, R_{gb}, and R_{ext} with temperature for Co_2Z-P, Co_2Z-Si and Co_2Z-Bi samples which represents semiconducting behavior [249]. It is noted that $R_{gb} > R_g$ mainly due to accumulation of space charge along the grain boundaries [100]. Two distinct activation energies i.e. E_{g1} and E_{g2} obtained from Arrhenius plots are in comparison with energies calculated from relaxation frequencies suggested the adequacy of fitted circuits.

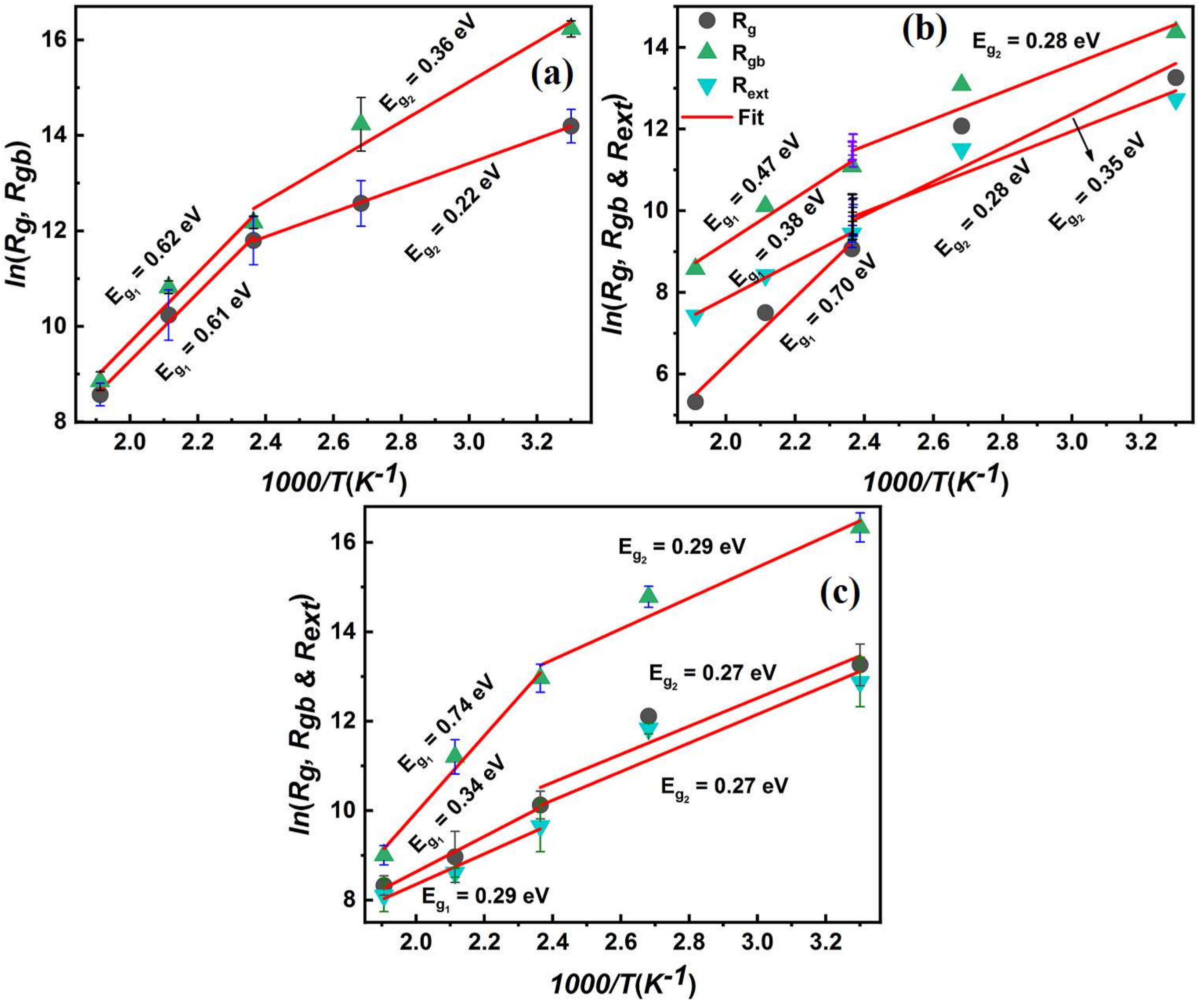

Fig. 6.11 Arrhenius plots of *dc* resistances with error bar analysis for grain, grain boundary and additive layer (a) Co_2Z-P, (b). Co_2Z-Si and (c) Co_2Z-Bi.

6.1.6. Electrical conductivity

The real part of *ac* conductivity (σ') with temperature demonstrates the correlation between relaxation and conduction process of the material and can be obtained by the relation $\sigma'(\omega) = \varepsilon_0\varepsilon''\omega$, where σ' is *ac* conductivity and ω angular frequency of the applied field [249, 100]. Fig. 6.12 (a-c) shows frequency dependent σ' for Co_2Z-P, Co_2Z-Si and Co_2Z-Bi at different temperatures. Initially, σ' is frequency independent and remains constant; above a certain frequency it increases and become frequency dependent. At low frequency regime, the flat plateau represents *dc* conductivity (σ_0), which is associated with relaxation of grain conduction. At higher frequency the dispersion behavior is related to grain boundary relaxation [250]. The increase in σ' with temperature is due to hopping of thermally activated charges.

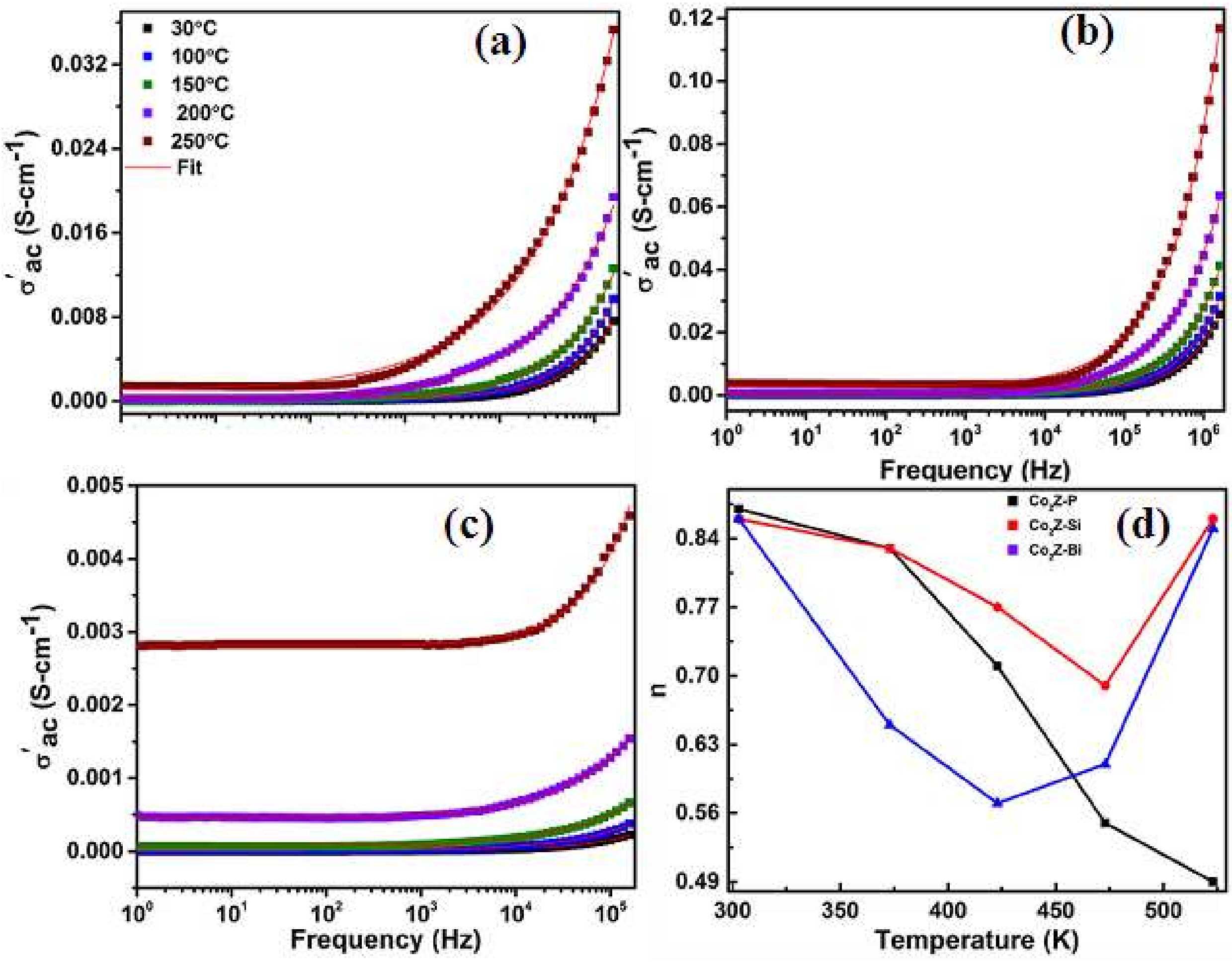

Fig. 6.12 *ac* conductivity at different temperatures (a) Co_2Z-P, (b) Co_2Z-Si, (c) Co_2Z-Bi & (d) variation of n with temperature.

The frequency dispersion σ' can be described by the Jonscher universal power law [249], $\sigma' = \sigma_0 + A\omega^n$, where σ_0 is *dc* conductivity, $A\omega^n$ is called dispersion phenomena, constant A determines strength of polarizability and n is the dimensionless frequency exponent. The value of n decides the strength of the conduction and the interaction of mobile charge carriers. For all samples the value of n is less than 1, suggesting that conduction is taking place by short range hopping. For Co_2Z-P, n decreases with increasing temperature and follows the correlated barrier hopping (CBT) model [251-254]. On the other hand, the value of n first decreases reaches to its minimum and then increases which is in accordance with the overall polaron tunneling (OLPT) model [213, 251, 252]. A decrease in n with temperature corresponds to hopping of large polaron and an increase is due to small polaron hopping split from large polarons [255].

Sub-conclusion

The influence of different sintering additives such as SiO_2, MgO, Al_2O_3, and Bi_2O_3 (with 1.0, 2.0 & 3.0 wt. %) was investigated on the structural, magnetic, and dielectric properties of Co_2Z hexaferrite. X-ray patterns confirmed that the Z-type phase coexisted with a minor M-type for SiO_2 additive. The M_s was decreased for nonmagnetic additives and was maximum with the M-type phase for SiO_2. The dielectric study indicated that the $tan\delta_\varepsilon$ decreased significantly with the various additives. Impedance spectroscopy analysis confirmed that the relaxation, conduction, and mobility of the electric charge carriers were effectively shifted towards lower frequencies compared to the pure Z-type hexaferrite. The sintering additives showed an additional electric resistance along the grain boundary as obtained from complex impedance data fitting with the equivalent electrical circuit. The magnitude of impedance was higher for Bi_2O_3 compared to SiO_2 due to the grain encapsulation effect. The scaling behavior demonstrates that the distribution of the relaxation was temperature dependent. Two activation energies corresponding to grain and grain boundary suggested that the multiple charge carriers were associated with the conduction process. The summarized magnetic and dielectric properties of 3.0 wt. % sintering additives are given in Table 6.4.

Table 6.4 The value of M_s, H_c, ε', ε'' & $tan\delta_\varepsilon$ for additives series.

3.0 wt. %	**M_s (emu/g)**	**H_c (Oe)**	**At 1 MHz**		
			ε'	**ε''**	**$tan\delta_\varepsilon$**
Co_2Z	45.3	79.2	231.4	101.7	0.0076
SiO_2	55.6	185.7	693.6	584.6	0.0147
MgO	36.1	124.2	2998.2	1811.4	0.0105
Al_2O_3	41.9	23.8	37.6	7.7	0.0036
Bi_2O_3	44.5	26.6	37.5	5.1	0.0023

Table 6.4 shows the magnetic and dielectric properties of Co_2Z ferrite synthesized with 3.0 wt. % of different sintering additives. The sintering additives showed wide variation in magnetic and dielectric properties. The low dielectric constant observed for Bi_2O_3 and Al_2O_3 at 1 MHz suggests a further decrease at a frequency above 1 GHz, which may show permittivity comparable to permeability.

Chapter 7

Conclusion

Overview

In this chapter important experimental results obtained from the studies are summarized. First, the effect of various processing conditions (temperature & time) on magnetic and dielectric properties of Co_2Z is given followed by effect of additives (SiO_2, MgO, Al_2O_3 & Bi_2O_3) and ion substitution (La^{2+} & Ca^{3+} for Ba^{2+} and Al^{3+} for Fe^{3+}) is summarized. The comparative study, magnetic properties and dielectric properties are tabulated at in the end. Last but not the least, the future scope in Z-type ferrite is suggested.

In the present work, Co_2Z hexaferrite was synthesized by solid state method and their magnetic and dielectric properties with additives and various substitutions were investigated. Firstly, the effect of synthesis condition by varying different processing parameters namely calcination temperature and sintering temperature were studied. Secondly the influence of the different ions substitution (La^{3+}, Ca^{2+} for Ba^{2+} & Al^{3+} for Fe^{3+}) and sintering additives (SiO_2, MgO, Al_2O_3 & Bi_2O_3) were carried out.

The processing of single phase Z-type hexaferrite is very critical and inadequate calcination temperature and time causes the formation of secondary phases. Further, sintering of single Z-type phase at higher temperature also causes the formation of secondary phase, whereas a low sintering temperature affect sintered density. We have prepared successfully the single phase Z-type ferrite by calcining and recalcining at 1150 °C for 6 hours each. We also find that sintering at 1250 °C is sufficient to achieve a high sintered density without the formation secondary phases.

The cation substitution studies significantly affect the structural, magnetic and dielectric properties. It was found that phase purity depends upon the substitution amount. Z-type phase is more sensitive for Ba^{2+} ion substitution, as La greater than $x = 0.2$ causes improve W-type phase, whereas with Ca^{2+} substitution, it was impossible to achieve pure Z-type phase. A minor amount of W-type phase were always present. Al^{3+} substitution for Fe^{3+} site provides more compositional flexibility and able to achieve single Z-type phase up to $x = 0.8$. La^{3+} and Ca^{2+} both have diverse effect on microstructure. Substitution La^{3+} causes a slight decrease in grain size followed by an increase, whereas very large grain size were observed for Ca^{2+} substitution irrespective to substitution amount. Al^{3+} substitution also changes the grain morphology. At higher concentration hexagonal shape grain is converted to elongated rod like structure. The La^{3+} & Ca^{2+} substitution do not affect the saturation magnetization unless the formation of W-type phase which enhances saturation magnetization whereas in Al^{3+} substitution saturation magnetization is decreased. The dielectric losses are relatively increased with La^{3+} & Al^{3+} substitution. Ca^{2+} substituted sample shows lower relaxation frequency compared to La^{3+} substitution. Distribution of the relaxation was found to be narrow for Al^{3+} substituted samples. The impedance spectroscopy showed the higher electric resistance of grain and grain boundaries. The charge storage capacitance increased with Ca^{2+} substitution relative to La^{3+} & Al^{3+} substitution.

The sintering additives influenced the microstructural, magnetic and dielectric properties of the Co_2Z ferrite. The single Z-type phase were obtained with different additives except SiO_2 which causes the formation of a minor M-type phase. Up to 1.0 wt. % of additive amount does not affect the microstructure, however at 3.0 wt. %, the grain size decreased for Al_2O_3, and MgO, whereas Bi_2O_3 and SiO_2 showed larger grains. The magnetic properties with additive remained same however sample with SiO_2 showed higher magnetization as M-type phase is formed. The dielectric constant increased and losses decreased with additives amount. The relaxation frequency and the impedance of the charge carriers is observed to be higher for Bi_2O_3 sample compared to SiO_2. The dielectric relaxation process is temperature independent. The simulated impedance data for 1.0 wt. % of Bi_2O_3 and SiO_2 showed that the additive resistance is higher for Bi_2O_3 compared to SiO_2.

With the above studies, it can be concluded that substitution and additive affects the microstructure, magnetic and dielectric properties. The charge transfer mechanism, their relaxation frequency, activation energy varies depending on the type of the substitution and additive. The focus of the present work was for impedance studies only up to 1 MHz frequency. Therefore, within this frequency range, there applicability for antenna substrate cannot be predicted, which requires a studies in the frequency range of 400 MHz to 3 GHz.

Future Scope

Recently, the magneto-electric (*ME*) is observed in Z-type ferrite particularly in $Sr_3Co_2Fe_{24}O_{41}$. The effect has been reported at room temperature, which are relatively small (1-1.5 mV/cm Oe). This *ME* effect arises due to the coupling between polarization vector and magnetic spins and such materials are called multiferroics. Nowadays, these are widely used in sensors, actuators, and memory devices. The room temperature single phase multiferroics are limited or more strictly only one i.e. $BiFeO_3$ that also has very weak *ME*-coupling. Therefore, further magneto-electric investigation on substituted Z-type ferrite would be of interest. As reported in present work substitution affect the magnetic structure and polarization as well.

Also this ferrite possess temperature dependent three different kinds of magnetic anisotropies, i.e. direction of magnetic vector varies with temperature. Therefore, below 220 K, magnetization vector makes an angle with *c*-axis, at *RT* lies along the basal plane and above 480 K aligned along *c*-axis (Refer Fig. 1.2 for crystal structure). These three different direction of magnetic vectors may show different *ME* coupling. Therefore, the investigation on *ME* effect in Z-type ferrite could be the future scope of investigation.

References

1. V.G. Harris, Modern microwave ferrites, IEEE Trans. Magn. **48**, 1075–1104 (2012).
2. M. Pardavi-Horvath, Microwave applications of soft ferrites, J. Magn. Magn. Mater. **215**, 171–183 (2000).
3. V. Sunny, P. Kurian, P. Mohanan, P.A. Joy, M.R. Anantharaman, A flexible microwave absorber based on nickel ferrite nanocomposite, J. Alloys Compd. **489**, 297–303 (2010).
4. V.P. Singh, R. Jasrotia, R. Kumar, P. Raizada, S. Thakur, K.M. Batoo, M. Singh, A Current Review on the Synthesis and Magnetic Properties of M-Type Hexaferrites Material, World J. Condens. Matter Phys. **08**, 36–61 (2018).
5. Y. Kitagawa, Y. Hiraoka, T. Honda, T. Ishikura, H. Nakamura, T. Kimura, Low-field magnetoelectric effect at room temperature, Nat. Mater. **9**, 797–802 (2010).
6. H. Kojima, Chapter 5, Fundamental properties of hexagonal ferrites with magnetoplumbite structure, Handbook of Ferromagnetic materials **3**, 305–391 (1982).
7. R.C. Pullar, Hexagonal ferrites: A review of the synthesis, properties and applications of hexaferrite ceramics, Prog. Mater. Sci. **57**, 1191–1334 (2012).
8. K. Singha, R. Jasrotia, V.P. Singh, M. Chandel, R. Kumar, S. Kalia, A study of magnetic properties of Y–Ni–Mn substituted Co_2Z-type nanohexaferrites via vibrating sample magnetometry, J. Sol-Gel Sci. Technol. **97**, 373–381 (2021).
9. S. Mahadevan and P. Sharma, Charge transport mechanism in $BaFe_{12}O_{19}$ and $BaFe_{11}CoO_{19}$, J. Magn. Magn. Mater. **514**, 167174 (2020).
10. Y. Liu, Q. Liu, C. Wu, Y. Wang, J. Li, L. Gao, H. Zhang, Investigation on Zn-Sn co-substituted M-type hexaferrite for microwave applications, J. Magn. Magn. Mater. **444**, 421–425 (2017).
11. J. Chen, Y. Wang, Y. Liu, H. Wang, Q. Yin, Q. Liu, C. Wu, Y. Chen, Investigation of oriented Co^{3+} doped M-type hexaferrite $Sr_{0.5}Ba_{0.5}Fe_{12-x}Co_xO_{19}$ for microwave application, J. Mater. Sci. Mater. Electron. **29**, 14371–14377 (2018).
12. J. Smit and H.P.J. Wijn, Ferrites, Philips Technical Library, Eindhoven, 150 (1959).
13. B. Ahmad, M.N. Ashiq, S. Mumtaz, I. Ali, M. Najam-Ul-Haq, I. Sadiq, Synthesis and electrical behavior of Ni-Ti substituted Y-type hexaferrites for high frequency application, J. Magn. Magn. Mater. **451**, 787–792 (2018).
14. J. Lee, Y.K. Hong, W. Lee, G.S. Abo, J. Park, W.M. Seong, S. Bae, Role of small permeability in gigahertz ferrite antenna performance, IEEE Magn. Lett. **4**, 3–6 (2013).
15. I. Coondoo, Ferroelectrics, InTech, Crotia (2010).

16. J.R. Macdonald, Impedance Spectroscopy, Ann. Biomed. Eng. 20, 289-305 (1992).
17. O. Heaviside, Electromagnetic Theory, 3rd Edition Chelsea Publishing Company New York (N.Y.) (2003).
18. A.E. Kennelly, Vector Power in alternating current circuits, Proceeding of the American Institute of Electrical Engineers **29**, 1023-1057 (1910).
19. C.P. Steinmetz and E.J. Berg, Theory and Calculation of Alternating Current Phenomena, Electrical World & Engineering, New York, 4 (1916).
20. L. Solymar and D. Walsh, Electrical properties of materials, 8th Edition, Oxford University press (2010).
21. A.K. Jonscher in Phys. Thin Films, Edited by M.H. Francombe, Acadmic Press London & New York, 11, (1980).
22. B.M. Greenhoe, M.K. Hassan, J.S. Wiggins and K.A. Mauritz, Universal Power Law Behavior of the AC Conductivity Versus Frequency of Agglomerate Morphologies in Conductive Carbon Nanotube-Reinforced Epoxy Networks, J. Polym. Sci. Pol. Phys. **54**, 1918-1923 (2016).
23. A. Dhahri, E. Dhahri and E.K. Hlil, Electrical conductivity and dielectric behavior of nanocrystalline $La_{0.6}Gd_{0.1}Sr_{0.3}Mn_{0.75}Si_{0.25}O_3$, RSC Adv. **8**, 9103-9111 (2018).
24. A.K. Jonscher, The universal dielectric response, Nature **267**, 673-679 (1977).
25. K.C. Kao, Dielectric Phenomena in Solids, Elsevier Academic Press, California, USA (2004).
26. T.V. Dijk and A.J. Burggraaf, Grain Boundary Effects on Ionic Conductivity in Ceramic $Gd_xZr_{1-x}O_{2-(x/2)}$ Solid Solutions, Phys. Stat. Sol. A **63**, 229 (1981).
27. A.J. Burggraaf, T.V. Dijk and M.J. Verkerk, STRUCTURE AND CONDUCTIVITY OF PYROCHLORE AND FLUORITE TYPE SOLID SOLUTIONS, Solid State Ionics **5**, 519-522 (1981).
28. E. Barsoukov and J.R. Macdonald, Impedance Spectroscopy Theory, Experiment and Applications, 2nd Edition, John Willey & Sons Inc., New Jersey (2005).
29. A.R. Long, Frequency-dependent loss in amorphous semiconductors, Adv. Phys. **31**, 513-637 (1982).
30. G.E. Pike, *ac* Conductivity of Scandium Oxide and a new Hopping Model for Conductivity, Phys. Rev. B **6**, 1572-1580 (1972).
31. S.R. Ellott, Temperature dependence *a.c.* conductivity of chalogenide glasses, Philosophical Magazine B **3**, 553-560 (1978).
32. A. Ghosh, *ac* conduction in iron bismuthate glassy semiconductors, Phys. Rev. **42**, 1388-

1393 (1990).

33. S. Bae, Y.K. Hong, J.J. Lee, J. Jalli, G.S. Abo, W.M. Sung, G.H. Kim, S.H. Park, J.S. Kum and H.M. Kwon, Co_2Z Hexaferrite T-DMB Antenna for Mobile Phone Applications, IEEE Trans. Magn. **45**, 4199-4202 (2009).
34. J.H. Jonker and P.B. Braun, FERROXPLANA FERRIMAGNETIC IRON OXIDE, Philips Tech. Rev. **18**, 145-154 (1957).
35. H.M. Sung, C.J. Chen, W.S. Ko and H.C. Lin, Fine Powder Ferrite for Multilayer Chip Inductors, IEEE Trans. Magn. **30**, 4906-4908 (1994).
36. H. Zhang, L. Li, J. Zhou, Z. Yue and Z. Gui, Low-Temperature Sintering, Densification, and Properties of Z-type Hexaferrite with Bi_2O_3 Additives, J. Am. Ceram. Soc. **84**, 2889-2894 (2001).
37. X. Wang, L. Li, J. Zhou, S. Su and Z. Gui, Effect of Copper Substitution on the Dielectric and Magnetic Properties of Low-Temperature-Sintered Z-type Ferrites, Jpn. J. Appl. Phys. **41**, 7249-7253 (2002).
38. H. Zhang, J. Zhou, Y. Wang, L. Li, Z. Yue and Z. Gui, Dielectric characteristics of novel Z-type planar hexaferrite with Cu modification, Mater. Lett. **55**, 351-355 (2002).
39. H. Zhang, J. Zhou, Y. Wang, L. Li, Z. Yue and Z. Gui, The effect of Zn ion substitution on electromagnetic properties of low-temperature fired Z-type hexaferrite, Ceram. Int. **28**, 917-923 (2002).
40. H. Zhang, J. Zhou, Y. Wang, L. Li, Z. Yue, X. Wang and Z. Gui, Investigation on physical characteristics of novel Z-type $Ba_3Co_{2(0.8-x)}Cu_{0.40}Zn_{2x}Fe_{24}$ hexaferrite, Mater. Lett. **56**, 397-403 (2002).
41. H. Zhang, L. Li, Y. Wang, J. Zhou, Z. Yue and Z. Gui, Low-Temperature Sintering and Electromagnetic Properties of Copper-Modified Z-type Hexaferrite, J. Am. Ceram. Soc. **85**, 1180-1184 (2002).
42. X. Wang, L. Li, S. Su, Z. Gui, Z. Yue and J. Zhou, Low-temperature sintering and high frequency properties of Cu-modified Co_2Z hexaferrite, J. Europ. Ceram. Soc. **23**, 715-720 (2003).
43. X.H. Wang, L.T. Li, Z.X. Yue and S.Y. Su, Effect of SiO_2 additive on the high-frequency properties of low-temperature fired Co_2Z, J. Magn. Magn. Mater. **271**, 301-306 (2004).
44. X. Wang, L. Li, S. Su and Z. Yue, Electromagnetic properties of low-temperature-sintered $Ba_3Co_{2-x}Zn_xFe_{24}O_{41}$ ferrites prepared by solid state reaction method, J. Magn. Magn. Mater. **280**, 10-13 (2004).
45. X. Wang, L. Li, S. Su and Z. Gui, Novel Ferrimagnetic Material for Fabricating

Multilayer Chip Inductors-Low-Temperature-Sintered $Ba_3Co_{2-x}Zn_xFe_{24}O_{41}$ Hexaferrites, J. Am. Ceram. Soc. **88**, 478-480 (2005).

46. H. Hsiang, L.T. Mei, C.S. His, W.C. Wu, L.B. Cheng and F.S. Yen, Glass additive influence on the sintering behavior, microstructure and microwave magnetic properties of Cu-Bi-Zn co-doped Co_2Z ferrites, J. Magn. Magn. Mater. **323**, 1011-1014 (2011).
47. N. Hiratsuka, Soft Magnetic Hexagonal Ferrites for High Frequency Devices, J. Magn. Soc. Jpn. **37**, 141-146 (2013).
48. P. Chang, L. He and H. Wang, Effect of $BaCu(B_2O_5)$ additives on the sintering behaviors and dielectric-magnetic properties of Co_2Z hexaferrite, J. Mater. Res. **30**, 2747-2752 (2015).
49. K. Singha, R. Jasrotia, V.P. Singh, M. Chandel, R. Kumar and S. Kalia, A study of magnetic properties of Y-Ni-Mn substituted Co_2Z-type nanohexaferrite via vibrating sample magnetometry, J. Sol-Gel Sci. Tech. **97**, 373-381 (2021).
50. Z.W. Li, G.Q. Lin and L.B. Kong, Microwave Reflection Characteristics of Co_2Z Barium Ferrite Composites with Various Volume Concentration, IEEE Trans. Magn. **44**, 2255-2261 (2008).
51. X. Wang, T. Ren, L. Li, Z. Gui, S. Su, Z. Yue and J. Zhou, Synthesis of Cu-modified Co_2Z hexaferrite with planar structure by a citrate precursor method, J. Magn. Magn. Mater. **234**, 255-260 (2001).
52. S. Kračunovska and J. Töpfer, On the thermal stability of Co_2Z hexagonal ferrites for low-temperature ceramic cofiring technologies, J. Magn. Magn. Mater. **320**, 1370-1376 (2008).
53. H. Zhang, L. Li, J. Zhou, Z. Ma and Z. Gui, Microstructure characterization and properties of chemically synthesized Co_2Z hexaferrite, J. Europ. Ceram. Soc. **21**, 149-153 (2001).
54. M.M. Rashad, H.M.E. Sayed, M. Rasly, A.A. Sattar and I.A. Ibrahim, Magnetic and dielectric properties of polycrystalline La doped barium Z-type hexaferrite for hyper-frequency applications, J. Mater. Sci: Mater. Electron **24**, 282-289 (2013).
55. S. Bae, Y.K. Hong, J.J. Lee, J. Jalli, G.S. Abo, A. Lyle, I.T. Nam, W.M. Seong, J.S. Kum and S.H. Park, New Synthesis Route of Z-Type ($Ba_3Co_2Fe_{24}O_{41}$) Hexaferrite Particles, IEEE Trans. Magn. **45**, 2557-2560 (2009).
56. X. Wang, L. Li, Z. Yue, S. Su, Z. Gui and J. Zhou, Preparation and magnetic characterization of the ferroplana ferrites $Ba_3Co_{2-x}Zn_xFe_{24}O_{41}$, J. Magn. Magn. Mater. **246**, 434-439 (2002).
57. J.J. Xu, C.M. Yang, H.F. Zou, Y.H. Song, G.M. Gao, B.C. An and S.C. Gan,

Electromagnetic and microwave absorbing properties of Co_2Z-type hexaferrites doped with La^{3+}, J. Magn. Magn. Mater. **321**, 3231-3235 (2009).

58. J. Zhang, B. Wang, Z. Li, L. Qiao, T. Wang and F. Li, Synthesis and Microwave absorption properties of Co_2Z barium ferrite by salt-molten method, Adv. Mater. Res. **160-162**, 957-961 (2011).
59. M.J.P. Asl, A. Ghasemi and G.R. Gordani, Characterization and Investigation of Magnetic and Microwave Properties of Al-Cr-substituted Z-type Barium Hexaferrite Nanoparticles, J. Supercond. Nov. Magn. **29**, 795-801 (2016).
60. S.B.S. Magham, M. Sharma, S.R. Shannigrahi, H.R. Tan, V. Sharma, Y.S. Meng, S. Idapalpati, R.V. Ramanujan and D.V.M. Repaka, Development of Z-type hexaferrites for high frequency EMI shielding applications, J. Magn. Magn. Mater. **441**, 303-309 (2017).
61. D. Guo, W. Kong, J. Feng, X. Li and X. Fan, Synthesis, electromagnetic and microwave absorption properties of $Ba_3Co_2Fe_{24}O_{41}$ hexaferrite for GHz application, Mater. Sci. Eng. B **228**, 213-217 (2018).
62. D. Basandrai, R.K. Bedi, A. Dhami, J. Sharma, S.B. Narang, K. Pubby, A. Gupta and A.K. Srivastava, Aluminum and chromium substituted Z-type hexaferrites for antenna and microwave absorber applications, J. Sol-Gel Sci. Tech. **85**, 59-65 (2018).
63. D. Guo, W. Kong, J. Feng, X. Li and X. Fan, Microwave absorption properties of $Sr_xBa_{3-x}Co_2Fe_{24}O_{41}$ hexaferrites in the range of 0.1-18 GHz, J. Alloys Compd. **751**, 80-85 (2018).
64. P.N. Dhruv, R.C. Pullar, C. Singh, F.E. Carvalho, R.B. Jotania, S.S. Meena and J. Singh, Design and development of Ga-substituted Z-type hexaferrites for microwave absorber applications: Mössbauer, static and dynamic properties, Ceram. Int. **47**, 1145-1162 (2021).
65. S. Kolev, P. Penevo, K. Krezhov, T. Malakova, C. Ghelev, T. Koutzarova, D. Kovacheva, B. Vertruyen, R. Closset, L.M. Tran and A. Zaleski, Structural, Magnetic and Microwave Characterization of Polycrystalline Z-Type $Sr_3Co_2Fe_{24}O_{41}$ Hexaferrite, Mater.**13**, 2356 (2020).
66. Y. Lei, W. Wang, G. Tan, X. Shang, X. Huang and Q. Man, Effects of dysprosium substitution on the structure, magnetic properties and microwave absorption properties of Z-type hexaferrite $Ba_3Co_2Fe_{24}O_{41}$ synthesized by the sol-gel method, J. Mater. Res. Tech. **20**, 1603-1615 (2022).
67. P.N. Dhruv, S.S. Meena, R.C. Pullar, F.E. Carvalho, R.B. Jotania, P. Bhatt, C.L. Prajapat, J.P. B. Machado, T.V. Chandrasekhar Rao and C.B. Basak, Investigation of structural, magnetic properties of Gallium substituted Z-type $Sr_3Co_{2-x}Ga_xFe_{24}O_{41}$ hexaferrites for Microwave absorbers, J. Alloys Compd. **822**, 153470 (2020).

68. H. Zhang, L. Li, J. Zhou, J. Bao, Z. Yue, and Z. Gui, Microstructure and properties of Co_2Z hexaferrite prepared by gel self-propagating method, J. Mater. Sci: Mater. Electron. **11**, 619-622 (2000).
69. R.C. Pullar and A.K. Bhattacharya, The synthesis and characterization of the hexagonal Z-ferrite, $Sr_3Co_2Fe_{24}O_{41}$, from a sol-gel precursor, Mater. Res. Bull. **36**, 1531-1538 (2001).
70. J. Temuujin, M. Aoyama, M. Senna, T. Masuko, C. Ando and H. Kishi, Benefits of mild wet milling of the intermediates for the synthesis of Phase-pure Z-type hexaferrite, J. Mater. Res. **20**, 1939-1942 (2005).
71. S. Bae, Y.K. Hong, J.J. Lee, J. Jalli, G.S. Abo, A. Lyle, I.T. Nam, W.M. Seong, J.S. Kum and S.H. Park, New Syntheis Route of Z-type ($Ba_3Co_2Fe_{24}O_{41}$) Hexaferrite Particles, IEEE Trans. Magn. **45**, 2557-2560 (2009).
72. T. Kikuchi, T. Nakamura, T. Yamasaki, M. Nakanishi, T. Fujii, J. Takada, Y. Ikeda, Synthesis of single –phase $Sr_3Co_2Fe_{24}O_{41}$ by polymerizable complex method, Mater. Res. Bull. **46**, 1085-1087 (2011).
73. L. Qin and H. Verweij, Modified Pechini synthesis of hexaferrite Co_2Z with high permeability, Mater. Lett. **68**, 143-145 (2012).
74. A.P. Daigle, M. Geiler, A. Geiler, E. DuPré, J. Modest, Y. Chen, C. Vittoria and V.G. Harris, Permeability spectra of Co_2Z hexaferrite compacts produced via a modified aqueous co-precipitation technique, J. Magn. Magn. Mater. **324**, 3719-3722 (2012).
75. T. Tainaka, T. Kikuchi, T. Nakamura, T. Yamasaki, M. Nakanishi, T. Fujii, J. Takada and Y. Ikeda, Synthesis of the $Sr_3Zn_2Fe_{24}O_{41}$ Z-type ferrite by polymerizable complex method, Key Eng. Mater. **566**, 231-234 (2013).
76. N. Solanki, G. Packiaraj and R.B. Jotania, Effect of Heat treatment on Structural, Magnertic and Electrical properties of Z-type Barium Cobalt Hexaferrite powder, Adv. Mater. Res. **938**, 24-29 (2014).
77. L. Jia, X. Wen, Y. Li and H. Zhang, Hydrothermal Synthesis and Magnetic Properties of Hexagonal $Sr_3Co_2Fe_{24}O_{41}$ Particles, IEEE Trans. Magn. **51**, 2004004 (2015).
78. X. Zhang, Z. Yue, S. Meng, B. Peng and L. Yuan, Magnetic and electrical properties of Z-type hexaferrites sintered in different atmosphere, Mater. Res. Bull. **65**, 238-242 (2015).
79. C.H. Rhee, K.L. Cho and C.S. Kim, Heat treatment Effect on Z-type Hexaferrite for RF Device Application, J. Korea Phys. Soc. **66**, 96-99 (2015).
80. R. Tang, C. Jiang, Y. Fang and H. Yang, Chemical states of air annealed $Sr_3Co_2Fe_{24}O_{41}$ Z-type hexaferrite an X-ray photoelectron spectroscopy study, Mater. Technol. **30**, A181-A185 (2015).

81. W. Lee, Y.k. Hong, J. Park, G.L. Rochelle and J. Lee, Low-loss Z-type he4xaferrite ($Ba_3Co_2Fe_{24}O_{41}$) for GHz antenna applications, J. Magn. Magn. Mater. **414**, 194-197 (2016).
82. E.S. Alhwaitat, S.H. Mahmood, M.A. Hussein, O.E. Mohsen, Y. Maswadeh, I. Bsoul and A. Hammoudeh, Effects of synthesis route on the structural and magnetic properties of $Ba_3Zn_2Fe_{24}O_{41}$ (Zn_2Z) nanocrystalline hexaferrites, Ceram. Int. **44**, 779-787 (2018).
83. D. Guo, W. Kong, J. Feng, X. Li and X. Fan, Synthesis, electromagnetic and microwave absorption properties of $Ba_3Co_2Fe_{24}O_{41}$ hexaferrites for GHz application, Mater. Sci. Eng. B **228**, 213-217 (2018).
84. W. Salazar, J.W. S.D. Busto, L.C. M. Aldana, A.R. Rivera, D.A.L. Tellez and J.R. Rojas, Magnetic feature of the Z-type hexaferrite produced by the citrate and Pechini synthesis routes, J. Low Temp. Phys. **197**, 485-494 (2019).
85. W. Salazar, L.C.M. Aldana and J.W.S.D. Busto, Magnetic domain structures of Sr_3Co_2Z hexaferrite by TEM, J. Magn. Magn. Mater. **501**, 166423 (2020).
86. S. Lather, S. Singh, S. Dahiya, R. Singhla , R. Tripathi and A. Ohlan, Effect of mechanical milling on magnetic, dielectric and magneto-electric properties of Z-type (Ba,Sr) hexaferrites, J. Alloys Compd. **902**, 163807 (2022).
87. Zhang, Y.G. Zhao, Y.F. Cui, L. D. Ye, J.W. Wang, S. Zhang, H.Y. Zhang and M.H. Zhu, Magnetodielectric effect in Z-type hexaferrite, Appl. Phys. Lett. **100**, 032901 (2012).
88. J. Wu, Z. Shi, J. Xu, N. Li, Z. Zheng, H. Geng, Z. Xie and L. Zheng, Synthesis and room temperature four state memory prototype of $Sr_3Co_2Fe_{24}O_{41}$ multiferroics, Appl. Phys. Lett. **101**, 122903 (2012).
89. K. Ebnabbasi, Y. Chen, A. Geiler, V. Harris and C. Vittoria, Magneto-electric effects on Sr Z-type hexaferrite at room temperature, J. Appl. Phys. **111**, 07C719 (2012).
90. K. Okumura, K. Haruki, T. Ishikura, S. Hirose and T. Kimura, Multilevel magnetization switching by electric field in *c*-axis oriented polycrystalline Z-type hexaferrite, Appl. Phys. Lett. **103**, 032906 (2013).
91. X. Wang, Z. Su, A. Sokolov, B. Hu, P. Andalib, Y. Chen and V.G. Harris, Giant magnetoresistance due to magnetoelectric currents in $Sr_3Co_2Fe_{24}O_{41}$ hexaferrites, Appl. Phys. Lett. **105**, 112408 (2014).
92. C.C. Xiang, Y. Nie, Z.K. Feng, R.Z. Gong and Z. Yuan, Low loss Z-type hexaferrite for microwave antenna miniaturization application, Mater. Sci. Forum, **687**, 309-314 (2011).
93. S. Sharma, K.S. Daya, S. Sharma and M. Singh, Ultra low loss soft magnetic nanoparticles for applications up to S-band, Appl. Phys. Lett. **103**, 112402 (2013).

94. R. Tang, C. Jiang, J. Jiang, Y. Liang, X. Zhang, H. Wang and H. Yang, Impedance spectroscopy and scaling behaviors of $Sr_3Co_2Fe_{24}O_{41}$, Appl. Phys. Lett. **106**, 022902 (2015).

95. C.L. Li, S. Huang, X.H. Chen, T.Y. Yan, Q.S. Fu, R. Zhang, C.M. Zhu and S.L. Yuan, Colossal dielectric response and relaxation properties in Co_2Z type hexaferrites, **43**, 12435-12441 (2017).

96. C.L. Li, T.Y. Yan, G.O. Barasa, Y.H. Li, R. Zhang, S. Huang and S.L. Yuan, Colossal dielectric response in $Ba1_{.5}Sr_{1.5}Co_2Fe_{24}O_{41}$ ceramics at high temperature, J. Mater. Sci.: Mater. Electron. **29**, 9971-9978 (2018).

97. A.M. Gadalla, H.E. Schutz and H.W. Hennicke, Effect of Some Additions on the Sinterability and Magnetic Properties of Barium Hexaferrite, J. Magn. Magn. Mater. **1**, 241-250 (1976).

98. H. Zhang, L. Li, J. Zhou, Z. Yue and Z. Gui, Low Temperature Sintering, Densification and Properties of Z-type Hexaferrite with Bi_2O_3 Additives, J. Am. Ceram. Soc. **84**, 2889-28894 (2001).

99. H. Zhang, J. Zhou, Y. Wang, L. Li, Z. Yue and Z. Gui, Microstructure and Magnetic Characteristics of Low Temperature Fired Modified Z-type Hexaferrite with Bi_2O_3 Addtive, IEEE Trans. Magn. **38**, 1797-1802 (2002).

100. X. Wang, L. Li, J. Zhou, S. Su and Z. Gui, Effect of Copper substitution on the Dielectric and Magnetic Properties of Low Temperature Sintered Z-type Ferrites, Jpn. J. Appl. Phys. **41**, 7249-7253 (2002).

101. T. Umemoto, H. Yoshikawa and H. Hirano, Oxide Magnetic Material and Production Method of the same, United States Patent: US 6773620 B2 (2004).

102. M. Endo and A. Nakano, Magnetic Ferrite Powder, Magnetic Ferrite Sinter, Layered Ferrite Part, and Process for Producing Layered Ferrite Part, United States Patent: US 6749768 B2 (2004).

103. X.H. Wang, L.T. Li, Z.X. Yue and S.Y. Su, Effect of SiO_2 additive on the high frequency properties of low temperature fired Co_2Z, J. Magn. Magn. Mater. **271**, 301-306 (2004).

104. P. Huang, L.J. Deng, J.X. Xie, D.F. Liang and L. Chen, Effect of BST additive on the complex permeability and permittivity of Z-type hexaferrite in the range of 1 MHz- 1 GHz, J. Magn. Magn. Mater. **271**, 97-102 (2004).

105. L. Jia, H. Zhang, Z. Zhong and Y. Liu, Effect of different sintering temperature and Nb_2O_5 content on structural and magnetic properties of Z-type hexaferrites, J. Magn. Magn. Mater. **310**, 92-97 (2007).

106. S. Kracunovska and J. Topfer, On the thermal stability of Co_2Z hexagonal ferrites for low temperature ceramic cofiring technologies, J. Magn. Magn. Mater. **320**, 1370-1376 (2008).

107. L. Jia, J. Luo, H. Zhang, Y. Jing and Y. Shi, Effect of Y_2O_3 additive on the microstructure and high frequency properties of Z-type hexaferrites, J. Magn. Magn. Mater. **321**, 77-80 (2009).

108. L. Jia, J. Luo, H. Zhang, G. Xue and Y. Jing, High frequency properties of Si-doped Z-type hexaferrites, J. Alloys Compd. **489**, 162-166 (2010).

109. L. Jia, H. Zhang, J. Luo, Y. Liu and Q. Wen, Effect of MgO additive on the high frequency properties of Z-type hexaferrites, J. Magn. Magn. Mater. **322**, 1934-1938 (2010).

110. L. Jia, Y. Tang, H. Zhang, P. Deng, Y. Liu and B. Liu, Effect of Perovskite Additives on the Electromagnetic Properties of Z-type Hexaferrites, Jpn. J. Appl. Phys. **49**, 063001 (2010).

111. C.H. Mu, Y.L. Liu, H.W. Zhang, Y.Q. Song, Q.Y. Wen and J. Shen, Influence of $MgTiO_3$ on the magnetic and dielectric properties of $Ba_3Co_2Fe_{24}O_{41}$ hexaferrite, J. Appl. Phys. **107**, 09A511 (2010).

112. L. Zhang, A. Puri, K. Sertel, J.L. Volakis and H. Verweij, Low Loss Z-type $Ba_3Co_2Fe_{24}O_{41}$ Hexaferrites for Antennas and RF Devices, IEEE Trans. Magn. **47**, 2149-2152 (2011).

113. B.H. Ryou, W.M. Sung and J.S. Kum, Method for Producing Ferrite, United States Patent: US 2012/0119135 A1 (2012).

114. Z. Cao, M. Han, M. Guan, Z. Song and L. Deng, High Frequency Magnetic Properties of A Composite Material Prepared from Z-type Hexaferrite and Bi_2O_3, Adv. Mater. Res. **833**, 99-102 (2014).

115. L. Gan, Y. Liu, Y. Wang, K. Yang and H. Zhang, Influence of SiO_2 Additive on the High frequency Magnetic Properties of Sr-doped Co_2Z Hexaferrite, Mater. Sci. Forum **787**, 332-337 (2014).

116. Z. Su, H. Chang, X. Wang, A.S. Sokolov, B. Hu, Y. Chen and V.G. Harris, Low loss factor Co_2Z ferrite composites with equivalent permittivity and permeability for ultrahigh frequency applications, Appl. Phys. Lett. **105**, 062402 (2014).

117. T. Zhang, H. Su, X. Tang, H. Zhang, Y. Jing and Y. Li, Low loss Co_2Z hexaferrite with matched permeability and permittivity in HF and VHF bands, J. Magn. Magn. Mater. **382**, 283-287 (2015).

118. P. Chang, L. He and H. Wang, Effect of $BaCu(B_2O_5)$ additions on the sintering behaviors and dielectric magnetic properties of Co_2Z hexaferrites, J. Mater. Res. **30**, 2747-2752 (2015).

119. L. Guo, H. Zhang, R. Lu, Y. Liao, Y. Jing and J. Li, Low temperature cofired Co_2Z barium-strontium ferrite materials with BBSC glass, J. Mater. Sci. Mater. Electron. **27**, 2841-2845 (2016).

120. V.A. Rane and G.J. Phatak, $(CoZn)_2$-Z hexaferrite material for fabrication of integrated inductors in LTCC technology, ISSS J. Micro. Smart. Syst. **6**, 77-81 (2017).

121. H. Chen, D. Liang, W. Li and C. Pang, Magnetic materials for mobile communication antennas substrate application, IOP Conf. Series: Mater. Sci. Eng. **265**, 1-5 (2017).

122. Z. Zheng, Q. Feng and V.G. Harris, Low loss Z-type barium hexaferrite composites from nanoscale $ZnAl_2O_4$ addition for high frequency applications, AIP Adv. **8**, 056107 (2018).

123. M.M. Rashad, M. Rasly, I.A. Ibrahim, H.M.E. Sayed and A.A. Sattar, Magnetic Properties of La^{3+} ion doped Polycrystalline Z-type Hexaferrite Powders Synthesized via the co-precipitation Method, J. Korean Phys. Soc. **63**, 821- 825 (2013).

124. M.M. Rashad, H.M.E. Sayed, M. Rasly, A.A. Sattar and I.A. Ibrahim, Magnetic and dielectric properties of polycrystalline La doped barium Z-type hexaferrite for hyper frequency applications, J. Mater Sci: Mater. Electron, **24**, 282-289 (2013).

125. J. Xu, G. Ji, H. Zou, Y. Song and S. Gan, Influence of Sm –substitution on structure and electromagnetic properties of $Ba_{3-x}Sm_xCo_2Fe_{24}O_{41}$, J. Magn. Magn. Mater. **323**, 157-162 (2011).

126. P. Kumar and A. Gaur, Multiferroicity in La, Pr & Sm doped Z-type strontium hexaferrite, Superlattice Microst. **120**, 305-312 (2018).

127. N. Tran, T.L. Phan, N.T. Dang, D.S. Yang and B.W. Lee, Crystalline and electronic structure and magnetic properties of La doped $Ba_3Co_2Fe_{24}O_{41}$ hexaferrites, J. Phys. Chem. Solids, **131**, 55-61 (2019).

128. M. Aoyama, J. Temuujin, M. Senna, T. Masuko, C. Ando and H. Kishi, Preparation and characterization of Z-type hexaferrites, $Ba3_{(1-x)}Sr_{3x}Co_2Fe_{24}O_{41}$ with x = 0-0.5, via a two-step calcination with an intermediate wet milling, J. Electroceram. **17**, 61-64 (2006).

129. J.T. Lim, T. Kouh and C.S. Kim, Investigation of Magnetic Properties of Sr-Doped $Ba_{3-x}Sr_xCo_2Fe_{24}O_{41}$ Z-type Hexaferrite by Mössbauer Spectroscopy, IEEE Trans. Magn. **51**, 180604 (2015).

130. A. Manhas, K.M. Batoo and M. Singh, Magnetic and Mossbauer investigations of soft Co_2Z-type hexa nanoferrites, J. Alloys Compd. **767**, 188-194 (2018).

131. J. Xu, G. Ji, H. Zou, Y. Zhou and S. Gan, Structural, dielectric and magnetic properties of Nd-doped Co_2Z-type hexaferrites, J. Alloys Compd. **509**, 4290-4294 (2011).

132. M. Kim, K. Lee, C. Bae and J. Kim, Magnetic and morphological properties of Ca substituted M-type hexaferrite powders synthesized by the molten salt method, AIP Advances **11**, 055310 (2021).

133. A.U. Rehman, S.F. Shaukat, M.N. Akhtar and M. Ahmad, A study of structure, magnetic and various dielectric parameters of Ca substituted W-type hexaferriters for applications at 1– 6 GHz frequency, J. Electron Mater. **48**, 7149-7161 (2019).

134. Z. Zheng, Q. Feng, Y. Chen and V.G. Harris, High Frequency Magnetic Properties of Ca-Substituted Co_2Z and Co_2W Barium Hexaferrite Composites, IEEE Trans. Magn. **54**, 2800506 (2018).

135. M. Zareen, N. Yasmin, I.A. Malik, M. Zahid, M.N. Ashiq, A. Kiran, H. Javed, M. Safdar and M. Mirza, Influence of Ce-Mn substitution on dielectric and magnetic properties of strontium based X-type hexaferrites, J. Magn. Magn. Mater. **497**, 165943 (2020).

136. A.R. Kagdi, N.P Solanki, F.E. Carvalho, S.S. Meena, P. Bhatt, R.C. Pullar, R.B. Jotania, Influence of Mg substitution on structural, magnetic and dielectric properties of X-type barium –zinc hexaferrites $Ba_2Zn_{22-x}Mg_xFe_{28}O_{46}$, **741**, 377-391 (2018).

137. J.H. You and S.I. Yoo, Improved magnetic properties of Zn-substituted strontium W-type hexaferrites, J. Alloys Compd. **763**, 459-465 (2018).

138. Y. Liu, M. Popov, I. Zavislyak, H. Qu, T. Zhang, J. Zhang, M.R. Page, A.M. Balbashov and G. Srinivasan, Nonlinear magnetoelectric effects in Al-substituted strontium hexaferrite, Sci. Rep. **11**, 1-12 (2021).

139. G. Han, R. Sui, Y. Yu, L. Wang, M. Li, J. Li, H. Liu and W. Yang, Structure and magnetic properties of the porous Al-substituted barium hexaferrites, J. Magn. Magn. Mater. **528**, 167824 (2021).

140. A.U. Rehman, S.F. Shaukat, A.S. Haidyrah, M.N. Akhtar and M. Ahmad, Synthesis and investigations of structural, magnetic and dielectric properties of Cr-sub substituted W-type Hexaferrites for high frequency applications, J. Electroceram. **1-14** (2021).

141. V. Pratap, A.K. Soni, S.M. Abbas, A.M. Siddiqui and N.E. Prasad, Effect of zinc substitution on U-type barium hexaferrite-epoxy composites as designed for microwave absorbing applications, J. Alloys Compd. **865**, 158280 (2012).

142. V.V. Gudkov, M.N. Sarychev, S. Zherlitsyn, I.V. Zhevstovskikh, N.s. Averkiev, D.A. Vinnik, S.A. Gudkova, R. Niewa, M. Dressel, L.N. Alyabyeva, B.P. Gorshunov and I.B. Bersuker, Sub-lattice of Jahn-Teller centers in hexaferrite crystal, Sci. Rep. **10**, 1-15

(2020).

143. S. Choi, J.H. You, C.Y. Bon, S.Y. Park and S.I. Yoo, Enhanced microwave absorption properties of Zn-substituted SrW-type hexaferrite composites in the Ku-band, Ceram. Int. **47**, 7571-7581 (2021).

144. G. Mukhtar, J. Mohammed, T.T. Carol T., N. Halilu, S. Sharma, U.m. Isah, S.K. Godara and A.K. Srivastava, Investigation of crystal structure, dielectric response and magnetic properties of Tb^{3+} substituted Co_2Y-type barium hexaferrites, Solid State Sci. **113**, 106549 (2021).

145. X. Huo, H. Su, Y. Wang, Y. Li and X. Tang, Effects of Zn substitution on high frequency properties of $Ba_{1.5}Sr_{1.5}Co_{2-x}Zn_xFe_{22}O_{41}$, Ceram. Int. **47**, 17120-17127 (2021).

146. B.X. Gu, Magnetic properties of $Ba_2(Zn_xFe_{1-x})_2Fe_{28}O_{46}$ X-type hexaferrites, J. Appl. Phys. **75**, 4114 (1994).

147. Q. Li, S. Yan, X. Wang, Y. Nie, Z. Feng, Z. Su, Y. Chen and V.G. Harris, Dual-ion substitution induced high impedance of Co_2Z hexaferrites for ultra-high frequency applications, Acta Mater. **98**, 190 (2015).

148. J. Bao, J. Zhou, Z. Yue, L. Li and Z. Gui, Dielectric behavior of Mn-substituted Co_2Z hexaferrites, J. Magn. Magn. Mater. **250**, 131-137 (2002).

149. J.E. Bao, J. Zhou, Z.X. Yue, L.T. Li and Z.L. Gui, Electrical and magnetic studies of $Ba_3Co_2Fe_{23-12x}Mn_{12x}O_{41}$ Z-type hexaferrites, Mater. Sci. Eng. B **99**, 98-101 (2003).

150. K. Singha, V.P. Singh, M. Chandel, N.J.S. Negi, S. Kalia and R.K. Kotnala, Infulence of Ho-Ni-Mn substitution on the structural and magnetic behavior of Ba-Sr Co_2Z-type nanohexaferrites extension up to Mossbauer investigations, Appl. Phys. A **125**, 824 (1-11) (2019).

151. M. Ahmad, R. Grossinger, M. Kriegisch, F. Kubel and M.U. Rana, Magnetic and microwave attenuation behavior of Al-substituted Co_2W hexaferrites synthesized by sol-gel autocombustion process, Curr. Appl. Phys. **12**, 1413-1420 (2012).

152. M. Ahmad, R. Grossinger, I. Ali, I. Ahmad and M.U. Rana, Synthesis and characterization of Al-substituted W-type hexagonal ferrites for high frequency applications, J. Alloys Compd. **577**, 382-388 (2013).

153. C. Wang, X. Ma, C. Xu, H. Chen, Y. Chen, F. Chen, B. Kang, W. Lu, J. Zhang and S. Cao, Magnetic field induced polarization reversal in Y-type hexaferrites $Ba_{0.7}Sr_{1.3}CoZnFe_{11}AlO_{22}$, single crystals, Ceram. Inter. **47**, 19356-19361 (2021).

154. T. Wu, H. Su, Q. Ding, H. Zhang, Y. Jing and X. Tang, Aluminum substituted low loss Z-type hexaferrites for antenna applications, Physica B **429**, 85-89 (2013).

155. S. Tiwari and S. Vitta, Effect of Trivalent Substitution on the Magnetic and Dielectric Properties of Z-type Hexaferrite, $Sr_3Co_2Fe_{24}O_{41}$, AIP Conf. Proc. **1731**, 130041 (2016).

156. M.J.P. Asl, A. Ghasemi and G.R. Gordani, Characterization and Investigation of Magnetic and Microwave Properties of Al-Cr substituted Z-type Barium Hexaferrite Nanoparticles, J. Supercond. Nov. Magn. **29**, 795-801 (2016).

157. J.T. Lim and C.S. Kim, Site Preference and Hyperfine Structure in Doped Z-type Hexaferrite $Ba_{1.5}Sr_{1.5}Co_2(Fe_{1-x}Al_x)_{24}O_{41}$ investigated by Mossbauer Spectroscopy, IEEE Trans. Magn. **53**, 1-4, 1800304 (2017).

158. C. Wu, Y. Liu, Q. Liu, Y. Wang, Q. Yin, J. Chen, V.G. Harris and H. Zhang, Room temperature magnetoelectric effect in Al doped $Sr_3Co_2(Fe_{1-x}Al_x)_{24}O_{41}$ hexaferrites, J. Alloys Compd. **820**, 153130 (2020).

159. C. Wu, Q. Liu, Q. Yin, J. Chen, H. Zhang and Y. Liu, Room temperature multiferroic properties of Al-doped hexaferrites sintered at high oxygen atmosphere concentrations, Ceramic Inter. **47**, 21398-21403 (2021).

160. C. Mu, Y. Liu, Y. Song, L. wang and H. Zhang, Improvement of high frequency characteristics of Z-type hexaferrite by dysprosium doping, J. Appl. Phys. **109**, 123925 (2011).

161. M. Rasly and M.M. Rashad, Structural and magnetic properties of Sn-Zn doped $BaCo_2Z$ hexaferrite powders prepared by citrate precursor method, J. Magn. Magn. Mater. **337-338**, 58-64 (2013).

162. Z.W. Li and Z.H. Yang, Effect of Ti substitution on dynamic and static magnetic properties for $Ba_3Co_2Fe_{24-x}Ti_xO_{41}$ hexaferrites, J. Magn. Magn. Mater. **334**, 5-10 (2013).

163. P. Kulik, G. Winter, A. Sokolov, K. Murphy, C. Yu, K. Qian, O. Fitchorova and V. Harris, Broadband free space impedance in Co_2Z hexaferrites by substitution of high valency heavy transition metal ions for miniaturizaed RF devices, Appl. Phys. Lett. **116**, 202404 (2020).

164. S. Katlakunta, S.S. Meena, S. Srinath, M. Bououdina, R. Sandhya and K. Praveena, Improved magnetic properties of Cr^{3+} doped $SrFe_{12}O_{19}$ synthesized via microwave hydrothermal, Mater. Res. Bull. **63**, 58-66 (2015).

165. D.Y. Chen, Y.Y. Meng, D.C. Zeng, Z.W. Liu, H.Y. Yu and X.C. Zhong, CTAB-assisted low temperature synthesis of $SrFe_{12}O_{19}$ ultrathin hexagonal platelets and its formation, Mater. Lett. **76**, 84-86 (2012).

166. M. Hashim, S.E. Shirsath, S.S. Meena, M.L. Mane, S. Kumar, P. Bhatt, R. Kumar, N.K. Prasad, S.K. Alla, J. Shah, R.K. Kotnala, K.A. Mohammed, E. Şentürk and Alimuddin,

Manganese ferrite prepared using reverse micelle process: Structural and magnetic properties characterization, J. Alloys Compd. **642**, 70-77 (2015).

167. P. Kaur, S.K. Chawla, S.S. Meena, S.M. Yusuf, K. Pubby and S.B. Narang, Modulation of Physico-chemical, magnetic, microwave and electromagnetic properties of nanocrystalline strontium hexaferrite by Co-Zr doping synthesized using citrate precursor sol-gel method, Ceram. Int. **43**, 590-598 (2017).
168. C.C. Piras, S.F. Prieto and W.M. Borggraeve, Ball milling: a green technology for the preparation and functionalization of nanocellulose derivatives, Nanoscale Adv. **1**, 937-947 (2019).
169. W.D. Callister (Jr.) and D.G. Rethwisch, Materials Science and Engineering an Introduction, 8th Edition, John Wiley & Sons Inc., Hoboken (U.S.A.) (2010).
170. M.J. Joshi, Importance of Impedance Spectroscopy Technique in Materials characterization: A Brief Review, Mech. Mater. Eng. 1-7, **9** (2017).
171. S. Saha and T.P. Sinha, Low-temperature scaling behavior of $BaFe_{0.5}Nb_{0.5}O_3$, Phys. Rev. B **65**, 134103 (2002).
172. E.V. Colla, E.Y. Koroleva, N.M. Okuneva and S.B. Vakhrushev, Low-frequency dielectric response of $PbMg_{1/3}Nb_{2/3}O_3$, J. Phys.: Condens. Matter **4**, 3671-3677 (1992).
173. Lily, K. Kumari, K. Prasad and R.N.P. Choudhary, Impedance spectroscopy of $(Na_{0.5}Bi_{0.5})(Zr_{0.25}Ti_{0.75})O_3$ lead free ceramic, J. Alloys Compd. **453**, 325-331 (2008).
174. A. Omri, M. Bejar, E. Dhahri, M.E. Souni, M.A. Valente, M.P.F. Graça and L.C. Costa, Electrical conductivity and dielectric analysis of $La_{0.75}(Ca,Sr)_{0.25}Mn_{0.85}Ga_{0.15}O_3$ perovkite compound, J. Alloys Compd. **536**, 173-178 (2012).
175. H. Zhang, J. Zhou, Y. Wang, L. Li, Z. Yue and Z. Gui, Dielectric characteristics of novel Z-type planar hexaferrite, Mater. Lett. **55**, 351-355 (2002).
176. M.B. Hossen and A.K.M.A. Hossain, Complex impedance and electric modulus studies of magnetic ceramic $Ni_{0.27}Cu_{0.10}Zn_{0.63}Fe_2O_4$, J. Adv. Ceram. **4(3)**, 217-225 (2015).
177. R. Tang, C. Jiang, W. Qian, J. Jian, X. Zhang, H. Wang and Hao Yang, Dielectric relaxation, resonance and Scaling behaviors in $Sr_3Co_2Fe_{24}O_{41}$, Sci. Rep. **5**, 13645 (2015).
178. A.P. Barranco and J.D.S. Guerra, Dielectric relaxation related to single ionized oxygen vacancies in $(Pb_{1-x}La_x)(Zr_{0.90}Ti_{0.10})_{1-x/4}O_3$ ceramics, Mater. Res. Bull. **45**, 1311-1313 (2010).
179. A. Bendahhou, K. Chourti, R.E. Bouayadi, S.E. Barkany and M.A. Salama, Structural, dielectric and impedance spectroscopy analysis of $Ba_5CaTi_{1.94}Zn_{0.06}Nb_8O_{30}$

ferroelectric ceramic, RSC Adv. **10**, 28007-28018 (2020).

180. C.T. Moynihan, Description and analysis of electrical relaxation data for ionically conducting glasses and melts, Solid State Ionics, **105**, 175-183 (1998).
181. N. Ortega, A. Kumar, P. Bhattacharya, S.B. Majumdar and R.S. Katiyar, Impedance spectroscopy of multiferroic $PbZr_xTi_{1-x}/CoFe_2O_4$ layered thin films, Phys. Rev. B **77**, 014111 (2008).
182. J. Liu, C.G. Duan, W.G. Yin, W.N. Mei, R.W. Smith and J.R. Hardy, Large dielectric constant and Maxwell-Wagner relaxation in $Bi_{2/3}Cu_3Ti_4O_{12}$, Phys. Rev. B **70**, 144106 (2004).
183. A. Chandra, M.S. Samuel, J. Koshy and K.C. George, Dielectric relaxation behavior of CdS nanoparticles and nanowires, J. Mater. Sci. **46**, 4646-4653 (2011).
184. N.J. Kidner, N.H. Perry and T.O. Mason, The brick layer Model Revisited: Introducing the Nano-Grain Composite Model, J. Am. Ceram. Soc. **91**, 1733-1746 (2008).
185. J.H. Hwang, D.S. Mclachlan and T.O. Mason, Brick Layer Model Analysis of Nanoscale to Microscale Cerium Dioxide, J. Electroceram. **3**, 7-16 (1999).
186. J. Fleig, Impedance Spectroscopy on Solids: The Limits of Serial Equivalent Circuit Models, J. Electroceram. **13**, 637-644 (2004).
187. J. Jamnik and J. Maier, Generalised equivalent circuits for mass and charge transport: chemical capacitance and its implications, Phys. Chem. Chem. Phys. **3**, 1668-1678 (2001).
188. M. Atif, M. Idrees, M. Nadeem, M. Siddique and M.W. Ashral, Investigation on the structural, dielectric and impedance analysis of manganese substituted cobalt ferrite i.e. $Co_{1-x}Mn_xFe_2O_4$ ($0.0 \leq x \leq 0.4$), RSC Adv. **6**, 20876-20885 (2016).
189. S.A. Mazen and N.I.A. Elsaad, AC impedance studies on $Li_{0.5+0.5x}Ge_xFe_{2.5-1.5x}O_4$ system, Appl. Phys. A **122**, 26 (2016).
190. R.S. Devan, Y.D. Kolekar and B.K. Chougule, Effect of cobalt substitution on the properties of nickel -copper ferrite, J. Phys.: Condens. Mat. **18**, 9809-9821 (2006).
191. T. Mondal, S. Das, T.P. Sinha and P.M. Sarun, Dielectric relaxation and study of electrical conduction mechanism in $BaZr_{0.1}Ti_{0.9}O_3$ ceramics by correlated barrier hopping model, Mater. Sci. Poland **36**, 112-122 (2018).
192. Q. Zhu, R. Tang, H. Zhou, Y. Wang, S. Xu, J. Zhang, C. Jiang, X. Su and H. Yang, Impedance spectroscopy and conduction mechanism of magneto-electric hexaferrite $BaFe_{10.2}Sc_{1.8}O_{19}$, J. Am. Ceram. Soc. **102**, 4038-4047 (2019).
193. M.A. Rahman and A.K.M. Hossain, Electrical transport properties of Mn-Ni-Zn ferrite

using complex impedance spectroscopy, Phys. Scr. **89**, 025803 (2014).

194. R. Ranjan, R. Kumar, N. Kumar, B. Behera and R.N.P. Choudhary, Impedance and electric modulus analysis of Sm modified $Pb(Zr_{0.55}Ti_{0.45})_{1-x/4}O_3$, J. Alloys Compd. **509**, 6388-6394 (2011).
195. Y. Wang, Y. Pu, Z. Wang, X. Li and Y. Cui, Dielectric, modulus and impedance analysis of $(Ba_{0.9}Bi_{0.1})(Ti_{0.9}Al_{0.1})O_3$ ceramics, J. Mater. Sci: Mater. Electron **28**, 4245-4252 (2017).
196. K. Kumari, A. Prasad and K. Prasad, Dielectric, Impedance/Modulus and Conductivity Studies on $[Bi_{0.5}(Na_{1-x}K_x)_{0.5}]_{0.94}Ba_{0.06}TiO_3$ $(0.16 \leq x \leq 0.20)$ Lead free ceramics, Am. J. Mater. Sci. **6(1)**, 1-18 (2016).
197. F. Chen, X. Wang, Y. Nie, Q. Li, J. Ouyang, Z. Feng, Y. Chen and V.G. Harris, Ferromagnetic resonance induced large microwave magneto-dielectric effect in cerium doped $Y_3Fe_5O_{12}$ ferrites, Sci. Rep. **6**, 28206 (2016).
198. D.R. Day, T.J. Lewis, H.L. Lee and S.D. Senturia, The Role of boundary layer capacitance at Blocking Electrodes in the Interpretation of Dielectric Cure Data in Adhesives, J. Adhesion **18**, 73-90 (1985).
199. V.V. Kharton, Solid State Electrochemistry II, Electrodes, Interfaces and Ceramic Membranes, Wiley-VCH Verlag & Co. KGaA Boschstr **12**, 69469, Weinheim, Germany (2011).
200. J.J. Xu, C.M. Yang, H.F. Zou, Y.H. Song, G.M. Gao, B.C. An and S.C. Gan, Electromagnetic and microwave absorbing properties of Co_2Z hexaferrites doping with La^{3+}, J. Magn. Magn. Mater. **312**, 3231-3235 (2009).
201. M.M. Rashad, M. Rasly, I.A. Ibrahim, H.M. El-Sayed and A.A. Sattar, Magnetic Properties of La^{3+}-ions-doped Polycrystalline Z-type Hexaferrite Powders Synthesized via the Co-precipitation Method, J. Korean Phys. Soc. **63**, 821-825 (2013).
202. Z. Zheng, Q. Feng, Y. Chen and V. Harris, High-Frequency Magnetic Properties of Ca-Substituted Co_2Z and Co_2W Barium Hexaferrite Composites, IEEE Trans. Magn. **56**, 1-6 (2018).
203. Z. W. Li, Y. P. Wu, and G. Q. Lin, Doping effect on complex permeability and permittivity for W-type barium ferrite composites, J. Appl. Phys. **102**, 083908 (2007).
204. X. Liu, W. Zhong, S. Yang, Z. Yu, B. Gu, and Y. Du, Influences of La^{3+} substitution on the structure and magnetic properties of M-type strontium ferrites, J. Magn. Magn. Mater. **238**, 207–214 (2002).

205. Y. Marouani, J. Massoudi, M. Noumi, A. Benali, E. Dhahri, P. Sanguino, M.P.F. Graca, M.A. Valente and B.F.O. Costa, Electrical conductivity and dielectric properties of Sr doped M-type barium hexaferrite $BaFe_{12}O_{19}$, RSC Adv. **11**, 1531-1542 (2021).

206. K. Prabakar and S.P.M. Rao, Complex impedance spectroscopy studies on fatigued soft and hard PZT ceramics, J. Alloys Compd. **437**, 302-310 (2007).

207. R. Tang, C. Jiang, W. Qian, J. Jian, X. Zhang, H. Wang and H. Yang, Dielectric relaxation, resonance and scaling behaviors in $Sr_3Co_2Fe_{24}O_{41}$ hexaferrite, Sci. Rep. **5**, 13645 (2015).

208. D. Barrionuevo, N. Ortega, A. Kumar, R. Chatterjee, J.F. Scott and R.S. Katiyar, Thickness dependent functional properties of $PbZr_{0.52}Ti_{0.48}O_3/La_{0.67}Sr_{0.33}MnO_3$ heterostructures, J. Appl. Phys. **114**, 234103 (2013).

209. S. Majumdar, H. Huhtinen, P. Paturi and H.S. Majumdar, Effect of strain and grain boundaries on dielectric properties in $La_{0.7}Sr_{0.3}MnO_3$ thin films, J. Mater. Sci. **48**, 2115-2122 (2013).

210. S. Damerio, P. Nukala, J. Juraszek, P. Reith, H. Hilgenkamp and B. Noheda, Structure and magnetic properties of epitaxial $CaFe_2O_4$ thin films, njp Quantum Mater. **5**, 33 (2020).

211. M.N.U. Haq, V.V. Shvartsman, S. Salamon, H. Wende, H. Trivedi, A. Mumtaz and D.C. Lupascu, A new (Ba, Ca) (Ti, Zr)O_3 based multiferroic composite with large magnetoelectric effect, Sci. Rep. **6**, 32164 (2016).

212. C.Y. Tsay, Y.H. Lin, Y.M. Wang, H.Y. Chang, C.M. Lei and S.U. Jen, Electrical transport properties of $CoMn_{0.2-x}Ga_xFe_{1.8}O_4$ ferrites using complex impedance spectroscopy, AIP Adv. **6**, 055909 (2016).

213. M. Coskun, O. Polat, F.M. Coskun, Z. Durmus, M. Caglar and A. Turut, The electrical modulus and other dielectric properties by the impedance spectroscopy of $LaCrO_3$ and $LaCr_{0.90}Ir_{0.10}O_3$ perovskites, RSC Adv. **8**, 4634-4648 (2018).

214. G.R. Gajula, L.R. Buddiga, K.N. C. Kumar and M. Dasari, Study on electric modulus, complex modulus and conductivity properties of Nb/Sm, Gd doped barium titanate lithium ferrite ceramic composites, Results Phys. **17**, 103076 (2020).

215. M. B. Hossen and A.K.M. A. Hossain, Complex impedance and electric modulus studies of magnetic ceramic $Ni_{0.27}Cu_{0.10}Zn_{0.63}Fe_2O_4$, J. Adv. Ceram. **4(3)**, 217-225 (2015).

216. W. Chen, W. Zhu, O.K. Tan and X.F. Chen, Frequency and temperature dependent impedance spectroscopy of cobalt ferrite composite thick films, J. Appl. Phys. **108**, 034101 (2010).

217. S. Dutta and R.N.P. Choudhary, Microstructural studies of (PbLa)($ZrTiO_3$) ceramic using complex impedance spectroscopy, J. Appl. Phys. **96**, 1607 (2004).

218. P. Ravindernathan and K. C. Patil, Novel solid solution precursor method for the preparation of ultrafine Ni-Zn ferrites, J. Mater. Sci. **22**, 3261-3264 (1987).

219. M. J. Miah and A. K. M. A. Hossain, Magnetic, Dielectric and Complex Impedance Properties of $xBa_{0.95}Sr_{0.05}TiO_3$-(1-x)$BiFe_{0.9}Gd_{0.1}O_3$ Multiferroic Ceramics, Acta Metall. Sin. **29**, 505-517 (2016).

220. A. T. Raghavender, K. Zadro, D. Pajic, Z. Skoko and N. Biliškov, Effect of grain size on the Neel temperature of nanocrystalline nickel ferrite, Mater. Lett. **64**, 1144-1146 (2010).

221. S. Thakur, R. Rai, I. Bdikin and M.A. Valente, Impedance and modulus spectroscopy characterization of Tb modified $Bi_{0.8}A_{0.1}Fe_{0.9}Ti_{0.1}O_3$ ceramics, Mater. Res. **19**, 1-8 (2016).

222. A. Shukla, R.N.P. Choudhary and A.K. Thakur, Effect of Mn^{4+} substitution on thermal, structural, dielectric and impedance properties of lead titanate, J. Mater. Sci: Mater. Electron. **20**, 745-755 (2009).

223. K. S. Cole and R. H. Cole, Dispersion and Absorption in Dielectrics I. Alternating Current Characteristics, J. Chem. Phys. **9**, 341 (1941).

224. M. M. Costa, G. F. M. Pires Junior and A. S. B. Sombra, Dielectric and impedance properties studies of the of lead doped (PbO)-Co_2Y type hexaferrite ($Ba_2Co_2Fe_{12}O_{22}$ (Co_2Y)), Mater. Chem. Phys. **123**, 35–39 (2010).

225. K.P. Padmasree, D.K. Kanchan and A.R. Kulkarni, Impedance and Modulus studies of the solid electrolyte system $20CdI_2$-80[xAg_2O-y($0.7V_2O_5$-$0.3B_2O_3$)], where $1 \leq x/y \leq 3$, Solid State Ionics, **177**, 475-482 (2006).

226. A. Dutta and T.P. Sinha, Dielectric relaxation in perovskite $BaAl_{1/2}Nb_{1/2}O_3$, J. Phys. Chem. Solids **67**, 1484-1491 (2006).

227. B.D. Cullity, Elements of X–ray powder diffraction. Addison–Wesley Publishing Company, Inc., USA (1978).

228. A. Taylor, H. Sinclair, On the determination of lattice parameters by the Debye-Scherrer method, Proc. Phys. Soc. **57**, 126–135 (1945).

229. C. Koops, On the dispersion of resistivity and dielectric constant of some semiconductors at audio frequencies, Phys. Rev. **83**, 121–124 (1951).

230. S. Supriya, S. Kumar and M. Kar, Correlation between AC and DC transport properties of Mn substituted cobalt ferrite, J. Appl. Phys. **120**, 1–14 (2016).

231. K. Verma and S. Sharma, Impedance spectroscopy and dielectric behavior in barium strontium titanate-nickel zinc ferrite composites, Phys. Status Solidi Basic Res. **249**, 209–216 (2012).

232. N. Kumar, A. Shukla, C. Behera and R.N.P. Choudhary, Structure, electric and magnetic properties of $Bi(Ni_{0.45}Ti_{0.45}Fe_{0.10})O_3$, J. Alloys Compd. **688**, 858-869 (2016).

233. A. Kumara, B. P. Singh, R. N. P. Choudhary and A. K. Thakur, Characterization of electrical properties of Pb-modified $BaSnO_3$ using impedance spectroscopy, Mater. Chem. Phys. **99**, 150–159 (2006).

234. B. Behera, P. Nayak and R. N. P. Choudhary, Impedance spectroscopy study of $NaBa_2V_5O_{15}$ ceramic, J. Alloys Compd. **436**, 226–232 (2007).

235. A. Chandra, M. S. Samuel, J. Koshy and K.C. George, Dielectric relaxation behavior of CdS nanoparticles and nanowires, J. Mater. Sci. **46**, 4646-4653 (2011).

236. A.K. Jonscher, Dielectric relaxation in solids, Chelsea Dielectrics Press, London (1983).

237. S. Karmakar and D. Behera, Almond-West type grain and grain boundary conduction modified dielectric relaxation in $NdCoO_3$, Appl. Phys. A, **124**, 745 (2018).

238. R. S. T. M. Sohn, A. A. M. Macedo, M. M. Costa, S. E. Mazzetto and A. S. B. Sombra, Studies of the structural and electrical properties of lithium ferrite ($LiFe_5O_8$), Phys. Scr. **82**, 055702 (2010).

239. X.Z. Yuan, C. Song, H. Wang and J. Zhang, Electrochemical Impedance Spectroscopy in PEM Fuel Cells: Fundamentals and Applications, Springer London Doedrecht Heidelberg New York (2010).

240. L. Drewniak and S. Kochowski, The origin of constant phase element in equivalent circuit of MIS (n) GaAs structures, Mater. Electron. **31**, 19106-19118 (2020).

241. J. Deng, L. Liu, X. Sun, S. Liu, T. Yan, L. Fang and B. Eloudi, Dielectric relaxation behavior and mechanism of $Y_{2/3}Cu3Ti_4O_{12}$ ceramic, Mater. Res. Bull. **88**, 320-329 (2017).

242. S. Hajlaoui, I. Chaabane and K. Guidara, Conduction mechanism model, impedance spectroscopic investigation and modulus behavior of the organic $[(C_3H_7)N][SnCl_5(H_2O)].2H_2O$ compound, RSC Adv. **6**, 91649 – 91657 (2016).

243. A. Sharma and N. Mehta, Study of dielectric relaxation and thermally activated a.c. conduction in lead containing topological glassy semiconductors, RSC Adv. **7**, 19085-19097 (2017).

244. J. Koaib, N. Bouguila, H. Abassi, N. Moutia, M. Kraini, A. Timoumi, C. V. Vazquez, K. Khirouni and S. Alaya, Dielectric and electrical properties of annealed ZnS thin films.

The appearance of the OLPT conduction mechanism in chalcogenides, RSC Adv. **10**, 9549–9562 (2020).

245. J. Tahalyani, K.K. Rahangdale and K. Balasubramanian, The dielectric properties and charge transport mechanism of π- conjugated segments decorated with intrinsic conducting polymer, RSC Adv. **6**, 69733-69742 (2016).

246. A. Hadded, J. Massoudi, E. Dhahri, K. Khirouni and B.F.O. Costa, Structural, optical and dielectric properties of $Cu_{1.5}Mn_{1.5}O_4$ spinel nanoparticles, RSC Adv. **10**, 42542–42556 (2020).

Supplementary Studies

The supplementary work carried out with La^{3+} substituted Co_2Z ferrite (La-Z) and described as given below:

Magneto-dielectric analysis

Magneto-dielectric (*MD*) effect demonstrates the coupling between polarization and magnetization vectors described as $MD = \{[\varepsilon'(H) - \varepsilon'(0)]/\varepsilon'(0)\} \times 100\%$, where $\varepsilon'(H)$ & $\varepsilon'(0)$ represent the dielectric constant in the presence and absence of magnetic field, respectively. Fig. S (a & b) shows frequency dependent *MD* effect at different magnetic field for Co_2Z & La-Z, respectively. Here, the main motto is to find out the role of La^{3+} substitution in *MD* effect. The different substitution creates lattice strain which enhanced the value of *MD* effect due to the lattice distortion. The variation of the refined lattice parameters of La-Z confirms the *MD* effect arises due the intrinsic cause. On the other hand, the formation of magnetization and dipoles are the fundamental intrinsic properties of the material. Therefore, *MD* effect is mainly originated by the intrinsic cause in both Co_2Z & La-Z. In low frequency range, *MD* for Co_2Z increases with the applied magnetic field and gradually decreases with increase in frequency. Above 10^4 Hz, *MD* effect is almost frequency independent. Fig. S (b) shows that La^{3+} substituted sample has different characteristic of *MD* effect compared with Co_2Z. As magnetic field increases, *MD* effect also increases and is found maximum at 1500 Oe. Further increase in magnetic field to 1200 Oe & 2500 Oe, MD effect decreases. The maximum percentage of *MD* effect for La-Z at 1500 Oe is 80 % compared with Co_2Z (16 %) at 2500 Oe. It is also to be noted that after a gradual decrease in *MD* with frequency; an instant rise between the frequency 10^4 Hz – 10^5 Hz were observed (inset Fig. S (b)) where peaks are marked 1, 2, & 3 at different magnetic fields. La^{3+} substitution causes additional Fe^{2+} & Fe^{3+} dipoles which enhances the electron exchange coupling between Fe^{2+} - Fe^{3+}. Therefore, *MD* effect increases because of a nonmagnetic ion, La doped at nonmagnetic site of Ba^{2+}. The magnitude of peak-1 is found to be higher at 250 Oe suggests strong electron exchange coupling. With increasing frequency, the decrease in peak magnitude may be due to the electron fluctuation. The increasing and decreasing trend of peaks is also related to orientation change of the Fe^{2+} & Fe^{3+} dipoles.

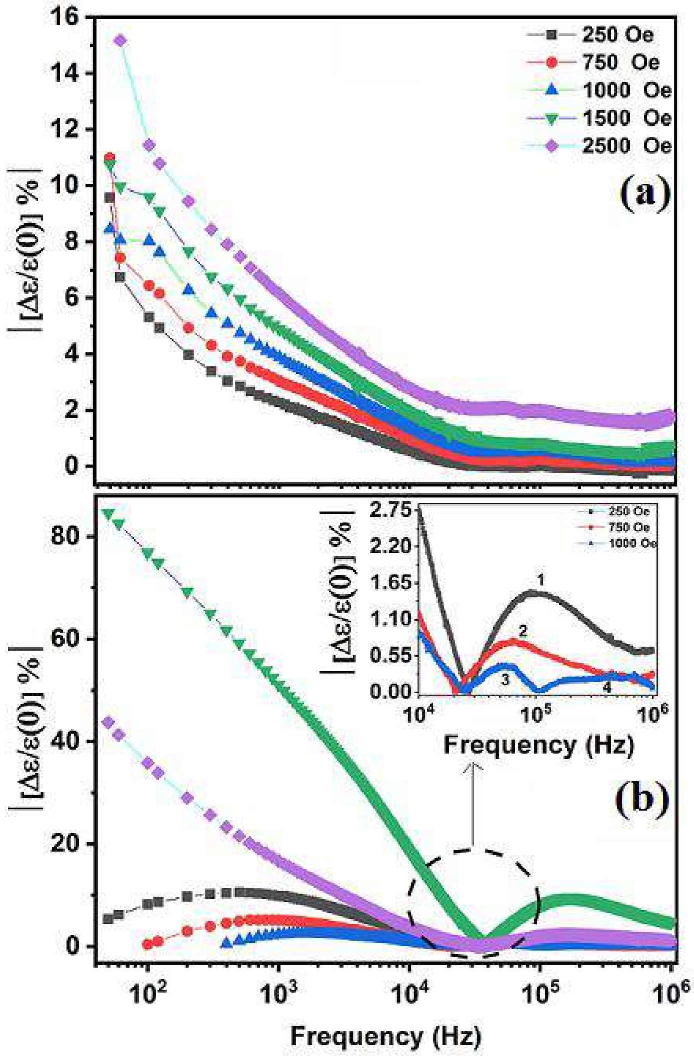

Fig. S Frequency dependent magneto-dielectric (*MD*) properties of (a) Co_2Z and (b) La-Z at different applied magnetic field.

Journal of Superconductivity and Novel Magnetism (2020) 33:519–526
https://doi.org/10.1007/s10948-019-05202-9

ORIGINAL PAPER

Effect of Sintering Additives on Structural, Magnetic, and Dielectric Properties of $Ba_3Co_2Fe_{24}O_{41}$ Ferrite

Anoop Pratap Singh[1] · O. P. Pandey[1] · Puneet Sharma[1]

Received: 6 May 2019 / Accepted: 26 June 2019 / Published online: 29 July 2019

Abstract

Z-type $Ba_3Co_2Fe_{24}O_{41}$ (Co_2Z) ferrite with different additives (Bi_2O_3, SiO_2, Al_2O_3, and MgO) was prepared by solid-state synthesis method. Effect of sintering additives on structural, magnetic, and dielectric properties has been investigated. All XRD patterns confirmed the single-phase Z-type ferrite; however, a minor trace of M-type ferrite was observed with SiO_2 additive. FTIR studies verified that the additive ions do not occupy any crystallographic sites of Co_2Z ferrite. SEM micrographs revealed that SiO_2, Al_2O_3, and Bi_2O_3 promote hexagonal platelet-shaped structure of different size. Magnetic measurements showed that coercivity increased and saturation magnetization decreased with sintering additives. All the sintering additives effectively reduced complex permittivity and dielectric losses of Co_2Z ferrite.

Keywords Z-type hexaferrite · Magnetic properties · Sintering additives · Microstructures

1 Introduction

Z-type $Ba_3Co_2Fe_{24}O_{41}$ (Co_2Z) ferrite has gained considerable attention for high-frequency microwave devices. The ferromagnetic resonance of 1.3 GHz and low losses at microwave frequencies makes it a suitable material for miniaturized mobile and wireless LAN communication [1, 2]. Co_2Z ferrite also exhibits magneto-electric (ME) coupling for application in nonvolatile memories, spintronics, and microwave devices [3–5]. The characteristic properties of Z-type ferrite lie in its crystal structure which is a superposition of M-type ($BaFe_{12}O_{19}$) and Y-type ($Ba_2Co_2Fe_{12}O_{22}$) hexaferrites. In the unit cell of Co_2Z, Ba^{2+} ions occupy 2b and 4f sites and Fe^{3+} ions are located at six octahedral positions ($12k_{VI}$, $4f_{VI}$, $4e_{VI}$, $4f_{VI}$*, $12k_{VI}$*, $2a_{VI}$), three tetrahedral sites ($4e_{IV}$, $4f_{IV}$, $4f_{IV}$*), and one fivefold site ($2d_V$). Co-ions are located at five sites $12k_{VI}$, $12k_{VI}$*, $2a_{VI}$, $4e_{VI}$, and $2d_V$. Contrary to M-type ferrite, Co_2Z ferrite possesses soft magnetic nature with in-plane magnetic anisotropy [6].

Considering its important technological applications, Z-type ferrites were extensively studied for its magnetic and microwave properties. The intrinsic magnetic and electrical properties were tailored by various cation substitutions for Ba^{2+}, Co^{2+}, and Fe^{3+} ions [7–10]. Besides Z-type hexaferrite, the M-type ferrites were also explored for its magnetic and dielectric properties with various ion substitutions [11–14]. In addition, to improve microstructural characteristic and densification at lower temperatures, various sintering additives were added and investigated [15–17]. It is well reported that suitable oxide additives simultaneously lower down sintering temperature and microstructural porosity. The low melting point sintering additive such as Bi_2O_3, CuO, and PbO–CuO improves densification by liquid-phase sintering at low temperatures [15–17]. Also, high melting point additives MgO, WO_3, Al_2O_3, and SiO_2 reportedly promote low-temperature sintering [18–21]. However, low-temperature liquid-phase sintering with high melting point additives (above 1500 °C) is quite ambiguous. Therefore, to achieve adequate densification, a high sintering temperature may be required [22]. These additives may control predominant grain growth at high temperature by pinning mechanism. In summary, the melting point of sintering additive could be a defining factor for controlling microstructure along with sintering temperature. In the present work, high-temperature sintered Co_2Z ferrites with different melting point additives (Bi_2O_3, SiO_2, Al_2O_3, and MgO) were prepared. The effect of additives on structural, magnetic, and dielectric properties was studied with an aim to use them in magneto-dielectric (MD) substrates for microwave antennas.

✉ Puneet Sharma
puneet.sharma@thapar.edu

[1] School of Physics & Materials Science, Thapar Institute of Engineering &Technology, Patiala, Punjab 147004, India

ARTICLE IN PRESS

Ceramics International xxx (xxxx) xxx

Contents lists available at ScienceDirect

Ceramics International

journal homepage: www.elsevier.com/locate/ceramint

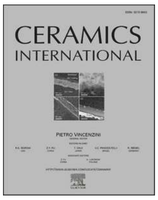

Impedance spectroscopy and magneto-dielectric analysis of La^{3+} substituted Co_2Z hexaferrite

Anoop Pratap Singh, O.P. Pandey, Puneet Sharma *

Magnetic Materials Laboratory, School of Physics & Materials Science, Thapar Institute of Engineering & Technology, Patiala, 147004, Punjab, India

ARTICLE INFO

Keywords:
Impedance spectroscopy
Relaxation time
Cole-cole plots
Hexaferrite and magnetodielectric effect

ABSTRACT

Single phase $Ba_3Co_2Fe_{24}O_{41}$ (Co_2Z) and $Ba_{2.8}La_{0.2}Co_2Fe_{24}O_{41}$ (La-Z) were prepared by solid state ceramic method. The dielectric, impedance and electric modulus were systematically investigated as a function of temperature from 50 °C–250 °C and in the frequency range of 1 Hz–1 MHz. Frequency dependent imaginary impedance and electric modulus implies that La^{3+} substitution significantly affect hopping and relaxation mechanism of charge carriers. Cole-Cole plots (Z'' *vs* Z') has been fitted with suitable equivalent circuit for both Co_2Z & La-Z. The obtained grain and grain boundary resistances confirmed that charge carriers experienced lower resistance in La-Z. Arrhenius plots of relaxation time (τ) *vs* $1/T$ showed parallel conduction mechanism in system. Complex electric modulus spectrum distinguished the capacitive contribution of grain, grain boundary and electric effect. A very high magnetodielectric effect at low frequencies has been observed for La-Z.

1. Introduction

Z-type, (Ba, Sr)$_3Co_2Fe_{24}O_{41}$ (Co_2Z) is a mixed hexaferrite having complex crystal structure with superimposition of M-type ($BaFe_{12}O_{19}$) and Y-type ($Ba_2Co_2Fe_{12}O_{22}$) ferrites. The elementary hexagonal cell consisted of 22 closed packed oxygen layers stacked in four spinel S-blocks (Fe_6O_8), two hexagonal R-blocks $(BaFe_6O_{11})^{2-}$ and two hexagonal T-blocks ($Ba_2Fe_8O_{14}$) in RSTSR*S*T*S* sequence, where the asterisk (*) represents a rotation of blocks by 180°° around the *c*-axis [1,2], the respective crystal structure of Co_2Z unit cell is shown in Fig. 1. Z-type ferrites are remarkable case of possessing three type of anisotropy; at room temperature (*RT*) the magnetization direction is along basal plane (planar anisotropy), above 480 K, *c*-axis (perpendicular to basal plane) is preferred orientation and below 220 K, it exhibits conical alignment of magnetization [3–5]. Also, at *RT*, the in-plane rotation of magnetization around *c*-axis is easy which make its magnetic moment to follow alternating field and retain high permeability (μ) up to 3 GHz [1,6]. This material also exhibits high dielectric constant and show field induced polarization in a wide frequency range [6–8]. Its high μ along with high permittivity (ε) is vastly exploited as substrate for antenna miniaturization, multilayer chip inductors and other electronic devices for telecommunications [9–13]. Further, magnetic and dielectric properties of Z-type hexaferrites can be modified by changing the intrinsic (composition/substitution) and extrinsic (sintering conditions) parameters. Magnetic properties are largely influenced by cationic substitution and has been extensively investigated for powders prepared by various processing techniques [14–17]. The dielectric properties, i.e. ε and dielectric loss primarily depend upon the localized electric charge carriers and were mostly studied in two frequency domains. For the technological applications, the studies were mainly focused on high frequency (>1 GHz) dielectric behavior and well investigated [11,16, 18–20]. However, for the understanding of intriguing physics of charge conduction and polarization; dielectric studies below 1 MHz are very crucial, where the charge carriers and oxygen vacancies (originated during sintering) leads to make a complex system of dielectric relaxation and conduction mechanism [14,15]. In general, the relaxations of non-permanent dipoles at grain boundaries can be observed up to 10 kHz. However, the information about conduction mechanisms associated with grain, grain boundaries and other interfaces can be acquired between 10 kHz to 1 MHz. This is well explained by Maxwell-Wagner and Koop's phenomenological brick-layer model [21–23]. The low frequency charge conduction studies on Z-type ferrites showed two types of dielectric relaxations due to thermally activated carriers [24]. The dielectric studies on Z-type ferrite with equimolar ratio of Ba/Sr i.e. $Sr_{1.5}Ba_{1.5}Co_2Fe_{24}O_{41}$ were also carried out and suggested that electric response is originated from grain and grain boundaries [25].

However, electrical transport studies on substituted Z-type ferrites are rare, and most of them were carried out in GHz frequency range.

---

* Corresponding author.
E-mail address: puneet.sharma@thapar.edu (P. Sharma).

https://doi.org/10.1016/j.ceramint.2021.04.266
Received 17 February 2021; Received in revised form 10 April 2021; Accepted 27 April 2021

Please cite this article as: Anoop Pratap Singh, *Ceramics International*, https://doi.org/10.1016/j.ceramint.2021.04.266

Materials Chemistry and Physics 277 (2022) 125574

Contents lists available at ScienceDirect

Materials Chemistry and Physics

journal homepage: www.elsevier.com/locate/matchemphys

Impedance spectroscopy and magnetic studies on Co_2Z ferrite sintered with SiO_2 and Bi_2O_3 additives

Anoop Pratap Singh, O.P. Pandey, Puneet Sharma *

Magnetic Materials Laboratory, School of Physics & Materials Science, Thapar Institute of Engineering & Technology, Patiala, 147004, Punjab, India

HIGHLIGHTS

- Polycrystalline $Ba_3Co_2Fe_{24}O_{41}$ ceramics were prepared with SiO_2 and Bi_2O_3 additives by solid state reaction method.
- Phase identification and microstructural analysis were done by X-ray diffractometer and Scanning Electron Microscopy.
- Impedance studies as a function of frequency (1 Hz–1 MHz) and temperature (30 °C–250 °C) were carried out.
- The *ac* conductivity behaviors of different additives are analyzed with measured temperatures.
- The Nyquist plots for additives showed an additional resistance which is required to satisfy Maxwell-Wagner model.

ARTICLE INFO

Keywords:
Hexaferrite
Impedance spectroscopy
ac conductivity

ABSTRACT

Z-type ($Ba_3Co_2Fe_{24}O_{41}$) ferrites with Bi_2O_3 and SiO_2 additives were prepared by solid-state reaction method. The electrical transport properties were systematically investigated and analyzed by impedance spectroscopy in the frequency range of 1 Hz to 1 MHz at different temperatures. The peak broadening in real and imaginary part of impedance spectra demonstrates the existence of multiple relaxations. Two distinct slopes of relaxation time observed represent the deviation from non-Debye type relaxation. Partially overlapped scaling behavior illustrated that the dynamic process of charge carriers was temperature dependent. The additives got segregated along the grain boundaries and exhibit their own resistance, which is verified by fitting of the Nyquist plots. This relaxation process was explained on the basis of Maxwell-Wagner effect with three heterogeneous dielectric media (grain, grain boundary and additive layer). The translatory motion of dynamic charge carriers and lattice ions is governed by small and large polaron hopping in the material. The saturation magnetization of Co_2Z-Si is higher compared to Co_2Z-P and Co_2Z-Bi samples, due to formation of minor M-type phase.

1. Introduction

Co_2Z hexaferrite is utilized in the development of miniaturized antenna and electromagnetic shielding devices [1–4]. The unit cell of Z-type hexaferrite is comprised of M-type ($BaFe_{12}O_{19}$), Y-type ($Ba_2Co_2Fe_{12}O_{22}$) structures with ten different interstitial sub lattice sites ($4f_{IV}$, $4f_{IV}$*, 12_{kVI}*, $4f_{VI}$*, $4e_{IV}$, $12k_{VI}$, $2d_V$, $2a_{VI}$, $4f_{VI}$ and $4e_{VI}$) [5]. The high permeability, strong planar magneto-crystalline anisotropy and low ferromagnetic resonance frequency are promising properties of Z-type ferrite for ultra-high frequency (0.3–3 GHz) applications [6,7]. Generally, dielectric losses depend upon its microstructural characteristics such as grain size, shape and porosity of the material [8,9]. It has been observed that high temperature sintering enhances dielectric losses due to exaggerated grain growth and reduction of Fe^{3+} to Fe^{2+} [10]. However, the magnetic and dielectric properties can be tuned especially sintering time and temperature with minimum losses by controlling the processing conditions. Addition of suitable sintering additives is commonly adopted to reduce the sintering temperature and for modifying the structure [11]. Basically, sintering additives facilitates the formation of liquid phase along the grain boundaries, which helps to improve the sinterability and microstructural features [12].

The role of various sintering additives on vast variety of electroceramics were largely investigated and their influence on microstructure is well established [13–18]. Apart from microstructural control, the presence of additive also affects magnetic and dielectric properties [19, 20]. The pinning effect caused by additive increases the coercivity,

---

* Corresponding author.
E-mail address: puneet.sharma@thapar.edu (P. Sharma).

https://doi.org/10.1016/j.matchemphys.2021.125574
Received 1 September 2020; Received in revised form 23 August 2021; Accepted 11 December 2021

Turnitin Originality Report

Processed on: 04-Mar-2022 12:26 IST
ID: 1776225032
Word Count: 18204
Submitted: 1

Similarity Index	Similarity by Source	
14%	Internet Sources:	6%
	Publications:	12%
	Student Papers:	3%

Anoop Singh Thesis By Anoop Singh

1% match (Internet from 28-Sep-2019)
https://link.springer.com/chapter/10.1007%2F978-3-642-55375-2_7

1% match (student papers from 28-Apr-2020)
Submitted to Thapar University, Patiala on 2020-04-28

1% match (Internet from 11-Jan-2022)
https://www.nature.com/articles/srep13645?code=ba922be8-cd28-495a-9367-88680e7c532d&error=cookies_not_supported

< 1% match (Internet from 19-Mar-2020)
https://link.springer.com/article/10.1007%2Fs10854-012-0740-7

< 1% match (Internet from 03-Apr-2018)
https://link.springer.com/article/10.1007/s10854-016-4549-7

< 1% match (Internet from 29-Jan-2020)
https://link.springer.com/article/10.1007%2Fs40995-018-0631-8

< 1% match (Internet from 24-Feb-2022)
https://link.springer.com/article/10.1007/s10854-016-4714-z?code=d984c6ad-e034-4f7a-ba43-5b6422c1a918&error=cookies_not_supported

< 1% match (Internet from 04-Mar-2020)
https://link.springer.com/article/10.1007%2Fs10854-018-0359-4

< 1% match (student papers from 23-Sep-2020)
Submitted to Thapar University, Patiala on 2020-09-23

< 1% match (publications)
Pawan Kumar, Anurag Gaur. "Multiferroicity in La, Pr & Sm doped Z-type strontium hexaferrite", Superlattices and Microstructures, 2018

< 1% match (Internet from 06-Oct-2021)
http://irgu.unigoa.ac.in/drs/bitstream/handle/unigoa/6021/coutinho_d_m_2019.pdf?isAllowed=y&sequence=1

< 1% match (publications)
Neha Solanki, G. Packiaraj, Rajshree B. Jotania. "Effect of Heat Treatment on Structural, Magnetic and Electric Properties of Z-Type Barium Cobalt Hexaferrite Powder", Advanced Materials Research, 2014